Sedimentary Processes on Earth and Mars: Canyon Erosion, Sand-Ripple Formation, and Mineral Composition

Thesis by

Mathieu G. A. Lapôtre

In Partial Fulfillment of the Requirements for

the degree of

Doctor of Philosophy

Caltech

CALIFORNIA INSTITUTE OF TECHNOLOGY

Pasadena, California

2017

(Defended May, 8th 2017)

Mathieu G. A. Lapôtre
ORCID: 0000-0001-9941-1552

There is life on Mars, and it is us — extensions of our eyes
in all directions, extensions of our mind,
extensions of our heart and soul
have touched Mars today.

—Ray Bradbury

ACKNOWLEDGEMENTS

This thesis is neither the end of my scholarly training nor the start of my scientific career, but it shall serve as proof that my advisors, mentors, colleagues, friends, and family have successfully fulfilled and surpassed their roles. To them, I am deeply indebted and grateful.

I thank Prof. Michael Manga of UC Berkeley, who initiated me to the world of academic research in 2009, when as an undergraduate student who could barely speak English I asked him if I could take my first research steps in his lab. I thank Chris Huber and Profs. Taylor Perron of MIT and Andrew Woods of Cambridge University for helping me solidify my commitment to research and pave my way to graduate school. I am forever grateful to my Ph.D. advisors at Caltech – Profs. Bethany Ehlmann and Michael Lamb. I could not have hoped for better mentors. Both were generous with their ideas but let me pursue my own. They inspired me to work on big, multidisciplinary, and exciting problems. I am also thankful to other members of the Caltech faculty for their advice and/or mentorship during the past five years, and in particular to Profs. John Grotzinger, Woody Fischer, Joe Kirschvink, Dave Stevenson, Ken Farley, and Dr. Matt Golombek of JPL. My coauthors have been a boundless source of knowledge and ideas, and I thank them for all they taught me. In particular, I thank Profs. Ray Arvidson, Ryan Ewing, Nathan Bridges, and Drs. Dave Rubin, Sarah Minson, Rebecca Williams, and François Ayoub for countless email discussions. I also thank Dr. Ashwin Vasavada of JPL and the entire MSL team for allowing me to join them in this incredible adventure that is driving a rover on Mars.

Numerous officemates over the years have made my graduate life joyful and fun. I thank the “pit” of 2012-2013 – Jennifer Buz, Brooke Dallas, Max Lloyd, Hayden Miller, Daven Quinn, Lewis Ward, and Junjie Yu, and all previous and subsequent officemates, including Austin Chadwick, Lauren Edgar, Ajay Limaye, Jeff Prancevic, Joel Scheingross, Katie Stack Morgan, and Jessica Watkins. Members of the Ehlmann and Lamb research groups have been a great source of support, inspiration, and fun. I give special thanks to Janice Grancich and Ulrika Terrones for their great support. While I cannot enumerate all group members who have contributed to my time at Caltech, I would like to thank Fanny Brun, Roman DiBiase, Chris Edwards, Abby Fraeman, Vamsi Ganti, Hima Gudipati, Alistair Hayden, Isaac Larsen, Ben Mackey, Luca Malatesta, Odin Mark, Peter Martin, Lu Pan, Nathan Stein, and Cindy Tran for their individual help, from processing data to swaping MSL shifts, for stimulating conversations, and for their friendship.

I simply cannot thank my friends enough for all they have contributed to my daily life at Caltech. In addition to those listed in previous paragraphs, I extend my gratitude to Kirsten Siebach for indulging my love of long walks on the beach, Nat Prunet, Murray Brightman, and Etienne Donckèle for our many runs and lunches, Perla Castillo, Quentin Maillet, and Paul-Hervé Tamokoué Kamga for our LA adventures, Christy Swann for letting me play in the NASA Ames wind tunnel with her, the French crew of my early Caltech days, Kristel Chanard, Rémi Lam, Baptiste Rousset, Quentin Bletery, and Marion Thomas, and those from back home who visited me and/or kept me entertained via Facebook – Sophie Bouscarat, Floriane Mottet, Alexandre Pachoud, Bruno Gavazzi, Michi Ruhnke, Marine Collignon, Marion Barbaray, and many others.

I arrived in California in 2012 having one family, and found myself a few years later with three of them. First, my French family – mom, dad, and Sandrine – thank you for your unconditional love and infinite support. You mean the world to me. Second, my American family, the Coltons, who have welcomed me in their home throughout my time in Pasadena – Sue and Ed, Tony, George, Michael (a.k.a. Grand Bonhomme), and Bailey – thank you for your boundless generosity. Thank you Grand Bonhomme for being my friend, for all the "fun stuffs", and thank you for introducing me to my playa family. Thank you awesomesaucers for being the best campmates in the world and all the fun and joy you bring into my life.

Finally, I would like to thank Monique, my car, for staying alive over the years despite her old age. Living in Los Angeles sure would not have been the same if it wasn't for our rides to the beach, the mountains, and the grocery store.

ABSTRACT

Over the past few decades, orbiters, landers, and rovers have significantly expanded our understanding of Mars' hydrology and climate; however, significant knowledge gaps stand in the way of our quest for martian life. In particular, the global drying of the planet remains one of the grandest unsolved mysteries in planetary science. To help unravel this puzzle, we develop new quantitative theories for sedimentary processes with implications for both Earth and Mars. This thesis revolves around three main sedimentary processes – erosion (Chapters 2-4), deposition (Chapters 5-6), and sediment transport (Chapters 7-8). In Chapters 2-4, we focus on the erosion of bedrock canyons by water on Earth and Mars. After showing that groundwater seepage erosion is only efficient at carving canyons in restricted conditions (Chapter 2), we develop a new hydraulic theory for flow focusing upstream of horseshoe-shaped waterfalls (Chapter 3) and combine it with waterfall-erosion mechanics to constrain the discharge, duration, and volume of canyon-carving floods on Earth and Mars (Chapter 4). We show that martian Hesperian floods were large but short-lived. In Chapters 5-6, we investigate fluid and sediment controls on the equilibrium size of bedforms. We develop a comprehensive scaling relation to predict the size of ripples forming in various sedimentary environments, including martian brines and methane flows on Titan (Chapter 5), and show that the scaling relation predicts the size of large wind ripples forming under a thin martian atmosphere (Chapter 6). This new theory, combined with observations of large-ripple cross-strata in wind-blown sandstones of the Burns formation at Victoria crater, suggests that Mars had a thin atmosphere around the Noachian-Hesperian boundary. Finally, in Chapters 7-8, we use orbiter-based inferences of the mineralogy of sands of the Bagnold dunes of Gale crater to disentangle the magnitude of wind sorting and local sediment sources. We first develop a new probabilistic framework to invert for surface mineralogy (Chapter 7), groundtruth our predictions with compositional datasets provided by the Curiosity rover, and discuss the implications of our findings for mineral sorting by martian winds and paleoenvironmental interpretations of martian wind-blown sandstones (Chapter 8). Collectively, these results provide new mechanistic and quantitative constraints on the past hydrology and climate of Mars that are key to assess Mars' astrobiological potential through space and time.

PUBLISHED CONTENT AND CONTRIBUTIONS

Chapter 2 is under consideration by *Nature Geoscience* as: Lapôtre, M. G. A., and M. P. Lamb, Substrate Controls on Valley Formation by Groundwater on Earth and Mars.

M. Lapôtre and M. Lamb conceived the study. M. Lapôtre developed the model and performed the analysis. M. Lapôtre wrote the manuscript with help from M. Lamb.

Chapter 3 is published as: Lapôtre, M. G. A., and M. P. Lamb (2015), Hydraulics of Floods Upstream of Horseshoe Canyons and Waterfalls, *Journal of Geophysical Research: Earth Surface*, *120*(7), 1227-1250, DOI:10.1002/2014JF003412.

M. Lapôtre and M. Lamb conceived the study. M. Lapôtre performed the numerical modeling and analysis. M. Lapôtre wrote the manuscript with help from M. Lamb.

Chapter 4 is published as: Lapôtre, M. G. A., et al. (2016), Canyon Formation Constraints on the Discharge of Catastrophic Outburst Floods of Earth and Mars, *Journal of Geophysical Research: Planets*, *121*(7), 1232-1263, DOI:10.1002/2016JE005061.

M. Lapôtre and M. Lamb conceived the study. M. Lapôtre developed the theory and implemented the model. M. Lapôtre performed the data analysis with help from R. Williams. M. Lapôtre wrote the manuscript with help from all coauthors.

Chapter 5 is published as: Lapôtre, M. G. A., et al. (2016), Large Wind Ripples on Mars: A Record of Atmospheric Evolution, *Science*, 353(6294), 55-58, DOI: 10.1126/science.aaf3206.

M. Lapôtre, R. Ewing, and M. Lamb conceived the study. R. Ewing and M. Ballard performed the orbital measurements. M. Lapôtre performed the rover-based measurements, developed the theory, and implemented the model. M. Lapôtre performed the data analysis with help from R. Ewing, M Lamb, and W. Fischer. M. Lapôtre wrote the manuscript with help from all coauthors.

Chapter 6 is published as: Lapôtre, M. G. A., et al. (2017), What Sets the Size of Current Ripples?, *Geology*, 45(3), 243-246, DOI: 10.1130/G38598.1.

M. Lapôtre and M. Lamb conceived the study. M. Lapôtre performed the data compilation and scaling analysis. M. Lapôtre wrote the manuscript with help from all coauthors.

Chapter 7 is published as: Lapôtre, M. G. A., et al. (2017), A Probabilistic Approach to Remote Compositional Analysis of Planetary Surfaces, *Journal of Geophysical Research: Planets*, in press, DOI: 10.1002/2016JE005248.

M. Lapôtre and B. Ehlmann conceived the study. M. Lapôtre and S. Minson implemented the MCMC algorithm based on a published algorithm from S. Minson. M. Lapôtre performed the analysis. M. Lapôtre wrote the manuscript with help from all coauthors.

Chapter 8 is published as: Lapôtre, M. G. A., et al. (2017), Compositional Variations in Sands of the Bagnold Dunes at Gale Crater, Mars, from Visible-Shortwave Infrared Spectroscopy and Comparison with Ground Truth from the Curiosity Rover, *Journal of Geophysical Research – Planets*, in press, DOI: 10.1002/2016JE005133.

M. Lapôtre and B. Ehlmann conceived the study. M. Lapôtre and S. Minson implemented the MCMC algorithm based on a published algorithm from S. Minson. M. Lapôtre performed the analysis. M. Lapôtre wrote the manuscript with help from all coauthors. This work benefited from the work of those involved in engineering and operations of the Mars Science Laboratory rover.

TABLE OF CONTENTS

LIST OF ILLUSTRATIONS

LIST OF TABLES

LIST OF ACRONYMS

APXS. Alpha Particle X-ray Spectrometer.
ASTER. Advanced Spaceborne Thermal Emission and Reflectin Radiometer.
ATO. Along-Track Oversampled.
ChemCam. Chemical Camera.
CheMin. Chemistry and Mineralogy.
CRISM. Compact Reconnaissance Imaging Spectrometer for Mars.
CTX. Context Camera.
DEM. Digital Elevation Model.
DISORT. Discrete Ordinates Radiative Transfer.
FRT. Full-Resolution Target.
GEL. Global Equivalent Layer.
HiRISE. High Resolution Imaging Science Experiment.
HRSC. High-Resolution Stereo Camera.
JPL. Jet Propulsion Laboratory.
MAHLI. Mars Hand Lens Imager.
MAP. Maximum A posteriori Probability.
Mastcam. Mast Camera.
MCMC. Markov-Chain Monte Carlo.
MSL. Mars Science Laboratory.
MOLA. Mars Orbiter Laser Altimeter.
MRO. Mars Reconnaissance Orbiter.
NASA. National Aeronautics and Space Administration.
OMEGA. Observatoire pour la Mineralogie, l'Eau, les Glaces, et l'Activite.
Pancam. Panoramic Camera.
RELAB. Reflectance Experiment Laboratory.
ROI. Region Of Interest.
SSA. Single Scattering Albedo.
SWIR. Shortwave Infrared.
TES. Thermal Emission Spectrometer.
USGS. United States Geological Survey.
VSWIR. Visible Shortwave Infrared.
XRD. X-Ray Diffraction.

Chapter 1

INTRODUCTORY REMARKS

1. Mars: A Promising Target for Finding Life Elsewhere.

The possibility of extraterrestrial life has fascinated and inspired humankind for centuries [e.g., *Lowell*, 1895; *McKay et al.*, 1996; *Grotzinger et al.*, 2014]. However, despite over 50 years of successful missions flown to and landed at Mars, the search for martian life continues in 2017. In its quest for extraterrestrial life, the strategy of NASA's Mars Exploration Program over the past few decades has been to "follow the water". In doing so, a lot was learned about the past hydrology and climate of Mars – much more than can possibly be summarized in this introductory chapter. Recent and more extensive reviews of the geologic, hydrologic, and climate history of Mars may be found in *Ehlmann et al.* [2016] and *Wordsworth* [2016]. Based on crater density and morphologic characteristics of the martian surface, the geologic history of Mars was divided into three main periods – the Noachian, Hesperian, and Amazonian periods – which roughly coincide with transitions in surface mineralogy [e.g., *Bibring et al.*, 2006] (Figure 1.1). Rocks found stratigraphically below Noachian strata are termed Pre-Noachian and are largely thought not to be represented at the martian surface. Numerous lines of evidence suggest that Noachian Mars hosted a well integrated hydrologic system, including dendritic valley networks [e.g., *Craddock and Howard*, 2002], lakes [e.g., *Fassett and Head*, 2008a], and perhaps a northern "ocean" [e.g., *Parker et al.*, 1989] (Figure 1.1). While fan-shaped deposits [e.g., *Di Achille and Hynek*, 2010] and valley networks [e.g., *Fassett and Head*, 2008b] indicate a relatively wet episode at the Late Noachian to Early Hesperian boundary, geologic evidence suggests that surface water flow became more sparse and episodic throughout the Hesperian period. Notably, the planetary-scale outflow channels of Mars formed during the Hesperian period through the catastrophic release of liquid water to the surface and subsequent erosion of the bedrock [e.g., *Carr and Head*, 2010] (Figure 1.1). Finally, the Amazonian period displays little to no evidence for sustained and stable flows of liquid water at the martian surface. Observations of surface mineralogy from orbiting spectrometers support the geomorphologic evidence of a global drying of Mars, with a transition from Fe/Mg-smectites found in exposures of Noachian crust, to Al-phyllosilicates, carbonates, chlorides, and sulfate minerals in Hesperian to Early Amazonian outcrops and deposits, to the predominance of Fe-oxides throughout Amazonian terrains [e.g., *Ehlmann and Edwards*, 2014]. Ultimately, the decline of water on Mars is thought to be intimately related to the thinning of the martian atmosphere [e.g., *Carr and Head*, 2010].

With wetter conditions and a thicker, perhaps warmer atmosphere, Mars was thus habitable when life first arose on Earth [e.g., *Grotzinger et al.*, 2014] (Figure 1.1), such that it is reasonable to speculate that life might also have arisen on Mars. Furthermore, Mars did not develop Earth-like mantle convection leading to plate tectonics [e.g., *Golombek and Phillips*, 2010], such that a significant fraction of the martian surface dates back to those ancient times, when life might have first evolved. Mars thus constitutes a prime exploration target to look for signs of early life in the solar system. Building on the success of its recent missions, NASA’s Mars Exploration Program has, in recent years, been transitioning to new phases – those of “exploring habitability” and “looking for signs of life”. The success of this next exploration phase will be determined by our ability to assess the astrobiological and preservation potentials of Mars through space and time in a quantitative manner. This thesis fits within the framework of placing such quantitative constraints on the hydrology, climate, and habitability of Mars from a physics-based understanding of sedimentary processes at the martian surface.

2. Sedimentary Processes: From Earth to Mars and Back

Sedimentary processes are both the creator and destroyer of landforms at the surface of planets (herein generalized to include any planetary body with a solid surface). They arise from complex interactions between external fluid layers (e.g., the atmosphere and hydrosphere) and a solid planetary surface, such that the landforms they leave behind record their formation environment. However, deciphering these sedimentary clues requires a rigorous physics-based understanding of sedimentary processes. In this thesis, we use a “liberal” definition of sedimentary processes that encompass all physical processes from erosion of a parent rock into sediment, to transport of the sediment, to the formation of sedimentary deposits.

While Earth-based geological knowledge is commonly applied to the study of other planetary surfaces and rocks, extraterrestrial landscapes and rocks hold clues about Earth that are largely underutilized. In this thesis, in particular, we intend to take full advantage of similarities and differences between the sedimentary processes of Earth and Mars. We use Earth-based work to better understand fundamental processes in fluids, sediment transport, and landscape evolution, which may in turn be applied to Mars. In addition, Mars offers the unique opportunity to test and challenge our understanding of how geological processes are affected by alien boundary conditions that are unachievable on Earth. This is particularly important because experimental work on Earth is often limited by our ability to explore a wide range of conditions.

The content of this thesis roughly follows the three main sets of sedimentary processes – erosion (Chapters 2-4), deposition (Chapters 5-6), and sediment transport (Chapters 7-8) – and illustrates how Earth-based knowledge may be applied to Mars and how new observations of the martian surface feed back onto our mechanistic understanding of sedimentary processes.

3. Canyon Erosion by Water

Despite significant recent advances in understanding the ancient hydrology of Mars, the decline of surface liquid water in the Late Noachian to Hesperian remains quantitatively unconstrained. In particular, two fundamental unknowns are (i) the relative importance of groundwater and overland flow during the Late Noachian to Mid-

Hesperian period, and (ii) the amount of liquid water involved in the formation of the giant outflow channels and related outburst floods. In the absence of a good mechanistic understanding of canyon formation in bedrock, groundwater sapping is often assumed to be responsible for martian amphitheater canyons by analogy to the sapping valleys formed in loose sediments and sedimentary rocks on Earth. This hypothesis has the significant implication that the erosive work was done by groundwater, as opposed to overland flow, making amphitheater-headed canyons prime astrobiological targets. Nevertheless, seepage erosion has not been observed in crystalline rock on Earth, and many martian canyons appear to be carved in basaltic lava flows, raising the issue that groundwater discharges may not be sufficient to erode canyons.

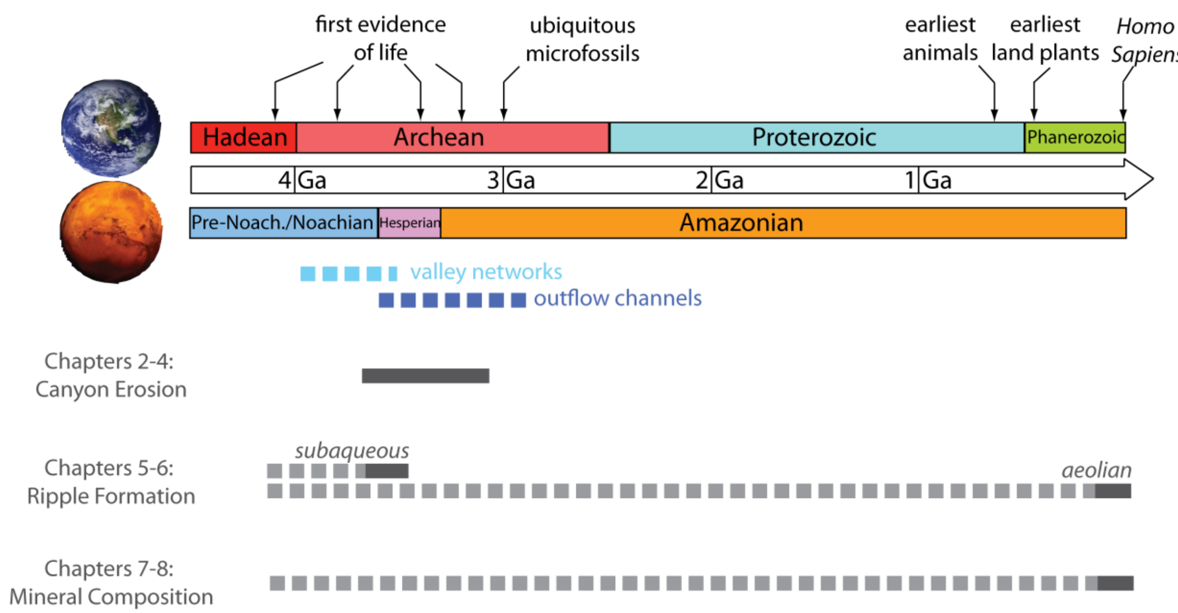

Figure 1.1: Geologic timescales of Earth and Mars. Periods of relevance of the following chapters are highlighted – darker continuous lines indicate that chapters directly address a geologic feature of the highlighted time period, while lighter dashed lines indicate that the work presented in the chapters is relevant to geologic features of the highlighted periods.

In Chapters 2-4, we explore the relative roles played by groundwater and overland flow in carving amphitheater-shaped canyons on Earth and Mars. Chapter 2 investigates lithological controls on the feasibility of forming a bedrock canyon by groundwater-fed spring erosion. To test the alternative hypothesis – that of waterfall-erosion by overland floods – we first develop a new hydraulic model for the convergence of water flow towards horseshoe-shaped waterfalls in Chapter 3. We then combine the new hydraulic model with waterfall-erosion mechanics in Chapter 4 to place tight constraints on flow discharge, duration, and volume of several canyon-carving floods on Earth and Mars. Work presented in these chapters is most relevant to the time of decline of surface hydrology on Mars, from the Late Noachian to the Early Amazonian periods (Figure 1.1).

4. Sand-Ripple Formation

Fluid flow over a granular bed leads to the formation of sedimentary structures, or bedforms, such as ripples and dunes. Because they arise from feedbacks between sediment grains and fluid flow, bedforms are a record of the environmental conditions in which they form, and their signature in sedimentary rocks, or cross-stratification, may be used to reconstruct paleoenvironments. Ripples are ubiquitous on the surface of Earth and one of the key sedimentary structures used to reconstruct the patterns and properties of flowing fluids on Earth and Mars from the sedimentary record. Despite their importance, we lack a unifying theory to relate the size of ripples to the environmental conditions in which they formed.

In Chapter 5-6, we focus on the formation of sand ripples by fluid flow over a granular bed. In Chapter 5, we develop a new scaling relation to predict the equilibrium size of current ripples from an extensive compilation of bedforms in flume experiments and natural rivers. This scaling relation can be applied under various environmental conditions, including flows of concentrated brines on Mars and of methane on Titan. In Chapter 6, we report on the discovery of a previously unidentified type of aeolian bedform on Mars using orbiter and rover-based imagery, and explore the applicability of the scaling relation developed in Chapter 5 to those bedforms. This work, which is primarily based on observation of modern active bedforms has surprising implications for atmospheric density around the Noachian-to-Hesperian boundary (Figure 1.1) and about our understanding of terrestrial aeolian bedforms.

5. Mineral Composition of Sands Sorted by Martian Winds

Sorting of sand grains during transport by the wind, e.g., by size, density, and shape, has been studied on Earth for a long time because it affects the composition of subsequently deposited aeolian sandstones. However, the distinct weathering environments and long transport pathways lead to wind-blown sands on Earth that are very homogeneous and, for the most part, made of quartz grains. Martian dune fields, however, are subjected to different boundary conditions and are largely made of polymineralic basaltic sand grains.

These fundamential differences between terrestrial and martian aeolian systems make it difficult to apply our Earth-based knowledge to martian dune fields and aeolian sedimentary rocks.

In Chapters 7-8, we use visible-shortwave infrared (VSWIR) spectroscopy to invert for mineralogy and grain sizes of sands within the active Bagnold Dunes of Gale crater, Mars, and disentangle the magnitude of mineral sorting and mixing during sediment transport by martian winds. VSWIR spectra of planetary surfaces are often used to constrain mineral composition and grain size. In particular, mineral abundances, and more rarely grain sizes, are typically found by finding a best fit model to spectra of the considered planetary surface. However, this inverse problem is highly non-unique, and suffers from instrumental noise, systematic errors in the forward radiative transfer models, and uncertainties associated to the precise chemical composition of mineral endmembers in the target, such that a best fit model may in fact not be representative of the true composition. In Chapter 7, we develop a new probabilistic framework to invert for ranges in mineral composition and grain sizes that are permitted by the data, and use this new framework to characterize uncertainties and errors associated with radiative transfer modeling of planetary surface composition. In Chapter 8, we apply the new technique to Compact Reconnaissance Imaging Spectrometer for Mars (CRISM) observations of the sands of the Bagnold Dunes at Gale crater, Mars, and groundtruth our orbiter-based predictions with compositional datasets from the Mars Science Laboratory (MSL) Curiosity rover. Quantitative inferences of mineralogy from CRISM data at several locations across the dune field are used to assess the degree to which martian winds sort basaltic sands today, and to discuss the implications for interpreting the composition of ancient martian aeolian sandstones (Figure 1.1).

Chapter 2

SUBSTRATE CONTROLS ON VALLEY FORMATION BY GROUNDWATER ON EARTH AND MARS

Mathieu G. A. Lapôtre and Michael P. Lamb

Abstract. Large valleys with amphitheater-shaped headwalls on Mars have been used to constrain early martian hydrology and, importantly, have been interpreted as eroded from groundwater flow [*Harrison and Grimm*, 2005; *Sharp and Malin*, 1975]. Groundwater-fed springs that have carved valleys are rare on Earth; however, where they do occur these valleys are in loose sandy sediments and weakly cemented sandstones [*Laity and Malin*, 1985; *Lamb et al.*, 2006; *Schumm et al.*, 1995]. Therefor, it is unclear whether groundwater is also an effective erosion agent in the basaltic bedrock and boulders observed at martian valleys. Here we develop a theoretical model for the efficiency of valley formation by groundwater seepage erosion, and show that valley formation by groundwater is limited to narrow ranges in aquifer permeabilities and sediment sizes that are characteristic of loose or weakly consolidated sand. The model explains the occurrence of groundwater carved valleys in loose sand in physical experiments [*Howard and McLane*, 1988; *Lobkovsky et al.*, 2004; *Lobkovsky et al.*, 2007; *Marra et al.*, 2014; *Schorghofer et al.*, 2004] and examples on Earth [*Laity and Malin*, 1985; *Lamb et al.*, 2008; *Lamb et al.*, 2014; *Larsen and Lamb*, 2016; *Schumm et al.*, 1995]. Applied to valleys near Echus Chasma, Mars, our model precludes formation by seepage erosion due to the inferred basaltic bedrock, and instead implies valley formation during floods of surface water, with implications for the hydrology, climate, and habitability of ancient Mars.

1. Introduction

The decline of surface hydrology from the Late Noachian to the Early Amazonian on Mars is one of the most dramatic examples of climate change known in the solar system [*Bibring et al.*, 2006], and appears to be genetically related to the loss of a once thicker CO_2 atmosphere [*Wordsworth*, 2016]. However, thinning of the atmosphere seems to have preceded the complete loss of surface-water activity [*Mangold et al.*, 2004; *Hu et al.*, 2015; *Grotzinger et al.*, 2015; *Lapôtre et al.*, 2016b; *Wordsworth*, 2016], at least in part through the episodic input of liquid water from the subsurface to the surface throughout the Hesperian and into the Early Amazonian period [*Harrison and Grimm*, 2005; *Sharp and Malin*, 1975]. In particular, amphitheater-headed valleys carved in Hesperian terrains have been interpreted as indicators of an increased relative contribution of groundwater to erosion from the Late Noachian into the Hesperian period [*Harrison and Grimm*, 2005]. These valleys, pending a rigorous understanding of their formation mechanism, thus represent a prime target to temporally resolve the fate of surface water on early Mars.

Because planform geometry of valleys is readily observable from satellite imagery, it is often used to constrain hydrologic regimes. However, valley morphology is not a unique indicator of formation process [*Lamb et al.*, 2006]. For example, groundwater seepage [*Schumm et al.*, 1995], overland flow [*Lamb et al.*, 2008], and combinations of the two [*Laity and Malin*, 1985; *Pelletier and Baker*, 2011] have all been proposed to explain the formation of amphitheater-shaped valleys on Earth and Mars (Figure 2.1), and have different astrobiological implications. Specifically, spring environments have been proposed as possible refugia for martian life and have high organics-preservation potential [*Farmer and Des Marais*, 1999]. Thus, there is a need to incorporate erosion mechanics into paleohydraulic reconstructions to better infer the formation process of amphitheater-headed valleys [*Lapôtre et al.*, 2016a].

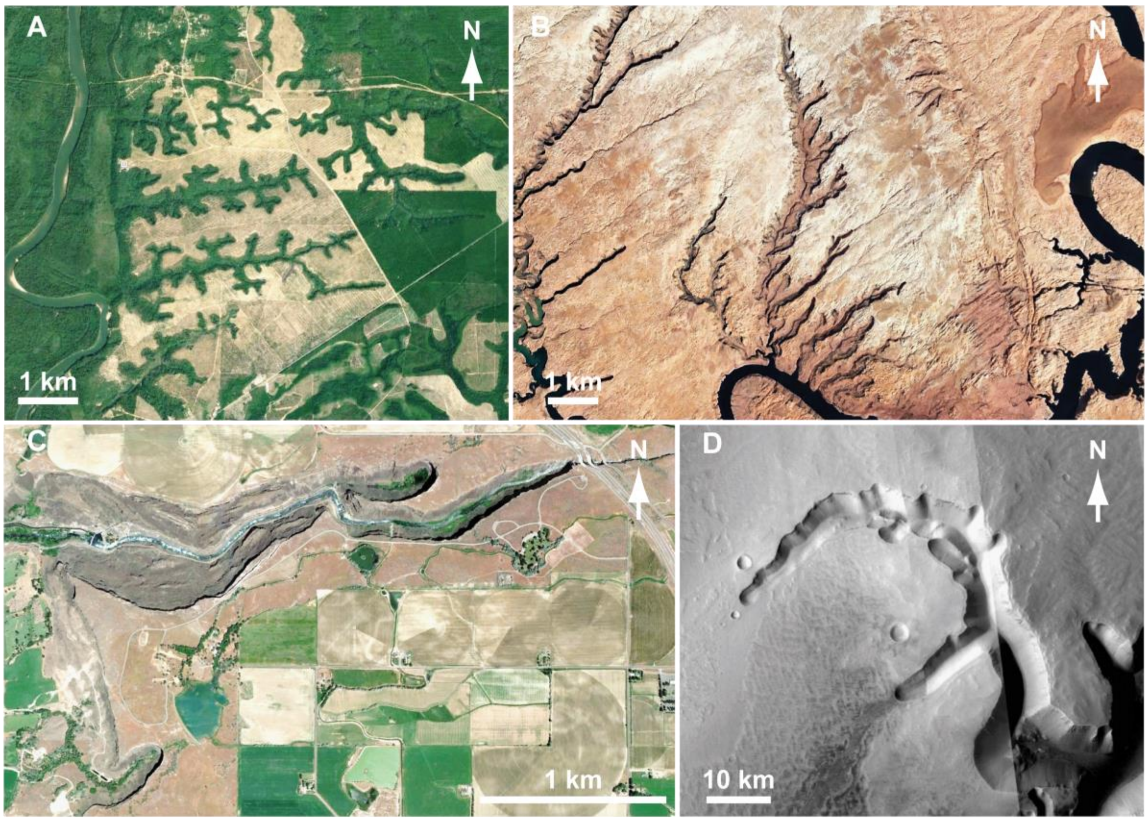

Figure 2.1: Amphitheater-headed valleys on Earth and Mars. Landsat mosaics of (A) seepage erosion valleys along the Apalachicola river, Liberty County, Florida (30.484ºN, -84.963E), (B) valleys carved in the Navajo sandstone near the Escalante river, Utah (37.393 ºN, -110.851 ºE), and (C) Malad Gorge valleys, Idaho (42.860 ºN, -114.869 ºE). (D) Mars Reconnaissance Orbiter Context Camera mosaic of valleys near Echus Chasma, Mars (1.194 ºN, -82.098 ºE).

Seepage erosion refers to the breakdown, detachment, and transport of material away from a groundwater-fed spring, which can lead to the formation of valleys through undermining and upslope retreat of the valley headwall [*Dunne*, 1990; *Lamb et al.*, 2006]. While previous studies have formulated mechanistic models for the formation of valleys by seepage erosion in loose sediment [*Howard and McLane*, 1988; *Lobkovsky et al.*, 2004], there is not yet a model to predict the necessary conditions for seepage erosion to carve a valley, and whether groundwater can carve valleys in sediment of different sizes or in different rock types, such as the basaltic rock and boulder rubble that are common to martian valleys [*Tanaka et al.*, 2014]. Moreover, models for martian valleys often assume that seepage erosion rates on Mars are proportional to groundwater discharge [*Abrams et al.*, 2009; *Howard*, 1987; *Pelletier and Baker*, 2011], an assumption that has only been verified for loose sand [*Howard and McLane*, 1988; *Marra et al.*, 2014].

An alternative hypothesis is that floods of surface water formed the martian amphitheater valleys in basalt; floods have been argued to deliver sufficient water to entrain blocks of basaltic rock, transport boulders downstream, and form amphitheater-shaped headwalls through flood-flow focusing and block toppling at waterfalls [*Irwin et al.*, 2014; *Lamb and Dietrich*, 2009; *Lamb et al.*, 2008; *Lamb et al.*, 2007; *Lamb et al.*, 2014; *Lapôtre and Lamb*, 2015]. While numerical models have been used to argue that amphitheater headwalls are diagnostic of seepage erosion [*Pelletier and Baker*, 2011], these models do not include the physics of waterfall erosion that have been found to produce amphitheater headwalls [*Irwin et al.*, 2014; *Lamb and Dietrich*, 2009; *Lamb et al.*, 2008; *Lamb et al.*, 2007; *Lamb et al.*, 2006; *Lamb et al.*, 2014; *Lapôtre and Lamb*, 2015; *Lapôtre et al.*, 2016a]. Still, the morphologic similarity between the large bedrock canyons on Mars and seepage erosion experiments in sand, and the lack of a physics-based model to demonstrate the feasibility of seepage erosion in basalt, has led to the persistent assumption that amphitheater-headed valleys are diagnostic of seepage erosion [*Harrison and Grimm*, 2005; *Pelletier and Baker*, 2011; *Sharp and Malin*, 1975].

In order investigate the feasibility of seepage erosion in a wide range of substrates, including basaltic rock and granular material of different size, we formulate a conservative theoretical model which couples equations of groundwater flow and sediment transport. We focus on quantifying the necessary condition for valley formation by seepage erosion – spring flow must be able to evacuate sediment from the valley head [*Lamb et al.*, 2006]. In particular, for sediment substrates, we seek to characterize how grain size influences permeability and sediment transport, which leads to tradeoffs in seepage erosion potential. Likewise, for bedrock, certain combinations of substrate permeability and the sizes of collapsed blocks at the seepage face are required for valley formation.

2. Methods

Building on previous studies [*Howard*, 1987; *Howard and McLane*, 1988; *Lobkovsky et al.*, 2004], we consider a one-dimensional drainage basin of length L with a constant topographic slope, S, upstream of a vertical seepage face of height H_c. The latter defines the headwall of a valley of bed slope S_b (Figure 2.2). All groundwater is transmitted through the seepage face, as would be the case with an impermeable-rock unit at the seepage face base [*Laity and Malin*, 1985]. We define the seepage-erosion efficiency factor, f, as

$$f = \frac{h_n}{h_{im}}, \tag{2.1}$$

where h_n is flow depth within the valley, and h_{im} is the critical flow depth for sediment motion. When $f \geq 1$, eroded material can be transported, and valley formation by seepage is possible. Conversely, when $f < 1$, seepage is not sufficient to transport sediment and cannot carve a valley. We couple Darcy's law to equations of surface flow hydraulics and sediment transport (Section 5), and derive an equation that relates the seepage-erosion efficiency factor, f, to subsurface flow, aquifer and valley geometry, open-channel flow hydraulics, and sediment transport regime:

$$f^{3/2} = \frac{1}{2} \mathrm{Da}\, \mathrm{Re_p} \frac{H^*}{L^*} \frac{C_\mathrm{f}^{1/2} S_\mathrm{b}}{R^2 \tau_{*\mathrm{c}}^{3/2}} \left[\left(1 + SL^*\right)^2 - \left(\frac{\tau_{*\mathrm{c}} R}{\phi S_\mathrm{b} H^*} \right)^2 f^2 \right], \tag{2.2}$$

where $\mathrm{Da} = \frac{\kappa_\mathrm{eff}}{D^2}$ is the Darcy number of the flow (with κ_eff the aquifer permeability and D sediment-grain diameter), $\mathrm{Re_p}$ is the particle Reynolds number, $H^* = \frac{H_\mathrm{c}}{D}$ is a dimensionless valley depth, $L^* = \frac{L}{H_\mathrm{c}}$ is a dimensionless basin length, C_f is a bed-friction factor, S and S_b are the upstream and downstream bed slopes, respectively, R is the submerged specific density of the sediment, $\tau_{*\mathrm{c}}$ is the critical Shields stress for incipient motion of the sediment, and ϕ is porosity of the aquifer (Section 5). Particle Reynolds number, critical Shields stress, and bed-friction factor are parametrized as a function of grain diameter (Section 5), and the other parameters can be estimated from field observations or remote sensing (Table 2.1).

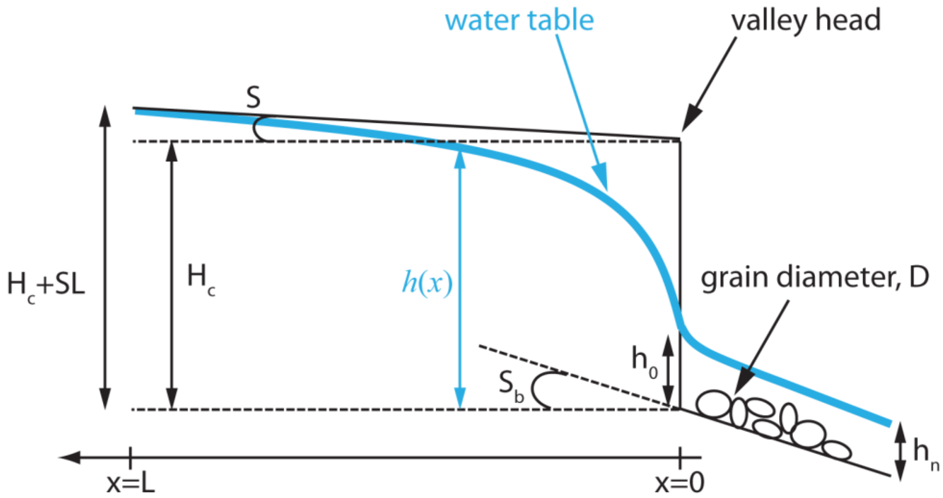

Figure 2.2: Conceptual cross-section of the seepage face at a valley head. A drainage basin of length L drains towards a vertical seepage face of height H_c. Topographic slopes upstream and downstream of seepage face are S and S_b, respectively. The water table upstream of the seepage face, defined by its height h above the base of the seepage face, breaks the land line near the drainage divide and emerges at a height h_0. Sediment of diameter D form by seepage erosion and is mobilized when flow depth in the valley, h_n, exceeds the critical depth for sediment transport.

Here, we solve Equation (2.2) for permeability (κ_{eff}) as a function of grain diameter (D) at $f=1$ in order to characterize the onset of valley seepage-erosion feasibility. We apply the model to: (1) physical experiments of seepage erosion in loose sand[*Howard*, 1987; *Lobkovsky et al.*, 2004; *Lobkovsky et al.*, 2007; *Schorghofer et al.*, 2004]; (2) valleys carved in loose sand by groundwater seepage erosion in the Florida Panhandle [*Schumm et al.*, 1995] (Figure 2.1A); (3) valleys carved in sandstones of the Colorado Plateau[*Howard*, 1987; *Laity and Malin*, 1985], whose origin as it relates to groundwater seepage erosion vs. surface water is debated [*Lamb et al.*, 2006] (Figure 2.1B); and (4) valleys carved in fractured basaltic bedrock on Earth (Figure 2.1C) and Mars (Figure 2.1D) [*Lamb et al.*, 2008; *Lamb et al.*, 2014; *Lapôtre et al.*, 2016a; *Larsen and Lamb*, 2016; *Mangold et al.*, 2008]. Through a sensitivity analysis, our results are found to constitute robust limits on seepage-erosion efficiency despite the one dimensional framework and simplified theory owing to the conservative assumptions made in deriving Equation (2.2) (Figures 2.4-2.9). We compare the results to an empirical relationship between permeability and grain size for natural granular materials, using loose well sorted and weakly consolidated sediment as conservative upper and lower bounds, respectively. Because competent rock, such as fractured basalt, does not follow this relation, we also compiled grain size and permeability bounds for various locations on Earth (Figure 2.3A-C).

3. Results

Model results show that seepage erosion for loose, unconsolidated sediment is only possible for sediment sizes within the range of coarse-silt to very-fine-gravel. Despite large differences in scale, we find the $f = 1$ boundary for kilometer-scale Florida Panhandle valleys to roughly coincide in (D, κ_{eff})-space with meter-scale valleys produced in physical experiments (Figure 2.3A). For poorly sorted or consolidated sediment, seepage erosion is limited to only sand sizes (Figure 2.3A). In general, finer grains are easier to transport, but seepage discharges are insufficient to mobilize the grains due to low permeabilities. Seepage discharges are larger for coarser sediment due to large permeabilities, but remain below the threshold needed for sediment transport owing to heavier grains.

For competent rock, seepage erosion is only predicted to occur for very limited eroded grain sizes and permeability combinations that are characteristic of unconsolidated or weakly consolidated sand. In the weakly cemented sandstones that compose valleys within the Colorado Plateau, we find that grain sizes and permeabilities place valleys near the onset of seepage erosion feasibility (Figure 2.3B). This result is consistent with the argument that despite efficient salt-weathering and enhanced groundwater discharge at the Kayenta-Navajo lithological contact, episodic flash floods are required to flush eroded material away from valley heads [*Howard*, 1987; *Laity and Malin*, 1985; *Lamb et al.*, 2006]. In contrast, and despite some of the largest aquifer permeabilities on Earth [*Meinzer*, 1927], amphitheater-headed valleys of the basaltic Snake River plain, Idaho, and the Channeled Scabland, Washington, clearly fall within the $f<1$ regime, inconsistent with a seepage erosion mechanism, but consistent with field evidence of valley formation by large-scale flooding in those regions [*Lamb et al.*, 2008; *Lamb et al.*, 2014; *Lapôtre et al.*, 2016a; *Larsen and Lamb*, 2016] (Figure 2.3C). Thus, both experimental and field data support our new theoretical model, which can be applied to martian valleys.

The walls of selected valleys near Echus Chasma [*Lapôtre et al.*, 2016a; *Mangold et al.*, 2008] appear to consist of Hesperian age basaltic lava-flow beds, with sub-vertical fractures similar to cooling joints [*Lapôtre et al.*, 2016a], that break down to meter-scale boulders. Using orbiter-based topographic measurements (Section 5), we find that the $f=1$ boundary for the considered valleys roughly coincides with that for terrestrial valleys in Idaho and Washington, and that observed block sizes and estimated permeabilities do not permit a groundwater seepage origin of the valleys (Figure 2.3C).

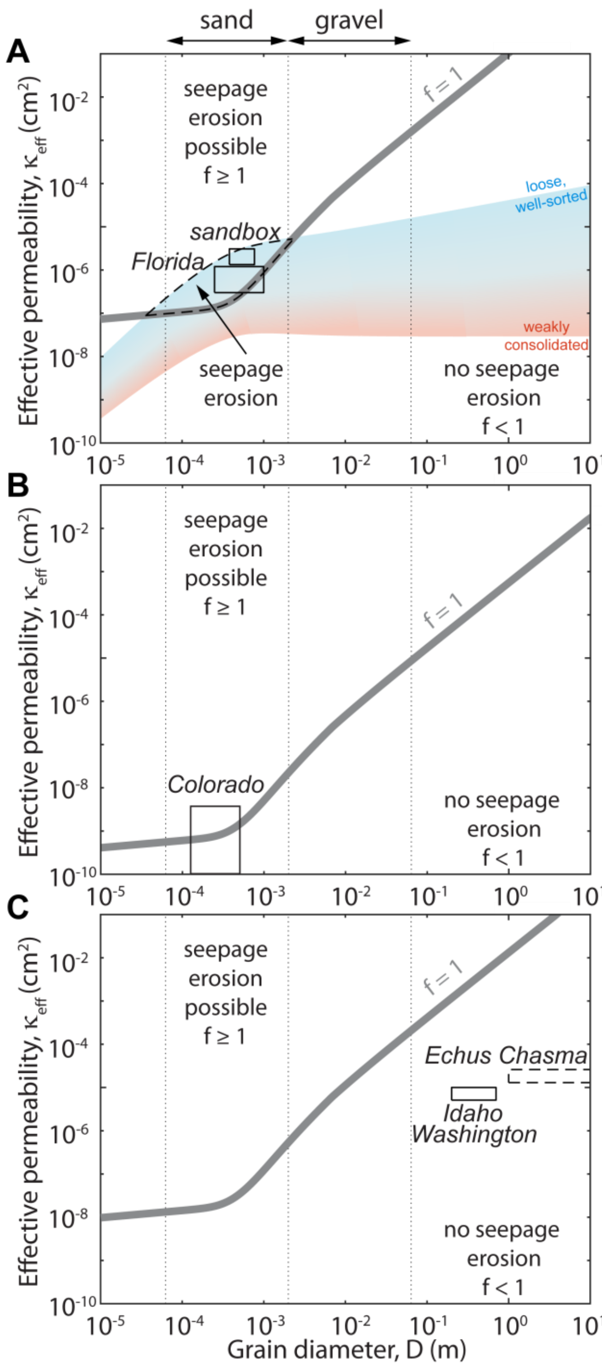

Figure 2.3: Seepage erosion efficiency. Seepage-erosion feasibility ($f = 1$) as function of grain diameter and aquifer permeability for (A) physical experiments and Florida panhandle valleys in loose sand, (B) Colorado Plateau valleys in sandstone, and (C) basaltic valleys on Earth and Mars. Boxes outline reported (solid) or estimated (dashed) values (Table 2.1). In (A), we report known permeabilities of weakly consolidated and loose well sorted sediment as conservative bounds [*Shepherd*, 1989] (see Section 5.2). The $f = 1$ line is at lower permeabilities for the Colorado Plateau valleys due to steep bed slopes upstream and downstream of the seepage face, which increase hydraulic head and facilitate sediment transport.

Valley formation by seepage erosion near Echus Chasma appears to require the unlikely scenario of permeabilities approximately ten-thousand-fold greater than those observed in some of the most permeable basaltic aquifers on Earth.

4. Discussion

Our findings cast doubt on the assumption in most analytical and numerical models [*Abrams et al.*, 2009; *Howard*, 1987; *Pelletier and Baker*, 2011] for valley formation by groundwater seepage erosion that headwall-retreat rate is proportional to seepage discharge. While the groundwater scenario may be valid in loose sand [*Howard and McLane*, 1988; *Marra et al.*, 2014], we find that a more plausible scenario for the large valleys in competent rock on Mars is erosion by floods of surface water [*Irwin et al.*, 2014; *Lamb and Dietrich*, 2009; *Lamb et al.*, 2008; *Lamb et al.*, 2007; *Lamb et al.*, 2014; *Lapôtre and Lamb*, 2015].

Valley erosion by surface flow, rather than groundwater, has significant implications for the ancient hydrology, climate, and habitability of Mars. While both valley formation mechanisms may require similar water volumes, they involve different water sources, radically different flow discharges, and thus different hydrologic pathways and timescales over which liquid water was thermodynamically stable at the martian surface. By exploiting valley morphology, lithology, and erosion mechanics, our model supports the case for active valley-carving floods throughout the decline of surface water hydrology on Mars.

5. Supplementary Information

5.1. Seepage-Erosion Efficiency

Combining momentum conservation and a bed-friction law yields, for steady uniform flow depth within the valley (h_{n}),

$$h_{\mathrm{n}} = \left(\frac{C_{\mathrm{f}} q_0^2}{g S_{\mathrm{b}}} \right)^{1/3}, \tag{2.3}$$

where C_{f} is a dimensionless bed-friction factor, q_0 is the discharge per unit width, and S_{b} is bed slope within the valley. Under the assumption of steady uniform flow within the valley, the critical flow depth for incipient motion of the sediment is

$$h_{\mathrm{im}} = \frac{\tau_{*\mathrm{c}} R D}{S_{\mathrm{b}}}, \tag{2.4}$$

where D is grain diameter, $R = \frac{(\rho_{\mathrm{s}} - \rho)}{\rho}$ is submerged specific density of the sediment (with ρ_{s} and ρ the sediment and water densities, respectively), and $\tau_{*\mathrm{c}}$ is the critical Shields stress for incipient motion of the sediment (which is a function of $\mathrm{Re}_{\mathrm{p}} = \frac{\sqrt{RgD}D}{\nu}$) [*Parker et al.*, 2003]. Combining Equations (2.3) and (2.4) yield, the seepage-erosion efficiency factor,

$$f = \frac{h_{\mathrm{n}}}{h_{\mathrm{im}}} = \frac{(n q_0)^{3/5} S_{\mathrm{b}}^{7/10}}{\tau_{*\mathrm{c}} R D}. \tag{2.5}$$

From Darcy's law, and assuming mass conservation at the seepage face,

$$q_0 = \frac{g \kappa_{\mathrm{eff}}}{\nu} h \frac{dh}{dx}, \tag{2.6}$$

where g is gravitational acceleration, κ_{eff} is effective aquifer permeability, ν is kinematic viscosity of water, and h is the height of the water table above a horizontal datum leveled with the bottom of the seepage erosion face (Figure 2.2). Combined with the boundary condition $h(x=0)=h_0$, Equation (2.6) yields

$$h(x)=\sqrt{\frac{2q_0\nu}{g\kappa_{\mathrm{eff}}}x+h_0^2}\,. \tag{2.7}$$

From the considered valley geometry (Figure 2.2), it can be seen that $h(x=L)=H_{\mathrm{c}}+SL$ (with H_{c} the height of the seepage face, S the topographic slope upstream of the seepage face, and L the drainage-basin length), such that the Darcy discharge per unit width is given by

$$q_0=\frac{g\kappa_{\mathrm{eff}}}{2L\nu}\left\{\left(H_{\mathrm{c}}+SL\right)^2-h_0^2\right\}. \tag{2.8}$$

From mass conservation at the cliff face,

$$\phi h_0=h_{\mathrm{n}}, \tag{2.9}$$

where ϕ is the porosity of the aquifer. Combining Equations (2.5), and (2.8)-(2.9) yields

$$f^{3/2}=\frac{1}{2}\left(\frac{C_{\mathrm{f}}}{g}\right)^{1/2}\frac{g\kappa_{\mathrm{eff}}}{\nu D^{1/2}}\frac{H*}{L*}\frac{S_{\mathrm{b}}}{\left(\tau_{*\mathrm{c}}R\right)^{3/2}}\left[\left(1+SL*\right)^2-\left(\frac{\tau_{*\mathrm{c}}R}{\phi S_{\mathrm{b}}H*}\right)^2 f^2\right], \tag{2.10}$$

which, using the definitions of Da and Re_{p} can be rewritten as Equation (2.2).

We parametrize the bed-friction coefficient as a function of bed roughness, k, and normal-flow depth, h_{n}, through [*Brownlie*, 1983]

$$C_{\mathrm{f}}=\frac{1}{(8.1)^2}\left(\frac{k}{h_{\mathrm{n}}}\right)^{1/3}. \tag{2.11}$$

Combining Equations (2.1) and (2.4), we can substitute for h_n into Equation (2.11),

$$C_\mathrm{f} = \frac{1}{65.6}\left(\frac{kS_\mathrm{b}}{f\,\tau_{*\mathrm{c}}RD}\right)^{1/6}. \tag{2.12}$$

We parametrize the effect of channel-form roughness and grain-size on bed roughness through

$$k = \begin{cases} k_0, \text{ for } D < D_0 \\ \alpha D, \text{ for } D \geq D_0 \end{cases}, \tag{2.13}$$

where $k_0 \approx 1.7$ cm corresponds to a smooth sand-bedded terrestrial channel (Manning's *n* value of 0.02) [*Chow*, 1959], and α is a constant equal to 2.5 [*Brownlie*, 1983; *Kamphuis*, 1974]. To ensure continuity of roughness as a function of grain size, the cross-over grain size, D_0, is defined as the grain size for which both formulations of k are equal (i.e., $D_0 \approx 6.8$ mm).

5.2. Permeability

We use empirical fits to hydraulic conductivity on consolidated and loose well sorted sediment [*Shepherd*, 1989] as conservative lower and upper bounds, and thus calculate conservative bounds on intrinsic permeability, κ,

$$\kappa_\mathrm{min} = 11.9\left(\frac{\nu}{g}\right)D^{1.5} \tag{2.14}$$

and

$$\kappa_\mathrm{max} = 6695\left(\frac{\nu}{g}\right)D^{1.85}. \tag{2.15}$$

In order to incorporate fluid inertia at high flow rates, we use an apparent permeability [*Barree and Conway*, 2004; *Bear*, 1972],

$$\kappa_{\text{eff}} = \frac{\kappa}{1+\text{Re}_\beta}, \tag{2.16}$$

where $\text{Re}_\beta = \frac{u(\beta\kappa)}{\nu}$, with u the water discharge per unit area, and β the Forchheimer coefficient (or inertial factor). It was shown experimentally [*Barree and Conway*, 2004] that $(\beta\kappa) \approx 2D$ for unconsolidated material. We assume that the latter relation holds for consolidated sediment. Under the assumption of steady uniform flow,

$$\tau_* = \frac{u_*^2}{RgD} = \frac{h_\text{n} S_\text{b}}{RD}, \tag{2.17}$$

where u_* is the flow shear velocity in the valley, and is defined as $\sqrt{\frac{\tau_b}{\rho}}$ with τ_b the boundary shear stress imparted by flow on the valley bed, such that

$$f = \frac{\tau_*}{\tau_{*\text{c}}}. \tag{2.18}$$

Using mass conservation, $u \sim \phi u_*$, and combining Equations (2.16) - (2.18), we find that

$$\kappa_{\text{eff}} = \frac{\kappa}{\left(1+2\phi\sqrt{f\tau_{*\text{c}}}\,\text{Re}_\text{p}\right)}, \tag{2.19}$$

where κ is bounded by $\kappa_{\min}$ and $\kappa_{\max}$. At low water discharges, $\kappa_{\text{eff}} = \kappa$, and κ_{eff} deviates from κ as water discharge increases due to inertial effects, which causes the *f* = 1 line in Figure 2.3 to plateau for larger grain sizes. Because we assume detached-sediment sizes are representative of the grain sizes/fracture spacing in the aquifer rocks, our model implicitly neglects other detachment mechanisms (such as salt weathering or aeolian abrasion).

5.3. Why is the Model Conservative?

Our formulation for the seepage erosion efficiency factor is conservative (i.e., most favorable to seepage erosion) because:

(1) It neglects inertial effects at high groundwater discharges; solving for the full Forcheimer equation, for example, would yield lower seepage discharges for a given permeability, effectively shifting the $f = 1$ boundary to lower grain sizes.

(2) We assume that all of the groundwater is transmitted to the valley through the seepage face, i.e., that no groundwater discharge is lost to seepage underneath the valley bottom.

(3) We assume that erosion is transport-limited while in reality seepage discharge may not be sufficient to surpass any relevant detachment threshold.

(4) We solved for the onset of sediment transport (f = 1). However, f needs to be greater than unity for sediment to be removed from the valley head. Solving Equation (2.2) for $f > 1$ shifts the f boundary to higher permeabilities and the $\kappa_{\text{eff}}(D)$ field to lower permeabilities (Figure 2.4).

5.4. Sensitivity Analysis.

We evaluate the effect of three-dimensional groundwater flow by way of a focusing factor, ω, defined as the ratio of actual to one-dimensional seepage discharge, such that Equation (2.8) is replaced with

$$q_0 = \frac{\omega g \kappa}{2L\nu}\left\{\left(H_{\text{c}} + SL\right)^2 - h_0^2\right\}. \tag{2.20}$$

In the case of the valleys of the Florida Panhandle, the maximum value of ω was found to be $\omega \approx 5$ by comparing highly-curved valley heads and linear escarpments (no curvature) [*Petroff et al.*, 2011]. Using $\omega = 5$, we find that seepage erosion remains confined to grain-sizes finer than fine gravel in loose sediment and sand-sized weakly consolidated sedimentary rocks. Even for an unrealistically large value of $\omega = 20$, we find that seepage erosion is not permitted for grain sizes coarser than ~1.5 cm and sand-sizes for weakly consolidated sediments (Figure 2.5).

We also evaluate the effect of varying valley depth by a factor of three (H_c; Figure 2.6), drainage-basin length by a factor of 100 (L; Figure 2.7), and upstream and downstream bed slopes by a factor of five (S and S_b; Figures 2.8 and 2.9, respectively). We find that in all of these cases, seepage erosion is only permitted in grain sizes between silt and medium gravel in loose sediment, and in sand-sizes for weakly consolidated sediments.

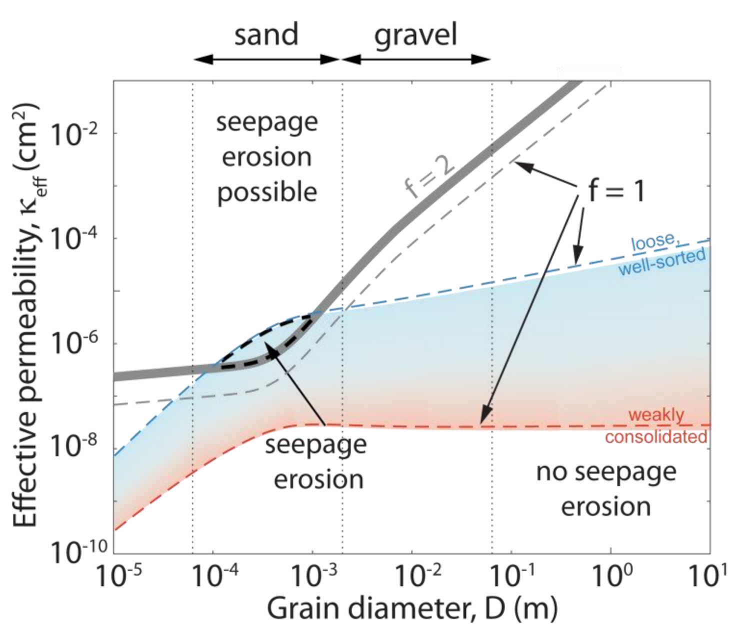

Figure 2.4: The case of $f = 2$ for unconsolidated sediment. Input parameters used are those of the Florida Panhandle (Table 2.1).

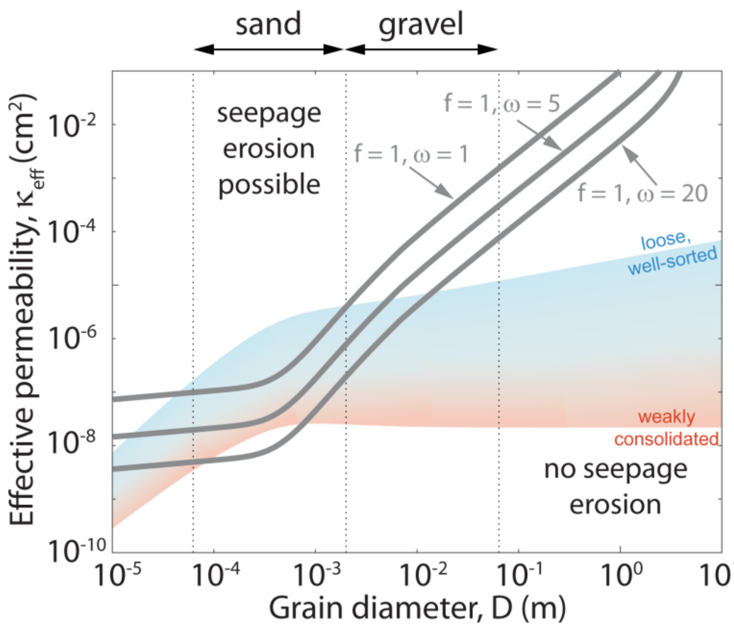

Figure 2.5: Effect of focusing of groundwater in the valley head (ω). Input parameters used are those of the Florida Panhandle (Table 2.1).

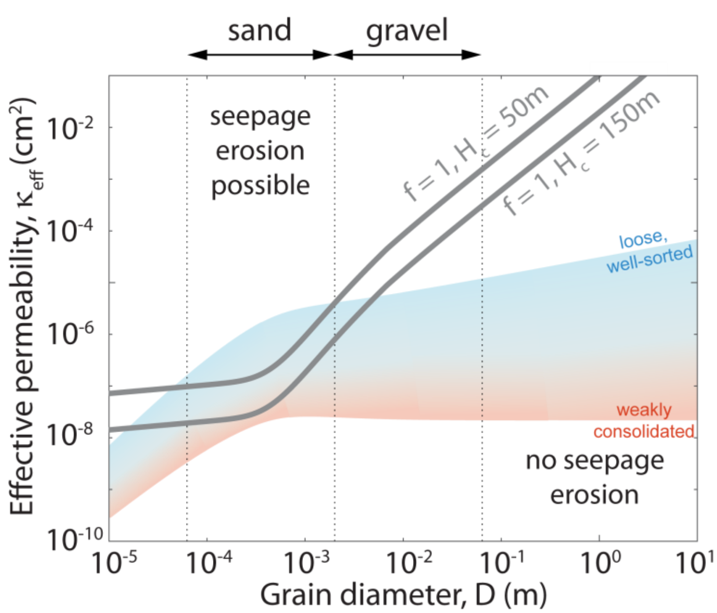

Figure 2.6: Effect of varying valley depth (H_c). Other input parameter values are $L = 10$ km, $S = 3\times10^{-3}$, and $S_b = 1\times10^{-2}$.

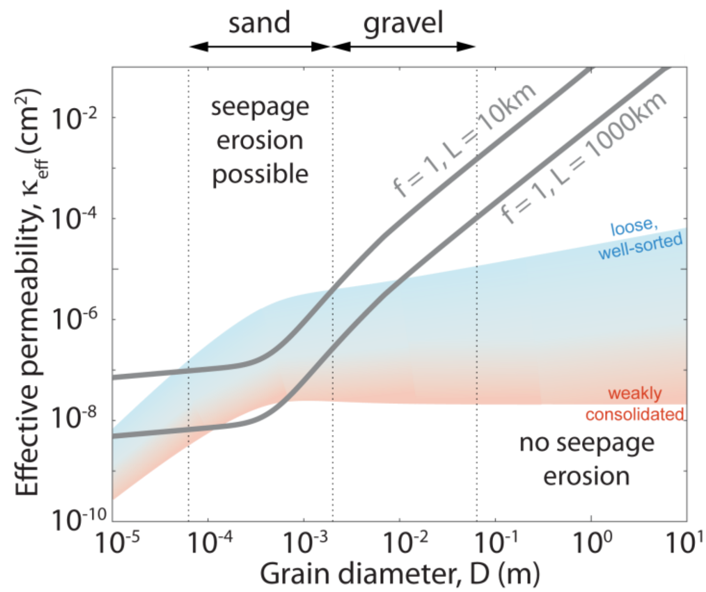

Figure 2.7: Effect of varying drainage-basin length (L). Other input parameter values are $H_c = 50$ m, $S = 3\times10^{-3}$, and $S_b = 1\times10^{-2}$.

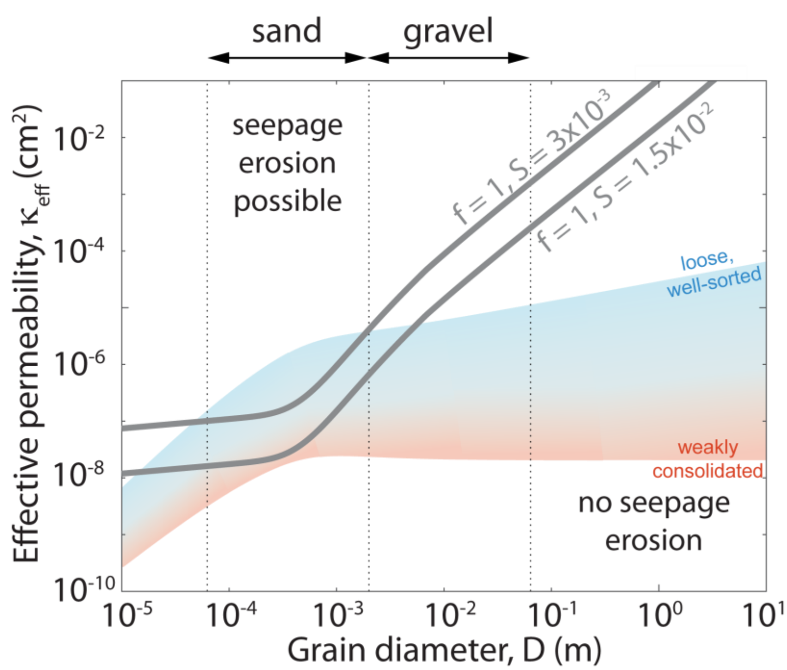

Figure 2.8: Effect of varying upstream bed slope (S). Other input parameter values are $H_c = 50$ m, $L = 10$ km, and $S_b = 1\times10^{-2}$.

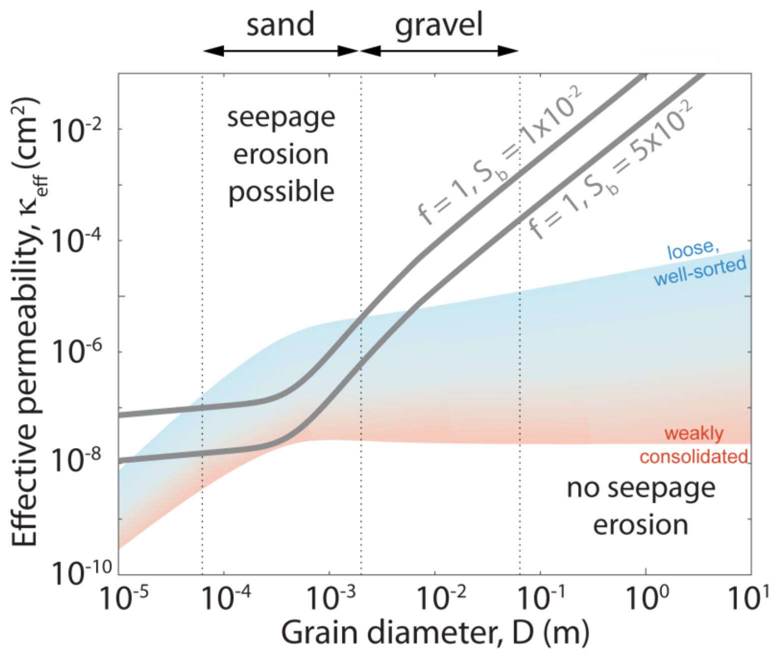

Figure 2.9: Effect of varying downstream bed slope (S_b). Other input parameter values are $H_c = 50$ m, $L = 10$ km, and $S = 3\times10^{-3}$.

5.5. Parameters Compilation for Case Studies

Table 2.1 summarizes input parameters. Data from physical experiments comes from previous studies [*Howard and McLane*, 1988; *Lobkovsky et al.*, 2004; *Lobkovsky et al.*, 2007; *Schorghofer et al.*, 2004]. Basin length was measured from 90-m Shuttle Radar Topography Mission [*Farr et al.*, 2007] topography for terrestrial valleys, and Mars Orbiter Laser Altimetry [*Smith et al.*, 2001] topography for martian valleys. Valley depth, as well as upstream and bottom slopes were measured from Advanced Spaceborne Thermal Emission and Reflection Radiometer [*Yamaguchi et al.*, 1998] and Mars Reconnaissance Orbiter Context Camera [*Malin et al.*, 2007] digital elevation models on Earth and Mars, respectively. Grain size and permeability ranges were compiled from previous studies [*Abrams et al.*, 2009; *Laity and Malin*, 1985; *Lamb et al.*, 2008; *Lamb et al.*, 2014; *Lapôtre et al.*, 2016a; *Petroff et al.*, 2011; *Shipton et al.*, 2002; *Zuluaga et al.*, 2014], with the exception of Echus Chasma, for which we assumed a hydraulic conductivity equal to the highly permeable Snake River plain basaltic aquifer, and converted to permeability by adjusting for martian gravity.

Submerged specific density of sediment, $R = 1.65$ for sediments and sedimentary rocks, and 1.9 for basalt on Earth and Mars. Acceleration of gravity is 9.81 m/s^2 on Earth and 3.78 m/s^2 on Mars. Aquifer porosity is assumed to be 35%, and kinematic viscosity of water is 1×10^{-6} m^2/s.

	Used to calculate seepage erosion-efficiency factor, f				Additional constraints	
	Basin length, L **(m)**	**Seepage-face height,** H_c **(m)**	**Upstream slope,** S	**Bottom slope,** S_b	**Grain diameter,** D **(m)**	**Permeability,** κ_{eff} **(cm²)**
Sandbox experiments [*Howard and McLane*, 1988; *Lobkovsky et al.*, 2004; *Lobkovsky et al.*, 2007; *Schorghofer et al.*, 2004]	2	1×10^{-2}	1×10^{-1}	1.5×10^{-1}	3.7×10^{-4} - 7.5×10^{-4}	1.3×10^{-6} - 3×10^{-6}
Florida [*Abrams et al.*, 2009; *Petroff et al.*, 2011]	1×10^{4}	50	3×10^{-3}	1×10^{-2}	2.8×10^{-4} - 1×10^{-3}	3×10^{-7} - 1.2×10^{-6}
Colorado Plateau [*Laity and Malin*, 1985; *Shipton et al.*, 2002; *Zuluaga et al.*, 2014]	1×10^{4}	100	3×10^{-2}	5×10^{-2}	1.25×10^{-4} - 5×10^{-4}	1×10^{-10} - 5×10^{-9}
Idaho & Washington [*Lamb et al.*, 2008; *Lamb et al.*, 2014; *Lapôtre et al.*, 2016a]	4.5×10^{5}	100	3×10^{-3}	1×10^{-2}	0.2-0.7	5.1×10^{-6} - 1×10^{-5}
Echus Chasma, Mars [*Lapôtre et al.*, 2016a]	3×10^{5}	440	3×10^{-3}	1×10^{-2}	1-10	1.3×10^{-5} - 2.5×10^{-5}

Table 2.1: Model input parameters. Model input parameters are representative of (1) materials and scales of physical experiments in sand [*Howard and McLane*, 1988; *Lobkovsky et al.*, 2004; *Lobkovsky et al.*, 2007; *Schorghofer et al.*, 2004], (2) measurements from orbital imagery and field observations for terrestrial valleys [*Abrams et al.*, 2009; *Laity and Malin*, 1985; *Lamb et al.*, 2008; *Lamb et al.*, 2014; *Lapôtre et al.*, 2016a; *Petroff et al.*, 2011; *Shipton et al.*, 2002; *Zuluaga et al.*, 2014], and (3) measurements from orbital imagery and an assumed permeability based on lithology for martian valleys. Parameters were chosen conservatively as described in Section 5. Permeability range for the Colorado Plateau valleys is large due to significant spatial and across-scale variability of the Navajo sandstone; however, a true upper bound on effective permeability is likely lower due to compression bands and permeability barriers at outcrop scale [*Shipton et al.*, 2002; *Zuluaga et al.*, 2014].

Chapter 3

HYDRAULICS OF FLOODS UPSTREAM OF HORSESHOE CANYONS AND WATERFALLS

Mathieu G. A. Lapôtre and Michael P. Lamb

This chapter was published as:
Lapôtre, M. G. A., and M. P. Lamb (2015), Hydraulics of Floods Upstream of Horseshoe Canyons and Waterfalls, *Journal of Geophysical Research: Earth Surface*, 120(7), 1227-1250, DOI:10.1002/2014JF003412.

Notations are summarized in Appendix A.1.

Abstract. Horseshoe waterfalls are ubiquitous in natural streams, bedrock canyons, and engineering structures. Nevertheless, water flow patterns upstream of horseshoe waterfalls are poorly known, and likely differ from the better studied case of a one-dimensional linear step because of flow focusing into the horseshoe. This is a significant knowledge gap because the hydraulics at waterfalls controls sediment transport and bedrock incision, which can compromise the integrity of engineered structures and influence the evolution of river canyons on Earth and Mars. Here we develop new semi-empirical theory for the spatial acceleration of water upstream of, and the cumulative discharge into, horseshoe canyons and waterfalls. To this end, we performed 110 numerical experiments by solving the 2-D depth-averaged shallow water equations for a wide range of flood depths, widths, and discharges, and canyon lengths, widths, and bed gradients. We show that the upstream, normal-flow Froude number is the dominant control on lateral flow focusing and acceleration into the canyon head, and that focusing

is limited when the flood-width is small compared to a cross-stream backwater length scale. In addition, for sheet floods much wider than the canyon, flow focusing into the canyon head leads to reduced discharge (and drying in cases) across the canyon side-walls, which is especially pronounced for canyons that are much longer than they are wide. Our results provide new expectations for morphodynamic feedbacks between floods and topography, and thus canyon formation.

1. Introduction

The hydraulics of waterfalls have been studied for over a century [e.g., *Bresse*, 1860], largely in response to the development of dams and other engineered structures [e.g., *Chanson*, 1994; 1995; 2002] (Figure 3.1F). In addition to their importance in hydraulic engineering, waterfalls play a major role in channel erosion [*Flint*, 1973; *Dietrich and Dunne*, 1993] and often form because of changes in climate, tectonics, and sea-level [*Brush and Wolman*, 1960; *Leopold and Bull*, 1979; *Gardner*, 1983; *Howard et al.*, 1994; *Bishop et al.*, 2005; *DiBiase et al., 2015*; *Lamb et al.*, 2014; *Mackey et al.*, 2014]. Waterfalls on Earth (Figure 3.1D, 3.1G and 3.1H) [*Gilbert*, 1907], but also dry cataracts on Earth and Mars (Figure 3.1E, 3.1I and 3.1J) are often horseshoe-shaped, and create canyons with amphitheater-shaped heads [*Bretz*, 1969; *Baker and Milton*, 1974; *O'Connor*, 1993; *Lamb et al.*, 2008; *Warner et al.*, 2010; *DiBiase et al., 2015*; *Lamb et al.*, 2014; *Baynes et al.*, 2015]. This geometry is observed at various scales, from decimeter scale rills (Figure 3.1C), to meter scale rivers and channel heads (Figure 3.1A, 3.1B and 3.1H), to hundreds of meters to kilometer scale megaflood canyons (Figure 3.1E, 3.1I and 3.1J).

The horseshoe shape of waterfalls likely influences plan-view flow patterns upstream by focusing water towards the center of the horseshoe [e.g., *Pasternack et al.*, 2006; 2007]. Water accelerates as it moves towards a waterfall due to the reduction in pressure to atmospheric at the waterfall brink. Acceleration and lateral flow convergence (i.e., flow focusing) control the velocity, discharge and size of the jet impinging in the plunge pool [*Chanson*, 1994; *Flores-Cervantes et al.*, 2006; *Tokyay and Yildiz*, 2007], which ultimately sets the pace of undercutting and potential collapse of the cliff face [*Dietrich and Dunne*, 1993; *Stein et al.*, 1993; *Alonso et al.*, 2002; *Stein and LaTray*, 2002; *Lamb et al.*, 2007]. Flow acceleration also enhances the bed shear stress exerted by the flow at the waterfall brink [*Stein and Julien*, 1993; *Haviv et al.*, 2006], and thus promotes plucking and toppling of jointed rock [*Annandale*, 1995; *Hancock et al.*, 1998; *Whipple et al.*, 2000; *Coleman et al.*, 2003; *Wohl*, 2008; *Chatanantavet and Parker*, 2009; *Lamb and Dietrich*, 2009; *Dubinski and Wohl*, 2013]. Moreover, larger flow discharges into canyon heads allow transport of larger sediment and higher sediment-transport rates downstream of the waterfall as long as sediment is available [*Meyer-Peter and Muller*, 1948; *Fernandez Luque and Van Beek*, 1976], which exert important controls on the stability of engineering dams and spillways, as well as canyon evolution over longer timescales [e.g., *Lamb et al.*, 2006]. *Petroff et al.* [2011] argued that amphitheater-headed canyons may arise from any erosional process for which erosion rate is proportional to plan-view curvature of the escarpment. Nevertheless, whether the erosion rate at waterfalls is proportional to plan-view curvature is yet to be shown. Investigating the hydraulics of waterfall escarpments is a necessary first step to mechanistic theories for canyon head and waterfall erosion [e.g., *Lamb and Dietrich*, 2009]. Lateral focusing of flow upstream of waterfalls may also influence the development of drainage networks (e.g., canyon spacing) driven by upstream canyon-head retreat [*Izumi and Parker*, 1995; 2000]. Despite its importance, flow focusing upstream and into horseshoe waterfalls has yet to be studied systematically, a knowledge gap we aim to address herein.

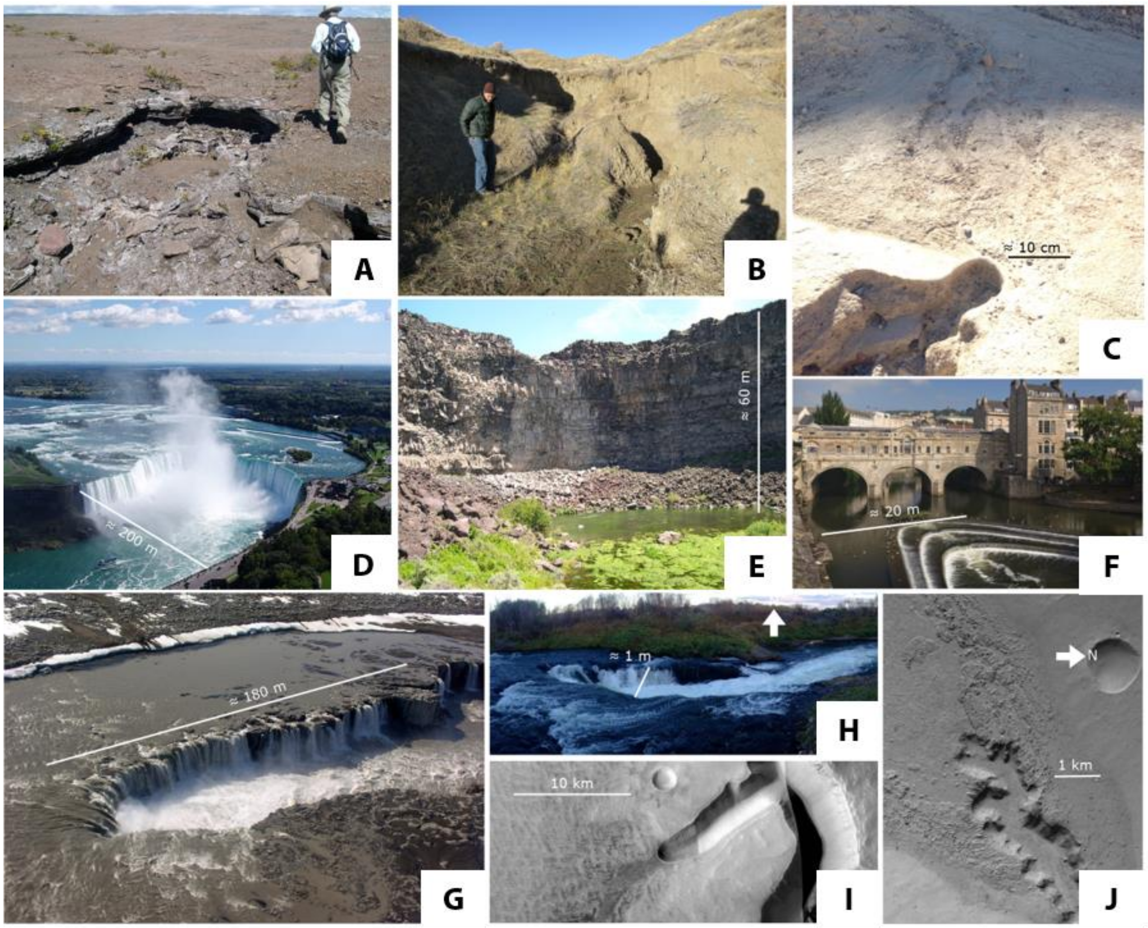

Figure 3.1: Horseshoe waterfalls. (A) Undercut horseshoe heads carved by overland flow in the Keanakākoʼi thephra, Kaʼū desert, Kīlauea volcano, Hawaiʼi [e.g., *Craddock et al.*, 2012]. (B) Gully head near West Bijou Creek, Colorado, USA [e.g., *Tucker et al.*, 2006; *Rengers and Tucker*, 2014]. (C) Undercut horseshoe-shaped rill carved by overland flow on non-cohesive soil in Gower Gulch, Death Valley. (D) Niagara Falls, NY, USA (Credit: Helen Filatova, released under CC-BY-SA-3.0). (E) View of the head of Stubby Canyon, Malad Gorge State Park, ID, USA, from the canyon floor [*Lamb et al.*, 2014]. (F) Horseshoe weir, Bath, UK (Credit: Jurgen Matern, released under CC-BY-SA-3.0). (G) Selfoss waterfall on the Jökulsá á Fjöllum river, Iceland (Credit: Hansueli Krapf, released under CC-BY-SA-3.0). (H) Amphitheater-headed waterfall near Potholes Reservoir, Potholes State Park, WA, USA. (I) CTX mosaic of an amphitheater-shaped canyon at Echus Chasma (Credit: NASA). (J) HiRISE image of an amphitheater-shaped cataract within Kasei Valles (PSP_002788_2010) [e.g., *Williams and Malin*, 2004].

Most work to quantify flow acceleration upstream of waterfalls is for linear escarpments with no topographic variation across the channel width, and hence are essentially 1-D [*Rouse*, 1936; *Rouse*, 1937; *Rouse*, 1950; *Delleur et al.*, 1956; *Rajaratnam and Muralidhar*, 1968; *Hager*, 1983; *Hager and Hutter*, 1984]. The acceleration factor in 1-D is defined as $\alpha_{1D} = U_0/U_n$, where U_0 is the velocity at the waterfall brink, and U_n is the normal flow velocity in the downstream direction [*Rouse*, 1936]. Normal flow is defined as steady and uniform flow (i.e., far upstream, where flow is not affected by the presence of the waterfall) [*Chow*, 1959]. Thus, $\alpha_{1D} > 1$ implies faster flow at the waterfall brink due to spatial acceleration.

Natural horseshoe waterfalls and many engineering structures depart from a purely one-dimensional linear step, and flow velocities at the waterfall brink and discharge into canyon head likely differ significantly from the 1-D case. In specific applications, waterfall geometry has been accounted for using sophisticated 3-D flow simulations [e.g., *Feurich et al.*, 2011]. However, no study has systematically investigated how flow acceleration, discharge into the canyon head, and lateral flow focusing are affected by waterfall planform geometry across a wide range of canyon sizes, flood sizes and Froude numbers.

We aim to test the hypotheses that the horseshoe geometry of waterfalls results in flow accelerations that differ from the 1-D case, and that flow discharge per unit width into the canyon head is increased owing to lateral flow focusing. To do this, we performed a series of numerical experiments. In Section 2, we describe our modeling objectives, identify potential controls on flow focusing upstream of horseshoe waterfalls, and explain our modeling strategy. In Section 3, we describe the numerical model ANUGA [*Roberts et al.*, 2008; *Roberts et al.*, 2009], which is used to investigate focusing of floods into canyons of different sizes. In Section 4, we synthesize results of the experiments. In Section 5, we develop semi-empirical functional relationships for flow acceleration and cumulative head discharge. Last, we discuss application to engineered horseshoe spillways, and controls on waterfall formation and shape.

2. Modeling Objectives

Our modeling goal is to systematically evaluate the cumulative discharge and flow acceleration factor around the brink of 2-D horseshoe waterfalls as a function of canyon width, length, upstream bed slope, flood-width, flood discharge, and normal-flow Froude number. In particular, we seek a generic relationship for the flow acceleration factor and flow discharge for 2-D waterfalls. To accomplish our goal, in this section we define quantitative metrics that will be used to define the effects of 2-D flow focusing. Next, we use dimensional analysis to formulate quantitative hypotheses for the functional relationships between these metrics and the relevant topographic and hydraulic parameters. Finally, we describe the modeling strategy and parameter space covered.

2.1. Two-Dimensional Flow-Focusing Metrics

In 1-D open-channel flow with constant channel width, the volumetric water discharge per unit width ($q = Uh$, where h is flow depth) is conserved such that the discharge over the waterfall ($q_0 = U_0 h_0$) is equal to the normal flow discharge upstream ($q_n = U_n h_n$), and therefore $\alpha_{1\mathrm{D}} = U_0 / U_n = h_n / h_0$ (Figure 3.2), where h_n is the normal flow depth, and h_0 is the flow depth at the waterfall brink. The acceleration factor in 1-D was found to be well approximated by [*Rouse*, 1936; *Hager*, 1983]

$$\alpha_{1D} \equiv \frac{U_0}{U_n} = \begin{cases} \dfrac{1+\varepsilon}{\mathrm{Fr}_n^{\,2/3}}, & \text{if } \mathrm{Fr}_n < 1 \\ \dfrac{\mathrm{Fr}_n^{\,2}+\varepsilon}{\mathrm{Fr}_n^{\,2}}, & \text{if } \mathrm{Fr}_n \geq 1 \end{cases}, \tag{3.1}$$

where $\varepsilon \approx 0.4$ is an empirical constant that accounts for the deviation of pressure from hydrostatic at the waterfall brink and $\mathrm{Fr}_n = U_n / \sqrt{gh_n}$ is the normal-flow Froude number. For subcritical flows ($\mathrm{Fr}_n < 1$), Equation (3.1) results in a Froude number at the waterfall brink, Fr_0, of about 1.66 (i.e., $\mathrm{Fr}_0 = \alpha_{1D}^{\,3/2}\mathrm{Fr}_n = (1+\varepsilon)^{3/2} \approx 1.66$) regardless of the upstream Froude number (Fr_n). For supercritical flow upstream of the waterfall ($\mathrm{Fr}_n > 1$), Equation (3.1) results in an acceleration factor that approaches unity (i.e., $\mathrm{Fr}_0 \approx \mathrm{Fr}_n$) as Fr_n increases.

Natural waterfall geometries can be complex. Because our goal is to study 2-D flow focusing as generically as possible, and because an analysis of this sort has not been conducted before, here we start with a simple geometric representation of waterfalls that remains faithful to the horseshoe shape typical of many waterfalls, canyon heads and engineered structures (Figure 3.3). We consider a canyon of spatially uniform width w (measured in the *y*-, or cross-slope direction) and length l (measured in the *x*-, or downslope direction) that has a semi-circular head of radius $w/2$. Downslope and cross-slope are directions defined by a fixed-Cartesian coordinate system, in which the *x*-axis follows the topographic slope at a constant gradient *S*, and thus the normal flow direction (Figure 3.3). Downstream and cross-stream refer to directions along or perpendicular to a streamline, and thus may deviate from the *x*- and *y*- directions due to flow focusing. A sheet flood of width W is centered about the canyon, and has a constant discharge per unit width q_n far upstream of the waterfall, where flow depth is equal to the normal flow depth h_n. There is no bed slope in the *y*-direction, such that any flow convergence towards the canyon is purely hydrodynamic. The drop height is sufficiently large such that the flow upstream of the knickpoint is not affected by flow in the plunge pool [e.g., *Bennett*, 1999; *Bennett and Casali*, 2001].

To quantify 2-D flow focusing, we define a local two-dimensional flow acceleration factor $\alpha_{2\mathrm{D}} \equiv U_p / U_n$, which is analogous to the acceleration factor in 1-D, except that here U_p is defined in the direction perpendicular to the local canyon brink (because it is this component only that will contribute to discharge into the canyon head), such that $\alpha_{2\mathrm{D}}$ is a local quantity that is likely to vary at different locations along the waterfall brink. To highlight truly 2-D effects, throughout this paper we will use an acceleration factor ratio $\alpha*$, defined as

$$\alpha* = \frac{\alpha_{2\mathrm{D}}}{\alpha_{1\mathrm{D}}}, \tag{3.2}$$

such that $\alpha* = 1$ corresponds to scenarios that show only 1-D flow acceleration.

To quantify changes in discharge to the waterfall as a result of lateral flow focusing, we define the local discharge per unit width as $q_0 = U_p h$. The total discharge entering the semi-circular canyon head is then $Q_h = \int_{\theta=-\pi/2}^{\pi/2} q_0(\theta) \frac{w}{2} \mathrm{d}\theta$, where θ is the azimuth with respect to the canyon centerline. The normalized cumulative head discharge $q*$ is defined as the ratio of Q_h to Q_n, in which $Q_n = q_n w$ is the normal-flow discharge flowing across a length *w*, i.e.,

$$q^* \equiv \frac{Q_h}{Q_n} = \frac{1}{q_n} \int_{\theta=0}^{\pi/2} q_0(\theta) d\theta \,. \tag{3.3}$$

A normalized cumulative head discharge of unity ($q^* = 1$) corresponds to the case where no lateral flow focusing is observed.

2.2. Dimensional Analysis and Hypotheses

To identify the controlling variables on flow acceleration (α^*) and normalized cumulative flow discharge (q^*), we use dimensional analysis for flow acceleration at steady state. Consequently, the flow variables (velocities and depth) around the canyon are time independent, and fully determined by seven dimensional variables: inflow discharge per unit width q_n, acceleration of gravity *g*, normal flow depth h_n, canyon width w, flood width W, canyon length l, and bed slope *S*. This problem can be recast in terms of five dimensionless parameters,

$$(\alpha^*, q^*) = f\left(\mathrm{Fr}_n, w^*, W^*, l^*, S\right), \tag{3.4}$$

where $w^* = \dfrac{w}{W}$ is the canyon-width to flood-width ratio, $W^* = \dfrac{(\mathrm{W} - \mathrm{w})S}{2h_n}$ is herein called the flood-width limitation factor, and $l^* = \dfrac{lS}{h_n}$ is herein called the downslope backwater factor (Figure 3.4). The normal flow depth can be defined as $h_n = \dfrac{C_f U_n^2}{gS}$, where $C_f = \dfrac{U_n{}^2}{u_*^2}$ is a bed-friction coefficient, and u_* is the bed shear velocity [e.g., *Chow*, 1959].

Dimensional analysis does not dictate which dimensionless numbers are best suited to describe the physics of flow focusing. In the rest of this section we describe why the dimensionless numbers we picked make intuitive sense and are likely relevant to flow focusing upstream of canyons.

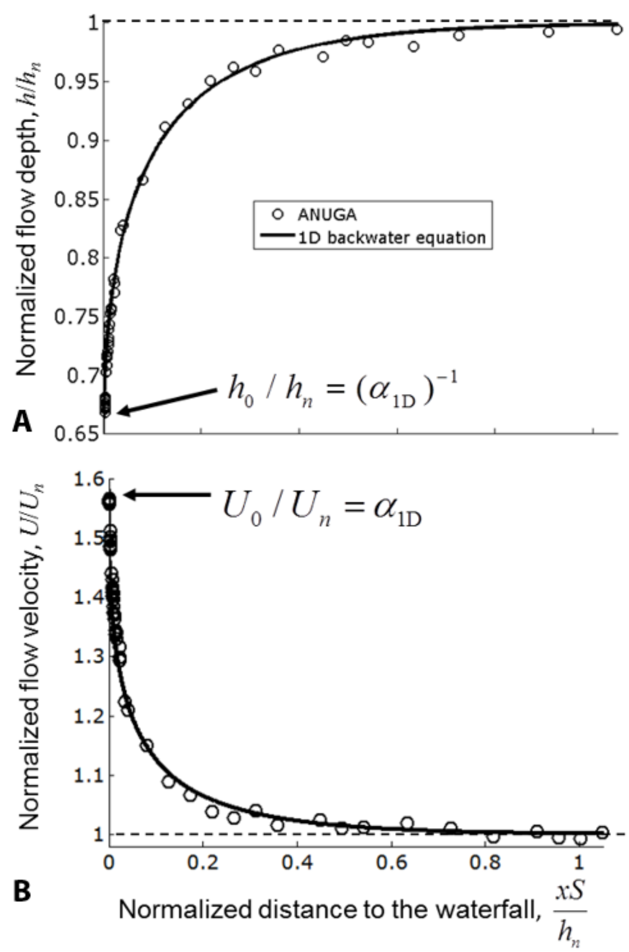

Figure 3.2: Benchmarking ANUGA. (A) Depth and (B) velocity profile approaching a waterfall for subcritical flow (at $xS/h_n = 0$, where x is the streamwise distance as measured from the waterfall and S is the bed slope). The solid black line (analytical 1-D backwater solution, Equation (3.6)) and the solid circles (as modeled from ANUGA, an implementation of the 2D-depth averaged shallow water equations) match and converge towards the normal flow depth and velocity at a backwater length ($x \approx L_b \approx h_n / S$) upstream of the waterfall. Dashed lines respectively indicate normal flow depth and velocity.

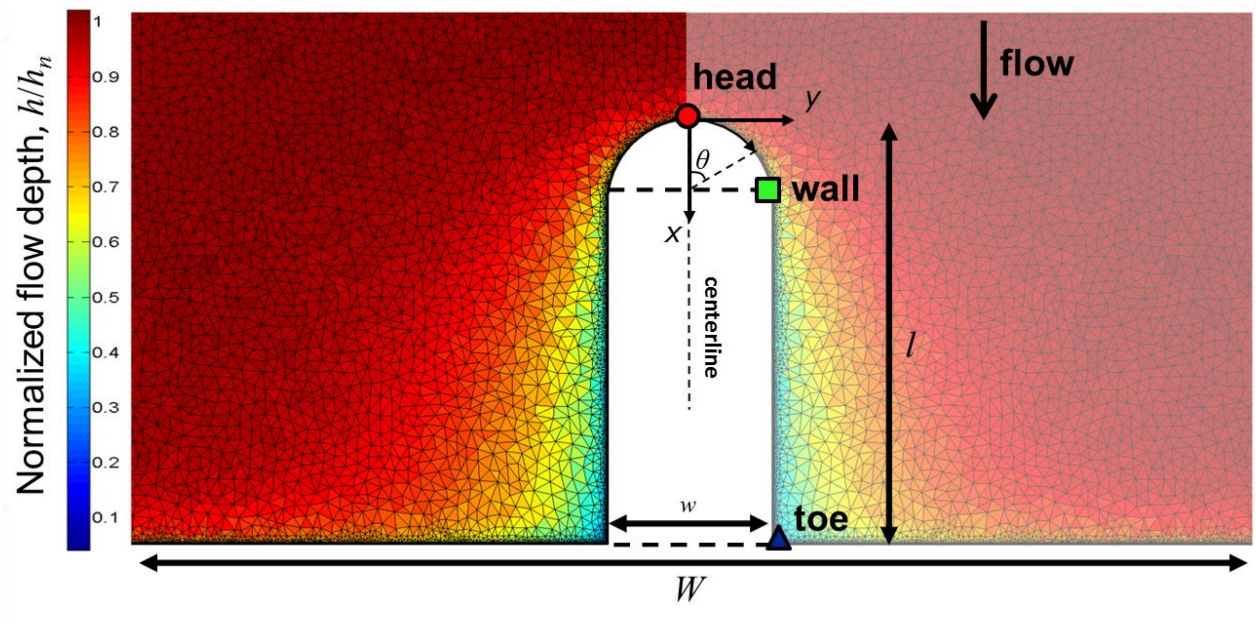

Figure 3.3: Numerical Domain. Plan-view geometry of a flood (width *W*) flowing downslope (*S*) towards a canyon (width *w*, length *l*). The head is semi-circular of radius *w/2*. The unstructured triangular mesh used in the model refines at the canyon brink to a resolution of 4x10^{-3} L_b, where L_b is the backwater length (Equation (3.7)). The red circle, green square and blue triangle show the locations of where we measure the acceleration factor at the head (α_h^*), the head to wall junction (α_w^*), and the toe (α_t^*), respectively. The angle θ is the azimuth as measured between the canyon centerline and any point around the canyon head. Color coded is an example of flow depths normalized by the normal flow depth of the flood.

The normal-flow Froude number ($\mathrm{Fr}_n = U_n / \sqrt{gh_n}$) describes the ratio of downstream oriented, normal-flow velocity to the shallow-water-wave speed. For $\mathrm{Fr}_n < 1$, the velocity of shallow water waves ($\sqrt{gh_n}$) is greater than the flow velocity (U_n), and thus waves can propagate in all directions. For $\mathrm{Fr}_n > 1$, the velocity of waves is smaller than that of the flow, and waves can only propagate downstream and cross-stream. Consequently, Froude number sets the direction and distance at which hydraulic information propagates, and is thus expected to exert a major control on the degree to which water is focused towards the canyon head.

The waterfall width relative to the flood-width (w^*) is important because it governs the proportion of water available to be focused into the canyon. Figure 3.4 shows that narrow floods ($w^* \approx 1$) will result in a canyon that is mostly a horseshoe without sidewalls because of the fixed semi-circular geometry of the head, at constant l^* and W^*. When $w^* << 1$, the canyon sidewalls make up most of the canyon length, and we expect that w^* ceases to be an important parameter.

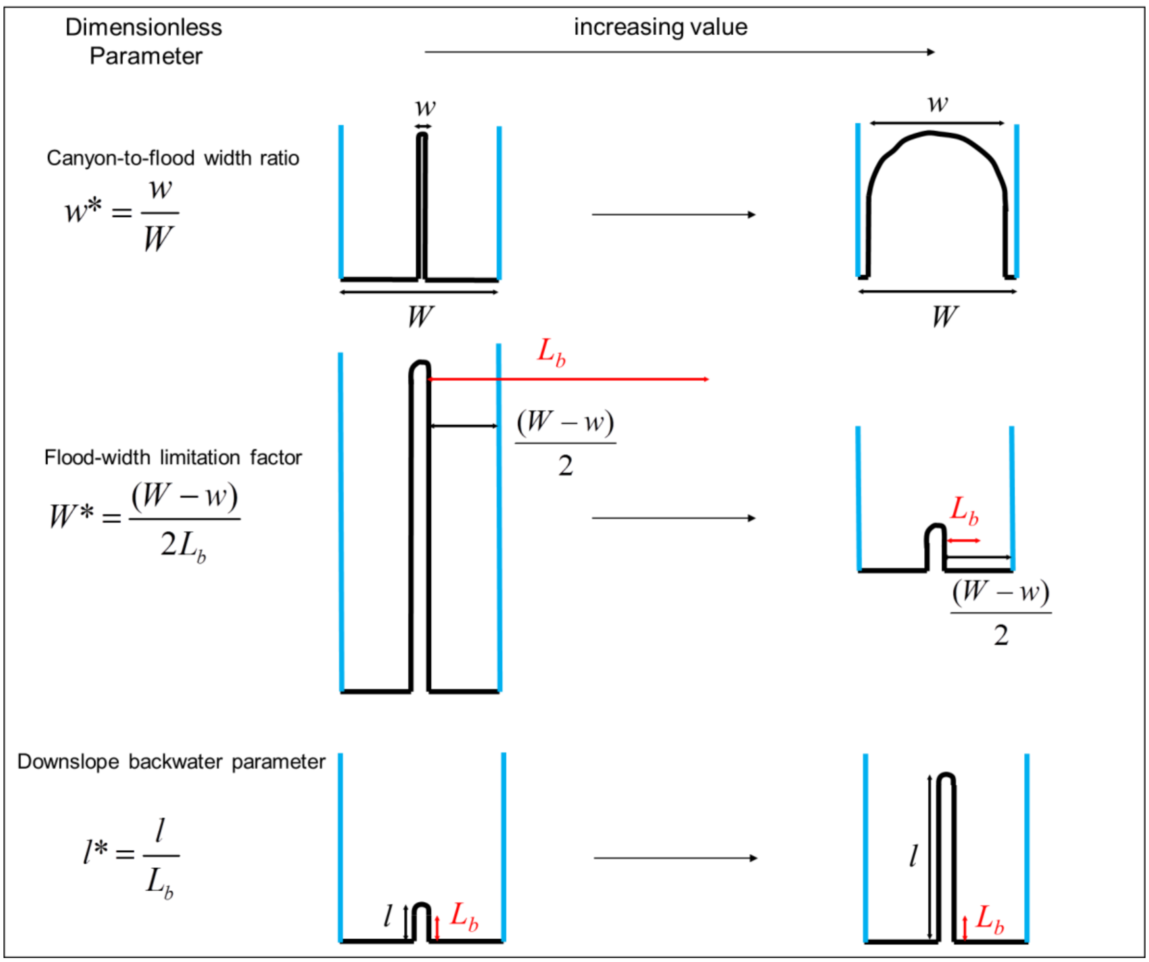

Figure 3.4: Parameter definitions. Conceptual plan-view cartoons of floods flowing over canyon escarpments to illustrate the dimensionless parameters w^*, W^*, and l^*. Blue lines delineate the flood width, while black lines delineate the waterfall brink. Red arrows represent the backwater length scale L_b. The black arrows pointing to the right indicate that a given dimensionless parameter is increased while all others are held

constant. The other two independent dimensionless parameters, Fr_n and S, are not shown.

The lateral-backwater limitation factor ($W*$) is the ratio of the half-flood-width $(W-w)/2$ measured from the canyon sidewalls, to the backwater length scale $L_b = \frac{h_n}{S}$. The backwater length is a typical length scale over which 1-D open-channel flows are affected by downstream boundary conditions [e.g., *Chow*, 1959]. Here we wish to describe cross-slope backwater dynamics (i.e., lateral flow focusing), thus C_f may be the more relevant scale (rather than S) in determining a characteristic backwater length. This notwithstanding, for normal flow, $\mathrm{Fr}_n = U_n / \sqrt{gh_n} = \sqrt{S / C_f}$, and therefore S and C_f can be used interchangeably if Fr_n is an independent parameter. Consequently, $W*>1$ indicates that the half-flooded-width from the canyon sidewalls is larger than the lateral-backwater length (Figure 3.4), and thus that hydraulics at the canyon sidewalls will not be affected by lateral backwater limitations due to the domain width. On the contrary, when $W*<1$, half of the flooded width is greater than the lateral-backwater length (Figure 3.4), and we expect hydraulics at the canyon side-walls will be affected by the boundaries of the flood, leading to decreased $\alpha*$ and $q*$. With all other non-dimensional parameters held constant, increasing $W*$ also results in canyons that are shorter with respect to the flood width if $w*$ and $l*$ are held constant (Figure 3.4). When a canyon widens, $w*$ increases and $W*$ decreases such that both effects may act in concert to decrease $\alpha*$ and $q*$ at the canyon sidewalls.

We expect that the downslope backwater factor ($l*$) also controls the degree of drying along the canyon side-walls. Longer canyons with higher $l*$ should capture more of the flood water at the canyon head or shortly downslope, potentially leaving canyon side-walls downslope of the canyon head dry. Figure 3.4 shows how canyon length and L_b vary for different values of $l*$.

Finally, we found that model simulations are exactly equivalent for different bed slopes (5x10^{-4} < S < 5x10^{-2}) if Fr_n and $W*$ are held constant. That is, bed slope has no effect on flow focusing independent of its role in determining the Froude number and the lateral-backwater length scale. Consequently, the number of independent variables in Equation (3.4) is simplified from five to four.

2.3. Modeling Strategy and Parameter Space

We performed a series of numerical experiments to test our hypotheses and to find functional relationships for Equation (3.4). We systematically varied one of the four dimensionless parameters (experiment series 1 to 4), while all the others were set constant (Table 3.1), and extracted the acceleration factors (normalized by their 1-D counterpart $\alpha_{1\mathrm{D}}$) at the center of the canyon head ($\alpha_h^* = \alpha^*(\theta = 0)$, red circle in Figure 3.3), at the most upstream node of the side-wall ($\alpha_w^* = \alpha^*(\theta = \pi / 2)$, green square in Figure 3.3), and at the toe of the canyon where it joins the downslope escarpment ($\alpha_t^* = \alpha^*$ at the downslope end of the canyon, blue triangle in Figure 3.3). We picked these three locations as representative of different canyon segments that are important for understanding canyon widening (e.g., erosion at the canyon head versus side-wall) and canyon lengthening (e.g., erosion at the canyon head versus toe), where erosion rate is likely a function of flow velocity. Note that the acceleration factor ratio at the toe α_t^* could be measured both in the downslope and the cross-slope directions. We chose to report its values in the downslope (x) direction because this is the direction that allows for a comparison between the dynamics of the canyon head and of the escarpment at the base of the canyon.

Two numerical simulations are common to experiment series 1 to 4, one subcritical ($\mathrm{Fr}_n = 0.5$) and one supercritical ($\mathrm{Fr}_n = 3$). We refer to these simulations as the base cases. The base cases simulate a low-sloping (S = 0.0075), wide sheet flood ($w^* = 0.1$) that has a lateral backwater length which is shorter than the half-flooded-width ($W^* = 4.5$), and that pours over the brink of a long canyon ($l^* = 30$). Under these conditions, we expect that mostly Froude number Fr_n will influence the distribution of acceleration factor ratios around the canyon head.

3. Numerical Methods

ANUGA is a finite-volume modeling suite that solves the two-dimensional time-dependent depth-averaged shallow water equations on an unstructured mesh of triangular cells where friction is implemented using Manning's equation [*Zoppou and Roberts*, 1999; *Roberts et al.*, 2008; *Roberts et al.*, 2009; *Mungkasi and Roberts*, 2011; *Mungkasi and Roberts*, 2013]. The shallow water equations describe conservation of mass and conservation of momentum, where the forcing terms are gravity, friction, and pressure gradients. In the case of no bed slope in the y-direction, the conservation equations are

$$\begin{cases} \dfrac{\partial h}{\partial t} + \dfrac{\partial (U_x h)}{\partial x} + \dfrac{\partial (U_y h)}{\partial y} = 0 \\ \dfrac{\partial (U_x h)}{\partial t} + \dfrac{\partial (U_x^2 h)}{\partial x} + \dfrac{\partial (U_x U_y h)}{\partial y} = -gh\dfrac{\partial h}{\partial x} - ghS - \dfrac{C_f U_x}{h}\sqrt{U_x^2 + U_y^2}, \\ \dfrac{\partial (U_y h)}{\partial t} + \dfrac{\partial (U_x U_y h)}{\partial x} + \dfrac{\partial (U_y^2 h)}{\partial y} = -gh\dfrac{\partial h}{\partial y} - \dfrac{C_f U_y}{h}\sqrt{U_x^2 + U_y^2} \end{cases} \tag{3.5}$$

in which U_x and U_y are the depth-averaged velocities in the *x*- and *y*- directions respectively, and C_f is related to Manning's *n* through $C_f = \frac{n^2 g}{h^{1/3}}$.

These equations are derived by depth-averaging the Navier-Stokes equations under the slender flow approximation, which assumes that the vertical length scale is negligible compared to the horizontal. A consequence of this assumption is that vertical pressure gradients are hydrostatic. The model implementation is capable of reproducing wetting and drying, flow around structures, and hydraulic jumps due to the ability of the upwind central scheme to accommodate discontinuities in the solution [*Kurganov et al.*, 2001].

Theoretically, the slender flow approximation does not hold at the waterfall brink because there pressure is not hydrostatic. It was shown that the distance upstream of a waterfall at which pressure becomes hydrostatic is about one to two critical depths h_c (i.e., the depth in which $\mathrm{Fr} = 1$; for the 1-D case, $h_c = (q_n^{\,2} / g)^{1/3}$) [*Hager*, 1983], which implies that the region that violates the shallow water equations is limited to very near the waterfall brink. Indeed, ANUGA has been successfully tested against dam-break experiments [*Nielsen et al.*, 2005], and was able to reproduce with great accuracy water surfaces and bed shear stress [*Barnes and Baldock*, 2006; *Mungkasi and Roberts*, 2013].

Despite that non-hydrostatic pressure at the brink is not accounted for in our modeling, its effect can be incorporated by assuming that the same non-hydrostatic pressure captured in the 1-D acceleration factor (Equation (3.1)) holds for 2-D canyons. This approximation is likely to be true given that 1) the boundary condition on pressure is the same all around the canyon brink – pressure at the waterfall is atmospheric, and 2) the length scale over which non-hydrostatic effects are important (a few critical depths) is much smaller than the radius of curvature of most horseshoe waterfalls, such that enhanced flow acceleration due to 2-D non-hydrostatic effects in such close proximity to the waterfall brink is unlikely to be significant in the cross-stream direction. As a result, we expect the acceleration factor ratio α^* to be unchanged by non-hydrostatic effects, and it is therefore possible to calculate the acceleration for a 2-D waterfall using our relationships for α^*, combined with Equation (3.1) that accounts for non-hydrostatic effects in 1-D.

We also tested ANUGA against the solution to the one-dimensional backwater equation [e.g., *Chow*, 1959] for subcritical flows (Figure 3.2) by solving

$$\frac{dh}{dx} = \frac{S - C_f \ \mathrm{Fr}^2}{1 - \mathrm{Fr}^2}\,. \tag{3.6}$$

Like ANUGA, Equation (3.6) also employs the slender flow approximation and does not capture non-hydrostatic effects at the brink. The solution to Equation (3.6) was computed with a predictor-corrector, central scheme finite difference code [e.g., *Butcher*, 2008]. In the 1-D model, we set $\mathrm{Fr}_n = 0.99$ at the downstream boundary to simulate the water surface drawdown at the waterfall. In ANUGA, we extracted flow depths along a line at the edge of a wide flood. Figure 3.2 shows that ANUGA is able to reproduce with good accuracy the water depth and velocity for 1-D flow towards a waterfall.

The user-defined parameters for ANUGA are (1) the mesh (topography and spatially variable resolution), (2) initial and boundary conditions, (3) Manning's *n*, and (4) duration of the simulation, which are described below. Time step intervals are internally-determined from spatial resolution to enforce stability of the solution.

3.1. Domain Geometry and Resolution

We model the same canyon and flood system as described in Section 2. The numerical domain was set to optimize computational time. We only model half of the domain, because it is symmetric with respect to the canyon axis. Depth and velocity gradients get steeper towards the brink (Figure 3.2). In order to capture these steep gradients and better resolve the acceleration factor at the brink, we defined the cliff as a set of three parallel lines, one downstream of the brink, one making up the brink, and one upstream of the brink. This setup allows us to extract flow variables along a line that runs parallel to the brink but is slightly upstream of it and thus not affected by numerical noise induced by the near-vertical step at the brink. For subcritical input flows, these lines are separated by a small distance of $4\text{x}10^{-3} L_b$ along the plane of the bed. To estimate L_b we used the analytical solution for subcritical flows in rectangular 1-D channels [*Bresse*, 1860],

$$L_{\mathrm{b}} = \lim_{r \to 1} \left\{ \frac{h_{\mathrm{n}}}{S} \left[r - \frac{h_{\mathrm{c}}}{h_{\mathrm{n}}} - (1 - \mathrm{Fr_n}^2) \left(\Gamma(r) - \Gamma\left(\frac{h_{\mathrm{c}}}{h_{\mathrm{n}}} \right) \right) \right] \right\}, \tag{3.7}$$

where $\Gamma(r) = \frac{1}{6} \ln\left(\frac{r^2 + r + 1}{(r-1)^2} \right) - \frac{1}{\sqrt{3}} \arctan\left(\frac{\sqrt{3}}{2r+1} \right)$, and $r = \frac{h(x = L_b)}{h_n} = 0.95$ is the assumed ratio of flow depths at the backwater extent [e.g., *Lamb et al.*, 2012]. For supercritical flows, we set the distance between the lines that define the cliff to be $4\text{x}10^{-3} h_c / S$. Outside of these lines, the resolution of the unstructured triangular mesh is about 25 times the brink resolution, which allows for a less dense sampling of flow variables where spatial gradients are less steep.

3.2. Initial and Boundary Conditions

The domain length upstream of the canyon head is set to L_b for subcritical floods, and h_c / S for supercritical floods. This ensures that the flow depth at the inflow boundary is equal to the normal flow depth and thus that brink vertices are not affected by the inflow boundary. The inflow boundary is set as a Dirichlet condition on stage and momenta, where stage is set to the normal flow depth, the downslope momentum is set to the desired discharge per unit width q_n, and the cross-slope momentum is set to zero. The side boundaries are reflective and frictionless, such that there is no flow across the edge of the domain. Finally, the downstream boundary condition is located a few vertices downstream of the cliff, and is fully transmissive, i.e., all flow is transmitted outside of the domain. The drop height is set to ten critical depths. The initial depth is set to the normal flow depth h_n everywhere, and the model is run in time until steady state is reached. We detect steady state by computing the quadratic residual in flow depth between consecutive time steps. When this residual becomes smaller than a threshold of 0.1%, the experiment is stopped.

The error bars on flow depths and velocities induced by instabilities at the brink are at most of 0.5% and 2% of the mean, respectively, as estimated from the variability of flow depth and velocity around the brink at 100 consecutive time steps. Error bars associated with numerical variability are smaller than symbol sizes in all figures of the paper.

4. Results

4.1. Base Cases

The two base case simulations (see Table 3.1 for parameter values) correspond to the case where the canyon head is not affected by the edges of the flood ($w^* << 1$ and $W^* > 1$) or the length of the canyon ($l^* >> 1$), i.e., they correspond to a sheet flood.

Figure 3.5A and 3.5B show the distribution of normalized discharge per unit width $(Uh)/q_n$ in plan-view for the sub- and supercritical base cases, respectively. Black lines with arrows follow streamlines, i.e., the trajectories of flow particles within the flood. In both base cases, discharge per unit width is slightly enhanced around the canyon head (i.e., $(Uh)/q_n \geq 1$) and is progressively depleted as water flows downslope towards the canyon toe (i.e., $(Uh)/q_n < 1$). The relative decrease in discharge per unit width compared to the normal flow discharge per unit width is caused by the loss of water into the canyon further upslope. The cross-slope extent of the relative decrease in discharge per unit width is larger in the subcritical than in the supercritical base case, and correlates with the plan-view curvature of the streamlines. In the subcritical case, streamlines strongly deviate from pure downslope trajectories, and a significant amount of water is focused into the canyon, which leads to a large decrease in normalized discharge per unit width downslope. In the supercritical case, streamlines only deviate from pure downslope trajectories close to the canyon walls, which leads to less focusing of water into the canyon, and thus a lower decrease in normalized discharge per unit width downslope.

Figure 3.5C and 3.5D show normalized flow depth profiles along downslope (blue) and a cross-slope (red) transects for both base cases as located by the blue and red lines in Figure 3.5A and 3.5B. In the subcritical case, water depth is equal to normal flow depth far from the waterfall brink in both profiles. Along the downslope profile, water depth is drawn down to the critical depth h_c at the waterfall due to spatial acceleration of water towards the brink. The length scale over which water is drawn down scales with the backwater length $L_b \propto h_n / S$ (Equation (3.7)). Along the cross-slope profile, water depth is also drawn down towards the waterfall brink, but over a longer spatial scale because there is no cross-slope topographic gradient. In the supercritical case, the normal flow and critical depths are equal (i.e., $h_n = h_c$), i.e., there is no draw-down effect in the downslope direction. Nevertheless, a backwater profile develops in the cross-slope direction, because cross-slope flow is subcritical, which results in the plan-view curvature of the streamlines in Figure 3.5B.

Figure 3.6A and 3.6B respectively show the acceleration factor ratio $\alpha*$ and normalized cumulative discharge into the canyon as a function of normalized distance along the canyon rim for the subcritical (blue) and supercritical (red) base cases. Both quantities are measured in the direction perpendicular to the brink. The distance along the canyon rim is projected along the canyon centerline, so that a normalized distance along the canyon rim of zero corresponds to the location of the tip of the canyon head (red circle in Figure 3.3), while a value of unity corresponds to the location of the canyon wall (green square in Figure 3.3). Consequently, the value of the cumulative head discharge $q*$ is found by reading the value of the normalized cumulative discharge into the canyon at an *x*-axis value of unity. The last measured acceleration factor ratios and normalized cumulative discharges correspond to the location of the canyon toe (blue triangle in Figure 3.3). Note that the value of the acceleration factor ratio at the toe is discontinuous because it is measured in the cross-slope direction along the side-walls, and in the downslope direction from the toe along the escarpment at the base of the canyon.

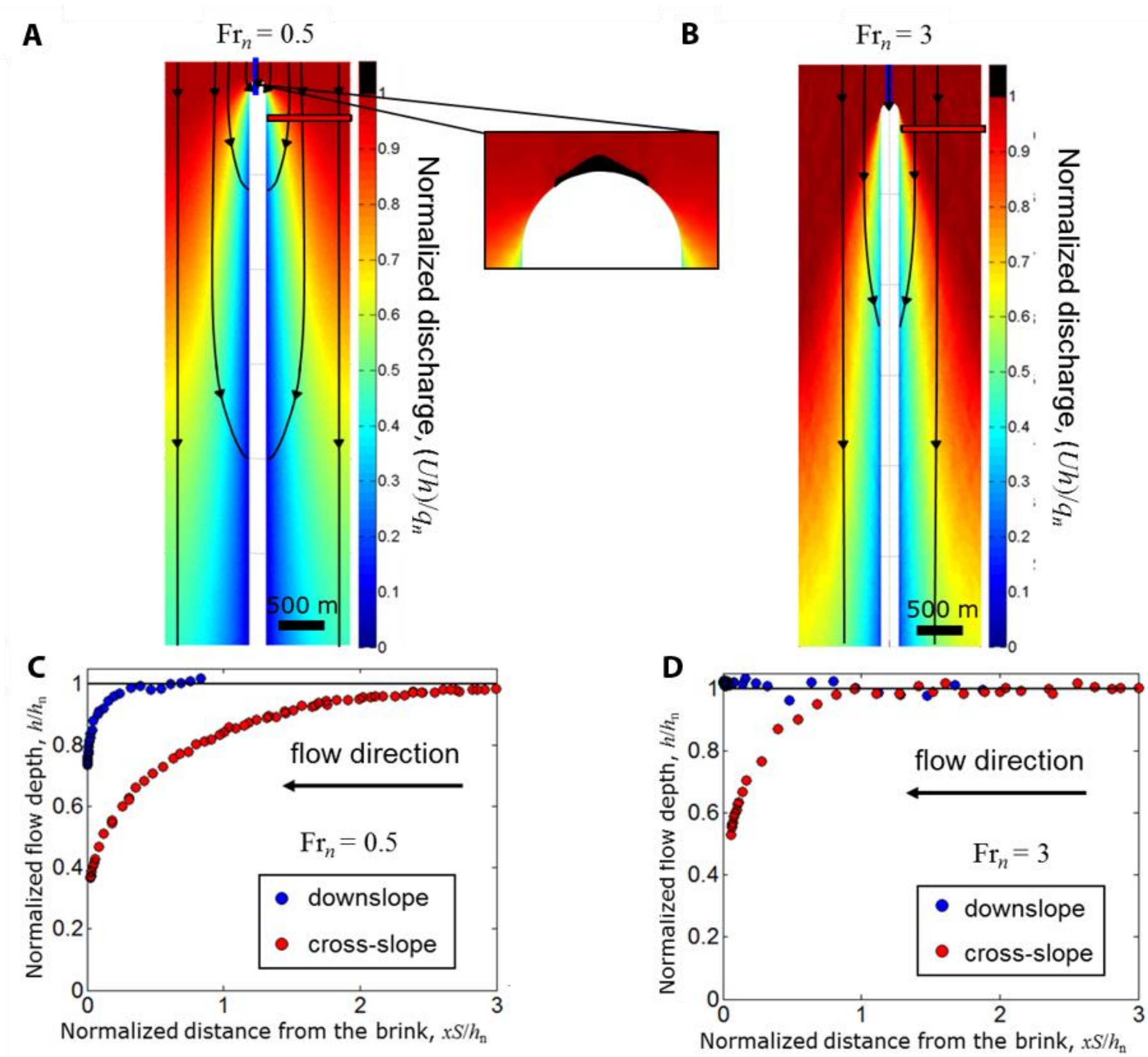

Figure 3.5: Effect of Froude number on backwater profiles. Normalized discharge map for the (A) subcritical ($\mathrm{Fr}_n = 0.5, w^* = 0.1, W^* = 4.5$, $l^* = 30$, S = 0.0075) and (B) supercritical ($\mathrm{Fr_n} = 3, w^* = 0.1, W^* = 4.5$, $l^* = 30$, S = 0.0075) base runs. Black lines with arrows show streamline directions. U is the magnitude of flow velocity such that $U = \sqrt{U_x^{\ 2} + U_y^{\ 2}}$. Inset in (A) shows the zone around the canyon head where discharge per unit width is enhanced from the 1-D case $\left(\text{i.e., } \dfrac{Uh}{q_n} \geq 1\right)$ highlighted in black. Discharge per unit width is not enhanced around the head for supercritical floods. Normalized depth profiles for the same (C) subcritical, and (D) supercritical base runs. The profiles were measured along the canyon centerline (blue line in (A) and (B), blue symbols in (C) and (D)) and along a cross-slope profile (red line in (A) and (B), red symbols in (C) and (D)).

Figure 3.6A shows that at $\mathrm{Fr}_n = 0.5$, the velocity perpendicular to the brink progressively decreases along the canyon rim from the center of the canyon head to the canyon side-wall because water is lost into the canyon due to flow focusing. At $\mathrm{Fr}_n = 3$, the change in velocity along the canyon rim is more pronounced due to higher momentum flow and less focusing of water into the canyon. Along the canyon side-wall, the cross-slope velocity is constant and very small because water is not efficiently focused into the canyon. Figure 3.6B shows that the cumulative discharge into the canyon is greater at $\mathrm{Fr}_n = 0.5$ than at $\mathrm{Fr}_n = 3$, again because water is more efficiently deflected towards the canyon head for subcritical flows, such that $q^* > 1$ in the subcritical case, while $q^* \approx 1$ in the supercritical case. Moreover, discharge is significantly larger in the cross-slope direction along the canyon walls in the subcritical than in the supercritical case. Nevertheless, flow focusing for supercritical normal flow is still finite because cross-slope Froude numbers are subcritical.

In summary, subcritical normal flow leads to the development of both downslope and cross-slope backwater profiles, which deflects streamlines and enhances flow focusing, α^* and q^*. In contrast, there is no downslope backwater profile for supercritical normal flow, and only cross-slope backwater profiles contribute to spatial acceleration of water.

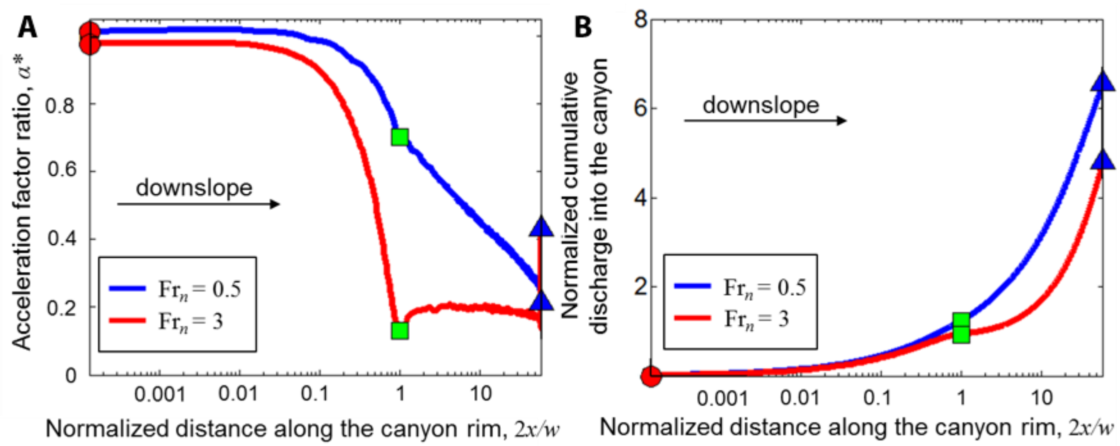

Figure 3.6: Rim distribution of acceleration factor ratio and normalized cumulative discharge around the head vs. Froude number. (A) Acceleration factor ratio α^* and (B) normalized cumulative discharge along the rim of the canyon for the base runs. The abscissa is the distance measured along the spatial *x*-axis (Figure 3) from the center of the canyon head, normalized by $w/2$, such that this distance equals unity at the head-to-wall junction (i.e., where $\theta = \pi/2$). The normalized cumulative head discharge q^* is thus found where $2x/w$ equals unity. Red circles indicate the canyon head center, green squares the head to wall junction, and blue triangles the canyon toe (Figure 3). Note that the acceleration factor at the toe (blue triangle) is measured in the downslope (*x*) direction, and hence is offset from the profile that shows acceleration in cross-slope (*y*) direction at the corner junction between the canyon and the escarpment.

4.2. Experiment Series 1: Froude Number Fr_n

Experiment series 1 was designed to investigate sheet floods of varying Froude number Fr_n. We varied Froude number from 0.4 to 5 (Table 3.1), and used $w^* = 0.1, W^* = 4.5$, $l^* = 30$, and S = 0.0075 (as in the base cases). This range of Froude numbers is typical of large scale floods [*Costa*, 1987]. These floods are much wider than the canyon width and the canyons are long.

In Figure 3.7, we show the value of α^* at three locations along the canyon brink – the center of the canyon head, the junction between the canyon head and the side-wall, and the junction between the canyon side-wall and the downstream escarpment (i.e., the canyon toe) (Figure 3.3). The acceleration factor at the canyon head is roughly equal to the 1-D acceleration factor (i.e., $\alpha^*_h \approx 1$), with a small enhancement of acceleration at lower Froude numbers (Figure 3.7A). For example, $\alpha^*_h = 1.03$ at $\mathrm{Fr}_n = 0.4$. The acceleration factor at the wall is smaller than at the head ($\alpha^*_w < 1$), but it is still significant for low Fr_n and decreases to near zero at high Froude number. Note that for a 1-D step, there is no cross-slope acceleration (i.e., $\alpha^*_w = 0$). The acceleration factor ratio at the toe α^*_t is lower than that at the wall (Figure 3.7A) and increases with Froude number. Flow focusing results in an enhancement of discharge to the canyon head of up to 34% for subcritical flows. The cumulative discharge over the waterfall head q^* decreases and eventually reaches unity as the upstream Froude number is increased (Figure 3.7b).

We interpret these trends as the result of higher Froude numbers producing streamlines that are oriented nearly parallel to the bed slope, whereas at lower Froude numbers more water is focused towards the canyon (e.g., Figure 3.5). The cross-slope component of flow velocity decreases as Froude number is increased, decreasing the velocity perpendicular to the side-wall brink. Consequently, higher Froude numbers imply that less water is lost into the canyon, and more water reaches the toe, thus increasing the acceleration factor α^*_t at the toe (e.g., Figure 3.5). Importantly, for critical and supercritical upstream Froude numbers $\mathrm{Fr}_n \geq 1$, the acceleration factor ratio at the canyon side-wall is non zero because flow in the cross-slope direction is still subcritical. Normal Froude number Fr_n must exceed ~5 for cross-slope flow into the canyon head to be negligible.

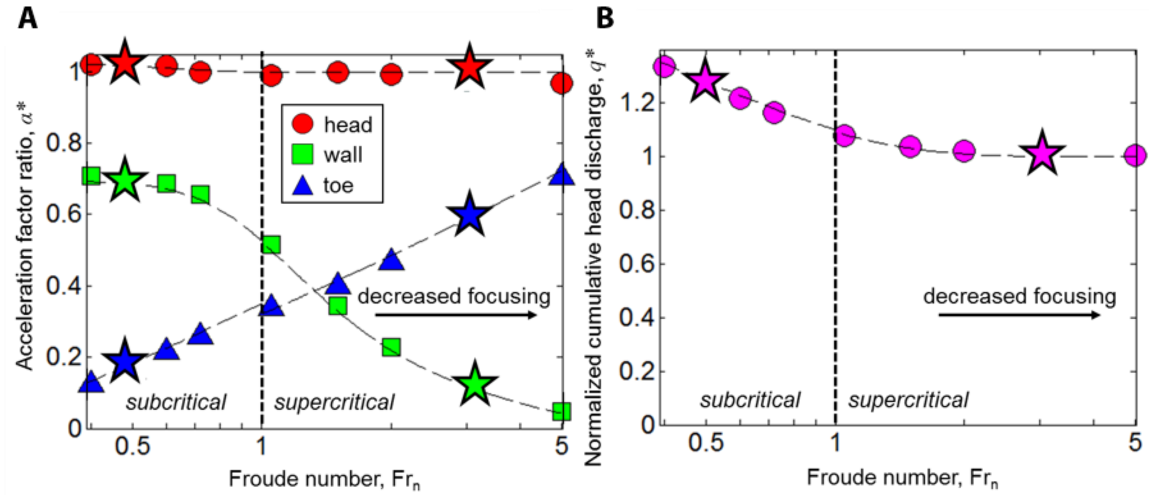

Figure 3.7: Acceleration factor ratio and normalized cumulative discharge vs. Froude number. (A) Acceleration factor ratio $\alpha *$ and (B) normalized cumulative head discharge $q*$ as a function of normal-flow Froude number Fr_n. The other parameters were held constant ($w* = 0.1, W* = 4.5, l* = 30$, S = 0.0075). Panel (A) shows the acceleration factor ratios along the brink of the canyon at the centerline of the head, junction of the head and side-walls ("wall") and junction between the canyon side-wall and the base of the escarpment ("toe") (Figure 3). The stars represent the subcritical ($\mathrm{Fr}_n = 0.5$) and supercritical ($\mathrm{Fr}_n = 3$) base runs. Thin dashed lines are the best fit solutions discussed in Section 5.

4.3. Experiment Series 2: Waterfall-Width to Flood-Width Ratio $w*$

In experiment series 2, we varied the canyon-width to flood-width ratio $w*$ from 0.1 to 0.9 for two different Froude numbers ($\mathrm{Fr}_n = 0.5$ and $\mathrm{Fr}_n = 3$), with all other parameters held to the base case values ($W* = 4.5, l* = 30$ and S = 0.0075, Table 3.1). By definition, $w*$ can only vary between zero (no canyon) and unity (fully channelized canyon). We expect that wider canyons will have decreased acceleration at their walls due to the increased amount of water lost to the head. As canyons widen while keeping a constant length, the horseshoe head progressively occupies a larger portion of the flood width, but also of the total canyon length (Figure 3.4). The latter effect is a direct consequence of the assumption that the canyon head is semi-circular.

For subcritical floods, the acceleration factor ratio is not affected by w^* around the canyon head, but it is lower along the walls and decreases to zero at the toe (drying) as w^* increases (Figures 3.8A and 3.9A). This decrease results from a geometric effect – as w^* increases, the horseshoe head occupies more of the total flood width and captures an increasing amount of water. In the endmember case of a semi-circular canyon ($w^* = 1$), the wall and the toe are at the same location, the flooded width adjacent to the wall/toe is zero, and we thus expect the acceleration there to drop to zero in the cross-slope direction.

For supercritical floods, the acceleration factor ratio does not vary much around the head and the wall (Figure 3.8A). Figure 3.9B shows that the acceleration factor ratio is greater at the toe than at the wall, which we interpret as the result of a decreased cross-slope component of velocity for supercritical floods (Section 4.2.). The acceleration factor ratio increases at the toe with increasing w^* because the canyon side-walls are shorter, and a smaller fraction of the water is lost over the brink along the side-walls (Figure 3.8B).

For subcritical floods, the cumulative head discharge q^* decreases with increasing relative waterfall width (w^*), whereas q^* is constant for supercritical floods (Figures 3.8B and 9C). These trends correlate with the acceleration factor ratio at the wall α_w^*. In subcritical cases, an increasingly wide horseshoe head captures more of the total available water, leading to smaller flow depths near the wall, and thus decreased lateral backwater effects. In supercritical cases, flow depth does not significantly deviate from its upstream value away from the canyon wall, such that lateral backwater effects are constant as w^* increases. The cumulative head discharge q^* should plateau at unity in both sub- and supercritical cases because all of the water enters into the head at $w^* = 1$ (Figure 3.9C).

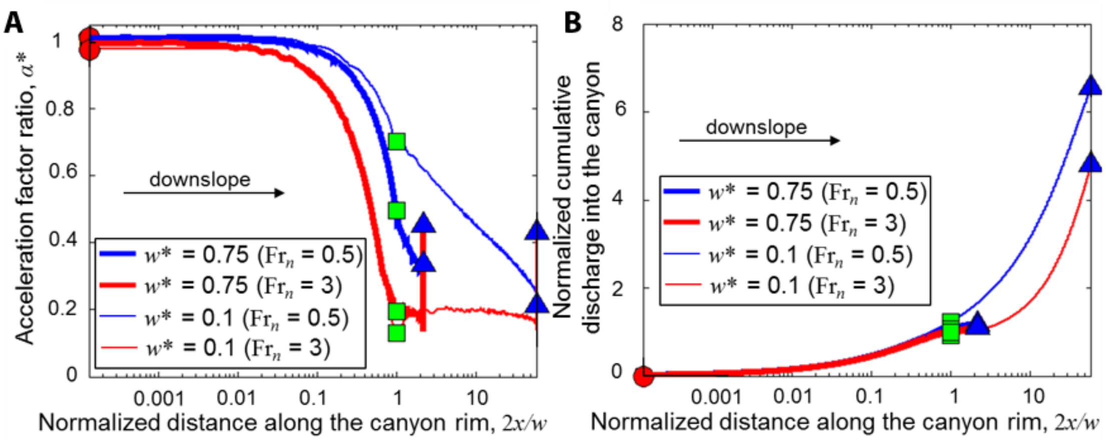

Figure 3.8: Rim distribution of acceleration factor ratio and normalized cumulative discharge around the head vs. canyon-width to flood-width ratio. (A) Acceleration factor ratio α^* and (B) normalized cumulative discharge along the brink of the canyon. The abscissa is the distance measured along the spatial *x*-axis (Figure 3) from the center of the canyon head, normalized by $w/2$, such that this distance equals unity at the head-to-wall junction (i.e., where $\theta = \pi/2$). Blue lines are subcritical runs, whereas red lines are supercritical runs. Thinner lines correspond to the base runs (with $w^* = 0.1$, Figure 5), while thicker lines have a canyon-width to flood-width ratio $w^* = 0.75$. Red circles indicate the canyon head center, green squares the head to wall junction, and blue triangles the canyon toe (Figure 3). Note that the acceleration factor at the toe (blue triangle) is measured in the downslope (*x*) direction, and hence is offset from the profile that shows acceleration in cross-slope (*y*) direction at the corner junction between the canyon and the escarpment.

4.4. Experiment Series 3: Flood-Width Limitation Factor W^*

In experiment series 3, we investigated the effect of varying lateral-backwater lengths for a given flood-width. We thus varied the flood-width limitation factor W^* from 0.12 to 15 for two different Froude numbers ($\mathrm{Fr}_n = 0.5$ and $\mathrm{Fr}_n = 3$), $w^* = 0.1$, $l^* = 30$ and *S* = 0.0075 (Table 3.1). Like the base cases, this corresponds to the case of a wide flood pouring over the brink of a long canyon. In theory, W^* can vary from values close to zero, when the lateral-backwater length is very long compared to the flood-width, to virtually infinity when the flood is very wide compared to the backwater length.

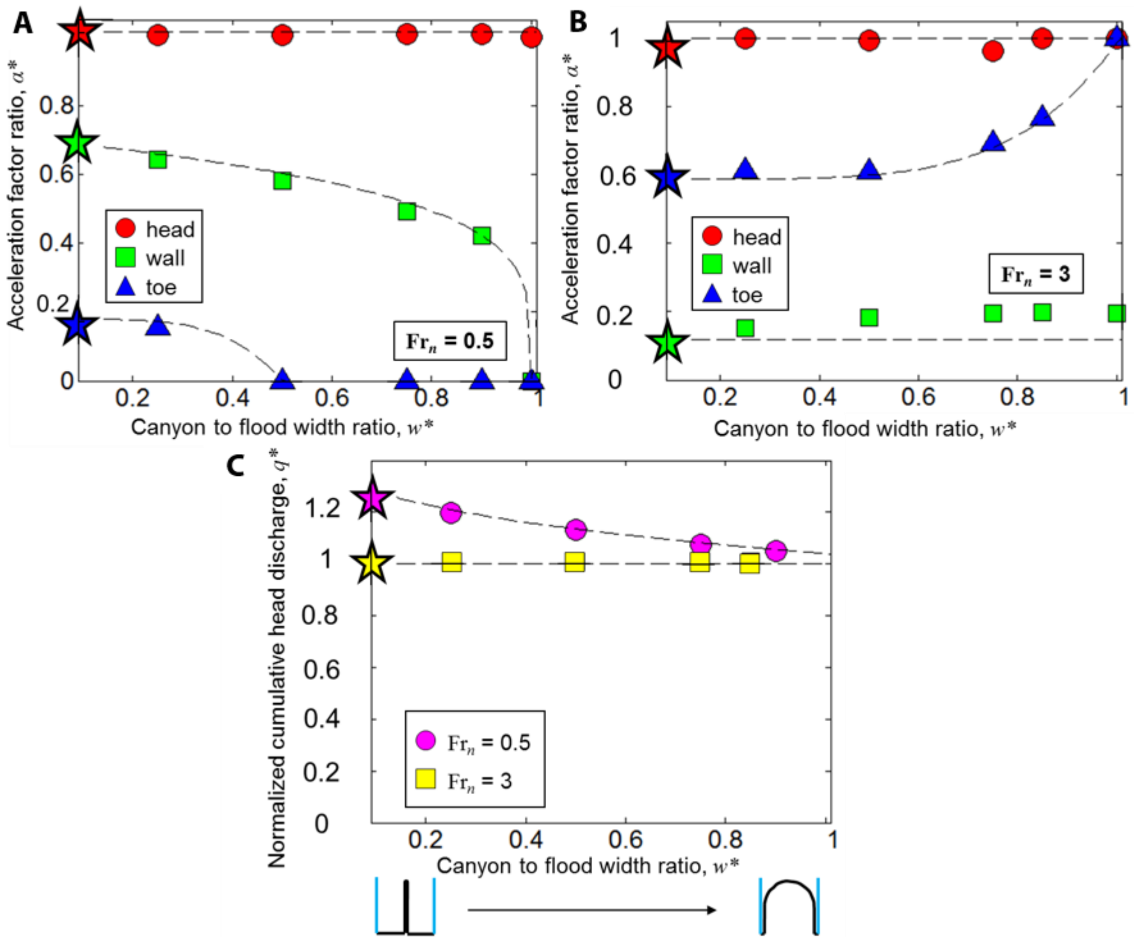

Figure 3.9: Acceleration factor ratio and normalized cumulative discharge around the head vs. canyon-width to flood-width ratio. Acceleration factor ratio $\alpha*$ as a function of the canyon-width to flood-width ratio $w*$ for (A) subcritical flows ($\mathrm{Fr}_n = 0.5$) and (B) supercritical flows ($\mathrm{Fr}_n = 3$). (C) Normalized cumulative head discharge $q*$ as a function of the canyon-width to flood-width ratio $w*$ for both subcritical ($\mathrm{Fr}_n = 0.5$) and supercritical flows ($\mathrm{Fr}_n = 3$). The other parameters are held constant ($W* = 4.5$, $l* = 30$, S = 0.0075). Stars represent the base case simulations. Dashed lines are the best fit solutions discussed in Section 5. Sketches at the bottom of (C) illustrate how plan-view geometry varies as $w*$ increases (Figure 3.4).

Figure 3.10A shows that the acceleration factor ratio decreases at the wall for lower $W*$. The acceleration factor ratio at the toe decreases to zero at $W* = 0.25$ for both sub- and supercritical flows, indicating complete drying. Interestingly, acceleration is locally enhanced along the walls downstream of the canyon head for small $W*$ (Figure 3.10A).

For this case, the canyon head radius is much smaller than the length scale over which flow convergence occurs (L_b). Thus, for $W^* \approx 0.25$, the zone of maximum flow convergence is pushed downstream of the canyon head. Overall normalized cumulative discharge into the canyon is enhanced for both sub- and supercritical floods when W^* is large. Nevertheless, the normalized cumulative head discharge q^* is only enhanced at large W^* in the subcritical case (Figure 3.10B).

Figure 3.11A shows over a wider range in parameter space how the acceleration factor ratios at the head, wall and toe vary as W^* increases for a subcritical flood. The acceleration factor ratio at the wall is maximum at $W^* \approx 1$. We interpret this transition at $W^* \approx 1$ as the interplay of flood-width limitations ($W^* < 1$) and enhanced flow focusing upstream of the head-to-wall junction ($W^* > 1$). For $W^* < 1$, flow focusing into the canyon head is limited by the flood width because the backwater length is larger than the flood width. In addition, the zone of maximum flow convergence may be pushed downstream of the head-to-wall junction as described above (Figure 3.10A). For large W^* and fixed w^*, the radius of the canyon head becomes large with respect to the backwater length, which again is the characteristic length over which flow focusing occurs. Thus, we interpret the reduction in α^*_w for large W^* to be caused by enhanced flow capture in the canyon head, upstream of the head-to-wall junction. Analogously to the acceleration factor ratio at the wall, cumulative head discharge q^* is maximum at $W^* \approx 1$ for subcritical flows (Figure 3.11C).

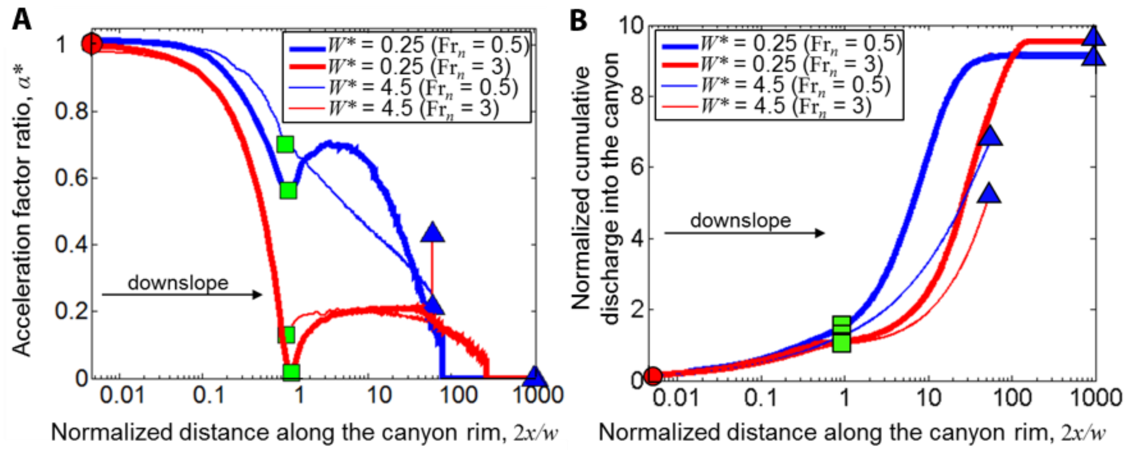

Figure 3.10: Rim distribution of acceleration factor ratio and normalized cumulative discharge around the head vs. lateral backwater parameter. (A) Acceleration factor ratio $\alpha*$ and (B) normalized cumulative discharge along the brink of the canyon. The abscissa is the distance measured along the spatial *x*-axis (Figure 3) from the center of the canyon head, normalized by $w/2$, such that this distance equals unity at the head-to-wall junction (i.e.,where $\theta = \pi/2$). Blue lines are subcritical runs, whereas red lines are supercritical runs. Thinner lines correspond to the base runs (with $W* = 4.5$, Figure 5), while thicker lines have a higher lateral-backwater parameter ($W* = 0.25$). Red circles indicate the canyon head center, green squares the head to wall junction, and blue triangles the canyon toe (Figure 3.3). Note that the acceleration factor at the toe (blue triangle) is measured in the downslope (*x*) direction, and hence is offset from the profile that shows acceleration in cross-slope (*y*) direction at the corner junction between the canyon and the escarpment.

Similar to the decrease in acceleration factor ratio at the wall, the acceleration factor ratio at the toe decreases as $W*$ gets smaller and the toe eventually dries at $W* \approx 0.5$. However, unlike α_w^*, the acceleration factor ratio at the toe does not decrease with increasing $W*$ because of the coincident shortening of the canyon which minimizes flow loss upstream (Figure 3.4).

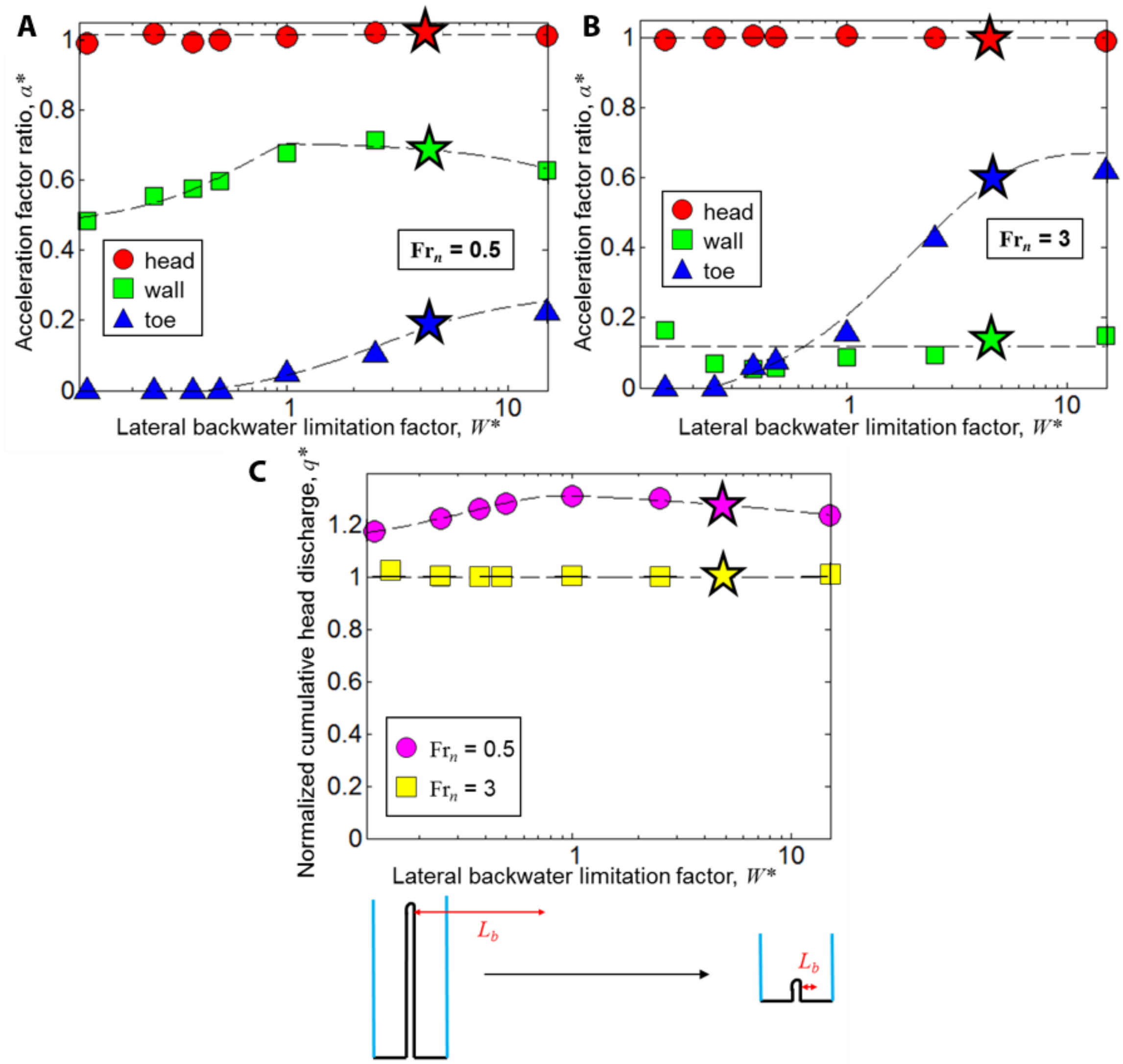

Figure 3.11: Acceleration factor ratio and normalized cumulative discharge around the head vs. lateral backwater parameter. Acceleration factor ratio α^* as a function of the lateral-backwater parameter W^* for (A) subcritical flows ($\mathrm{Fr}_n = 0.5$) and (B) supercritical flows ($\mathrm{Fr}_n = 3$). (C) Normalized cumulative head discharge q^* as a function of the lateral-backwater parameter W^* for both subcritical ($\mathrm{Fr}_n = 0.5$) and supercritical flows ($\mathrm{Fr}_n = 3$). The other parameters are held constant ($w^* = 0.1$, $l^* = 30$, S = 0.0075). Stars represent the base case simulations. Dashed lines are the best fit solutions discussed in Section 5. Sketches at the bottom of (C) illustrate how plan-view geometry varies as W^* increases (Figure 3.4).

For supercritical flows, the acceleration factor ratio at the head and wall (Figure 3.11B), and cumulative head discharge (Figure 3.11C), are roughly constant, which we interpret as the result of the decreased importance of lateral backwater effects for supercritical floods. However, the acceleration factor ratio at the toe integrates the backwater effects all along the canyon side-walls upslope of the toe, and thus α_t^* decreases with decreasing W^* due to water lost to the canyon, and drying ot the toe for $W^* < 0.3$.

4.5. Experiment Series 4: Downslope Backwater Parameter l^*

In experiment series 4, we investigated the effect of canyon lengthening. We varied the downslope backwater parameter l^* between 0.55 and 30 for two different Froude numbers ($\mathrm{Fr_n} = 0.5$ and $\mathrm{Fr_n} = 3$), with all other parameters set to the base case values ($w^* = 0.1$, $W^* = 4.5$ and S = 0.0075, Table 3.1).

As expected, the acceleration factor ratio around the head and walls does not vary for either sub- and supercritical floods as l^* increases with all other parameters held constant (Figure 3.12A). Similarly, cumulative head discharge does not vary with l^* and therefore is not shown.

In contrast to the head and side-walls, the acceleration factor at the toe is larger for relatively short canyons (smaller l^*). We interpret this trend as the result of water pouring over a shorter side-wall distance, and thus less water is lost along the walls for smaller canyons (Figure 3.12A). For subcritical floods, we observe a rapid decrease in acceleration at the toe as canyons lengthen (Figure 3.12B). For supercritical floods, the reduction in acceleration factor ratio at the toe with increasing l^* is more gradual due to less water lost into the canyon upstream (Figure 3.12C).

5. Semi-Empirical Approximations

Because our 2-D hydraulic simulations are computationally demanding, it is of interest to obtain semi-empirical approximations to our results in order to predict the acceleration factor ratios and cumulative head discharge, α_h^*, α_w^*, α_t^* and q^*, as a function of Fr_n, w^*, W^* and l^* in a way analogous to Equation (3.1). All parameters affect the acceleration factor ratios roughly independently. We were able to fit the data by addressing each parameter separately in the regime where other parameters do not matter through multiple nonlinear regressions. The fit relationships are given in Appendix A.2.

We first corrected the data for Froude number Fr_n by dividing the data by exponential or power function fits to experiment series 1. We then identified and ranked by decreasing importance the other dimensionless parameters driving the remaining variance (w^* then W^* for α_w^* and q^* ; l^* then W^* then w^* for α_t^*). Finally, we sequentially corrected for the variance induced by each of the ranked parameters by further dividing the data by the corresponding power law fits. When different functional fits were needed for different parameter ranges, we attempted to impose continuity of the fit across the range boundaries. Nevertheless, discontinuities in the fits still arise in cases because we did not model every possible combination of parameters.

Figure 3.13 shows a comparison between the acceleration factor ratios and cumulative head discharge as predicted by ANUGA and the best fit functions we derived. The root mean square error (RMS) between the fits and the data is equal to 1.1%. In order to test the ability of the semi-empirical fits to predict acceleration factor ratios and cumulative head discharge for parameter values that were not used when performing the fits, we designed a set of 45 additional test simulations that explored various other combinations of parameter values (Table 3.1). The fit functions are successful at predicting most of the additional simulations (Figure 3.13). The functions, however, did not fit as well α_t^* for supercritical floods at canyons that are relatively short and wide (shaded in gray in Figure 3.13), a configuration we did not explore extensively. The RMS between the additional test data and their fits is equal to 2.2% when the latter simulations are excluded, and to 4.1% when they are included.

Because Fr_n, W^* and l^* have no upper limit by definition, one might be interested in a case outside our explored parameter space. In most applications, the Froude number Fr_n falls within our modeled range. Higher Froude numbers would have acceleration factor ratios of unity at the head and zero at the wall due to the near-absence of flow focusing. At the toe, its value would still vary greatly with the amount of water lost along the canyon side-walls, and thus with the downslope backwater parameter l^*. The flood-width limitation factor W^* does not significantly affect the hydraulics at values higher than the range we tested (at $W^* = 5$, acceleration factor ratios at the wall do not vary significantly, and normalized cumulative head discharge decreases to unity). In cases where $\mathrm{Fr}_n < 1$ and W^* are very small, one can assume that α_w^* and α_t^* are small. Finally, almost no water is left at the toe of very long canyons ($l^* >> 1$), such that α_t^* can be assumed to be zero. Most of these endmember cases are reproduced by the fits. When the fits predict negative values for acceleration factor ratios, they should be set to zero.

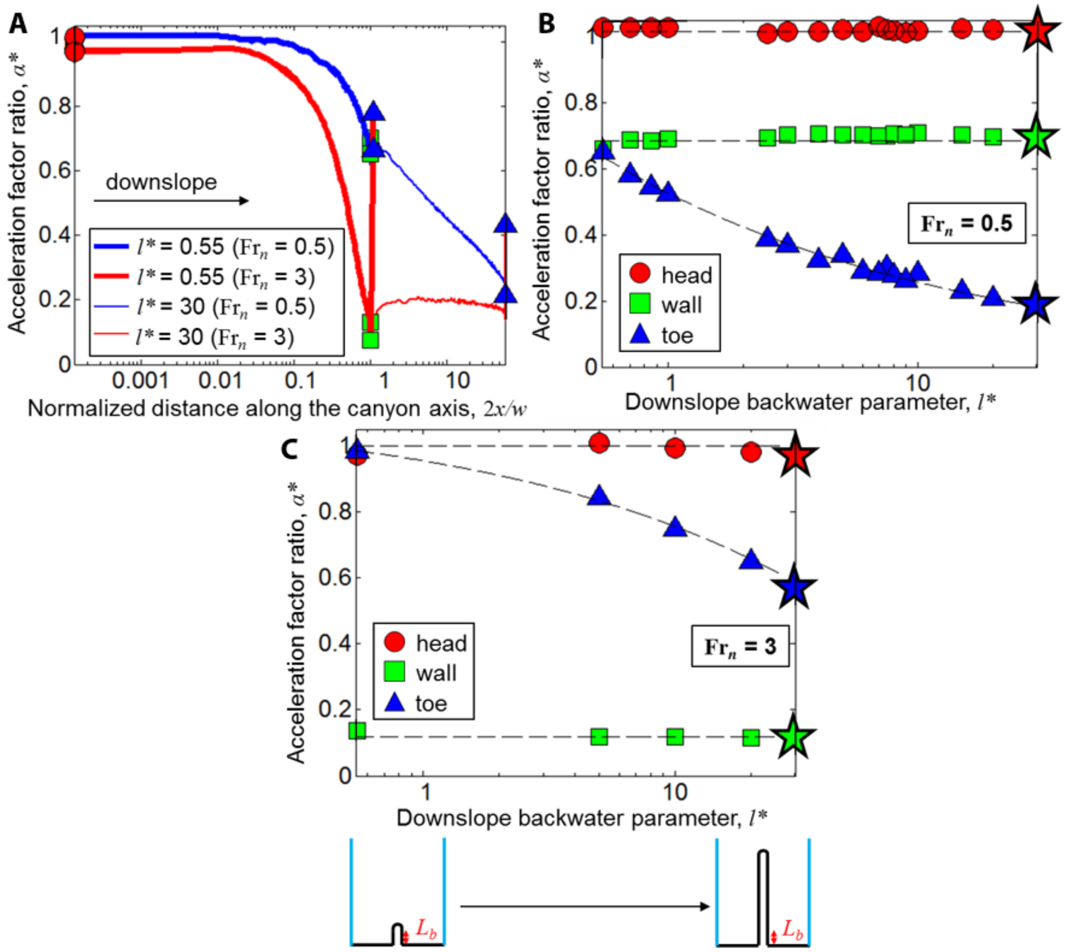

Figure 3.12: Acceleration factor ratio and normalized cumulative discharge around the head vs. downslope backwater parameter. (A) Acceleration factor ratio α^* along the brink of the canyon. The abscissa is the distance measured along the spatial *x*-axis (Figure 3) from the center of the canyon head, normalized by $w/2$, such that this distance equals unity at the head-to-wall junction (i.e., where $\theta = \pi/2$). Blue lines are subcritical runs, whereas red lines are supercritical runs. Thinner lines correspond to the base runs (with $l^* = 30$, Figure 5), while thicker lines have a canyon-width to flood-width ratio $l^* = 0.55$). Red circles indicate the canyon head center, green squares the head to wall junction, and blue triangles the canyon toe (Figure 3). Note that the acceleration factor at the toe (blue triangle) is measured in the downslope (*x*) direction, and hence is offset from the profile that shows acceleration in cross-slope (*y*) direction at the corner junction between the canyon and the escarpment. (B) and (C) show the normalized acceleration factor as a function of the downslope backwater parameter l^* for subcritical flows ($\mathrm{Fr}_n = 0.5$) and supercritical flows ($\mathrm{Fr}_n = 3$) respectively. Stars represent the base case simulations. Dashed lines are the best fit solutions discussed in Section 5. Sketches at the bottom of (C) illustrate how plan-view geometry varies as l^* increases (Figure 3.4).

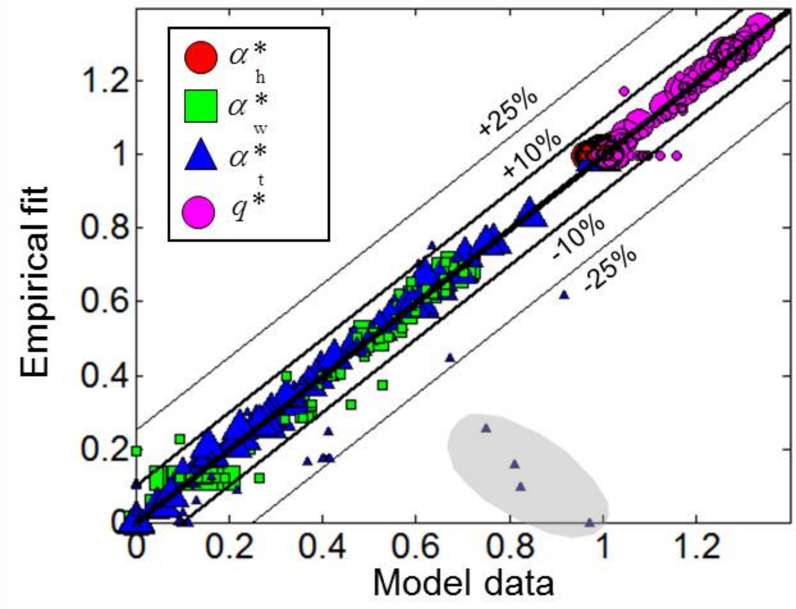

Figure 3.13: Best fit vs. model data (acceleration factor ratios at the head α^*_h, wall α^*_w, and toe α^*_t, and normalized cumulative head discharge q^*). Large symbols show runs that were used for the best fit, whereas small ones show runs that were not, and have two parameters or more that differ from the base runs (total of 4x110 = 440 symbols). The thin black lines highlight ±10%, and the intermediate ones indicate ±25%. A perfect fit falls on the 1:1 thick black line. Note that 180 of these symbols represent the test runs (those not taken into account to derive the semi-empirical fits), and their vast majority fall within ±10% of the values predicted by Equations (A1)-(A8). Toe accelerations highlighted in gray correspond to wide ($w^* \geq 0.75$), short canyons ($l^* \leq 6$) in supercritical floods. In this configuration, acceleration at the toe is high due to the high downslope inertia of the flow and the little amount of water lost to the walls in the cross-slope direction. Our scaling underestimates the acceleration at the toe in this configuration.

6. Discussion

6.1. Flow Regimes

Figure 3.14 illustrates how the best fit functions can be used to predict the acceleration factor around the brink of horseshoe waterfalls that widen and lengthen. Because the normalizing denominator for the acceleration factor ratios (α_{1D}, Equation (3.1)) and the cumulative head discharge ($q_n w/2$) can be calculated independently, one can invert for dimensional properties of the flow from the best fit equations (Equations A1-A8).

The effect of increasing the canyon width is best described by the acceleration factor ratio at the wall α_w^* and the cumulative head discharge q^* (Figure 3.14A and B). In natural systems with a normal flow depth that is constant over time, canyon widening will not only cause w^* to increase, but also W^* to decrease, and flow around the canyon brink will be affected by lateral backwater effects. Figure 3.14A and B show how α_w^* and q^* can be summarized in several flow regimes with coincident changes in w^* and W^*. In the subcritical regime ($\mathrm{Fr}_n < 1$) with focusing not limited by the width of the flood ($W^* > 1$), acceleration at the wall is mostly a function of Froude number, and cumulative head discharge is enhanced. As the canyon widens ($W^* < 1$), acceleration at the wall is mostly a function of canyon width and α_w^* decreases. Likewise, with canyon widening the cumulative head discharge goes from enhanced with respect to the 1-D case ($q^* > 1$) to normal ($q^* = 1$). In the supercritical regime, acceleration at the wall is a function of the flood Froude number only, and decreases with increasing Fr_n. Head discharge for supercritical floods is roughly equal to the corresponding 1-D discharge.

Canyon lengthening affects mostly the acceleration factor at the toe α_t^* (Figure 3.14C). Acceleration at the toe is reduced with larger canyons; however, this effect weakens at higher Froude numbers.

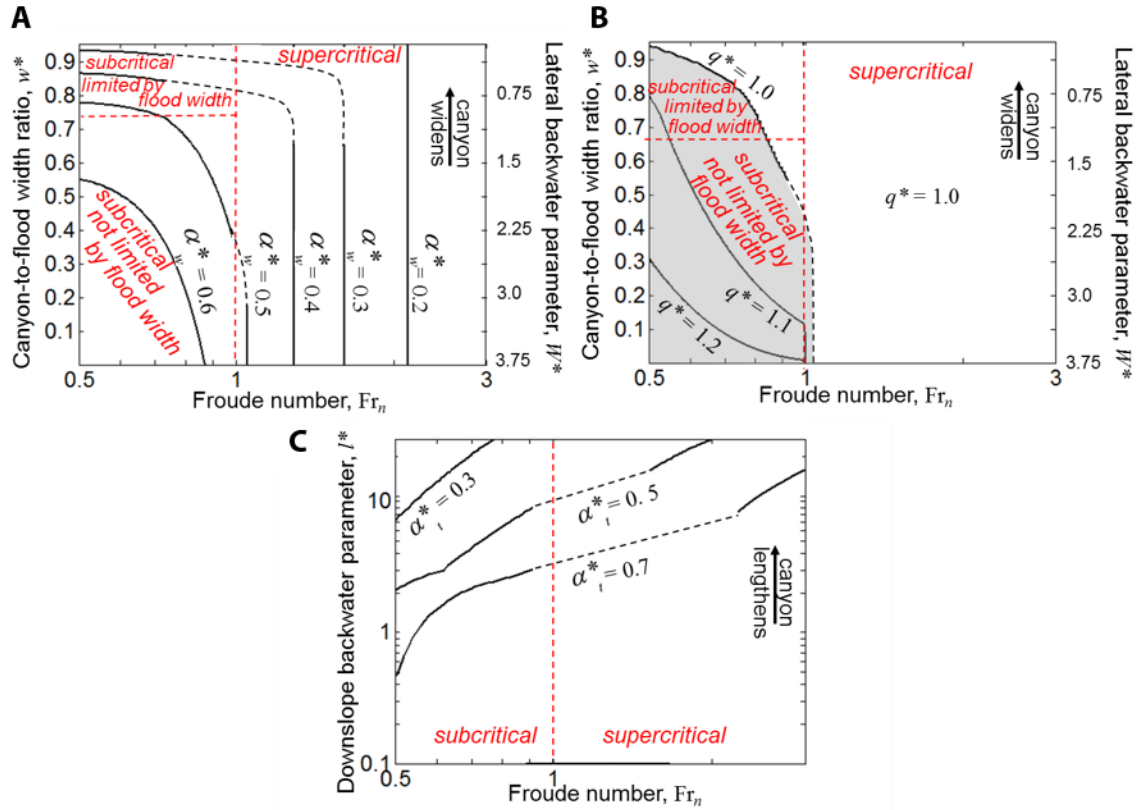

Figure 3.14: Flow-focusing regimes. (A) Wall acceleration factor ratio α^*_w and (B) normalized cumulative head discharge q^* contours for the case of canyon widening, where both the canyon-to-flood width ratio w^* and the lateral-backwater limitation factor W^* change ($l^* = 30$, S = 0.0075). The shaded area shows the parameter space where cumulative head discharge is enhanced ($q^* \geq 1$). As a canyon widens, one moves upwards on the plots. (C) Toe acceleration factor ratio α^*_t for the case of canyon lengthening ($w^* = 0.1, W^* = 4.5$, S = 0.0075). As a canyon lengthens, l^* increases and one moves upward on the plot. Contours are determined from the semi-empirical fits (Equations A1-A8). Contours are dashed where the semi-empirical fits produce discontinuities.

6.2. Engineering Applications

Hydraulic engineers typically employ full 3-D numerical models to study and design specific spillways with complex geometries [e.g., *Feurich et al.*, 2011]. Nevertheless, our results have implications for the early stages of designing spillways. A first important result of our modeling is that the acceleration factor ratio at the head of a horseshoe waterfall is only enhanced by less than 4% compared to the 1D case as long as there is no cross-stream topographic gradient (e.g., Figure 3.7). Consequently, in applications where the required precision is of a few percent, it can be assumed that acceleration at the head can be approximated by Equation (3.1).

Moreover, understanding flow focusing is essential to optimize the discharge into the head of the canyon. For example, one might need to minimize erosion at the base of a horseshoe spillway. This can be accomplished by decreasing the amount of flow focusing towards the canyon, and thus the velocity and width of the jet impinging the plunge-pool. If flow focusing is minimized, by making the canyon as wide as the flood ($w^* \approx 1$), the discharge per unit width at the center of the spillway will be that of the linear escarpment, and the discharge will be lower everywhere else along the brink, stabilizing the side-walls. If enhanced discharge is desired to increase the generated power of a water turbine, a horseshoe spillway should be narrower than the total flood-width ($w^* << 1$) such that flow focusing is maximum at the tip of the horseshoe (e.g., $W^* \approx 1$). Our results suggest that this design can enhance discharge by up to about 35% (e.g., Figure 3.7). Because hydropower is proportional to discharge [e.g., *Sayers*, 1990], such a design could increase energy production.

6.3. Implications for the Shape of Canyon Heads and Canyon Dynamics

Waterfalls retreat upstream as a consequence of erosion at the knickpoint, causing formation of canyons. Erosion occurs either through undercutting in the plunge-pool, or plucking and toppling of rock blocks upstream of the brink [e.g., *Gilbert*, 1907; *Haviv et al.*, 2006; *Lamb et al.*, 2006; *Lamb et al.*, 2007; *Lamb and Dietrich*, 2009; *Mackey et al.*, 2014]. Undercutting occurs as a result of scouring of rocks where the water jet impinges the plunge-pool, by the combined mechanical action of water and transported sediments [e.g., *Stein and Julien*, 1993; *Flores-Cervantes et al.*, 2006]. In particular, *Flores-Cervantes et al.* (2006) showed that bed shear stress at the base of the jet increase with flow velocity at the brink U_0. Moreover, higher water discharges cause higher sediment capacity of the flow [e.g., *Meyer-Peter and Muller*, 1948; *Fernandez Luque and Van Beek*, 1976], which enhances plunge-pool erosion. Consequently, more focusing towards the canyon head suggests that more erosional work is accomplished by water and sediment. Enhanced erosion at the head combined with drying of the sidewalls promotes upstream propagation of the canyon head as opposed to canyon widening. Our results indicate that higher head discharges are obtained for lower Froude numbers, and lateral-backwater lengths smaller than the half-flooded-width.

Plucking and toppling occur through the action of bed shear stress applied by water flow upstream of the waterfall brink [e.g., *Coleman et al.*, 2003; *Chatanantavet and Parker*, 2009]. The bed shear stress at the brink is given by

$$\tau_b = \rho C_f {U_p}^2 = \rho C_f \alpha^{*2} {U_n}^2, \tag{3.8}$$

where ρ is the density of water, and thus scales with the acceleration factor ratio squared. Assuming that erosion rate is proportional to bed shear stress to some positive power [e.g., *Howard and Kerby*, 1983], higher acceleration factor ratios should lead to higher erosion rate [*Stein and Julien*, 1993; *Haviv et al.*, 2006; *Lamb and Dietrich*, 2009].

Our modeling suggests that flow focusing enhances acceleration factor ratios around the head of canyons for low Froude numbers, and low lateral-backwater lengths (Equations A1, A2, A4, , and decreases acceleration factor ratios along the walls and toes as canyons lengthen and widen (Equations 3.A2-3.A7). If we make the assumption that erosion only occurs when a certain threshold shear stress is surpassed [e.g., *Lamb and Dietrich*, 2009], erosion is more likely to prevail where $\alpha *$ is higher. Consequently, different combinations of bed shear stress at the head and at the head-to-wall junction may determine whether the canyon widens or narrows, while bed shear stress at the head and the toe may control whether the canyon grows or shrinks.

We showed that plan-view curvature of the canyon rim drives cross-slope flow, and thus convergence of the flood waters towards the canyon. Flow focusing can in turn drive the creation of more curvature. Indeed, variations in flow velocities around the brink may lead to variable erosion rates around the brink, with higher erosion rates at the canyon head where velocities are enhanced, and decreased erosion rates along the walls where velocities are decreased [e.g., *Stein and Julien*, 1993; *Lamb and Dietrich*, 2009]. Consequently, feedbacks between flood hydraulics and canyon form may be similar to those observed in the formation of amphitheater-heads by groundwater sapping in sand [*Howard and McLane*, 1988], and may help to explain the origin of amphitheater-headed canyons in competent rock [e.g., *Lamb et al.*, 2006; *Lamb et al.*, 2014] (Figure 3.1). It is likely that canyon head shape differs for different degrees of focusing, and thus might be a function of flood attributes, such as Froude number Fr_n and flood-width limitation factor $W *$. This conclusion modifies that of *Petroff et al.* [2011], who proposed that erosion rates are proportional to local plan-view curvature of a canyon head. Our results suggest that erosion may be enhanced at the center of the canyon head due to flow focusing even in the absence of spatial changes in curvature (as in the case of a semi-circular head).

7. Conclusion

Horseshoe-shaped waterfalls modify the flow patterns upstream of waterfalls, flow acceleration at the waterfall brink, and cumulative discharge into the waterfall. The distribution of the acceleration factor around the canyon brink is mainly controlled by the normal-flow Froude number, the width of the flood compared to its lateral-backwater length and the canyon width, as well as the downslope length of the canyon relative to the backwater length.

In the case of a sheet flood, i.e., when the canyon is much narrower than the flood and lateral-backwater effects do not limit flow focusing, the acceleration factor is entirely determined by the Froude number and the length of the canyon. Higher Froude numbers decrease the amount of focusing and thus decrease the acceleration factor around the canyon side-walls (i.e., $\alpha^*_w \to 0$ for $\mathrm{Fr}_n >> 1$), increase it at the canyon toe, and lower the cumulative discharge into the canyon head. Longer canyons lose more water along their side-walls than shorter canyons, and thus have decreased acceleration factors at the canyon toe.

For non-sheet floods, the flow patterns are more complicated due to the influence of boundaries that limit flow focusing into the waterfall. Generally, wider waterfalls and/or higher lateral-backwater lengths decrease both the acceleration factor around the canyon head and walls, and the cumulative discharge into the canyon head. When the canyon is confined within the full width of the flood ($w^* \approx 1$), the walls and the toe are at the same location, and the acceleration factor in both the cross-slope and downslope directions are zero ($\alpha^*_w \approx \alpha^*_t \approx 0$).

Finally, when the lateral-backwater limitation factor is much smaller than unity ($W^* << 1$), the acceleration factor along the walls tends to zero ($\alpha^*_w \to 0$).

The semi-empirical relationships we derived to relate acceleration and discharge around the brink of waterfalls may provide some guidance during the early stages of spillway design and optimization. These relationships also provide a quantitative understanding of flow focusing that can be used to help explaining the shape of waterfalls, as well as their evolution.

		Dimensionless variables				Dimensional parameters						
	Number of simulations	$\mathrm{Fr}_n = \frac{U_n}{\sqrt{gh_n}}$	$w^* = \frac{w}{W}$	$W^* = \frac{(W-w)S}{2h_n}$	$l^* = \frac{lS}{h_n}$	S	w (m)	W (m)	l (m)	q_n (m^2/s)	n (s/m$^{1/3}$)	h_n (m)
Base cases subcritical	1	0.5	0.1	4.5	30	0.0075	200	2000	6000	2.88	0.059	1.5
Base cases supercritical	1	3	0.1	4.5	30	0.0075	200	2000	6000	17.26	0.0099	1.5
Experiment series 1: Froude number, Fr_n	9	0.4-5	0.1	4.5	30	0.0075	200	2000	6000	2.30-28.77	0.074-0.006	1.5
Experiment series 2: Canyon-width to flood-width ratio, w^*	12	0.5,3	0.1-0.9	4.5	30	0.0075	200-2595	2000-3000	1000-6000	0.31-17.26	0.007-0.06	0.25-1.5
Experiment series 3: Lateral backwater limitation factor, W^*	14	0.5,3	0.1	0.125-15	30	0.0075	1.5-112	15-1120	1620-6395	0.4-19.0	0.009-0.06	0.41-1.6
Experiment series 4: Downslope backwater parameter, l^*	22	0.5,3	0.1	4.5	0.55-30	0.0075	200	2000	110-4000	2.88	0.059	1.5
Test simulations	45	0.5-1.3	0.1-0.9	0.02-4.5	0.55-30	$5\mathrm{x}10^{-4}$-$5\mathrm{x}10^{-2}$	137.14-13714	480-48000	200-51429	2.88-472.74	0.02-0.10	1.5-45

Table 3.1: Dimensionless and dimensional parameter ranges encompassed by the simulations.

Acknowledgements

This work benefited from discussion with Gary Parker, Gareth Davies and Stephen Roberts. We thank Cailan Haliday for assistance with and testing of the numerical model setup. We also thank three anonymous reviewers for helpful and constructive reviews that improved this paper. Support was provided by the NASA Earth and Space Science Fellowship 12-PLANET12F-0071, NSF Grant EAR-1147381, and NASA Grant NNX13AM83G. All data in the present paper is available upon request to the corresponding author.

Chapter 4

CANYON FORMATION CONSTRAINTS ON THE DISCHARGE OF CATASTROPHIC OUTBURST FLOODS ON EARTH AND MARS

Mathieu G. A. Lapôtre, Michael P. Lamb, and Rebecca M. E. Williams

This chapter was published as:
Lapôtre, M. G. A., et al. (2016), Canyon Formation Constraints on the Discharge of Catastrophic Outburst Floods of Earth and Mars, *Journal of Geophysical Research: Planets*, 121(7), 1232-1263, DOI:10.1002/2016JE005061.

Notations are summarized in Appendix B.1.

Abstract. Catastrophic outburst floods carved amphitheater-headed canyons on Earth and Mars, and the steep headwalls of these canyons suggest that some formed by upstream headwall propagation through waterfall erosion processes. Because topography evolves in concert with water flow during canyon erosion, we suggest that bedrock canyon morphology preserves hydraulic information about canyon-forming floods. In particular, we propose that for a canyon to form with a roughly uniform width by the mechanism of upstream headwall retreat, erosion must occur around the canyon head, but not along the sidewalls, such that canyon width is related to flood discharge. We develop a new theory for bedrock canyon formation by megafloods based on flow convergence of large outburst floods towards a horseshoe-shaped waterfall. The model is developed for waterfall erosion by rock toppling, which is a candidate erosion mechanism in well-fractured rock, like columnar basalt. We apply the model to fourteen terrestrial (Channeled Scablands, Washington; Snake River Plain, Idaho; Ásbyrgi Canyon, Iceland) and nine martian (near Ares Vallis and Echus Chasma) bedrock canyons, and show that predicted flood discharges are nearly three orders of magnitude less than previously estimated, and predicted flood durations are longer than previously estimated, from less than a day to a few months. Results also show a positive correlation between flood discharge per unit width and canyon width, which supports our hypothesis that canyon width is set in part by flood discharge. Despite lower discharges than previously estimated, the flood volumes remain large enough for individual outburst floods to have perturbed the global hydrology of Mars.

1. Introduction

The largest floods in the Solar System are inferred to have occurred from the dramatic imprint they have left on the landscapes of Earth and Mars, and in particular from the presence of large bedrock canyons on both planets. For example, on Earth, the Big Lost River and Bonneville floods carved canyons along the Pleistocene Snake River valley [*Malde*, 1960; *Scott*, 1982; *O'Connor*, 1993; *Rathburn*, 1993] (Figure 4.1A-C), and the glacial outburst Missoula floods carved the Pleistocene Channeled Scablands of the northwestern United States [e.g., *Bretz*, 1969; *Baker*, 1973; *O'Connor and Baker*, 1992] (Figure 4.1E-G). Some of the largest floods on Mars carved the outflow channels of the Circum-Chryse region, for example at Ares Vallis [*Komatsu and Baker*, 1997; *Pacifici et al.*, 2009; *Warner et al.*, 2010] (Figure 4.1I) and Kasei Valles [*Robinson and Tanaka*, 1990; *Williams et al.*, 2000; *Williams and Malin*, 2004]. Two remaining outstanding unknowns are the water discharges associated with these floods, and the duration of the flood events. A better quantitative understanding of these floods is critical because (1) they are unlike anything we observe today, (2) they were so large that they may have altered global hydrology and climate on both planets [e.g., *Baker*, 2009], and (3) they represent one of the best indicators of flowing water during the decline of surface hydrology on Mars [e.g., *Carr and Head*, 2010].

Paleohydrologists mostly use two methods to infer discharge from canyon observations: (1) they calculate the required flow depth to initiate motion of the observed sediment sizes through a Shields stress criterion [e.g., *O'Connor*, 1993; *Lamb et al.*, 2008; *Lamb et al.*, 2014], or (2) they assume that observed channels or canyons were filled to the brim (brimful assumption) [e.g., *Baker et al.*, 1974; *Carr*, 1979; *Robinson and Tanaka*, 1990; *Komatsu and Baker*, 1997; *McIntyre et al.*, 2012]. Initial motion and brimful assumptions provide conservative lower and upper bounds on flow discharge, respectively, constraining its value with an uncertainty of many orders of magnitude.

Flow durations have been previously estimated from either (1) water discharge and eroded rock volume (assuming a water-to-rock ratio for erosion) [e.g., *Komar*, 1980; *Carr*, 1986; *Leask et al.*, 2007], or (2) sediment transport capacity and the volume of eroded rock assuming transport-limited conditions [e.g., *Lamb et al.*, 2008; *Lamb and Fonstad*, 2010]. Both methods require a priori knowledge of flow depth. In the absence of better estimates, flow depth has generally been assumed to be brimful, which leads to flood durations that are likely largely underestimated, and thus provide lower bounds.

While estimates of flood discharges and durations have been made from assumptions about flood hydraulics, we herein propose that tighter constraints can come specifically from coupling hydraulics to erosion mechanics. An important, but largely unutilized characteristic of flood-carved canyons in basalt is that they often have steep amphitheater-shaped headwalls [e.g., *Lamb et al.*, 2006]. In particular, amphitheater-headed canyons that have roughly uniform widths are thought to form by upstream propagation of the headwall [*Lamb and Dietrich*, 2009; *Petroff et al.*, 2011]. In the absence of quantitative mechanistic models for headwall retreat, radically different flow configurations have been proposed to explain the formation of various amphitheater-headed canyons on Earth and Mars, such as both long-lived [*Harrison and Grimm*, 2005; *Pelletier and Baker*, 2011; *Petroff et al.*, 2011] and catastrophic [*Amidon and Clark*, 2014] groundwater seepage erosion, as well as catastrophic overland flow and waterfall erosion [*Baker et al.*, 1974; *Carr*, 1979; *Komatsu and Baker*, 1997; *Lamb et al.*, 2006; *Warner et al.*, 2010].

Canyons carved from groundwater seepage exist in cohesionless sediments on Earth [e.g., *Pillans*, 1985; *Schumm et al.*, 1995; *Luo et al.*, 1997], are debated in sedimentary rocks [*Laity and Malin*, 1985; *Howard et al.*, 1987; *Lamb et al.*, 2006], and are not observed in more crystalline lithologies [*Lamb et al.*, 2006; *Lamb et al.*, 2007; *Lamb et al.*, 2008]. While mechanistic models combining both fluvial and mass wasting processes have been formulated for groundwater sapping in loose sediments [e.g., *Howard and McLane*, 1988], there is currently no tested theory for the mechanics of erosion by seepage in strong rocks. In contrast, canyons carved into crystalline bedrock likely form from waterfall erosion, either through undercutting in the plunge-pool, or through rock toppling at the waterfall brink [e.g., *Gilbert*, 1907; *Haviv et al.*, 2006; *Lamb et al.*, 2007; *Lamb and Dietrich*, 2009; *Lamb et al.*, 2014].

Undercutting occurs as a result of scouring of rocks where the water jet impinges the plunge-pool, by the combined mechanical action of water and transported sediments [*Mason and Arumugam*, 1985; *Stein et al.*, 1993; *Bollaert*, 2004; *Flores-Cervantes et al.*, 2006; *Pagliara et al.*, 2006], while plucking and toppling occur through the action of bed shear stress applied by water flow upstream of the waterfall brink [e.g., *Coleman et al.*, 2003; *Chatanantavet and Parker*, 2009; *Lamb and Dietrich*, 2009; *Lamb et al.*, 2015]. In the case of vertically fractured lithologies, *Lamb and Dietrich* [2009] proposed that toppling of rock columns by overland flow could explain the morphology of amphitheater-headed canyons. *Lamb et al.* [2015] showed that toppling is the dominant erosion mechanism in fractured bedrock as long as block height is at least half of block width, which is typical of canyons carved in basalt with sub-vertical cooling joints, a common lithology in megaflood terrain on Earth and Mars. For example, toppling during large-scale floods is thought to have been the main mechanism for erosion at Box Canyon and Malad Gorge, Idaho [*Lamb et al.*, 2008; *Lamb et al.*, 2014], and at Ásbyrgi in Iceland [*Baynes et al.*, 2015a; *Baynes et al.*, 2015b]. On Mars, lava flows are ubiquitous [e.g., *Christensen et al.*, 2000; *Ruff and Christensen*, 2002; *Bibring et al.*, 2005; *Ehlmann and Edwards*, 2014], and basaltic columns were observed from orbit [*Milazzo et al.*, 2009]. The ubiquity of fractured lithologies where bedrock canyons are found on Earth and Mars makes rock toppling a good candidate mechanism for the formation of canyons with amphitheater-heads during large floods [e.g., *Warner et al.*, 2010].

While mechanistic models for erosion are needed for both the groundwater and overland flood scenarios, we focus in this paper on toppling erosion because many canyons in fractured rock show evidence for this mechanism. Our intention is not to assert that all amphitheater canyons were formed by flood-driven block toppling, but rather to demonstrate how canyons carved by this mechanism can be used as paleohydraulic indicators of past floods. We investigate the hypothesis that the width of amphitheater-headed (i.e., horseshoe-shaped) canyons carved by overland flow can be used as a proxy for water discharge of canyon-forming floods. We first build on a previous study of hydraulics upstream of horseshoe canyons and waterfalls [*Lapôtre and Lamb*, 2015], and extend this work for bedrock canyon formation and dynamics. We then show how this model can be used as a paleohydraulic tool to predict the discharge of a canyon-carving flood. Finally, we apply the model to twenty-three terrestrial and martian bedrock canyons, and invert for discharge, Shields stress within the canyon, flood duration, and flood water volume.

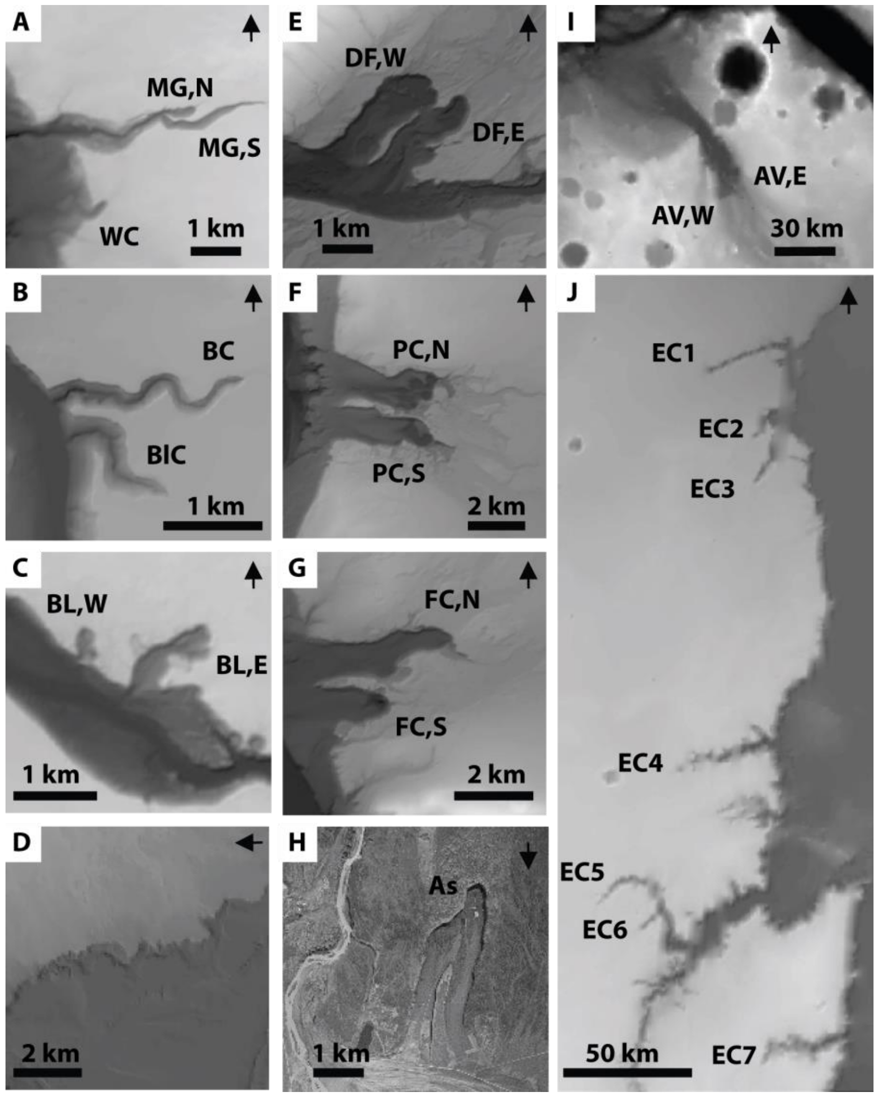

Figure 4.1: Bedrock canyons on Earth and Mars. (A) Malad Gorge (MG,N and MG,S) and Woody's Cove (WC), Idaho (ASTER), (B) Box Canyon (BC) and Blind Canyon (BlC), Idaho (ASTER), (C) Blue Lakes (BL,W and BL,E), Idaho (ASTER), (D) escarpment downstream of Malad Gorge, Idaho (SRTM), (E) Dry Falls (DF,W and DF,E), Washington (ASTER), (F) Pothole Coulee (PC,N and PC,S), Washington (ASTER), (G) Frenchman Coulee (FC,N and FC,S), Washington (ASTER), (H) Ásbyrgi canyon (As), Iceland (Aerial photograph source: Landmælingar Íslands), (I) canyons near Echus Chasma (EC1-7), Mars (MOLA), and (J) dry cataract near Ares Vallis (AV1-2), Mars (MOLA). Arrows indicate the North direction.

2. Model for the Stability of Canyons and Escarpments

In order to form a canyon by upstream canyon-head retreat while maintaining a uniform width, geometry requires that erosion must occur at the upstream end of the canyon head, but not along the canyon sidewalls. Figure 4.2 illustrates our hypothesized formation mechanism. As a sheet flood of steady discharge flows over a planar landscape and approaches an escarpment, loss of hydrostatic pressure at the escarpment draws the water surface down towards embayments in the escarpment (Figure 4.2A). Due to flow focusing and enhanced shear stresses around their rim, embayments grow into canyons via block toppling and capture water away from neighboring canyons. The wining proto-canyons both widen and lengthen (Figure 4.2B). This general competition mechanism is analogous to those proposed by *Howard* [1994] and *Izumi and Parker* [1995; 2000] for fluvially-eroded escarpments, and by *Dunne* [1990] for groundwater-dominated escarpment retreat. When the canyons are large enough to focus sufficient water into their heads, shear stresses along the sidewalls can drop below the threshold for erosion so that canyon widening stops, and the headwall retreats upstream maintaining a roughly uniform width (Figure 4.2C). In this scenario, it is the distribution of bed shear stresses exerted by water along the waterfall rim that dictates the canyon width. Because bed shear stresses are set by the pattern of flow focusing around the canyon head, which itself is tied to the flood discharge [*Lapôtre and Lamb*, 2015], we hypothesize that the width of the canyon head ultimately relates to flood discharge. More specifically, we hypothesize that, all else equal, larger floods produce wider canyons by this mechanism.

We focus on canyons formed by floods through upstream retreat of a headwall, where headwall erosion can be represented by a threshold erosion process, such as block toppling. Throughout our analysis we assume that the canyon topography evolves slowly relative to temporal changes in flow hydraulics so that the temporal acceleration terms in the equations of motion can be neglected during active canyon incision. This assumption is analogous to the quasi-steady assumption in fluvial morphodynamics and has been argued to hold when the volume of eroded or transported sediment is small compared to the volume of water, and hence that the sediment concentration is relatively dilute [*de Vries*, 1965]. In our analysis below we find that reconstructed sediment concentrations from megaflood-carved canyons are indeed small, ranging 8×10^{-5} to 1×10^{-2}, which is in support of the quasi-steady assumption, but is also tied to our assumption that sediment is evacuated from canyons by fluvial transport. Canyons carved by concentrated debris flows or by a bore at the front of a flood wave may violate the quasi-assumption, for example, but most of the canyons of interest here show evidence of dilute fluvial transport such as imbricated boulders, boulder bars, streamlined islands and terraces [e.g., *Baker*, 1973; *Lamb et al.*, 2008; *Warner et al.*, 2009; *Baynes et al.*, 2015a]. Note that the quasi-steady assumption does not necessarily imply that the floods themselves were steady flows, only that the temporal acceleration terms can be neglected in the momentum budget. Following our conceptual model (Figure 4.2), we envision that non-steady behavior can emerge due to temporal changes in input flood discharge or through the evolution of canyon geometry during canyon formation. For example, an input flood discharge that decreases in time might result in a narrowing zone over which canyon headwall erosion occurs, and hence a canyon with a systematic upstream decrease in width. In contrast, canyons that have relatively uniform widths are inferred to have formed under relatively steady flows.

In the rest of this section we develop theory to relate the discharge of a sheet flood to the shear stresses it imposes around the headwall of an amphitheater-headed canyon based on the steady state hydraulic simulations of 2-D flow focusing from *Lapôtre and Lamb* [2015]. We then use this theory in Section 3 to relate the pattern shear stresses around a canyon head to canyon formation by block toppling.

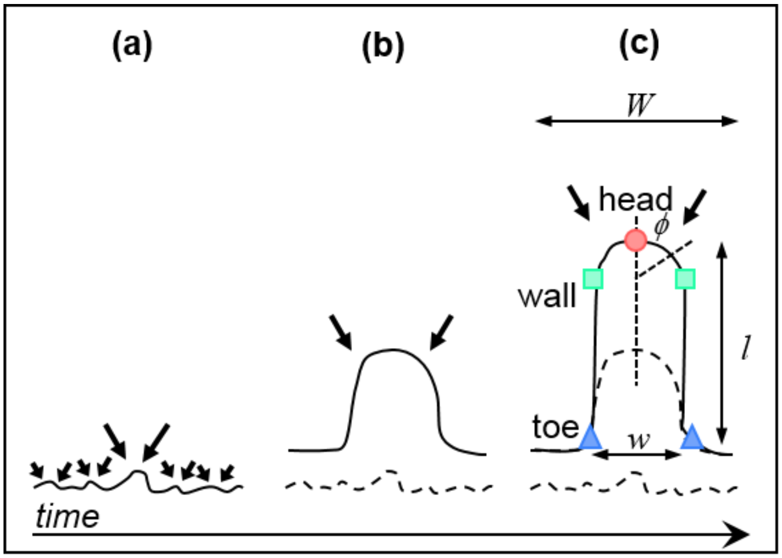

Figure 4.2: Hypothesis for the formation of bedrock canyons by knickpoint retreat. The sketches are in map view, with water flowing from top to bottom. Sinuous lines represent the geometry of the waterfall rim, and arrows indicate flow focusing into horseshoe-shaped defects or canyon heads along the rim. (A) Water focuses towards horseshoe-shaped defects along an otherwise linear escarpment. These defects compete for water, until (B) one of them focuses enough water such that it captures most of the flow. The winning defect is a proto-canyon that both widens and lengthens, until (C) the canyon head focuses enough water for shear stresses along the sidewalls to drop below a critical value for erosion to occur. Past that stage, the canyon lengthens (increased l) through upstream retreat of the headwall, maintaining a roughly uniform width, w. The red circle indicates the location of the head, the green squares are at the location of the wall, and the blue triangles are at the location of the toe. The azimuth angle ϕ is defined as the angle between the canyon centerline a point along the rim of canyon head.

2.1. Discharge

Horseshoe-shaped waterfalls and canyons modify flow patterns upstream of the brink by accelerating water from its steady, uniform value (i.e., the normal flow depth, h_n) towards the waterfall. For a steady flood over a planar, tilted plateau, this spatial acceleration leads to the formation of so-called drawdown profiles over a typical length scale of h_n / S, where S is the topographic gradient in the main flow direction [*Bresse*, 1866]. Downslope (i.e., in the direction of the topographic gradient) drawdown profiles develop for Froude subcritical floods only, while cross-slope (i.e., in the direction perpendicular to the topographic gradient) drawdown profiles develop for both subcritical and supercritical floods [*Lapôtre and Lamb*, 2015]. Because of the development of these drawdown profiles, water is focused into the heads of canyons, and the total discharge within the head may be greater than the discharge integrated over an equivalent width far upstream of the waterfall where the flow is steady and uniform. From mass conservation, the discharge into a horseshoe-shaped canyon head is given by

$$Q_{h,\mathrm{2D}} \equiv \frac{w}{2} \int_{\phi=-\pi/2}^{\pi/2} U_{0,\mathrm{2D}}(\phi) h_{0,\mathrm{2D}}(\phi) \mathrm{d}\phi , \tag{4.1}$$

where w is the canyon width, ϕ is the azimuth angle with respect to the canyon centerline (Figure 4.2), $U_{0,\mathrm{2D}}$ is the flow velocity component perpendicular to the rim of the horseshoe waterfall, and $h_{0,\mathrm{2D}}$ is the flow depth at the rim.

The degree to which $Q_{h,\mathrm{2D}}$ differs from the equivalent dimensional upstream discharge was addressed by *Lapôtre and Lamb* [2015], and parametrized into a non-dimensional canyon head discharge for steady non-uniform flow, $Q*$, such that

$$Q_{h,\mathrm{2D}} = Q* w q_n , \tag{4.2}$$

where q_n is the upstream discharge per unit width. The latter can be related to the upstream bed shear stress through conservation of mass and momentum. From conservation of mass for 1-D flow far upstream of the waterfall,

$$q_n = U_n h_n , \tag{4.3}$$

where the upstream normal-flow velocity, U_n, is given by Manning's equation

$$U_n = \frac{h_n^{2/3} S^{1/2}}{n} , \tag{4.4}$$

in which n is Manning's n. Combining Equation (4.3), (4.4) and conservation of momentum for steady and uniform flow,

$$\tau_n = \rho g h_n S , \tag{4.5}$$

where g is the acceleration of gravity, yields

$$q_n = \frac{1}{nS^{7/6}} \left(\frac{\tau_n}{\rho g} \right)^{5/3} . \tag{4.6}$$

Combining Equation (4.2) and (4.6) yields a relation between the discharge into the canyon head and the upstream bed shear stress,

$$Q_{h,2\mathrm{D}} = \frac{Q^* w}{nS^{7/6}} \left(\frac{\tau_n}{\rho g} \right)^{5/3} . \tag{4.7}$$

The normalized cumulative discharge to the canyon head, Q^*, is a dimensionless measure of how much the dimensional discharge into a horseshoe-canyon head, $Q_{h,2\mathrm{D}}$, is enhanced by flow focusing compared with the upstream normal-flow discharge, and depends on four dimensionless parameters, namely the upstream Froude number, Fr_n, the canyon-width to flood-width ratio, $w^* = \frac{w}{W}$, where W is the flood width, the flood width limitation factor, $W^* = \frac{(W-w)S}{2h_n}$, and the downslope backwater parameter, $l^* = \frac{lS}{h_n}$, where l is the canyon length (Figure 4.2) [*Lapôtre and Lamb*, 2015].

Semi-empirical relations, summarized in Appendix A.2, were determined by *Lapôtre and Lamb* [2015] from simulations of steady, non-uniform sheet floods upstream of horseshoe waterfalls using ANUGA, a finite-volume modeling suite that solves the 2-D time-dependent depth-averaged shallow water equations [*Roberts et al.*, 2009]. The key results are that floods with lower upstream Froude numbers, $\mathrm{Fr_n}$, experience more convergence towards the rim of the waterfall. Escarpment length and width also affect the hydraulics upstream of the brink, for example, through the interaction of drawdown profiles and the edges of the flood. In particular, when $W^{*}<1$, lateral drawdown profiles do not reach a uniform flow depth near the edges of the flood, and flow acceleration is reduced in the direction perpendicular to the wall. Also, longer canyons loose more water over their sidewalls, and have relatively less water at their toe (Figure 4.2).

According to our hypothesis, in order to form a canyon through canyon-head retreat while maintaining a roughly uniform width, the upstream discharge must be such that the shear stresses along the sidewalls are below the critical value for erosion, while the shear stress at the canyon head is above the critical value. In the following subsections, we show how normal bed shear stress, τ_n, can be related to shear stress along the canyon rim.

2.1.1. Shear Stresses along the Canyon Rim

Bed shear stress at the rim of a horseshoe waterfall, $\tau_{0,\mathrm{2D}}$, can be written as

$$\tau_{0,\mathrm{2D}} = \rho C_{f\,0,\mathrm{2D}} U_{0,\mathrm{2D}}{}^{2}, \tag{4.8a}$$

where ρ is the density of water, and $C_{f\,0,\mathrm{2D}} = \dfrac{n^2 g}{h_{0,\mathrm{2D}}^{1/3}}$ is the friction coefficient at the canyon rim [e.g., *Stein and Julien*, 1993]. Flow velocity at the rim, $U_{0,\mathrm{2D}}$, can be written in terms of the upstream normal-flow velocity, U_n, such that Equation (4.8a) becomes

$$\tau_{0,\mathrm{2D}} = \rho C_{f\,0,\mathrm{2D}} \left(\alpha_{\mathrm{2D}} U_n\right)^2, \tag{4.8b}$$

in which $\alpha_{\mathrm{2D}} \equiv \frac{U_{0,\mathrm{2D}}}{U_n}$ is defined as the acceleration factor at the rim of a horseshoe waterfall [*Lapôtre and Lamb*, 2015]. The acceleration factor at the rim of a horseshoe waterfall, α_{2D}, takes into account both lateral flow focusing and drawdown of the water surface in response to the loss of hydrostatic pressure at the waterfall. It can also be defined as

$$\alpha_{2D} \equiv \alpha^* \alpha_{\mathrm{1D}}, \tag{4.9}$$

where $\alpha^* = \frac{\alpha_{\mathrm{2D}}}{\alpha_{\mathrm{1D}}}$ is the acceleration factor ratio defined in the work of *Lapôtre and Lamb* [2015] that accounts for lateral flow focusing, and $\alpha_{\mathrm{1D}} = \frac{U_{0,\mathrm{1D}}}{U_n} = \frac{h_n}{h_{0,\mathrm{1D}}}$, which accounts for drawdown in 1-D along the centerline, in which $U_{0,\mathrm{1D}}$ and $h_{0,\mathrm{1D}}$ are the flow velocity and depth at the brink of a linear escarpment, respectively. The 1-D acceleration factor, α_{1D}, is a function of the upstream Froude number only, with $\alpha_{\mathrm{1D}} = \frac{1.4}{\mathrm{Fr}_{\mathrm{n}}^{2/3}}$ when $\mathrm{Fr}_{\mathrm{n}} \leq 1$, and $\alpha_{\mathrm{1D}} = \frac{0.4 + \mathrm{Fr}_{\mathrm{n}}^2}{\mathrm{Fr}_{\mathrm{n}}^2}$ when $\mathrm{Fr}_{\mathrm{n}} > 1$ [*Rouse*, 1936; *Delleur et al.*, 1956; *Hager*, 1983]. The acceleration factor ratio, α^*, is a measure of the enhancement or decrease in flow acceleration at the brink of a horseshoe waterfall compared with that at a 1-D escarpment: for a linear escarpment, $\alpha^* = 1$, so that $\alpha_{\mathrm{2D}} = \alpha_{\mathrm{1D}}$, while at the center of a canyon head, $\alpha^* \geq 1$. *Lapôtre and Lamb* [2015] evaluated α^* at three different locations around the rim of semi-circular-headed canyons (Figure 4.2) – the head (upstream end of the canyon head, α_h^*), the wall (junction between the horseshoe head and the straight sidewall, α_w^*), and the toe (downstream end of the canyon sidewall, α_t^*). Analogous to the semi-empirical relationships derived for Q^*, *Lapôtre and Lamb* [2015] developed semi-empirical relationships to predict the acceleration factor ratio $\alpha *$. The semi-empirical relationships for $\alpha *$ were also derived using the same numerical simulations, and are summarized in Appendix A.2.

Equation (4.8b) and (4.9) yield the shear stress along the canyon rim. We wish to relate these shear stress values to water discharge to use for paleohydraulic reconstruction. To do this, we combine Equation (4.8b), (4.9), and Manning's equation (Equation (4.4)) to express the bed shear stress at the rim of a horseshoe waterfall as

$$\tau_{0,2\mathrm{D}} = \alpha_{1\mathrm{D}}^{7/3} A^* \tau_n , \tag{4.10a}$$

in which A^* is defined here as the shear stress enhancement factor that is given by

$$A^* \equiv \frac{\tau_{0,2\mathrm{D}}}{\alpha_{1\mathrm{D}}^{7/3}\tau_n} = \alpha *^2 \left(\frac{h_n}{\alpha_{1\mathrm{D}} h_{0,2\mathrm{D}}} \right)^{1/3} . \tag{4.10b}$$

The shear stress enhancement factor is the ratio of the shear stress at the rim of horseshoe waterfall, which takes into account both lateral flow focusing and drawdown of the water surface, relative to the shear stress at the rim of a linear escarpment. A^* is expected to vary around the canyon rim.

Equation (4.10) shows that the upstream bed shear stress, τ_n, can be related to $\alpha_{1\mathrm{D}}$ (which is a function of $\mathrm{Fr_n}$), A^* and the bed shear stress at the canyon rim, $\tau_{0,2\mathrm{D}}$, (which is unknown). The next steps are thus to determine A^*, which can be constrained from the flood simulations of *Lapôtre and Lamb* [2015], and $\tau_{0,2\mathrm{D}}$, which comes from canyon erosion mechanics (Section 3).

2.1.2. Shear Stress Enhancement Factor

The shear stress enhancement ratio, A^*, given by Equation (4.10b), is a function of the acceleration factor ratio, $\alpha *$, which was determined by *Lapôtre and Lamb* [2015], but also varies with the ratio of the flow depths at the canyon rim and upstream, which are unknown, but can be extracted from the simulations of *Lapôtre and Lamb* [2015]. In these simulations, sheet floods were modeled over a tilted plateau and flow towards a waterfall with a semi-circular head and a constant width. The domain geometry was analogous to that described in Figure 4.2C. At steady state, the flow velocity, $U_{0,2\mathrm{D}}$, and depth, $h_{0,2\mathrm{D}}$, were measured along the rim of a horseshoe waterfall as upstream Froude number ($\mathrm{Fr_n}$), canyon-width to flood-width ratio ($w*$), flood-width limitation factor ($W*$) and downslope backwater parameter ($l*$) were varied. We used these flow velocities and depths to calculate shear stress enhancement ratios at the canyon head (A_h^*) in the downslope direction, head-to-wall junction (A_w^*) in the cross-slope direction, and toe (A_t^*) in the downslope direction as a function of $\mathrm{Fr_n}$, $w*$, $W*$, and $l*$. We derive semi-empirical relationships for shear stress enhancement factor as a function of these parameters for 110 numerical simulations with different flood and canyon geometries following the technique described in *Lapôtre and Lamb* [2015]. These relationships are summarized in Appendix B.2. Overall, the dependency of $A*$ on the aforementioned parameters is very similar to that of the acceleration factor ratios squared, described in *Lapôtre and Lamb* [2015], due to the fact that $A* \propto \alpha*^2$ (Equation (4.10b)). We find that the effect of the additional depth factor makes $A*$ deviate from $\alpha*^2$ by up to 65% where flow thins significantly, for example at the toe of the canyon, and should thus not be neglected.

2.1.3. Total Discharge into the Canyon Head

The total discharge into the canyon head, $Q_{h,2\mathrm{D}}$, that is required to generate a certain bed shear stress at the canyon rim, $\tau_{0,2\mathrm{D}}$, finally can be estimated by combining Equation (4.7) and (4.10) as

$$Q_{h,2\mathrm{D}} = \frac{Q^* w}{nS^{7/6}} \left(\frac{\tau_{0,2\mathrm{D}}}{\rho g \alpha_{1\mathrm{D}}^{7/3} A^*} \right)^{5/3} . \tag{4.11}$$

All parameters in Equation (4.11) can be estimated or calculated, except that of the shear stress value at the canyon rim during canyon formation, $\tau_{0,2\mathrm{D}}$, which must come from erosion mechanics, which is discussed in Section 3.

2.2. Total Flood Duration and Water Volume

Because we are interested in large catastrophic floods that rapidly erode large rock volumes, it is plausible that erosion of the headwall is limited by the rate at which flow within the canyon head can carry the eroded sediment out of the canyon [e.g., *Lamb and Fonstad*, 2010; *Lamb et al.*, 2014; *Lapôtre and Lamb*, 2015]. If the flow cannot carry the eroded sediment away from the canyon head, talus will accumulate and buttress the headwall against further retreat [*Lamb et al.*, 2006]. We thus approximate the total cumulative duration of canyon-carving floods, T_f, by dividing the volume of eroded rock by the volumetric sediment flux from flow within the canyon, Q_{sc} [e.g., *Lamb and Fonstad*, 2010; *Lamb et al.*, 2015]. In addition to the transport-limitation assumption, we assume that the porosity of rock is zero and that flow width within the canyon is equal to the full canyon width. Under these assumptions, the total duration of canyon-carving floods is approximated by

$$T_f \approx \frac{lA_c}{Q_{sc}}, \tag{4.12}$$

in which $A_c = \gamma H_c w$ is the canyon cross-sectional area with γ being a shape factor varying between 0 and 1. Many canyons carved in basalt on Earth have rectangular cross-sections [e.g., *Lamb et al.*, 2006], i.e., $\gamma = 1$. Martian canyons are thought to have formed billions of years ago [e.g., *Warner et al.*, 2010], and their geometries may have been significantly modified by subsequent mass wasting or periglacial processes making the original cross-section difficult to constrain [e.g., *Head et al.*, 2006]. We thus assume a rectangular geometry. Equation (4.12) shows that a minimum estimate of total flood duration can be calculated from canyon length (l) and cliff height (H_c), which can both be measured, and sediment capacity per unit width ($q_{sc} = Q_{sc} / w$), which can be estimated from sediment transport theory. In the case of canyons formed by multiple floods, Equation (4.12) represents the summed duration of all flood events that contributed to canyon formation.

Many empirical relationships exist to predict sediment capacity of bedload. In the following, we use that of *Fernandez Luque and Van Beek* [1976], i.e.,

$$q_{sc} = 5.7\left(Rgd^3\right)^{1/2}\left(\tau_* - \tau_{*c}\right)^{3/2}, \tag{4.13}$$

where $R = \dfrac{(\rho_r - \rho)}{\rho}$, d is the grain diameter, and τ_* and τ_{*c} are the Shields and critical Shields stresses, respectively. The Shields stress [*Shields*, 1936] is the ratio of driving to resisting stresses acting on an eroded block, and we estimate it under the assumption of normal flow conditions (i.e., steady and uniform flow) within the canyon through

$$\tau_* = \frac{h_{nb} S_b}{Rd}, \tag{4.14}$$

where h_{nb} and S_b are the normal flow depth and bed slope in the canyon respectively, and d is grain diameter. The critical Shields stress, τ_{*c}, is a function of particle Reynolds number, and reaches a value of ~0.045 for larger grains of interest here [e.g., *Miller et al.*, 1977; *Yalin and Karahan*, 1979].

We need to estimate flow depth within the canyon in order to calculate Shields stress downstream of the waterfall. Assuming again that flow is steady and uniform within the canyon, flow depth [e.g., *Chow*, 1959] is given by

$$h_{nb} = \left(\frac{nQ_{h,2\mathrm{D}}}{wS_b^{1/2}} \right)^{3/5}, \tag{4.15}$$

where $Q_{h,2\mathrm{D}}$ comes from Equation (4.11). Our minimum bound on total flood duration thus can be calculated by combining Equation (4.12)-(4.15) as

$$T_{f,\min} = \frac{lH_c}{5.7\left(Rgd^3\right)^{1/2}\left[\frac{S_b^{7/10}}{Rd}\left(\frac{nQ_{h,2\mathrm{D}}}{w}\right)^{3/5} - 0.045\right]^{3/2}}. \tag{4.16}$$

Finally, total water volume to the canyon head during canyon formation, $V_{2\mathrm{D}}$, is obtained by multiplying the total discharge to the canyon head (Equation (4.11)) by the total duration of canyon-carving floods (Equation (4.16)), i.e.,

$$V_{2\mathrm{D}} = Q_{h,2\mathrm{D}} T_{f,\min}. \tag{4.17}$$

2.3. Comparison with Other Paleohydraulic Indicators

It is of interest to compare the results of our paleohydraulic method to more commonly used techniques. A lower bound on discharge per unit width in the canyon can be estimated by setting the Shields stress to its critical value for initiation of motion of the observed grain sizes on the bed. Consequently, the normal flow depth required to initiate sediment transport, h_i, can be estimated by setting $\tau_* = \tau_{*c}$ in Equation (4.14), i.e., $h_i = (\tau_{*c} RD) / S_b$. Further substituting for flow depth into Equation (4.3) and (4.4) yields the corresponding normal discharge at incipient motion:

$$Q_i = \frac{h_i^{5/3} S_b^{1/2}}{n} w . \quad (4.18)$$

Conversely, an upper bound on flow discharge may be estimated from the assumption that canyons were filled in to the brim. We define brimful flow depth, h_{bf}, as the thalweg depth, which is equal to H_c regardless of channel cross-sectional geometry. Corresponding discharges, Q_{bf}, can be calculated using Equation (4.4) as

$$Q_{bf} = \frac{H_c^{5/3} S_b^{1/2}}{n} w . \quad (4.19)$$

It is not immediately clear how to calculate the duration of canyon incision under the brimful hypothesis because the hypothesis seems to require the existence of a canyon prior to the flood, or for the flood discharge to increase during progressive canyon incision, to maintain a brimful state. Nonetheless, total flood duration under the brimful hypothesis has been estimated previously by assuming transport-limited and brimful conditions ($h_{nb} = H_c$ in Equation (4.14)), or by assuming a volumetric water-to-rock ratio δ, and dividing the estimated volume of water δlwH_c by the brimful water discharge Q_{bf} (Equation (4.19)) [e.g., *Baker*, 1973; *Carr*, 1996] . The water-to-rock ratio method was originally developed for hyperconcentrated flows (i.e., more than 40% sediment by weight, or $\delta \geq 4.6$), which are relatively common in arid environments on Earth, and was argued to be relevant for martian floods [*Komar*, 1980; *Carr*, 1996; *Leask et al.*, 2007]. Corresponding water volumes are estimated by multiplying water discharge by total flood duration.

3. Erosion Constraints on Stable-Width Canyons

In this section, we show how the discharge of canyon-carving floods, given by Equation (4.11), can be constrained from what we know about flow focusing, the distribution of bed shear stresses, and rock toppling. In order to do so, we consider two different paleohydraulic constraints on flood discharge. The 2-D minimum-discharge model takes into account the effect of flow focusing, and assumes that for erosion to occur, the critical shear stress for rock toppling, τ_c, must at least be attained where shear stress is the greatest, i.e., at the canyon head. Thus, $\tau_h = \tau_c$, in which τ_h is the value of $\tau_{0,2\mathrm{D}}$ at the canyon head. The 2-D minimum-discharge model is similar to what was used by *Lamb et al*. [2014] and *Baynes et al.* [2015b], but they did not include 2-D flow focusing, and instead assumed hydraulics for a 1-D escarpment. The 2-D maximum-discharge model assumes that either the shear stress at the wall, τ_w, or at the toe, τ_t, are at the threshold for toppling. In other words, $\max(\tau_w, \tau_t) = \tau_c$, where τ_w and τ_t are the values of $\tau_{0,2\mathrm{D}}$ at the wall and toe, respectively. Otherwise, if $\tau_w > \tau_c$, the canyon would widen, or if $\tau_t > \tau_c$, both the canyon head and toe would erode, such that a preexisting canyon might not lengthen in time depending on the relative erosion rates at the head and toe. We thus expect the maximum-discharge model to be a better estimate of formative discharge in that it takes into account canyon formation considerations. The 2-D maximum model applies only to canyons that formed by upstream headwall retreat via block toppling while maintaining a roughly uniform width.

In order to apply the threshold models described above, we need to calculate $\tau_{0,2\mathrm{D}}$ at the canyon head, wall, and toe. Rearranging Equation (4.10b) and substituting for the shear stress enhancement factor at the canyon head, wall, and toe, respectively, we find

$$\tau_h = \alpha_{1\mathrm{D}}^{7/3} A_h * \tau_n, \tag{4.20a}$$

$$\tau_w = \alpha_{1\mathrm{D}}^{7/3} A_w * \tau_n, \tag{4.20b}$$

$$\tau_t = \alpha_{1\mathrm{D}}^{7/3} A_t * \tau_n, \tag{4.20c}$$

where the shear stress enhancement factors can be calculated from the relationships in Appendix B.2. Equation (4.20) is a sole consequence of flow hydraulics as described in *Lapôtre and Lamb* [2015], and does not assume any erosional mechanism. Erosional mechanics are incorporated into the model by setting the shear stress at the canyon head, wall, or toe equal to the critical shear stress for erosion, so that Equation (4.20) becomes

$$\text{Minimum-discharge model:} \quad \frac{\tau_n}{\tau_c} = \frac{1}{\alpha_{1\mathrm{D}}^{7/3} A_h^*}, \tag{4.21a}$$

$$\text{Maximum-discharge model:} \quad \frac{\tau_n}{\tau_c} = \frac{1}{\alpha_{1\mathrm{D}}^{7/3} \max\left(A_w^*, A_t^*\right)} . \tag{4.21b}$$

Equation (4.21) is useful because it relates the critical shear stress for erosion to the upstream normal-flow bed shear stress, which in turn is related to flood discharge.

3.1. Canyon Formation Regimes

Figure 4.3 shows an example of how $\frac{\tau_n}{\tau_c}$, given by Equation (4.21), varies with flood Froude number. As Froude number increases, the normalized upstream shear stress required to erode the wall and toe respectively increases and decreases because lateral flow focusing becomes less efficient. Because the normalized upstream shear stress is a function of upstream flow depth, data from *Lapôtre and Lamb* [2015] and the corresponding semi-empirical relationships listed in Appendix B.2 can be used to calculate the upstream flow depths that bound canyon formation regimes. When the normalized upstream shear stress of a given flood is smaller than that required to erode the head, no erosion can occur anywhere along the canyon rim. When it is larger than that required to erode the head, but smaller than the normalized upstream shear stresses required to erode the wall and toe, erosion only occurs around the head, such that the canyon lengthens without widening – our minimum and maximum models are at the bounds of this regime that allows for the formation of canyons with uniform widths (Figure 4.1 a-c and E-J). Figure 4.3 illustrates the narrow range in normalized upstream stresses that allow for the formation of a canyon with a uniform width, which implies that canyons with uniform widths evolved under relatively steady flows. Conversely, if the normalized upstream shear stress is greater than that required to erode the walls but lower than that required to erode the toe, the canyon is inferred to both lengthen and widen. Finally, when the normalized upstream shear stress is greater than that required to erode the toe, we distinguish between two regimes in which the entire escarpment retreats. First, if the normalized upstream shear stress is greater than that required to erode the wall, then initial 2-D geometry in the escarpment is smoothed. Second, if the normalized upstream stress is lower than that required to erode the wall, then cliffs with strikes parallel to the main flow direction do not erode, and the initial roughness of the escarpment is preserved, but the roughness does not enlarge to form canyons. Figure 4.1D is an example of a linear escarpment south of Malad Gorge, Idaho, which may have retreated in one of the latter two regimes.

Widening canyons have increasing canyon width-to-flood width ratios, $w*$, and decreasing flood-width limitation factors, $W*$, and thus have decreasing shear stresses at their walls (Appendix B.2). Canyon widening can only occur until shear stress at the wall falls below the critical shear stress. At this point, widening stops, and the canyon headwall retreats upstream maintaining a uniform width. A condition for canyon formation while maintaining a uniform width thus is

$$\left.\frac{\tau_n}{\tau_c}\right|_h \le \frac{\tau_n}{\tau_c} \le \left(\left.\frac{\tau_n}{\tau_c}\right|_{\mathrm{w}}, \left.\frac{\tau_n}{\tau_c}\right|_t \right). \tag{4.22}$$

Consequently, $\left.\frac{\tau_n}{\tau_c}\right|_h$ and $\min\left(\left.\frac{\tau_n}{\tau_c}\right|_w, \left.\frac{\tau_n}{\tau_c}\right|_t\right)$, respectively, provide minimum and maximum bounds on the values of the normalized upstream bed shear stress which leads to the formation of a canyon that maintains a uniform width.

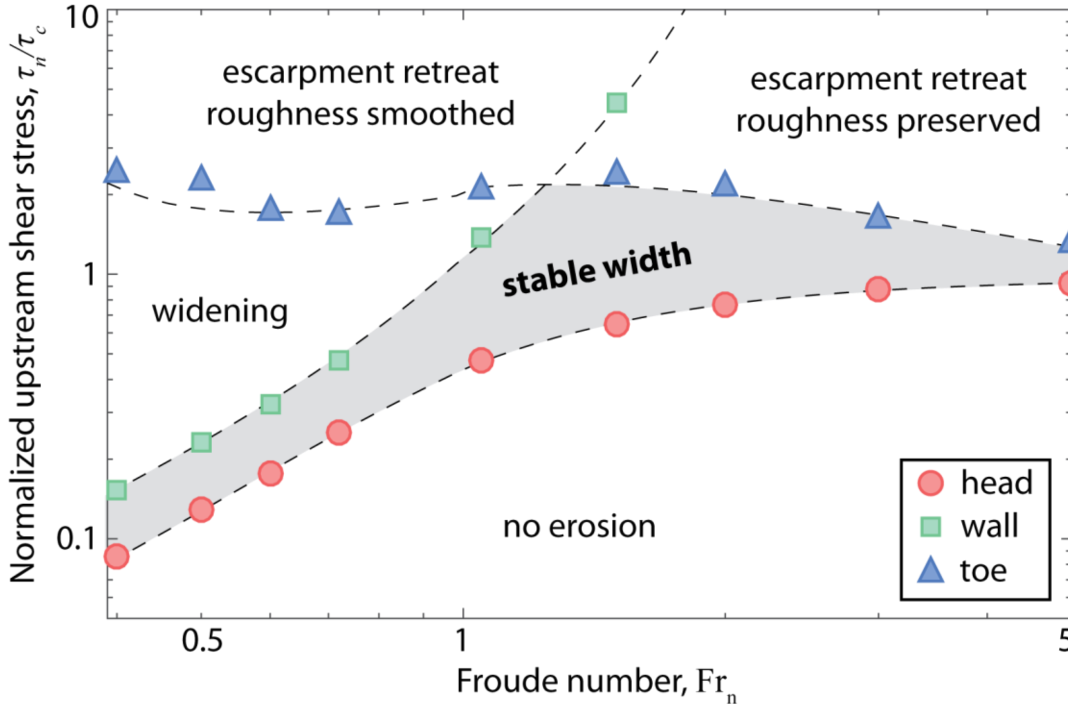

Figure 4.3: Canyon-formation regimes. Normalized upstream shear stress (Equation (4.19)) as a function of upstream Froude number $\mathrm{Fr_n}$ at three locations around the canyon rim (Figure 4.2) – the head (red circles), the wall (green squares), and the toe (blue triangle, see Figure 4.2C). This example corresponds to the case of a wide flood ($w^* = 0.1$, $W^* = 4.5$) flowing over a bed slope $S = 7.5\times10^{-3}$ towards a long canyon ($l^* = 30$), and corresponds to the runs of experiment series 1 of *Lapôtre and Lamb* [2015]. Dashed lines result from the semi-empirical relationships summarized in Appendix B.2. Based on the relative values of dimensionless 1D stresses at the canyon head, wall, and toe, we define several canyon formation regimes: Canyons do not form if the shear stress at the canyon head is less than the critical stress for erosion ("no erosion"). Canyons also do not form for very large normalized shear stresses because erosion is inferred to occur everywhere, including at the canyon toe, leading to the formation of 1-D escarpments that may smooth or preserve the initial topographic roughness of the escarpment. Canyons are predicted to form and lengthen where the shear stress at the canyon head exceeds the threshold for erosion, but the shear stress at the canyon toe does not. If the shear stress at the wall also exceeds the threshold for erosion, then canyons are inferred to widen as they lengthen, whereas stable width canyons have shear stresses that are below the threshold for erosion at the wall.

3.2. Threshold for Rock Toppling

To constrain the threshold for erosion, τ_c, we assume that waterfall retreat occurs through toppling of rock columns at the rim. Toppling erosion during a flood occurs when the torque exerted by water flow on top of a rock column is large enough to make the column rotate and fail [*Seidl et al.*, 1996; *Lamb and Dietrich*, 2009]. *Lamb and Dietrich* [2009] considered the torque balance on a rock column subjected to shear stress from water flow on top (torque T_s), drag from flow over rock protrusions (T_d), gravity (T_g), and buoyancy from a plunge-pool (T_b). Toppling of the rock column is predicted when the factor of safety, FS, defined as the ratio of resistive ($T_g - T_b$) to driving ($T_s + T_d$) torques, is less than unity. Because the torque associated with bed shear stress at the threshold of failure is $T_s = \tau_c H_c D$, where H_c is the column height and D is the column width (or fracture spacing), one can invert for the threshold bed shear stress accounting for 2-D flow focusing as

$$\tau_c = \frac{1}{2}\left[\rho_r g D \cos\theta \left(1 - \frac{H_c}{D} S\right) - \rho g D \frac{H_p}{H_c} - \rho C_d \frac{\eta}{D} \frac{\left(\alpha * \alpha_{1\mathrm{D}}\right)^2 h_n^{4/3}}{n^2}\right], \tag{4.23}$$

where the torques are explicitly written in terms of fracture spacing (D), cliff height (H_c), plunge-pool depth (H_p), column tilt angle ($S = \tan\theta$), protrusion height (η) (Figure 4.4), water and rock densities (ρ and ρ_r), and a drag coefficient (C_d) over rock protrusions.

3.3. Discharge at the Threshold for Toppling

Finally, to calculate the discharge for canyon formation, the critical shear stress for rock toppling given in Equation (4.23) is substituted into Equation (4.21) to calculate the corresponding normal bed shear stress, τ_n, for the minimum-discharge model (Equation

(4.21a)), in which the threshold for toppling is reached at the canyon head, and maximum-discharge (Equation (4.21b)) model, in which the threshold for toppling is reached at the canyon wall or toe. Using these bounds on the normal bed shear stress, the canyon-forming flood discharge into the canyon head is calculated using Equation (4.7) and the relations for the shear-stress and discharge enhancement factors, A^* and Q^*, given in Appendices A.2 and B.2. A^* and Q^* are functions of Fr_n, w^*, W^*, and l^* which can be estimated from the bounds on τ_n and using measurements of canyon geometry, as detailed in Section 4. Importantly, the effect of martian gravity is directly accounted for through Equation (4.7), (4.21), and (4.23), and Fr_n. In the next section, we introduce the field sites we chose to apply our new paleohydraulic theory, how the required topographic measurements and observations were performed, and how the inversion procedure was implemented.

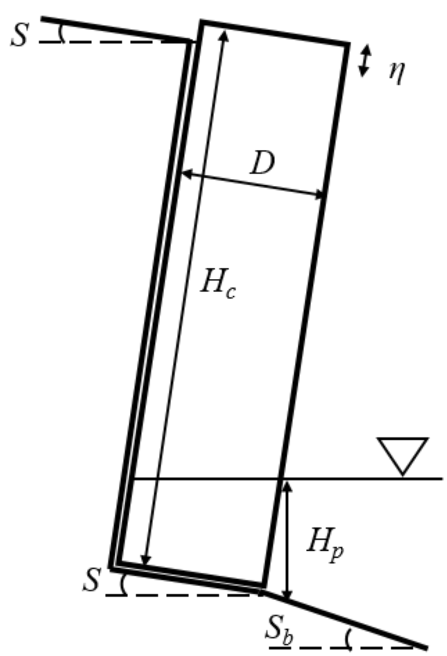

Figure 4.4: Definition sketch of toppling geometry in side view (adapted from *Lamb and Dietrich*, 2009). A column of width , D, and height, H_c, is partially submerged to a height, H_p, by water in the waterfall plunge-pool. The column protrudes over a height, η. Bed slopes upstream and downstream of the overall are denoted by S and S_b, respectively.

4. Field Sites and Methods

4.1. Field Sites

The field sites considered in this study are those shown in Figure 4.1A-C and E-J. On Earth, we consider seven canyons in the Snake River plain of Idaho, (Malad Gorge, North and South; Woody's Cove; Box Canyon; Blind Canyon; Blue Lakes, East and West), six canyons in the Channeled Scablands of Washington (Dry Falls, North and South; Pothole Coulee, North and South; Frenchman Coulee, North and South), and one canyon in Iceland (Ásbyrgi). All of our terrestrial examples are carved into well-fractured basaltic flows, and were previously suggested to have formed by waterfall retreat. Most of them still have lakes in their heads at the location of past plunge pools, which is further evidence for the existence of waterfalls at the time of carving. All studied terrestrial canyons have flat bottoms and talus slopes downstream of the canyon heads along the sidewalls. These boulders are generally angular and do not show evidence for fluvial transport. In contrast, some boulder bar deposits are observed and show evidence for bedload transport, such as rounding, polishing, and imbrication [e.g., *O'Connor and Baker*, 1992; *O'Connor*, 1993; *Lamb et al.*, 2008; *Lamb et al.*, 2014; *Baynes et al.*, 2015a; *Baynes et al.*, 2015b]. Other amphitheater-headed canyons exist, such as Niagara Falls, that are not considered here because they likely form by waterfall plunge-pool erosion processes that differ from the toppling model proposed herein (e.g., see *Lamb et al.*, 2006 for discussion).

The Malad Gorge canyons (MG,N and MG,S, Figure 4.1Aa), Woody's Cove (WC, Figure 4.1A), Box Canyon (BC, Figure 4.1B), Blind Canyon (BlC, Figure 4.1B), and the Blue Lakes canyons (BL,E and BL,W, Figure 4.1C) are all tributaries to the Snake River Canyon in Idaho, and are carved within the Snake River Plain, a broad depression filled with volcanic flows erupted between 15 Ma and 2 ka [*Malde*, 1991; *Kauffman et al.*, 2005]. The lava flows hosting the canyons are well-jointed, with typical fracture spacings of 30 to 60 cm (Table 4.1) [e.g., *Lamb and Dietrich*, 2009; *Baynes et al.*, 2015b]. The canyons formed during the Pleistocene Big Lost River, Bonneville, and other floods [e.g., *Malde*, 1960; *Malde*, 1968; *Scott*, 1982; *O'Connor*, 1993; *Rathburn*, 1993; *Lamb et al.*, 2008; *Lamb et al.*, 2014].

The Dry Falls canyons (DF,E and DF,W, Figure 4.1E), Pothole Coulee (PC,N and PC,S, Figure 4.1F), and Frenchman Coulee canyons (FC,N and FC,S, Figure 4.1G) are part of the Channeled Scablands, Washington, and were eroded into Miocene basalts [*Mackin*, 1961] by the Missoula floods [e.g., *Bretz*, 1969; *Baker*, 1973; *O'Connor and Baker*, 1992; *Benito and O'Connor*, 2003]. The basaltic flows in the Channeled Scablands are typically well-jointed, with characteristic fracture spacing similar to the measured size of toppled blocks (~60 cm; Table 4.1). The Channeled Scablands were cut from multiple episodes of catastrophic erosion [*Bretz*, 1969; *Baker*, 1973; *O'Connor and Baker*, 1992; *Benito and O'Connor*, 2003].

Ásbyrgi canyon was carved into basaltic lava flows (<0.8 Ma) [*Johannesson*, 2014] during a glacial outburst flood about 10 ka related to the Jökulsá á Fjöllum river in Iceland [e.g., *Tomasson*, 2002; *Alho et al.*, 2005; *Carrivick et al.*, 2013; *Baynes et al.*, 2015a; *Baynes et al.*, 2015b]. Typical joint spacings in the fractured lava flows hosting the canyon are of 50 to 80 cm (Table 4.1) [*Baynes et al.*, 2015b].

On Mars, we consider two canyon heads along a tributary to the main Ares Vallis outflow channel (Ares Vallis, East and West), and seven canyons along the western rim of Echus Chasma (Echus Chasma, 1-7), the source region of the Kasei Valles outflow channel system. Martian canyon geometries have likely been modified by the accumulation of debris talus and infilling by subsequent lavas and dust during the several billion years since they were carved, and original canyon bed geometry is not observable at either Ares Vallis or Echus Chasma. While there is no certitude that the martian canyons considered here formed from rock toppling, or even from waterfall retreat, there is evidence in support of this hypothesis: (1) the lithology is cliff forming, typical of columnar basalt that is prone to toppling [*Lamb and Dietrich*, 2009], (2) scoured channels clearly outline areas of overland flow upstream of the canyon heads (Figure 4.5A-B), (3) the two sets of martian canyons are located in the direct vicinity of the two largest outflow channels on the planet. We thus suggest that toppling of jointed basalt by floods is a plausible erosion mechanism at these locations.

The cataract of Ares Vallis (AV,E and AV, W, Figure 4.1I, Figure 4.5A) was carved by the Ares Vallis outflow [e.g., *Warner et al.*, 2010]. Several boulder deposits are found downstream of the cataract and the largest boulders are between 3 and 5.5 m in intermediate diameter (Figure 4.5C). The Ares Vallis cataract we consider is within a tributary to the main channel considered by *Komatsu and Baker* [1997], and despite being previously studied [e.g., *Pacifici et al.*, 2009; *Warner et al.*, 2010], has not yet been subjected to a paleohydraulic reconstruction.

Canyons at Echus Chasma (EC1-7, Figure 4.1J) are located in the source region of the Kasei Valles outflow channel, east of the Tharsis volcanoes, and were cut into Hesperian fractured volcanics and younger Hesperian volcanic flows [*Rotto and Tanaka*, 1995]. Further evidence for capping lava flows can be observed immediately north of the study area, where lava flows from Tharsis spill over the topographic step of the chasma (e.g., 51°6’31.06’’N, 80°14’42.51’’W). Figure 4.5B shows the location of two sample exposures of layers in the walls of EC5 and EC6 (defined in Figure 4.1J). Figure 4.5D-E show clear layers at these locations, likely competent lava flows, and potential rock columns that are 4.1 to 5.6 m wide. *Mangold et al*. [2004] showed evidence for overland flow upstream of these canyons (e.g., Figure 4.5B). *Harrison and Grimm* [2005] argue that waterfall erosion and groundwater sapping may have occurred simultaneously at

Echus Chasma. Analogously to the Channel Scablands, the formation of outflow channels on Mars is believed to have required numerous floods to transmit the large inferred water volumes from the subsurface [*Harrison and Grimm*, 2008].

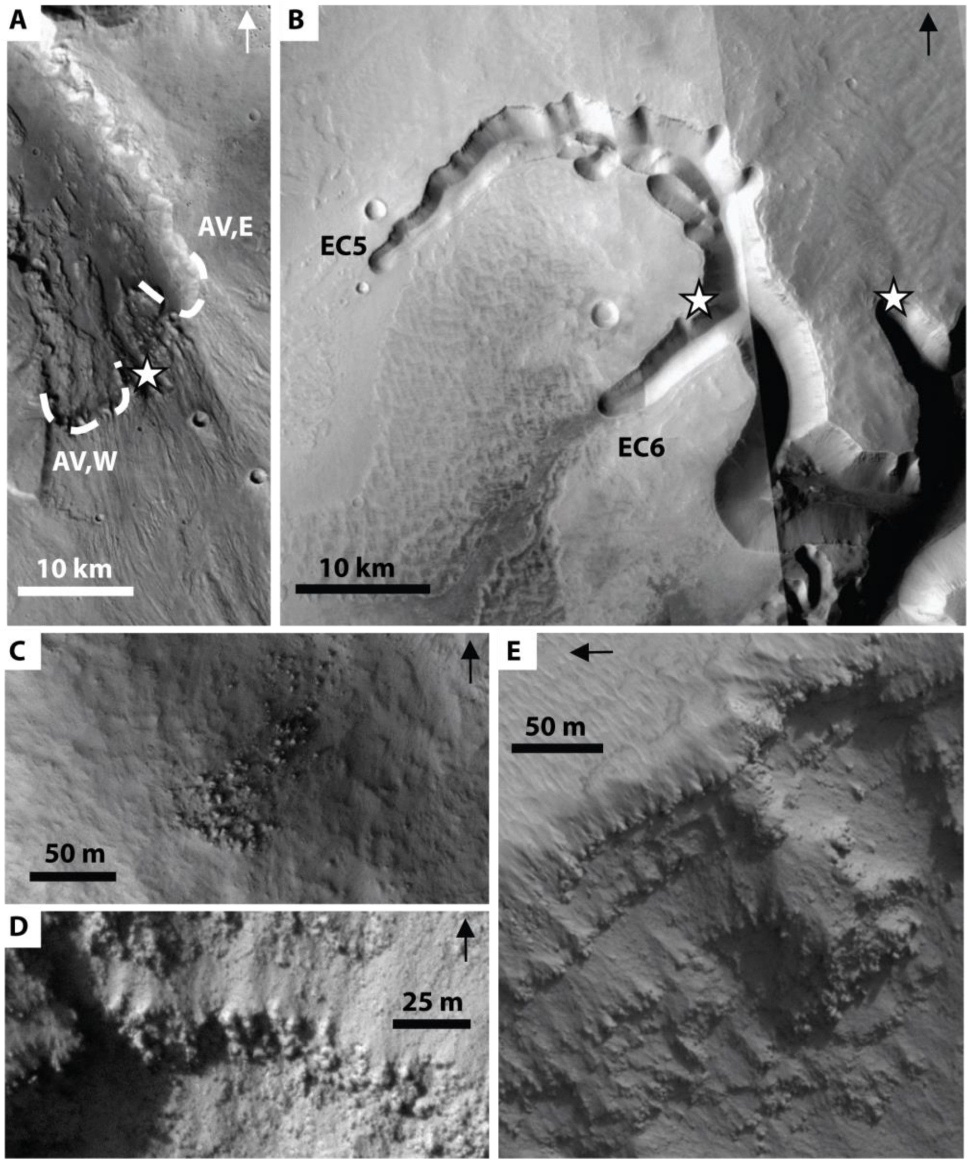

Figure 4.5: Morphology and substrate of martian canyons. (A) CTX mosaic at the Ares Vallis cataract. The cataract is made of two broad canyon heads (dashed lines). The star indicates the location of (C). (B) CTX mosaic centered on Echus Chasma canyons EC5 and EC6. The westernmost star indicates the location of (D), while the easternmost star indicates the location of (E). (C) HiRISE image PSP_00.538_1885 showing a boulder deposit within the Ares Vallis cataract. Largest boulder sizes are between 3 and 5.5 m. Arrows are indicating the North direction. (D) HiRISE image PSP_009513_1810 (50cm/pix) showing layering in the canyon walls, and a typical vertical joint spacing of 4.1 to 5.1 m. (E) HiRISE image PSP_009869_1810 (25cm/pix) showing layering and rock columns with a vertical joint spacing of 4.5 to 5.6 m.

4.2. Field Measurement Methods

Table 4.2 summarizes topographic measurements for each investigated canyon. All terrestrial topographic measurements are made from Advanced Spaceborne Thermal Emission and Reflection Radiometer (ASTER) digital elevation models (DEM), except at Ásbyrgi, for which we use data from *Baynes et al.* [2015b]. On Mars, upstream bed slope S, canyon length l, and flood width W are calculated from Mars Orbiter Laser Altimeter (MOLA) topography, while cliff height H_c, canyon width w and downstream bed slopes S_b are measured from Mars Reconnaissance Orbiter (MRO) Context Camera (CTX)-derived DEMs at Echus Chasma [*Shean et al.*, 2011]. All slopes are determined from linear fits to the topographic data (e.g., Figure 4.6A), while canyon head widths are measured by fitting a circle to the headwall (e.g., Figure 4.6B). The possibility of subsequent widening of the canyons, for example through glacial and/or mass wasting processes, lead to a possible overestimate of canyon width. Moreover, late-stage infilling of canyons by debris, dust, and/or lava flows may introduce error in downstream bed slope measurements. We thus measured canyon headwall width within the canyon head as opposed to using cross-sections along the sidewalls to minimize the effect of subsequent canyon widening. Moreover, the downstream bed slope averaged over the canyon length should be roughly parallel to that measured along original canyon centerlines provided that infilling rates are uniform along the canyon length. In the toppling model, column tilt angle is here assumed to be equal to the arctangent of S. Flood width, W, is estimated from the top width of channel-like topographic depressions upstream of the canyons. Note that w, l and W need not be measured with great accuracy because their exact value does not significantly influence results within the observed dimensionless parameter ranges [*Lapôtre and Lamb*, 2015]. Indeed, upstream Froude number has the strongest effect on flow focusing, and thus on the distribution of shear stresses along the canyon rim. Upstream Froude number is a function of upstream bed slope, which is measured accurately at the regional scale from ASTER and MOLA topographic data.

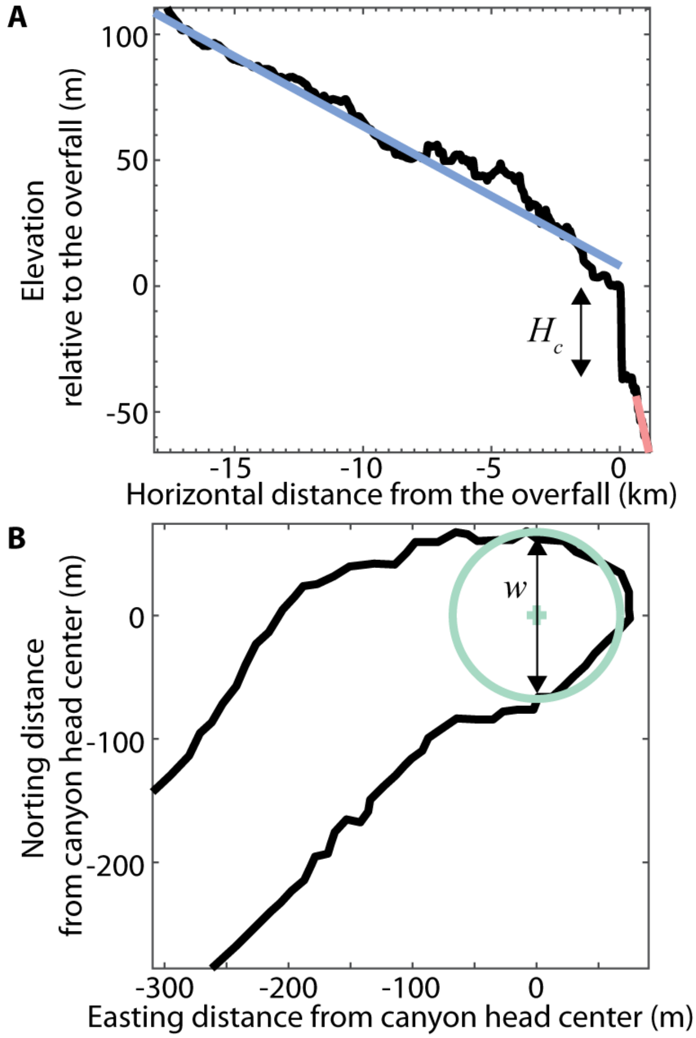

Figure 4.6: Example of topographic measurements for Box Canyon, Idaho. (A) Long profile showing topography (black), with corresponding linear fits to the upstream bed slope, S (blue) and the downstream bed slope, S_b (red). (B) Map view of delineated canyon headwall (black) and corresponding circle fit to the head (green) performed to measure headwall width, *w*.

Compiled fracture spacing and grain size data are summarized in Table 4.1. For the canyons in Idaho, we use a fracture spacing of 50 cm to be consistent with *Lamb and Dietrich* [2009]. In all other locations where only fracture spacings or grain sizes were measured, we assume $d = D$.

A basaltic density is assumed for rocks on both planets ($\rho_r = 2800$ kg/m^3), and the density of water is taken to be $\rho = 1000$ kg/m^3. A constant protrusion height to block size ratio is assumed equal to $\eta/D = 0.1$, and the form drag coefficient on rock protrusions is assumed to be $C_d = 1$ [*Lamb and Dietrich*, 2009; *Baynes et al.*, 2015b]. Bed roughness k is calculated from fracture spacing and grain size (i.e., $k = \eta = 0.1D$ upstream of the waterfall, and $k = 2.5d$ downstream to take into account alluviated eroded material) [*Kamphuis*, 1974; *Lamb and Dietrich*, 2009], and Manning's n is calculated from bed roughness through

$$n \approx \frac{k^{1/6}}{8.1\sqrt{g}} \tag{4.24}$$

[*Brownlie*, 1983]. Calculated Manning's n values range from 0.025 to 0.066. Acceleration of gravity was set to 9.81 m/s^2 on Earth, and 3.78 m/s^2 on Mars. Finally, the volumetric water-to-rock ratio we use to compare corresponding total flood durations to those estimated from the maximum-discharge model is $\delta = 4.6$. This corresponds to a basaltic sediment mixing ratio of 0.4 by weight, which is typical of hyperconcentrated flows in arid environments on Earth [*Komar*, 1980], and somewhat more reasonable than the maximum observed sediment mixing ratio of 0.65 by weight (i.e., 0.4 by volume), which was used in several studies [e.g., *Carr*, 1996; *Leask et al.*, 2007]. While *Craddock and Howard* [2002] argue that, in the case of indurated rock, water-to-rock ratios required for erosion and transport are significantly larger, from 10^4 to 10^5, we use the 0.4 by weight value to illustrate the endmember sediment hyperconcentration.

4.3. Solution Procedure

To solve for the canyon forming water discharge, the critical shear stress for toppling is calculated from field or orbital measurements using Equation (4.23), which is substituted into

Equation (4.21a) and (4.21b) to calculate normal bed shear stress for the minimum- and maximum-discharge models, respectively. Input parameters Fr_n, $w*$, $W*$, and $l*$ are calculated from topographic measurements and the constraints on normal bed shear stress, and are used to calculate $Q*$ and $A*$ from Appendices A.2 and B.2. Because the constraints on normal bed shear stress require estimates of $Q*$ and $A*$ (Equation (4.18)), and $Q*$ and $A*$ in turn are functions of normal bed shear stress (Appendices A.2 and B.2), an iterative procedure is used. Finally, normal bed shear stress is substituted into Equation (4.7) to obtain flood discharge into the canyon head. Table 4.3 summarizes the values of dimensionless parameters that result from the paleohydraulic inversions using the minimum-discharge and maximum-discharge models. Most inverted values fall within the parameter space that was investigated by *Lapôtre and Lamb* [2015], and thus in which the fitted relationships used to calculate shear stresses (Appendix B.2) are most valid.

5. Results

5.1. Discharges, Total Flood Durations, and Water Volumes

Figure 4.7A shows how our tightest estimated range of flow discharges within the head compares with those inferred from incipient motion and brimful conditions. Table 4.4 also summarizes head discharges we obtain for the minimum-discharge and maximum-discharge models. Because all of the estimated discharges are lower than the brimful estimate, even for the maximum-discharge model, the tightest estimate range is bounded by $\max(Q_i, Q_{h,\min})$ and $Q_{h,\max}$, where Q_i is calculated from Equation (4.18), and $Q_{h,\min}$ and $Q_{h,\max}$ correspond to the head discharges inverted from the minimum-discharge and maximum-discharge models respectively through Equation (4.7) and (4.18). On both Earth and Mars, flood discharges into the canyon heads as estimated from the minimum and maximum-discharge models are in cases more than two orders of magnitude smaller than those resulting from the brimful assumption (Figure 4.7A). Inverted ranges in discharges are consistent across canyons for any given geographic area, and are overall higher on Mars (~10^5-10^8 m^3/s) than on Earth (~10^3-10^6 m^3/s). Discharges at Ásbyrgi are similar to those associated to the Missoula floods (~10^5-10^6 m^3/s), and are generally higher than those associated to the Bonneville floods (~10^3-10^4 m^3/s).

Figure 4.7b shows the inverted total flood durations using the maximum-discharge model with the transport-limited assumption (large filled symbols), the brimful and transport-limited assumptions (large open symbols), and the brimful and water-to-rock ratio assumptions (small filled symbols). Note that flood duration cannot be estimated from the minimum-discharge model in many cases because the corresponding discharge is lower than that require for incipient motion. All canyons seem to have formed very rapidly, in a few days to a few months, assuming continuous flow. Mean canyon formation times are 18 days in Idaho, 23 days in Washington, about 4 months for Ásbyrgi, 28 days at Ares Vallis, and 54 days in Echus Chasma. Variations in flooding duration within a given region, for example at Malad Gorge and Woody's Cove mostly arises from the significant difference in canyon lengths, which may reflect that the flood branched upstream of the canyon heads, and that different flood reaches were active at different times, possibly due to focusing and pirating of flood waters by a larger adjacent canyon, as argued by *Lamb et al.* [2014]. Note that corresponding total flood durations estimated under the brimful and transport-limited assumptions are shorter by a factor 3 to 3,000, with canyon formation lasting from about 10 minutes to about 2 weeks only. Combining brimful and a water-to-rock ratio assumptions yield even shorter total flood durations, from less than a minute to about an hour. This latter result strongly argues against the hyperconcentration hypothesis. Consistent with the more reasonable volumetric water-to-rock ratios suggested by *Craddock and Howard* [2002], a water-to-rock ratio of 5x10[4] yields total flood duration that are very similar to those we estimate from the maximum-discharge model, and more typical of fluvial bedrock incision on Earth [e.g., *Lamb et al.*, 2015].

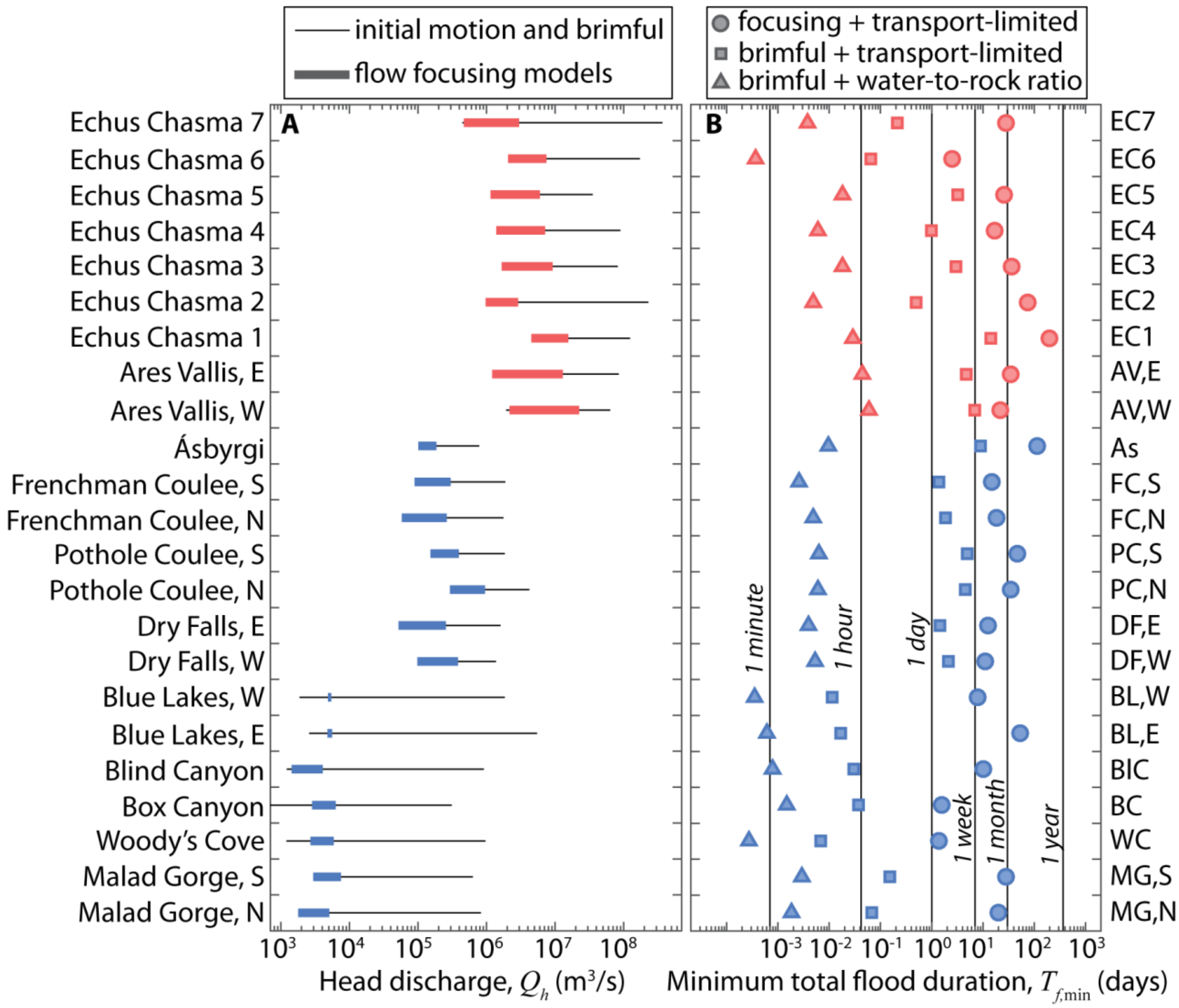

Figure 4.7: Discharges and durations of canyon-carving floods. (A) Total flood discharge to the canyon head, Q_h. Thin horizontal lines represent the range bounded by the discharge at initial motion of the observed block sizes (left) and the discharge in brimful conditions (right), while thick horizontal bars are bounded by the smaller of the incipient motion and the minimum-discharge model (left) and the maximum-discharge model (right). Incipient motion estimates are based on measured boulder sizes or fracture spacings (Table 4.1). (B) Inverted minimum flood duration, $T_{f,\min}$, for all considered canyons assuming continuous flow. Large filled symbols correspond to durations inverted from the maximum-discharge model combined to the transport-limited assumption, large open symbols correspond to brimful and transport-limited models, and small filled symbols correspond to brimful and water-to-rock ratio models. Blue and red symbols indicate terrestrial and martian canyons, respectively.

Because minimum total flood durations (Figure 4.7b) calculated from the maximum-discharge model (large circles) are shorter than those calculated assuming brimful conditions (small squares), the total water volumes are similar for both the maximum-discharge ($V_{2D,max}$) and brimful (V_{bf}) models, with $V_{bf}/V_{2D,max}$ ranging from ~45% to ~90%. Consequently, despite our lowered discharge estimates, the catastrophic floods that carved the amphitheater-canyons herein still involved large volumes of water.

5.2. Relationship between Flow Depths, Discharges, and Canyon Width

Our maximum-discharge toppling model constrains flow depths in the canyons, h_{nb}, to be consistently lower than brimful. Figure 4.8A shows the derived flow depths in the canyon relative to cliff height as a function of canyon widths. Symbols represent intra-canyon depths derived from averaging of the minimum and maximum normal flow depths, while the tips of the vertical bars represent results from the minimum (lower tip) and maximum (upper tip) models. There is no correlation with canyon width, and intra-canyon-to-brimful flow depth ratios vary between 2 and 33%. Thus, the toppling model allows for the likely scenario that the water surface drops below the canyon rim during progressive canyon incision, unlike the brimful hypothesis which requires the water surface to maintain elevation with the canyon rim throughout canyon formation. All intra-canyon flow depths, h_{nb}, inverted using the maximum-discharge model are greater than that required for incipient motion of the observed grain sizes, h_i. Nevertheless, some of the intra-canyon flow depths inverted using the minimum-discharge model are lower than the required flow depth for incipient motion. This result further emphasizes the relative ease with which floods can topple rock columns, and that the limiting factor in eroding the canyons is likely the transport of eroded material outside of the canyon head [e.g., *Lamb and Fonstad*, 2010; *Lamb et al.*, 2015].

Table 4.4 summarizes inverted normal flow depths upstream of the canyons, discharges per unit width, and total head discharges from the minimum-discharge and maximum-discharge models. Figure 4.8B shows that here is a positive correlation between the normal flow depth obtained from averaging the minimum-discharge and maximum-discharge models and canyon width (dashed line),

$$w \approx 107.8 h_n^{0.67}, \ (\mathrm{R}^2 = 0.77) . \tag{4.25a}$$

Symbols represent the average of the minimum and maximum normal flow depths, while the tips of the bars represent results from the minimum (left tip) and maximum (right tip) models. A linear fit instead provides a useful, order-of-magnitude approximation to Equation (4.25a) (dotted line),

$$w \approx 40 h_n, \ (\mathrm{R}^2 = 0.58) . \tag{4.25b}$$

There also exists a positive correlation between canyon width, w, and upstream discharge per unit width, q_n (Figure 4.8C). The best fit relationship between normal flow discharge per unit width and canyon width is

$$w = 54.4\, q_n^{0.51}, \ (\mathrm{R}^2 = 0.80). \tag{4.26}$$

Equation (4.26) can be used as a forward predictor of the width of canyons eroded by a flood of a given discharge. While there is an inevitable correlation between volumetric discharge to the canyon head and canyon width from mass conservation, it need not be the case for upstream discharge per unit width, and the existence of such a correlation supports our hypothesis that the width of canyons carved by floods is set in part by flood discharge. The best fit relationship between total head discharge and canyon width (Figure 4.8D) is

$$w = 10.6 Q_h^{0.36}, \ (\mathrm{R}^2 = 0.91) \ . \tag{4.27}$$

Our findings yield $Q_h / q_n = aw^b$, where $a \approx 3.6$, which is consistently greater than unity due to flow focusing, and $b \approx 0.82$, which is consistently close to unity, due to the inevitable correlation arising from mass conservation. In Section 6.3, we discuss how these relationships between width, depth, and discharge compare with those observed in coarse-grained rivers on Earth [e.g., *Parker et al.*, 2007].

6. Discussion

6.1. Sensitivity Analysis of Discharge Predictions

Our flow focusing model is most sensitive to upstream bed slope, S (in that it sets the value of upstream Froude number, $\mathrm{Fr_n}$), and canyon-to-flood width ratio, $w*$, when upstream Froude number is relatively low [*Lapôtre and Lamb*, 2015]. Moreover, the toppling model is most sensitive to column tilt angle and fracture spacing, D [*Lamb and Dietrich*, 2009]. For the canyons herein considered, focusing does not seem to have been strongly influenced by confinement (high $w*$ at low $\mathrm{Fr_n}$, Table 4.3). We thus illustrate the sensitivity of our model to upstream bed slope, S, and fracture spacing, D. In the following modeling exercise, acceleration of gravity was set to 9.81 m/s^2, rock and water density to 2800 and 1000 kg/m^3, respectively. The same values of protrusion height to block size ratio, η/D, form drag coefficient over rock protrusions, C_d, and bed roughness parametrization as for the case studies were used in the sensitivity analysis. Canyon length was set to 5 km.

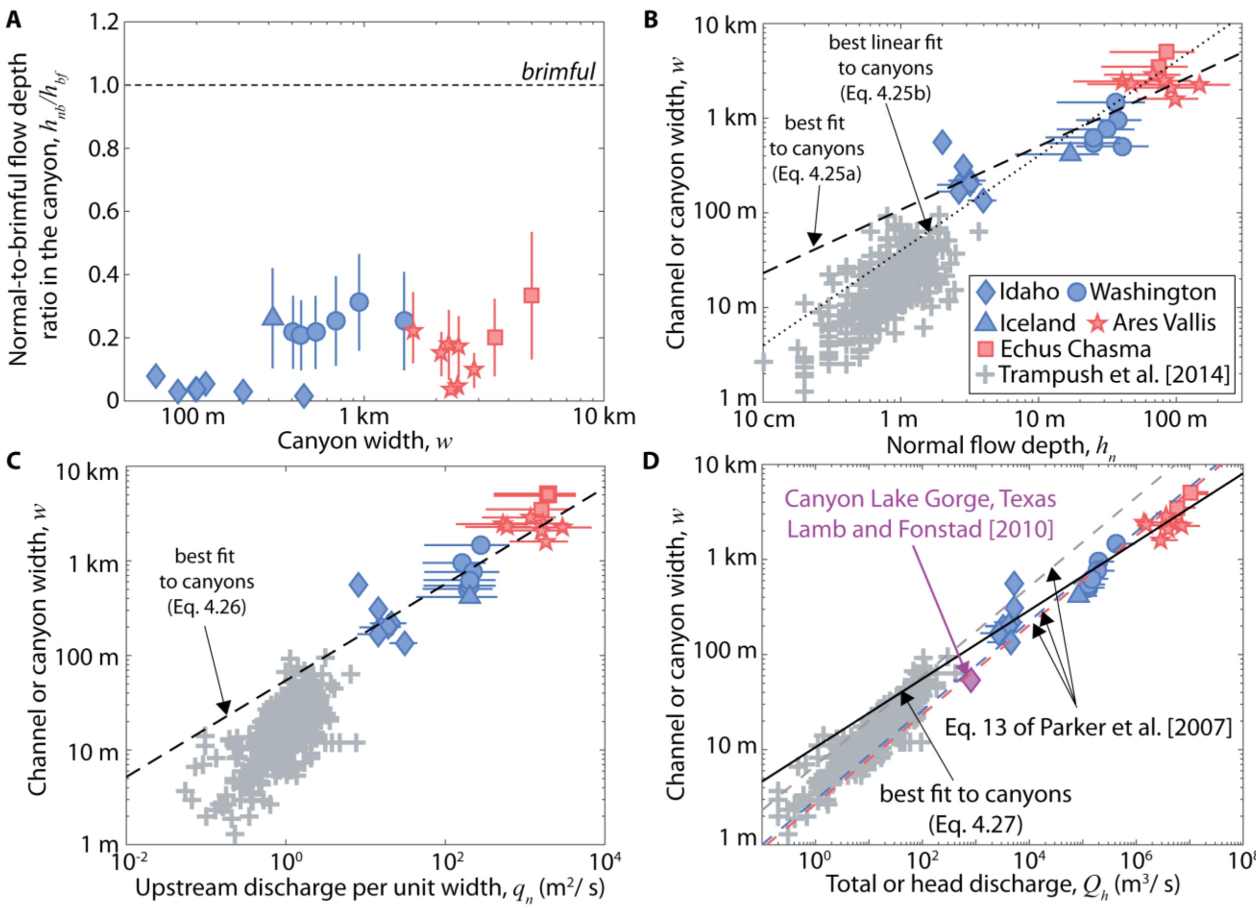

Figure 4.8: Flood hydraulics and canyon dimension. (A) Inverted normal to brimful flow depths ratio, h_{nb}/h_{bf}, in the canyons as a function of canyon headwall width (blue and red symbols indicate terrestrial and martian canyons respectively.). (B) Canyon width as a function of inverted normal flow depth for all considered canyons, compared with channel widths and depths of coarse-grained rivers on Earth (gray '+' symbols) [*Trampush et al.*, 2014]. Bars represent the range bounded by the minimum (left tip) and maximum (right tip) models, while the symbols are derived from an upstream normal flow depth that is the average of $h_{n,\min}$ and $h_{n,\max}$, the normal flow depths obtained from the minimum-discharge and maximum-discharge models, respectively. (C) Canyon width as a function of upstream normal discharge per unit width, compared with gravel-bed rivers on Earth (gray '+' symbols) [*Trampush et al.*, 2014]. (D) Canyon width as a function of head discharge for all considered canyons, compared with gravel bed rivers on Earth (gray '+' symbols) [*Trampush et al.*, 2014], predictions for gravel-bed rivers (dashed lines) [*Parker et al.*, 2007], and a modern canyon-erosion event at Canyon Lake Gorge, Texas (magenta diamond) [*Lamb and Fonstad*, 2010]. The continuous black line represents the best fit power law given in Equation (4.27), and the gray, blue, and red dashed lines are predictions from *Parker et al*. [2007], for $d = 4$ mm and $g = 9.81$ m/s², $d = 60$ cm and $g = 9.81$ m/s², and $d = 4$ m and $g = 3.78$ m/s², respectively.

Parameter values used to model the effect of bed slope, S, on rock toppling and flow focusing are summarized in Table 4.5 for subcritical to supercritical floods ($\mathrm{Fr_n} \approx 0.1 - 1.25$, $w^* \approx 0.08$, $W^* \approx 3\times10^{-4} - 5$, $l^* \approx 10^{-3} - 30$). Figure 4.9A-C shows how bed slope upstream of the waterfall affects inverted flow depth and cumulative head discharge. When slope is small, l^* is small, i.e., A_t^* is large. Up to a value of $S \approx 8\times10^{-5}$, $A_t^* > A_w^*$ decreases (Figure 4.9A), leading to higher flow depths and head discharges (Figure 4.9B-C). For $8\times10^{-5} \le S \le 1\times10^{-3}$, $A_w^* > A_t^*$ decreases due to an increasing upstream Froude number $\mathrm{Fr_n}$ (Figure 4.9A). Overall, increasing bed slope leads to lower critical shear stress for toppling, and smaller flood depths. This effect dominates when flow becomes critical at around $S \approx 1\times10^{-3}$, which leads to a decrease in dimensionless 1-D stress. At $S \approx 6\times10^{-3}$, rock columns become gravitationally unstable, i.e., no water is required for toppling to occur (Figure 4.9B). Bedrock canyons considered in this study have slopes ranging between 10^{-4} and $5\text{x}10^{-3}$. Within this range, flow focusing is set by A_w^*, which is relatively insensitive to bed slope S (Figure 4.9A). Flow focusing is most sensitive to bed slope when $A_t^* > A_w^*$, i.e., when l^* is small. Consequently, the Channeled Scablands canyons likely are the most sensitive to errors in bed slope measurements. For example, using the maximum-discharge model, underestimating a slope of 10^{-4} by 50% (i.e., $S = 5\times10^{-5}$) leads to a head discharge underestimated by 18%, while a 50% overestimate of the slope (i.e., $S = 2\times10^{-4}$) produces little error (<1%).

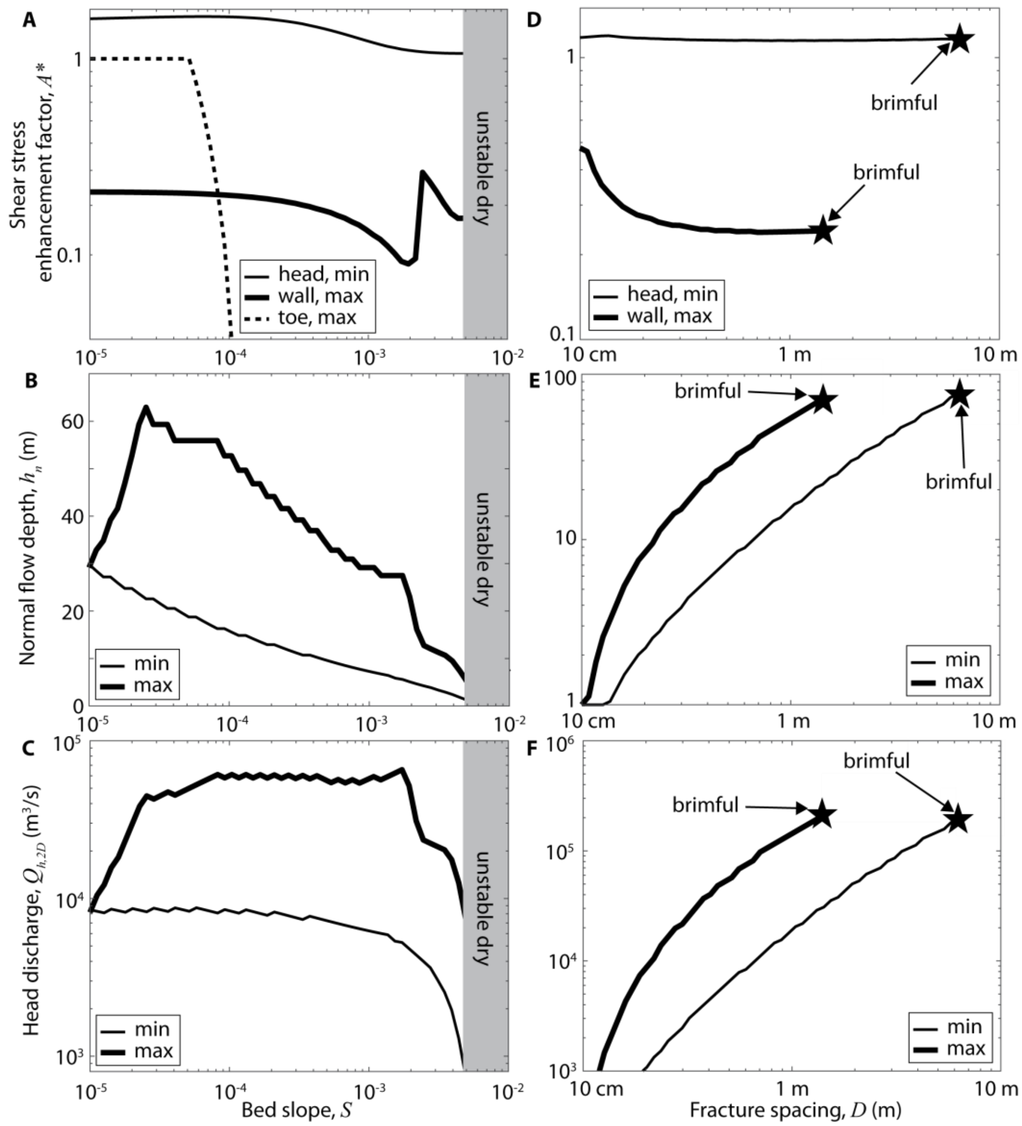

Figure 4.9: Sensitivity analysis. (a,d) Shear stress enhancement factor, A^*, (b,e) normal flow depth, h_n, and (c,f) cumulative head discharge, $Q_{h,2\mathrm{D}}$, as a function of bed slope, S, and fracture spacing, D, respectively. Hatched areas correspond to zones of gravitationally unstable rock column slope. Parameter values used here are summarized in Table 4.5.

Parameter values used to model the effect of fracture spacing on rock toppling and flow focusing are summarized in Table 4.5 for a subcritical flood ($\mathrm{Fr_n} \approx 0.1 - 0.75$, $w^* \approx 0.08$, $W^* \approx 10^{-2} - 1$, $l^* \approx 6 \times 10^{-2} - 5$). Figure 4.9D-F illustrates how fracture spacing, D, affects both rock toppling and flow focusing for a subcritical flood. When fracture spacing increases, larger normal flow depths are required to topple rock columns (Figure

4.9E). This effect causesthe flood width limitation factor, $W*$, to decrease and drop below unity because the lateral backwater length becomes larger than half of the flooded width, and flow focusing becomes limited by the size of the flood. Consequently, the shear stress enhancement factor at the wall, A_w^*, also decreases (Figure 4.9D). The increase in dimensionless 1-D stress leads to higher discharges needed to form a horseshoe canyon (Figure 4.9F). Note that the minimum-discharge model becomes brimful at $D \approx 6.5$ m, while the maximum-discharge model becomes brimful at $D \approx 1.5$ m. With the maximum-discharge model, underestimating a fracture spacing of 50 cm by 50% ($D \approx 25$ cm) leads to an underestimate in head discharge of 71%, while a 50% overestimate of fracture spacing ($D \approx 1$ m) causes the head discharge to be overestimated by 160%. Inverted normal flow depth and head discharge scale roughly linearly with fracture spacing, and the error introduced by erroneous fracture spacings is unlikely to produce order of magnitude uncertainty in flow depth and discharge.

6.2. Comparison with Previous Work for Case Studies

O'Connor [1993] estimated peak discharges of the Bonneville flood based on the elevation of high water marks and step-backwater flow modeling to approximately 10^6 m^3/s, and flood duration was estimated to about 100 days. In the Eden channel near Twin Falls, Idaho, where the two Blue Lakes Canyons are located, he estimated a peak discharge of 0.57×10^6-0.62×10^6 m^3/s. Our average estimate of minimum total flood duration of about 30 days is lower than that of *O'Connor* [1993]. The sum of our cumulative discharges into the head of both Blue Lakes canyons, which are located within the Eden channel, is approximately 1.0×10^4 to 1.1×10^4 m^3/s, which is consistently lower than estimates from *O'Connor* [1993]. These differences occur because (1) the Blue Lakes canyons only represent a portion of the total width of the Eden channel, and (2) estimates from high water marks provide an upper bound on flow discharge given that they may represent a flow stage associated to previous channel geometries that were subsequently further incised. At Box Canyon, *Lamb et al.* [2008] estimated that flood discharge was greater than 200 m^3/s based on observed block sizes, constrained normal discharge per unit width q_n to be greater than 3.2-11.2 m^2/s from the geometry of a channel upstream of the canyon head which overspilled, and estimated flood duration to about 35 to 160 days. We calculate a minimum total flood duration of about 1.6 days, and an upstream discharge per unit width of about 20 to 44 m^2/s, which are consistently lower and larger than the estimates of *Lamb et al.* [2008], respectively. This outcome makes sense because their estimate is a true minimum. At Malad Gorge, *Lamb et al.* [2014] estimated that flow discharge had to be greater than 1.25×10^3 m^3/s in order to transport the observed block sizes out of the canyon heads. We estimate discharges of 2×10^3 to 5×10^3, and 3×10^3 to 8×10^3 m^3/s in the heads of the North and South canyons at Malad Gorge respectively, which again is consistent with the true minimum discharges calculated by *Lamb et al.* [2014].

Peak discharges associated to the Missoula floods are typically thought to be $>10^7$ m^3/s as estimated from high water marks and 1-D flow hydraulics [e.g., *Baker*, 1973; *O'Connor and Baker*, 1992; *Amidon and Clark*, 2014]. Based on discharges estimated from the brimful assumption, *Baker* [1973] estimated that it took a maximum of 14 hours to pond water from Lake Missoula and overspill at the Wallula Gap, and associated waning flows would have lasted for one to two weeks. Downstream of the Dry Falls canyons, near Soap Lake, water discharge was estimated to be about 4.5×10^6 m^3/s based on the location of high water marks and assuming that current channels were brimful to the level of the high water marks [*Baker*, 1973]. We estimate a total water discharge required to carve the canyons at Dry Falls, Pothole Coulee, and Frenchman Coulee to be about 3.2×10^5 to 2.55×10^6 m^3/s, and a minimum total flood duration of about 23 days, which are consistently smaller flow magnitude and longer duration than the discharge and flood duration estimated by *Baker* [1973], respectively. This difference arises because our reconstruction puts flow stage at less than brimful. The sum of our two Dry Falls head discharges is approximately 9.9×10^4 to 6.4×10^5 m^3/s, which is smaller than the discharge estimate by *Baker* [1973] near Soap Lake, suggesting again that high water marks may have been deposited at an early flood stage and do not represent peak flow within the modern-day topography.

At Ásbyrgi canyon, *Baynes et al.* [2015a] estimated that the minimum discharge required to initiate transport of the observed block sizes as bedload is 3.9×10^4 m^3/s. Based on the toppling model of *Lamb and Dietrich* [2009], *Baynes et al.* [2015b] calculated the minimum discharge required to topple basalt columns at Selfoss, about 25 km upstream of Ásbyrgi, to be greater than 3.25×10^3 m^3/s. Other paleohydraulic approaches including flow routing over present-day topography have estimated the largest flood discharges along the Jökulsá á Fjöllum to be approximately 0.9×10^6 m^3/s [e.g., *Alho et al.*, 2005; *Carrivick et al.*, 2013]. At Ásbyrgi, we constrain the discharge to be between 1.8×10^4 and 1.9×10^5 m^3/s, which is consistent with the lower bound estimates from *Baynes et al.* [2015a, 2015b], and consistently lower than brimful conditions over present-day topography. *Baynes et al.* [2015a] proposed that Ásbyrgi formed in a single flood event based on the lack of evidence for diffusion of the cliff face over time. Nevertheless, our minimum total flood duration of about 4 months is longer than that of typical glacial outburst floods in Iceland [*Bjornsson*, 2003], and may represent the summed duration of multiple flood events instead.

In the main Ares Vallis channel, *Komatsu and Baker* [1997] estimated a flood discharge of 10^8-10^9 m^3/s assuming brimful flow conditions, while *Andrews-Hanna and Philips* [2007] estimate a total discharge of 10^6-10^7 m^3/s for the source region of the outflow channel near Ianis

Chaos by modeling the outburst of an overpressurized underground aquifer. We estimate that the discharge required to carve the Ares Vallis cataract is about 3.4×10^6 to 3.5×10^8 m^3/s, which overlaps with discharges estimated by *Andrews-Hanah and Philips* [2007] and the lower end of the range estimated by *Komatsu and Baker* [1997].

Echus Chasma is the source region for the Kasei Valles outflow channels system. *Robinson and Tanaka* [1990] estimated a total discharge of 1×10^9-2.3×10^9 m^3/s from the brimful assumption in Kasei Valles, while *Williams et al.* [2000] estimated lower discharges by constraining channel geometry from the elevation of fluvial terraces near the outlet of the outflow to Chryse Planitia of about 8×10^4 to 2×10^7 m^3/s, and *Kleinhans* [2005] estimated a larger discharge of 3.7×10^9 m^3/s using a different implementation for bed friction. Summing up our minimum-discharge and maximum-discharge models for the seven investigated canyons of Echus Chasma yields a total discharge of 6.4×10^6 to 5.1×10^7 m^3/s, which is consistently lower than the brimful estimates, and are similar to the discharges obtained by *Williams et al.* [2000] for the Northern Kasei Valles route, but higher than their Southern Kasei Valles route estimate. The relatively high value of our discharges compared with those of *Williams et al.* [2000] might arise because we calculate discharge near the source region at the canyon head, while they focused on terraces near the outlet of the channels to Chryse Planitia.

6.3. Controls on Canyon Morphology

Our model applies to canyon formation in lithologies that are prone to waterfall erosion by rock toppling, such as columnar basalt, such that canyons tend to evolve to a state set by the threshold for erosion. It is important to note that flow focusing towards a canyon head is found to be relatively weak such that there exists only a narrow range of parameter space in which flood-induced shear stresses exceed a threshold for erosion at the canyon head, while simultaneously falling below the erosion threshold along the canyon walls (Figure 4.3). It is these conditions that we infer lead to the formation of a canyon, through upstream canyon-head retreat, of uniform width. Thus, long canyons of uniform width contain useful and tightly constrained bounds on the minimum and maximum canyon-forming discharges (Figure 4.3). Our model also implies that flood discharges were relatively steady during canyon formation, at least where canyon width appears to have been uniform during canyon headwall retreat. Similar to Figure 4.2, our threshold model implies that feedbacks should exist that drive canyon widening or narrowing until an equilibrium width is established for a certain flood discharge. For example, bed shear stress will be large along the walls of an undersized canyon, which should lead to toppling along the canyon sidewalls and widening. For an even larger flood event, the model predicts that waterfalls retreat as linear escarpments (e.g., Figure 4.1D) if flood discharges are too high to produce bed shear stresses below the critical value for erosion along the sidewalls of an embayment (Figure 4.3). Thus, canyons that widen upstream and eroded linear escarpments indicate floods with shear stresses that greatly exceed the critical stress for erosion (Figure 4.3) or floods with increasing discharge in time, and thus imply larger paleo-discharges or unsteady flow as compared with uniform width canyons. A lower bound on the flood discharge responsible for the retreat of linear escarpments can be calculated from the maximum-discharge model. Conversely, canyons that narrow upstream may preserve information about the falling limb of flood discharge.

In the case of canyon-forming floods, the existence of a positive correlation between flood discharge per unit width and the width of canyons, over two orders of magnitude in canyon width and almost three orders of magnitude in discharge on two different planets (Figure 4.8C), is consistent with our hypothesis that flood discharge in part controls canyon width. Thus, bedrock canyon width represents a powerful paleohydraulic tool to reconstruct the discharge of past outburst floods from readily available datasets. Discharge and canyon width both contribute to setting flow depth within the canyon (Equation (4.15)), which ultimately sets the value of the Shields stress for sediment transport, which is a useful parameter to estimate flood discharge based on observations of grain size within a channel (Equation (4.14)). Figure 4.10 shows the inverted Shields stresses in the canyon heads normalized by the critical Shields stress. Thin lines represent the range bounded by incipient motion ($\tau_* / \tau_{*c} = 1$) and brimful conditions. For some canyons, the minimum-discharge model yields predicted Shields stresses in the head that are lower than that required for incipient motion. Consequently, the tightest lower bound constraint on Shields stress in the head is provided by $\max(h_i, h_{nb,\min})$, where $h_{nb,\min}$ is the intra-canyon depth obtained from the minimum-discharge model. Thick lines represent the range bounded by the tightest lower bound and the maximum-discharge model. We find that the empirical distribution of our tightest range in Shields stress to critical Shields stress ratio has a median of 1.6, for which the 68% confidence interval is 1.4 to 2.1.

Inverted Shields stresses are most sensitive to fracture spacing, D, and bottom slopes, S_b. Further uncertainty may arise from the fact that rock columns did not fail over their total height, H_c; however, inverted discharges are not sensitive to column height as long as $H_c >> D$. Uncertainty might also arise from the fit relationships (Appendix B.2), but most dimensionless focusing parameters fall within ranges tested in *Lapôtre and Lamb* [2015].

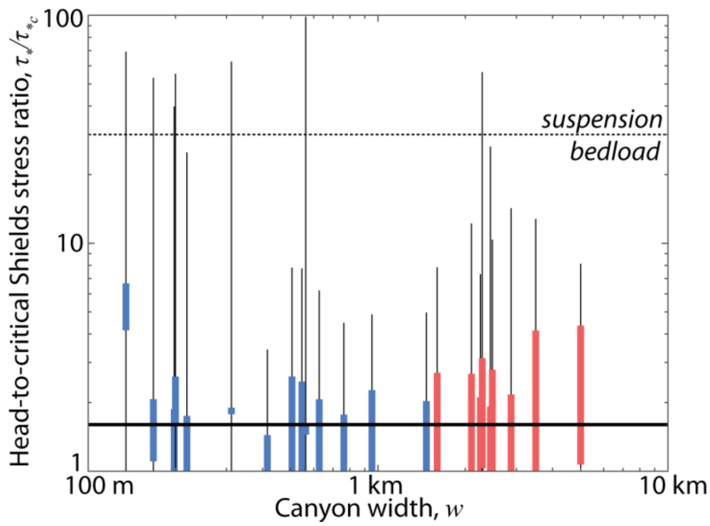

Figure 4.10: Inverted Shields stress within the canyon heads (τ_*) normalized by the critical Shields stress $(\tau_{*c} \approx 0.045)$ as a function of canyon width, w, for all considered canyons. Thin vertical lines represent the range bounded by initial motion (lower tip) and brimful (upper tip) conditions in the canyon. Only the maximum-discharge modeled values are systematically above unity. Thick vertical lines represent the tightest range of Shields stress to critical Shields stress ratios as determined by either incipient motion or the minimum-discharge model (lower tip) and the maximum-discharge model (upper tip). The continuous line represents the inverted median Shields stress within all canyon heads of $\tau_* \approx 1.6\tau_{*c}$. Dashed line represents the transition between bedload transport and suspension, estimated by equating the flow shear velocity u_* to the sediment fall velocity $v_s = \sqrt{\frac{4}{3}\left(\frac{Rgd}{C_d}\right)}$, and assuming a drag coefficient, C_d, of unity, consistent with large natural boulders [e.g., *Ferguson and Church*, 2004].

With inverted Shields stresses ranging between 1.4 and 2.1 times the critical value, sediment fluxes within the canyons were relatively low (Equation (4.13)), likely outpaced by the rate of toppling downstream of the canyon head, which supports the hypothesis that erosion was transport-limited, consistent with other theoretical considerations [*Lamb et al.*, 2015] and observations [*Lamb and Fonstad*, 2010]. In comparison, Shields stresses within the head under brimful conditions (upper tip of thin lines in Figure 4.10) indicate that observed sediment sizes would be transported in suspension in many cases, which is inconsistent with the presence of boulder bar deposits in most of our terrestrial examples, which are analogous to the bank-attached expansion bars of *Bretz et al.* [1956] and *Baker* [1973], and typically form from bedload transport in coarse-bedded rivers on Earth [e.g., *Costa*, 1983; *Wohl*, 1992]. Boulder bars could also form during the falling flood limb, but many have widths that are a large fraction of the canyon width, similar to bars in coarse-grained rivers [e.g. *Ikeda*, 1984; *Seminara and Tubino*, 1989; *Garcia and Nino*, 1993], and heights consistent with our estimated intra-canyon flow depths, suggesting that they formed in concert with canyon formation.

The fact that we invert for a consistent, low, and finite Shields stress within all canyon heads suggests that there may exist a morphodynamic feedback setting its value. For example in the case of gravel-bed rivers, it was shown that brimful width is set such that grains are transported at the bottom of the channel but are not entrained along the erodible banks (so-called *threshold channel theory*), with Shields stresses along the bed predicted by both theory and modeling to be roughly 1.1 to 1.5 times the critical Shields stress value [*Parker*, 1978; *Kovacs and Parker*, 1994; *Cao and Knight*, 1997; *Vigilar and Diplas*, 1997; 1998]. This range overlaps with the range of Shields stresses we inverted for the fourteen terrestrial and nine martian canyons. We suggest that in toppling terrain, the finite low range in Shields stresses results from (1) the similarity between the toppling threshold and the critical stress for incipient motion [e.g., *Lamb and Fonstad*, 2010; *Lamb et al.*, 2014; *Lamb et al.*, 2015], and (2) the relatively narrow range in rim shear stresses relative to the critical value that lead to the formation of canyons with uniform widths (Section 3). Indeed, the sizes of the transported blocks in the canyon are similar to rock column width, and the critical shear stress for toppling is mostly a function of column width. Bed shear stresses within the canyon head are inevitably close to the value of the shear stresses around the canyon head rim, which we showed ought to be close to the critical threshold for toppling. Thus, bed shear stresses within the canyon ought to be close to the threshold shear stress for incipient motion, and the range in Shields stresses is dictated by the range of rim stresses that allow for the formation of a canyon with a uniform width. Consequently, the inverted range in intra-canyon Shields stresses may serve as a convenient proxy to estimate bounds on flow discharge and duration in toppling terrain. The similarity between intra-canyon Shields stress and the critical shear stress for toppling also is consistent with the formation of boulder bars.

If canyons form at a near-threshold state, similar to gravel-bed rivers, we might expect a similarity in the hydraulic geometries of gravel-bed rivers and toppling-dominated canyons. This expectation contrasts with abrasion-dominated slot canyons, which have lower erosion rates than toppling-dominated canyons, and lower width-to-depth ratios than gravel-bed rivers [e.g., *Carter and Anderson*, 2006]. In Figure 4.8B, we compare our bedrock canyons to a compilation of coarse-grained rivers on Earth [*Trampush et al.*, 2014], and find that they appear to have similar width-to-depth ratios (47^{+36}_{-25} for bedrock canyons, and 18^{+15}_{-7} for coarse-grained rivers, where the +/- values represent the 68% confidence interval of the width-to-depth ratio). Figure 4.8D shows that the width of bedrock canyons correlates positively with head discharge, and that this correlation is very similar to that observed in gravel-bed rivers on Earth [*Trampush et al.*, 2014], and at a modern example of a flood-carved canyon: Canyon Lake Gorge, Texas [*Lamb and Fonstad*, 2010]. Canyon Lake Gorge is one of the few modern examples of an entire canyon forming by plucking-dominated waterfall erosion during a megaflood. Many other waterfalls exist on Earth, but most erode slowly through plunge-pool abrasion during more normal floods [e.g., *Crosby and Whipple*, 2006; *Lamb et al.*, 2007; *DiBiase et al.*, 2015], rather than block toppling during megafloods that is our focus here. The width-discharge relationship we infer for megaflood-carved canyons seems to be well-predicted by semi-empirical theory for gravel-bed rivers from *Parker et al.* [2007]. In the case of toppling-dominated canyons, our model suggests that flood width and Froude number may play an important role in that they affect flow focusing, and thus the length scale over which shear stresses drop below the critical value for toppling. Nevertheless, the apparent universality of Equation (4.27) likely arises from (1) the relative insensitivity of flow focusing on flood width when $w << W$, (2) the fact that floods typically have Froude numbers close to unity [e.g., *Costa*, 1987; *Grant*, 1997; *Tinkler*, 1997; *Richardson and Carling*, 2006], (3) relatively uniform block sizes on a given planetary body, and (4) the fact that some parameters covary, e.g., larger block sizes in a lower gravity field on Mars, possibly offsetting their relative effects on toppling mechanics.

6.4. Implications for Water on Mars

Individual martian outburst floods might have provided sufficient water to, at least transiently, enable the existence of a Northern ocean [e.g., *Parker et al.*, 1989; *Baker et al.*, 1991], which, depending on its volume and stability, could have altered the martian global climate [e.g., *Baker*, 2009]. Although our estimated discharges are much lower than previously thought, corresponding water volumes remain large. For example, estimated volumes to carve the two canyons at Ares Vallis and the seven canyons at Echus Chasma are about 8.0×10^{13} m^3 and 3.5×10^{14} m^3, respectively, or about 2-10% of the volume of the Mediterranean Sea. A water volume of 10^{14} m^3 delivered at once to the martian surface corresponds to a 70 cm-thick global equivalent layer (GEL). If concentrated to the Northern lowlands (about 1/3 of the martian surface), such a water volume would create a >2 m-deep body of water. Conversely, if it was derived from a 33%-porous global aquifer, the water outflow would perturb the global aquifer over a thickness of >2 m.

Although early Mars is thought to have hosted large volumes of water, more than a 137 m GEL [*Villanueva et al.*, 2015], remote and in situ D/H isotopic measurements show that the global water inventory decreased rapidly throughout the Noachian, and the measured total volume of water reservoirs on present-day Mars corresponds to a 20-30 m GEL [e.g., *Lasue et al.*, 2013]. These estimated volumes encompass all reservoirs in the surface and shallow subsurface. A ~137 m GEL, which likely is a conservative upper bound for the Late Noachian-Early Hesperian transition, is equivalent to the volume of ~ 200 floods (based on individual flood volumes of 10^{14} m^3). Thus, despite their lowered discharges, martian floods still constitute a significant fraction of the total water budget of the planet, and their outburst from the subsurface to the surface likely altered the global hydrology of Mars.

The source of catastrophic flood water is the subject of an active debate, but it is generally thought to result from pressurization of underground aquifers [*Carr*, 1979; *Burr et al.,* 2002; *Chapman and Tanaka*, 2002; *Manga*, 2004; *Hanna and Phillips*, 2006; *Wang et al.*, 2006; *Meresse et al.*, 2008; *Burr*, 2010; *Zegers et al.*, 2010; *Marra et al.*, 2014a; *Marra et al.*, 2014b]. Because water discharge transmitted by a porous aquifer is proportional to the medium's permeability, our lowered discharge estimates may help in resolving a long standing paradox: if the surface water that formed the martian outflow channels indeed emanated from the ground, martian regolith would be required to have the permeability of loose gravel to transmit the discharges inferred from the brimful assumption [e.g., *Wilson et al.*, 2004; *Pelletier and Baker*, 2011]. However, a two orders of magnitude decrease in water discharge, as suggested by our modeling, translates into required aquifer permeabilities that are two orders of magnitude lower, i.e., similar to those of moderately fractured rocks [*Bear*, 1972].

Finally, despite lowered discharges and thus, longer time-integrated flood durations, martian outburst floods remain short-lived, consistent with a catastrophic origin of the flood waters. Our revised durations, of up to two months, are on the higher end of typical durations for individual modern terrestrial glacial floods [e.g., *Bjornsson*, 2003], and these relatively long durations are consistent with the possibility that multiple flood events are responsible for the formation of the martian canyons, as has been inferred by others from observations of terraces and inner channels [e.g., *Harrison and Grimm*, 2008; *Pacifici et al.*, 2009; *Warner et al.*, 2009]. However, it is unclear whether a subsurface pressurization mechanism would be able to trigger episodic floods [e.g., *Manga*, 2004; *Wang et al.*, 2006].

7. Conclusion

Some canyons carved in fractured basaltic flows on Earth and Mars likely formed through waterfall retreat. Because of the crystalline and fractured nature of basaltic bedrock, toppling of rock columns under the action of water flow at the canyon head is a good candidate mechanism for waterfall retreat. We developed a new theory for canyon dynamics that takes into account the distribution of bed shear stresses imparted by flood water along the rim of amphitheater-headed canyons. We propose that canyons with a spatially uniform width must evolve such that flow focusing allows for erosion of the canyon head but not along the canyon sidewalls. Because flow focusing is in general limited, our model implies that canyons form under conditions very close to the threshold for erosion. Thus, all else being equal, larger floods should produce wider canyons. We applied this new paleohydraulic method to fourteen terrestrial (Malad Gorge, Woody's Cove, Box Canyon, Blind Canyon, Blue Lakes Canyons in Idaho, Dry Falls, Pothole Coulee, Frenchman Coulee in Washington, and the Ásbyrgi canyon in Iceland) and nine martian (Echus Chasma and Ares Vallis) canyons, and found a relationship between the formative discharge of floods and the headwall width of the canyons they carved, consistent with our hypothesis. We showed that the predicted discharges of those floods were in cases more than two orders of magnitude lower than previous estimates assuming brimful conditions. Under the assumption that canyon erosion was transport-limited, we showed that canyon formation typically lasted from less than a day to a few months, although this time may have been proportioned into shorter discrete flood events. We derived formative Shields stresses for sediment transport within the canyon heads, and found that they were within 1.4 to 2.1 times the critical value for incipient motion of the observed block sizes, which likely arises from the relatively narrow range in rim shear stresses that allow for a stable-width canyon, and the similarity between toppling and initial motion thresholds. Consequently, this range in Shields stresses may constitute a convenient closure to place bounds on flood discharge and duration in toppling terrain. Finally, we predicted that, despite their lowered discharges, the considered floods involved similar volumes of water compared with their corresponding brimful estimates. In particular, estimated water volumes suggest that the floods required to carve the observed canyons were large enough to have significantly perturbed the subsurface and surface hydrology of Mars at a global scale.

Location		Type	D_{16} (m)	D_{50} (m)	D_{84} (m)	Source
Idaho	BC	grain size	0.13	0.29	0.60	*Lamb et al.* [2008]
	MG	grain size	-	0.58	-	*Lamb et al.* [2014]
Drumheller channel, Washington		grain size	0.34	0.59	0.83	this study
As, Iceland		fracture spacing	0.50 (first quartile)	0.65	0.80 (third quartile)	*Baynes et al.* [2015b]
AV, Mars		grain size	-	4.25 (mean)	-	this study
EC, Mars		fracture spacing	-	4.85 (mean)	-	this study

Table 4.1: Grain size and fracture spacing data compiled at or near the studied canyons. Notations D_{16}, D_{50}, and D_{84} refer to the 16th, 50th, and 84th percentiles of the cumulative grain size distribution, respectively.

		Upstream bed slope, S	Downstream bed slope, S_b	Canyon width, w (m)	Canyon length, l (m)	Flood width, W (m)	Cliff height, H_c (m)
Idaho	MG, N	0.0053	0.029	198	2245	30000	64
	MG, S	0.0053	0.021	219	2763	30000	57
	WC	0.0047	0.041	200	387	30000	63
	BC	0.0055	0.044	135	1768	30000	37
	BlC	0.0047	0.029	168	1066	30000	74
	BL, E	0.0037	0.043	563	1200	30000	93
	BL, W	0.0037	0.034	312	516	30000	74
Washington	DF, W	$9.3\text{x}10^{-5}$	0.0037	953	2245	6000	63
	DF, E	$9.3\text{x}10^{-5}$	0.0037	505	2300	6000	101
	PC, N	$3.0\text{x}10^{-4}$	0.0021	1468	2826	3000	113
	PC, S	$3.0\text{x}10^{-4}$	0.0021	762	2803	3000	102
	FC, N	$5.4\text{x}10^{-4}$	0.0036	546	2813	7000	103
	FC, S	$5.4\text{x}10^{-4}$	0.0028	627	1385	7000	106
Iceland	As	0.002	0.002	415	3825	1325	90
Ares Vallis	AV, W	0.0044	0.010	5000	51200	70000	280
	AV, E	0.0044	0.011	3500	51200	70000	400
Echus Chasma	EC1	0.0016	0.0029	2254	30500	25000	991
	EC2	0.0039	0.0116	2443	9500	34000	900
	EC3	0.0037	0.0074	2480	20400	34000	551
	EC4	0.0024	0.0075	2100	7500	50000	640
	EC5	0.0024	0.0070	1600	17000	8000	440
	EC6	0.0032	0.0070	2876	516	5000	800
	EC7	0.0031	0.0214	2288	11000	17000	1035

Table 4.2: Values of topographic/geometric/toppling parameters used for the various canyon. Abbreviations used for the different locations are those shown in Figure 4.1.

		Upstream Froude number, $\mathrm{Fr_n}$		Canyon-to-flood width ratio, w^*	Flood width limitation factor, W^*		Downslope backwater parameter, l^*	
		Min	Max		Min	Max	Min	Max
Idaho	MG, N	1.07	1.20	0.01	43.1	22.8	6.5	3.4
	MG, S	1.11	1.23	0.01	35.8	19.1	6.6	3.5
	WC	1.06	1.15	0.01	28.9	18.0	0.8	0.5
	BC	1.19	1.29	0.005	26.9	16.6	3.2	2.0
	BlC	1.01	1.13	0.01	38.3	20.2	2.7	1.4
	BL, E	0.92	0.90	0.02	25.9	28.4	2.1	2.3
	BL, W	0.97	0.96	0.01	18.8	20.1	0.7	0.7
Washington	DF, W	0.2	0.24	0.16	0.01	0.004	0.01	0.004
	DF, E	0.2	0.25	0.08	0.01	0.004	0.01	0.003
	PC, N	0.35	0.45	0.49	0.02	0.004	0.1	0.01
	PC, S	0.35	0.43	0.25	0.02	0.01	0.1	0.02
	FC, N	0.45	0.56	0.08	0.2	0.04	0.1	0.04
	FC, S	0.45	0.56	0.09	0.2	0.04	0.1	0.02
Iceland	As	0.79	0.99	0.31	0.1	0.03	1.1	0.3
Ares Vallis	AV, W	1.11	1.4	0.07	4.4	1.1	6.9	1.7
	AV, E	1.08	1.38	0.05	5.1	1.2	7.9	1.9
Echus Chasma	EC 1	0.71	0.91	0.09	0.3	0.1	0.9	0.2
	EC 2	0.92	1.14	0.07	3.4	1.0	2.1	0.6
	EC 3	1	1.25	0.07	1.7	0.5	2.2	0.6
	EC 4	0.85	1.02	0.04	1.3	0.4	0.4	0.1
	EC 5	0.87	1.03	0.2	0.1	0.1	0.8	0.3
	EC 6	0.91	1.13	0.58	0.1	0.03	0.1	0.02
	EC 7	0.86	1.03	0.13	1	0.3	1.5	0.5

Table 4.3: Values of inverted dimensionless flow focusing parameters for the minimum-discharge and maximum-discharge models for the various canyons. Abbreviations used for the different locations are those shown in Figure 4.1.

		Normal flow depth (m)		Normal discharge per unit width (m^2/s)		Total head discharge ($x10^4$ m^3/s)	
		$h_{n,\min}$	$h_{n,\max}$	$q_{n,\min}$	$q_{n,\max}$	$Q_{h,\min}$	$Q_{h,\max}$
Idaho	MG, N	2	2	8	24	0.2	0.5
	MG, S	2	4	11	32	0.3	0.8
	WC	2	4	13	28	0.3	0.6
	BC	3	5	20	44	0.3	0.6
	BlC	2	3	8	23	0.1	0.4
	BL, E	2	2	9	8	0.5	0.5
	BL, W	3	3	15	14	0.5	0.5
Washington	DF, W	19	56	52	320	6.4	38.4
	DF, E	19	63	52	390	3.5	25.6
	PC, N	14	59	54	637	8.6	95.2
	PC, S	14	50	54	474	4.8	39.3
	FC, N	11	39	53	427	3.6	26.2
	FC, S	11	39	53	427	4.1	29.9
Iceland	As	7	27	43	448	1.8	18.6
Ares Vallis	AV, W	33	136	404	4323	216.6	2244.3
	AV, E	28	121	320	3549	120.6	1292.7
Echus Chasma	EC 1	52	245	517	6836	135.8	1561.4
	EC 2	18	63	136	1105	37.9	288.3
	EC 3	34	128	391	3513	106.0	918.3
	EC 4	45	136	502	3123	127.3	714.2
	EC 5	52	144	633	3447	102.0	599.5
	EC 6	30	107	288	2431	83.0	748.0
	EC 7	23	71	178	1200	46.7	297.9

Table 4.4: Values of inverted flow depths, discharges per unit width, and total head discharges for the minimum-discharge and maximum-discharge models for the various canyons. Abbreviations used for the different locations are those shown in Figure 4.1.

	Canyon width, w (m)	Flood width, W (m)	Bed slope, S	Cliff height, H_c (m)	Fracture spacing, D (m)
Bed slope	150	2000	10^{-5}-10^{-2}	80	0.5
Fracture spacing	150	2000	10^{-3}	80	0.1-10

Table 4.5: **Summary of values used for sensitivity analysis.**

Acknowledgements

The authors are grateful to Liliya Posiolova of Malin Space Science Systems for assistance with CTX DEM generation, and the students of Ge121a at Caltech for sharing grain size data collected within the Drumheller channel, Washington in the Fall of 2013. We also thank Paul Carling and an anonymous reviewer for constructive comments which improved this manuscript Support was provided by the NASA Earth and Space Science Fellowship 12-PLANET12F-0071, NSF Grants EAR-1147381 and 1529110, and NASA Grant NNX13AM83G. Derived data is available in Appendices and Tables.

Chapter 5

WHAT SETS THE SIZE OF CURRENT RIPPLES?

Mathieu G. A. Lapôtre, Michael P. Lamb, and Brandon McElroy

This chapter was published as:
Lapôtre, M. G. A., et al. (2017), What Sets the Size of Current Ripples?, *Geology*, 45(3), 243-246, DOI: 10.1130/G38598.1.

Abstract. Water flowing over sand in fluvial and marine settings often results in the formation of current ripples. Found in modern and ancient deposits on Earth and Mars, ripple stratification records flow directions and fluid properties that are crucial to interpreting sedimentary records. Despite decades of observations of current ripples, there is no universal scaling relation to predict their size or to distinguish them from dunes. Here, we use dimensional analysis and a new data compilation to develop a scaling relation that collapses data for equilibrium wavelengths of ripples forming under unidirectional flows. Results show that ripples are larger with more viscous fluids, coarser grains, smaller bed shear stresses, and smaller specific gravity of sediment. The scaling relation also segregates ripples from dunes, highlighting a narrow regime of transitional bedforms that have morphologic properties and sediment transport conditions that overlap with both ripples and dunes. Our analysis shows that previous absolute-size-based definitions of ripples and dunes only hold for certain conditions, such as water flows transporting siliciclastic grains on Earth. The new theory allows

estimates of ripple sizes in foreign fluids and on other planets including meter-scale ripples in methane flows on Titan or in viscous brines on Mars.

1. Introduction

Current ripples are migrating waves of sand that form under ocean currents, turbidity currents, and rivers. They tend to be 10–20 cm in wavelength (λ), but can be found in sizes ranging from ~8 cm to as large as ~60 cm [e.g., *Middleton and Southard*, 1984] (Figure 5.1A). Current ripples arise from a spatial lag between shear stresses exerted by the flow on the bed and sediment flux [*Smith*, 1970; *Richards*, 1980; *Charru et al.*, 2013], and linear stability analysis shows that their initial wavelength either scales with the thickness of the viscous sublayer or a sediment-transport saturation length, $L_{\mathrm{sat}} \propto \frac{u_* D}{\sqrt{RgD}}$ (where u_* is bed shear velocity, D is grain diameter, R is submerged specific density of sediment, and g is gravitational acceleration; *Charru et al.*, 2013). Once initiated, ripples grow until they reach an equilibrium wavelength [*Betat et al.*, 2002]; however, there exists no universal theory to predict it. Ripples are generally considered distinct from dunes in that (1) they are typically smaller (λ < 60 cm) [*Ashley*, 1990] (Figure 5.1A), (2) they comprise the smaller mode of what is often a bimodal distribution of sandy bedforms under unidirectional flows [*Middleton and Southard*, 1984] (Figure 5.1A), and (3) distinct physical processes are thought to control their formation and size [e.g., *Bennett and Best*, 1996]. For example, dunes are thought to increase in size with increasing flow depth and flow velocity and finer grain size [*Southard and*

Boguchwal, 1990a], behaviors that are not typically observed for ripples. Ripple size, on the other hand, is typically thought to be insensitive to flow velocity [*Baas*, 1994] and increase with grain size [*Allen*, 1982; *Raudkivi*, 1997]. However, a dynamical difference between ripples and dunes is debated.

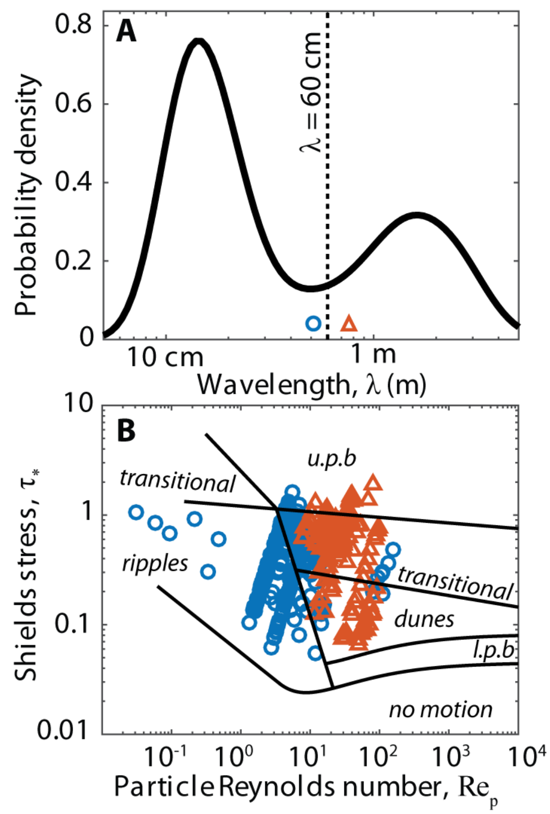

Figure 5.1: **Size and stability of fluvial bedforms.** (A) Probability density of bedform wavelength (Table 5.1), and the 60-cm threshold of *Ashley* [1990] (vertical line). (B) Bedform stability diagram (from *Southard and Boguchwal*, 1990a, and *van den Berg and van Gelder*, 2009, as synthesized by *Lamb et al.*, 2012) with ripples (blue circle) and dunes (red triangle) discriminated by the 60-cm threshold. “l.p.b” and “u.p.b” indicate lower- and upper-plane bed regimes.

For example, *Jerolmack and Mohrig* [2005] proposed that ripples and dunes are similar on the basis of spectral analysis of a riverbed that showed that all scales of sandy bedforms co-exist, spanning ripples and dunes. Thus, the bimodality of bedform wavelengths in Figure 5.1A might result from experimental or observational bias. Furthermore, *Bartholdy et al.* [2015] proposed that ripple size should scale with flow depth, an attribute normally associated with dunes. It is also unclear if the 60 cm break in scale proposed by *Ashley* [1990] (Figure 5.1A) provides a universal discriminant of ripples and dunes that can be applied on different planets, or whether it results from the similarity of sediment and fluid properties found on Earth [*Lamb et al.*, 2012a]. These studies highlight the need to unify previous work and develop a dynamic scaling relation for the equilibrium size of ripples that encompasses grain size, flow strength, sediment and fluid properties, and gravity.

Multiple studies have compared the size of ripples to various bed and flow characteristics. *Yalin* [1985] proposed that bedform wavelength depends on a number of flow and sediment parameters, but found that the wavelength of smaller bedforms (ripples) is proportional to the thickness of the viscous sublayer, i.e., $\lambda \propto \frac{\nu}{u_*}$ (where ν is kinematic viscosity of the fluid). In contrast, other studies suggested that ripple size scales with $\nu^{2/3}$ [e.g., *Boguchwal and Southard*, 1990; *Lamb et al.*, 2012a], but does not vary with u_* [e.g., *Baas*, 1994]. In addition to fluid properties, bed characteristics also affect ripple size. Ripple wavelength has been proposed to increase with grain size following linear [*Allen*, 1982], power-law [*Raudkivi*, 1997], and logarithmic [*Baas*, 1999] relations. *Middleton and Southard* [1984] suggested that wavelength appears to decrease with increasing grain density, a finding that is also supported by dimensional analysis [*Boguchwal and Southard*, 1990]. However, a single relation has yet to be proposed that can reproduce all observed ripple-size dependencies across wide ranges in grain size, viscosity, density, and flow strength.

Ripple theory provides a powerful proxy to decipher past and present environmental conditions on Earth and other planetary bodies, and has been used to infer the existence of water flows, viscous brines, and a low density paleo-atmosphere on Mars [*Southard and Boguchwal*, 1990b; *Lamb et al.*, 2012; *Lapôtre et al.*, 2016b]. Current ripples also are hypothesized to exist in rivers of methane on Titan [*Burr et al.*, 2013; *Grotzinger et al.*, 2013]. However, proper interpretation of ripples on other planets requires a dimensionless scaling relation that accounts for material properties and gravity that differ from Earth. Given that the Shields stress (τ_*) and particle Reynolds number (Re_p) reasonably segregate the occurrence of ripples and dunes [e.g., *Lamb et al.*, 2012a] (Figure 5.1B), it seems reasonable that these dimensionless quantities also affect ripple size.

Based on dimensional analysis and a comprehensive data compilation, we propose herein a new dimensionless number, the Yalin number, that allows for a unifying scaling relation for equilibrium ripple size. This work builds on that of *Lapôtre et al.* [2016b] who proposed a similar dimensionless scaling relation for analysis of large wind ripples on Mars, but they did not analyze an exhaustive data compilation of current ripples and dunes. Herein we show that ripple size data collapse into a dimensionless relation with Yalin number, which also yields a process-based discriminant of the ripple-dune transition that is applicable for wide ranges in fluids and sediment properties and gravity.

2. Theory

Physical parameters often attributed to bedform stability are fluid kinematic viscosity, ν (m^2/s), total bed shear velocity (skin friction + form drag), u_* (m/s), grain diameter, D (m), and submerged specific gravity of sediment, Rg (m/s^2) [e.g., *Boguchwal and Southard*, 1990]. These four quantities can be recast in terms of two dimensionless parameters. While the choice of these parameters is non-unique, here we choose the particle Reynolds number, $\mathrm{Re}_p = \frac{u_* D}{\nu}$, and Shields stress, $\tau_* = \frac{u_*^2}{RgD}$ (Figure 5.1B). Other authors have used different but mathematically equivalent combinations of these parameters [*Boguchwal and Southard*, 1990; *van den Berg and van Gelder*, 1993]. Current-ripple wavelength, which has been argued to scale with the thickness of the viscous sublayer [*Yalin*, 1985], or ν / u_*, introduces another variable. Following the same dimensional analysis, a third dimensionless variable becomes the dimensionless wavelength, $\lambda* = \frac{\lambda u_*}{\nu}$.

Yalin [1985] argued that the number of dimensionless parameters controlling ripple size can be further reduced to two by showing that ripple-wavelength data collapsed into the (X_Y, Y_Y)-parameter space, where

$X_Y = 3.38\,\mathrm{Re}_p^{1/2}\,\tau_*^{1/4}$, and $Y_Y = \dfrac{\lambda}{3.38D}\dfrac{\mathrm{Re}_p^{1/2}}{\tau_*^{1/4}}$. We recast the latter parameters to isolate $\lambda*$ as,

$$\begin{cases} \chi = \dfrac{X_Y^2}{11.42} = \mathrm{Re}_p\sqrt{\tau_*} \\ \lambda* = X_Y Y_Y = \dfrac{\lambda u_*}{\nu} \end{cases} . \tag{5.1}$$

We name the new parameter χ the Yalin number, after Mehmet Selim Yalin. The Yalin number can be interpreted as a metric for the susceptibility of a grain on the bed to be entrained by fluid flow, which not only depends on flow strength relative to the particle weight (τ_*), but also on the degree to which the particle is immersed within the viscous sublayer (Re_p) [e.g., *Niño et al.*, 2003]. The Yalin number also is proportional to $\dfrac{L_{\mathrm{sat}} u_*}{\nu}$, a metric previously proposed to control initial ripple wavelength [*Charru et al.*, 2013]. To explore this new parameter space, we compiled wavelength data for both ripples and dunes inferred to be at steady-state morphology; these data cover a wide range of fluid and sediment properties, including high viscosity fluids [e.g., *Grazer*, 1982], and thus a wide range in χ (Table 5.1). Our new compilation comprises 472 data points, from 15 flume and field studies, each of which is an average of tens of bedform-size measurements (Table 5.1).

3. Results

We first consider the often-used criterion of *Ashley* [1990], which classifies <60-cm wavelength bedforms as ripples (Figure 5.1). Figure 5.1B shows that while this criterion is overall consistent with commonly used bedform stability diagrams, a few bedforms that would be interpreted as ripples from a size-threshold criterion would be classified as dunes by *Southard and Boguchwal* [1990a] and *van den Berg and van Gelder* [1993] based on morphology. The inconsistency between the absolute size definition of *Ashley* [1990] and the bedform stability diagrams highlights the need for a better discriminant between ripples and dunes.

Figure 5.2A shows our data compilation in (χ, λ^*)-space. Most of the smaller bedforms collapse to a single power-law relation (R^2 = 0.79),

$$\lambda^* = 2504\chi^{1/3}. \tag{5.2}$$

Based on the above dimensional analysis, we expect such a collapse for ripples in this parameter space, whereas dunes are not expected to collapse because this space does not account for parameters such as flow depth, which is known to partially control dune size [e.g., *Southard and Boguchwal*, 1990a]. We thus interpret those bedforms that collapse to Equation (5.2) as ripples, which also correspond to $\chi <\sim 4$. For $4 \le \chi \le 9$, there is a sharp, order-of-magnitude increase in λ^*. The larger bedforms, at $\chi >\sim 9$, do not collapse to a single relation in this parameter space, and we therefore interpret them as dunes.

Our new definition of ripples and dunes, based on Yalin number, is consistent with the 60-cm threshold of *Ashley* [1990] for the majority of the data.

Figure 5.2B shows that bedforms with $\chi < 4$ have wavelengths generally <60 cm, with a mode at 12 cm, consistent with sizes commonly attributed to ripples. In contrast, bedforms with $\chi > 9$ are generally >60 cm, and therefore consistent with previous definitions of dunes based on size. Bedforms with $4 \le \chi \le 9$ have wavelengths from both size modes (Figure 5.2B) and are skewed to somewhat larger wavelengths than ripples (Figure 5.2B). Also consistent is that the boundary between ripples and dunes in the bedform stability diagram (Figure 5.2C) appears to be a line of constant χ (i.e., $\mathrm{Re}_p \propto \tau_*^{-1/2}$ or $L_{\mathrm{sat}} \propto \dfrac{\nu}{u_*}$), with $\chi = 4$ matching well the ripple regime upper bound (Figure 5.2C). Thus, the Yalin number discriminates between small sandy bedform data that collapse to a single relation in (χ, λ^*)-space and data from larger bedforms that do not collapse, providing a process-based, rather than absolute-size-based, metric to distinguish between ripples and dunes.

The collapse of ripple data allows for ripple size to be predicted as a function of sediment and fluid properties, such that λ^* can be contoured in bedform stability space (Figure 5.2C). In particular, Equation (5.2) can be rearranged in dimensional form as

$$\lambda = 2504 \frac{\nu^{2/3} D^{1/6}}{(Rg)^{1/6} u_*^{1/3}}, \tag{5.3}$$

which is valid within the ripple stability field (Figure 5.2D), and unifies previously proposed scaling relations that focused on single dependencies of ripple size. For example, the dependence on kinematic viscosity to the 2/3 power (Figure 5.3A) was inferred from dimensional analysis in multiple studies[e.g., *Middleton and Southard*, 1984]. *Yalin* [1985] argued that ripple wavelength scales linearly with kinematic viscosity (i.e., λ^* is constant); however, his dataset did not cover as wide of a range in χ as in our Figure 5.2A, and thus the relation $\lambda^* \propto \chi^{1/3}$ was not evident. Equation (5.3) is consistent with previously published grain size dependencies [*Raudkivi*, 1997; *Baas*, 1999], and shows an increase of ripple wavelength with grain size (Figure 5.3B). Earlier studies suggested that there is no dependence of ripple wavelength on flow strength [e.g., *Baas*, 1994], that $\lambda \propto u_*^{-1}$ [*Yalin*, 1985], or that wavelength increases with flow strength [e.g., *Baas*, 1999]. We find a weak decreasing trend of wavelength with shear velocity for ripples ($\chi < 4$; Figure 5.3C), and the bedforms analyzed by *Baas* [1999] fall into the transitional regime ($4 \le \chi \le 9$) by our definition. Equation (5.3) is also consistent with predictions from *Southard and Boguchwal* [1990b], showing a decrease in ripple wavelength with increasing specific submerged density (Figure 5.3D). While *Bartholdy et al.* [2015] suggested ripple wavelength depends on flow depth, we observed no improvement in the collapse of ripple data ($\chi < 4$) by further regressing based on flow depth; much of the data they used for comparison falls into our transitional ($4 \le \chi \le 9$) or dune ($\chi > 9$) regimes.

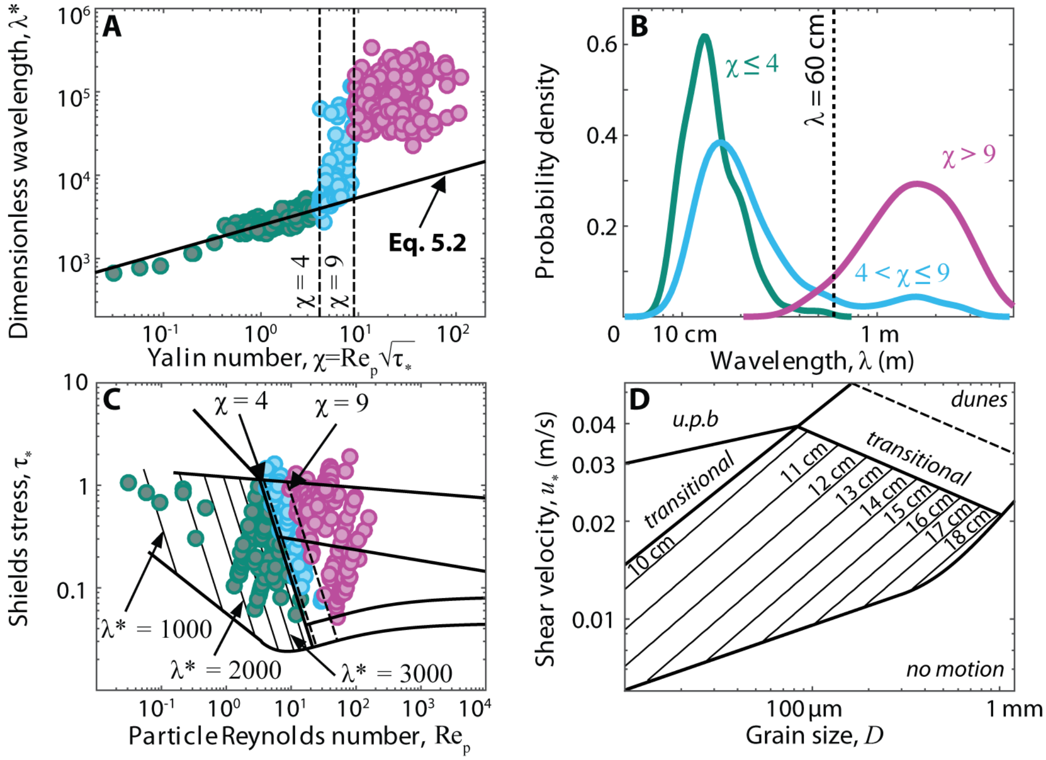

Figure 5.2: **Size and stability of fluvial bedforms vs. Yalin number.** (A) Dimensionless bedform wavelength versus Yalin number. Bedforms are discriminated by thresholds in χ (ripples in green, transitional in blue, dunes in pink). Best fit to ripple data, $\lambda^* = 2445\chi^{0.38}$ (R^2 = 0.80), is statistically undistinguishable from Equation (5.2). (B) Probability density of the bedform wavelength discriminated by Yalin numbers. (C) Bedforms classified by Yalin number on bedform stability diagram from Figure 5.1B. Bedform regimes are as in Figure 5.1B. Contours in the ripple regime indicate lines of constant λ^* at intervals of 500. (D) Close-up of the ripple field in dimensional bedform stability diagram with predicted ripple wavelength for freshwater on Earth (R = 1.65, g = 9.81 m/s^2, ν = 10^{-6} m^2/s.).

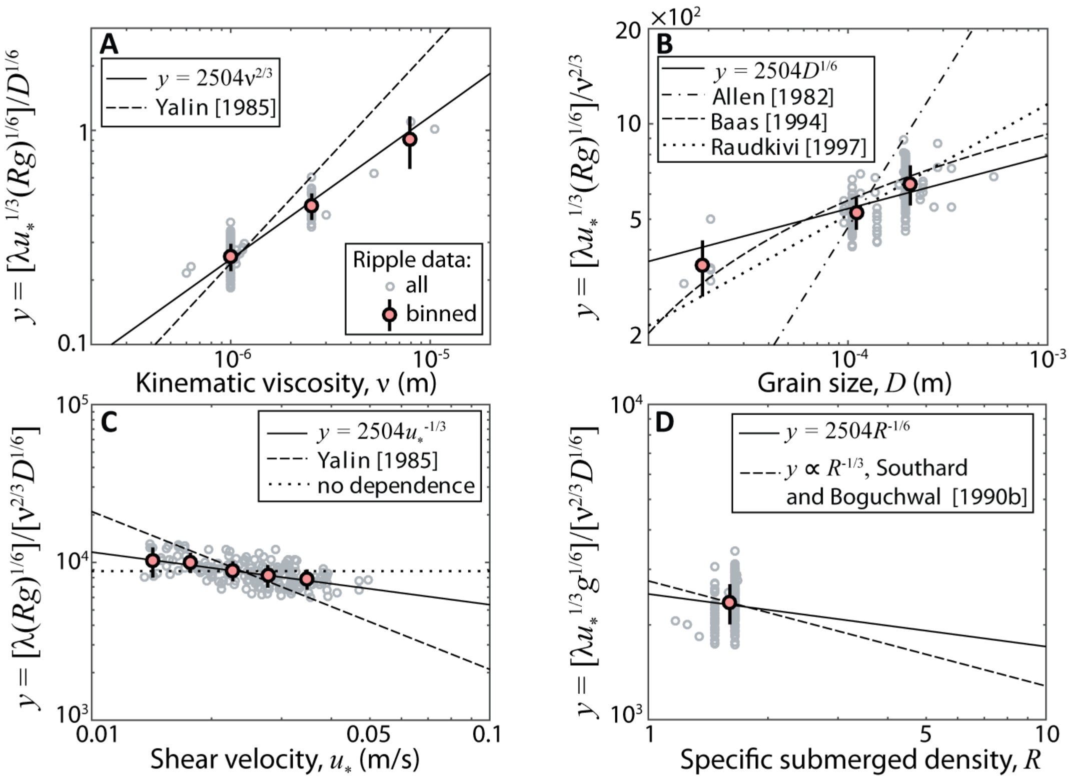

Figure 5.3: **Individual dependences of normalized ripple wavelength** on: (A) kinematic viscosity, (B) grain size, (C) shear velocity, and (D) submerged specific density as compared to Equation (5.3). Red-filled symbols are binned data, and error bars represent the geometric standard deviation within each bin. Normalized ripple wavelength (y-axes) was computed by rearranging Equation (5.3) to isolate the parameter of interest (x-axes) and eliminating constants. Solid line in each plot represents Equation (5.3).

4. Discussion and Conclusion

The collapse of ripple data to Equation (5.2), and the failure of dune data to collapse in the same parameter space, supports the hypothesis that different physical processes are involved in the formation of ripples and dunes. Importantly, the χ threshold for the upper bound on the ripple regime is more consistent with bedform stability diagrams (Figure 5.1A) than the absolute size threshold of *Ashley* [1990] (Figure 5.2C). Our analysis highlights a transition zone across the ripple-dune boundary ($4 \le \chi \le 9$). Transitional bedforms tend to have wavelengths <60 cm, typical of ripples, and yet plot in the dune regime based on previous bedform stability diagrams, where sediment transport is more vigorous (Figure 5.1B). Transitional bedforms thus may be a hybrid between ripples and dunes, for which dominant physical processes responsible for both ripples and dunes are operative. The Yalin number separates bedform data into two distinct wavelength modes, but the absolute size break of 60 cm likely results from an observational bias reflecting little variation in sediment and fluid properties, and gravity, investigated in most studies. For example, at the upper bound of the ripple regime $\chi \approx 4$ and $\lambda^* \approx 4000$, which when combined yields $\lambda \approx 2000 \nu^{1/2} \left(\frac{D}{Rg} \right)^{1/4}$. Thus, the χ threshold implies a different absolute size break between ripples and dunes for different viscosity and density fluids, different sediment sizes and densities, and different gravitational acceleration.

Why does the ripple domain exist for Yalin numbers less than four? Previous studies have suggested that ripples form under hydraulically smooth flow (defined as a roughness-Reynolds number <5; *Nikuradse*, 1933), or when the laminar sublayer is thicker than a grain diameter ($\mathrm{Re}_p <\sim 11.6$; *Engelund and Hansen*, 1967), both of which are vertical lines on Figure 5.2C that are not consistent with the observed sloping ripple-dune boundary. Another hypothesis is that ripples predominantly form under bedload transport [e.g., *Richards*, 1980]; however, the suspension threshold of *Niño et al.* [2003] also differs from a constant

χ (Figure 5.4). While a constant χ implies that L_{sat} is a multiple of viscous-sublayer thickness, it is unclear why such a criterion would control the ripple-dune transition. *Bennett and Best* [1996] attribute the ripple-dune transition to turbulent wake instabilities shed by ripples, leading to the formation of abnormally large ripples [*Leeder*, 1983] or bedform mergers that grow dunes [*Fernandez et al.*, 2006]. Ultimately, changes in the separation wake may be tied to a certain value of $\lambda*$ because it is a ripple-scale Reynolds number. For example, $\lambda* \approx 4000$ approximately matches the onset of fully developed turbulence downstream of backward-facing steps [e.g., *Armaly et al.*, 1983].

Equation (5.3) shows that if ν, g, and R do not vary significantly, as is often the case on Earth, then ripple size is a function of D and u_* only. If grain size and wavelength can be estimated from field observations, then Equation (5.3) can be used to calculate formative bed shear velocity, which can be related to current velocity. Figure 5.2D, for example, shows predicted ripple wavelengths that range from 8 to 18 cm for decreasing shear velocities, assuming fluid and sediment properties typical for Earth (g = 9.81 m/s^2, R = 1.65, ν = 10^{-6} m^2/s). Ripple size is more sensitive to kinematic viscosity than it is to bed shear velocity, and thus might be a better indicator of current or ocean paleo-temperatures. For freshwater, a 10°C change in temperature has an equivalent effect on ripple wavelength, through kinematic viscosity, as a twofold change in bed shear velocity.

Preserved ripple strata in martian sandstones were observed and proposed to have formed in highly concentrated brines [*Lamb et al.*, 2012a]. Fluvial transport on

Titan may also form ripples when ice grains are transported by methane flows [*Burr et al.*, 2013]. Because gravity, density, and viscosity are implicitly taken into account, Equation (5.2) can be applied to other planetary bodies. For example, equivalent freshwater flows on Mars would make ripples 14% larger than on Earth (e.g., for $R = 1.65$ and $g = 9.81$ m/s^2 on Earth, and $R = 1.9$ and $g = 3.78$ m/s^2 on Mars) consistent with *Southard and Boguchwal* [1990b]. A different kinematic viscosity, such as for viscous brines on Mars (e.g., ν = 4x10^{-5} m^2/s, R = 1.04) or methane flows on Titan (e.g., ν = 5x10^{-6} m^2/s, R = 0.85, g = 1.35 m/s^2), has a more significant effect on ripple size. For $D = 400$ μm and $u_* = 0.02$ m/s, predicted wavelengths are of ~0.15, 2.3, and 0.7 m in freshwater on Earth, brines on Mars, and ice grains in methane flows on Titan (Figure 5.5). Large ripples in viscous brines may be so large that they are limited in height by flow depth, as inferred by *Lamb et al.* [2012a], further complicating traditional definitions of ripples and dunes.

In summary, data for small sandy bedforms collapse to a single relation in dimensionless wavelength and Yalin number space. This observation and the lack of collapse for larger bedforms imply that different physical processes are involved in the formation of ripples and dunes. The new scaling relation allows for improved paleohydraulic reconstructions based on current ripple size on Earth and other planetary bodies, with different gravitational acceleration, and exotic sediments and fluids.

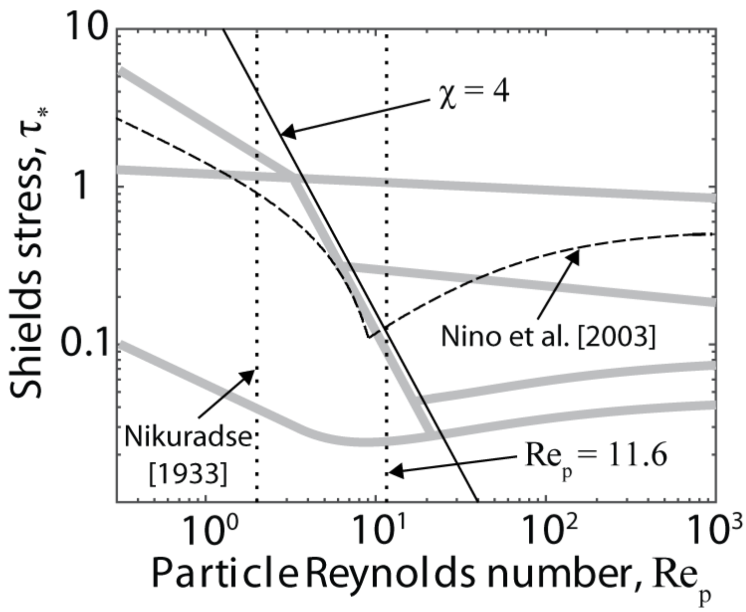

Figure 5.4: Different hypotheses for ripple-dune transition on the bedform stability diagram from Figure 5.1A (thick gray lines). Solid black line corresponds to a Yalin number of 4, which is the upper bound on the ripple regime in Figure 5.2A. The dashed line corresponds to threshold for the onset of suspension from *Niño et al.* [2003], converted to the $\left(\mathrm{Re_p}, \tau_*\right)$-space using the settling velocity formula of *Ferguson and Church* [2004]. The latter study uses a different definition of the particle Reynolds number, $r_\mathrm{p} = \frac{\sqrt{RgD}D}{\nu}$, such that $r_\mathrm{p} = \frac{\mathrm{Re_p}}{\sqrt{\tau_*}}$. The dotted lines correspond to the transition from hydraulically-smooth to hydraulically-rough flows [*Nikuradse*, 1933] and the critical condition for the laminar sublayer to become thicker than a grain diameter, at $\mathrm{Re_p} = 11.6$ [*Engelund and Hansen*, 1967], respectively.

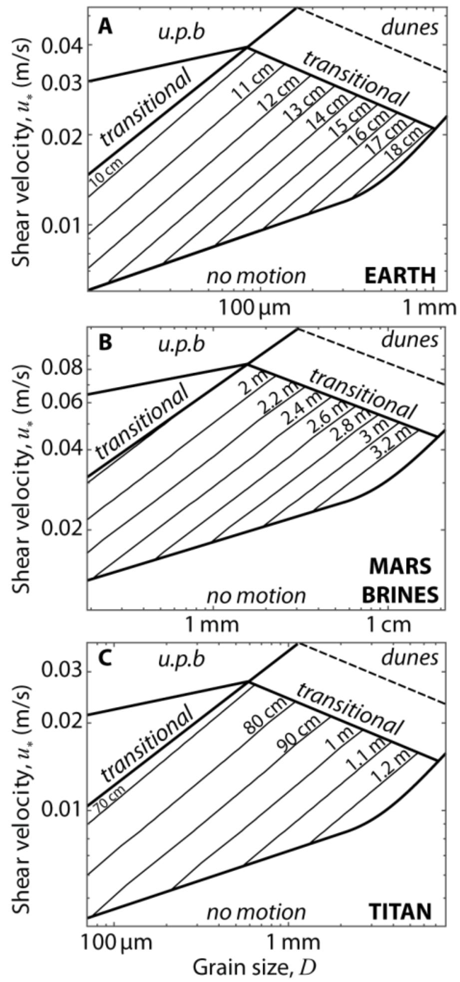

Figure 5.5: Ripple size and stability on Earth, Mars, and Titan. Close-up of the ripple field in the bedform stability diagram (as compiled by *Lamb et al.*, 2012a, based on previous diagrams by *Southard and Boguchwal*, 1990a, and *van den Berg and van Gelder*, 2009) with predicted ripple wavelength for (A) fresh water on Earth, (B) brines on Mars, (C) water ice clasts in methane on Titan. Acronym "*u.p.b.*" designates the "upper plane bed" regime. The transition zone between ripples and dunes (dashed lines) corresponds to Yalin numbers between 4 and 9.

Table 5.1: Bedform data compilation (in ancillary comma separated value or ".csv" file "Lapotre_Chapter5_Table_1")**.** We build on the data compilation of Yalin (1985), which comprises experiments with sand and glass beads and where the fluid was either water or glycerine and water solutions [*Barton and Lin*, 1955; *Vanoni and Brooks*, 1957; *Vanoni and Hwang*, 1967; *Alexander*, 1980]. We added datasets for both lower [*Mantz*, 1978; *Grazer*, 1982], and similar and higher [*Stein*, 1965; *Guy et al.*, 1966; *Williams*, 1967; *Bishop*, 1977; *Baas*, 1994; *Gabel*, 1993; *Baas*, 1999; *Leclair*, 2002; *Venditti et al.*, 2005] Yalin numbers.

Acknowledgments
We thank J. Southard, W. Fischer, and R. Ewing for discussions that motivated this work, and three anonymous reviewers and M. Perillo for comments that improved our manuscript.

Chapter 6

LARGE WIND RIPPLES ON MARS: A RECORD OF ATMOSPHERIC EVOLUTION

Mathieu G. A. Lapôtre, Ryan E. C. Ewing, Michael P. Lamb, Woodward W. Fischer, John P. Grotzinger, David M. Rubin, Kevin W. Lewis, Matthew J. Ballard, Mackenzie Day, Sanjeev Gupta, Steve G. Banham, Nathan T. Bridges, David J. Des Marais, Abigail A. Fraeman, John A. Grant, Ken E. Herkenhoff, Doug M. Ming, Michael A. Mischna, Melissa S. Rice, Dawn Y. Sumner, Ashwin R. Vasavada, and R. Aileen Yingst.

This chapter was published as:
Lapôtre, M. G. A., et al. (2016), Large Wind Ripples on Mars: A Record of Atmospheric Evolution, *Science*, 353(6294), 55-58, DOI: 10.1126/science.aaf3206.

Abstract: Wind blowing over sand on Earth produces decimeter-wavelength ripples and hundred-meter- to kilometer-wavelength dunes—bedforms of two distinct size modes. Observations from the Mars Science Laboratory Curiosity rover and the Mars Reconnaissance Orbiter reveal that Mars hosts a third stable wind-driven bedform with meter-scale wavelengths. These bedforms are spatially uniform in size, and typically have asymmetric profiles with angle-of-repose lee slopes and sinuous crest lines, making them unlike terrestrial wind ripples. Rather, these structures resemble fluid-drag ripples, which on Earth include water-worked current ripples, but on Mars instead form by wind due to the higher kinematic viscosity of the low-density atmosphere. A reevaluation of the wind-deposited

strata in the Burns formation (< ~3.7 Ga) identifies potential wind-drag ripple stratification formed under a thin atmosphere.

1. Introduction

Bedforms are repeating topographic forms on a granular surface that arise because of interactions between the sediment bed, sediment transport, and fluid flow [*Middleton and Southard*, 1984]. Bedforms typically manifest as ripples or dunes made of sand mobilized by air or water. They create spatial patterns that are recognizable on the surfaces of Venus, Earth, Mars, Titan, and comet 67P [e.g., *Grotzinger et al.*, 2013; *Thomas et al.*, 2015], and leave stratified sedimentary deposits. Because their morphology depends on formation mechanisms [*Wilson*, 1972; *Rubim and McCulloch*, 1980; *Kok et al.*, 2012], bedforms are a primary means to reconstruct active and ancient atmospheric and hydrologic conditions.

Wind-driven (eolian) bedforms on Earth display two distinct scales: decimeter-wavelength sand ripples, and hundred-meter- to kilometer-wavelength dunes [*Wilson et al.*, 1972] (Figure 6.1A). Grain-impact processes are thought to dominate the formation of wind ripples, whereas dune formation involves an aerodynamic instability [e.g., *Kok et al.*, 2012]. Orbital observations of Mars also show the superposition of two distinct scales of active bedforms (Figure 6.1B) [*Bridges et al.*, 2011]. Dunes form at a similar wavelength as on Earth; however, dunes are ubiquitously mantled with bedforms 1-5 m in wavelength (hereafter referred to as large martian ripples) [*Bridges et al.*, 2007].

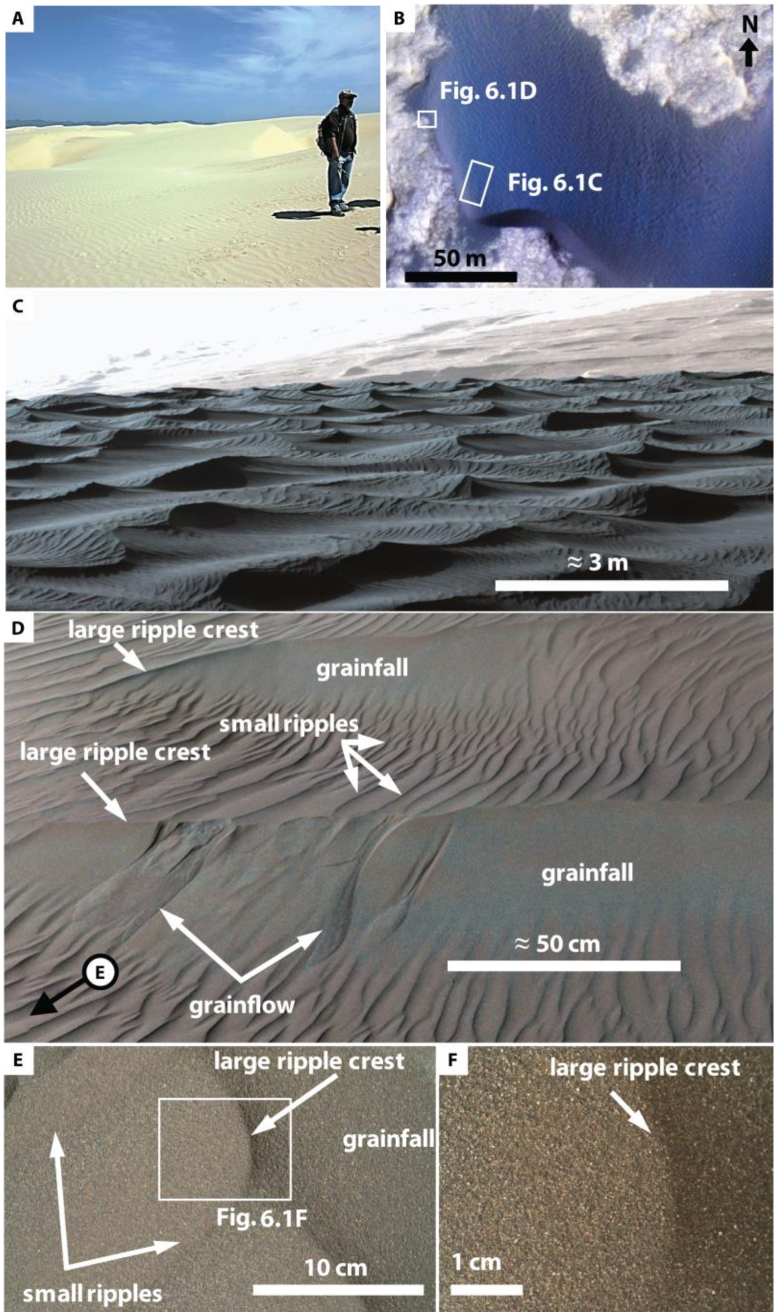

Figure 6.1: Aeolian bedforms on Earth and Mars. (A) Dunes and ripples at Oceano Dunes, California, United States (35.094960 N, -120.623476 E) (B-F) dune in the Bagnold Dune Field, Gale crater, Mars, as shown from (B) HiRISE image (ESP_035917_1755) and (C-F) the Curiosity rover. (C) Mastcam mosaic (mcam05410, sol 1192) showing small and large ripples on the dune. (D) Mastcam image (mcam05600, sol 1221) of large ripples with superimposed small ripples. (E) MAHLI 25 cm-standoff image (1223MH0005550010403094C00, sol 1223), ~1 m off-frame of (D) in the direction of the dot-and-arrow. (F) 5 cm-standoff image (1223MH0005560010403097C00, sol 1223) of the crest of a large ripple.

2. Observations

Large martian ripples were thought to have a similar origin to decimeter-wavelength aeolian impact ripples on Earth, but to be larger on Mars due to differences in saltation (ballistic hopping of grains) [e.g., *Kok et al.*, 2012]. An implicit assumption under this hypothesis is that small wind ripples should not coexist with large martian ripples. Until recently, the spatial coexistence of three scales of bedforms could not be tested because the resolution of orbital imagery is too coarse (25-50 cm/pixel with High Resolution Imaging Experiment (HiRISE) images; *McEwen et al.*, 2007) to detect decimeter-scale ripples, and rovers had not visited active dune fields – only sand sheets and coarse-grained ripples [e.g., *Sullivan et al.*, 2005; *Jerolmack et al.*, 2006; *Blake et al.*, 2013]. Observations made by the Curiosity rover [*Grotzinger et al.*, 2012] at an active dune field (the "Bagnold Dune Field") [*Silvestro et al.*, 2013] in Gale crater now show that large martian ripples are not simply larger versions of decimeter-scale wind ripples seen on Earth. Rather, we observe decimeter-scale ripples superimposed on larger, meter-scale ripples, which are in turn superimposed on dunes (Figure 6.1). Thus, two stable ripple-scale bedforms coexist on Mars, and are both superimposed on dunes, in contrast to the single scale of superimposed terrestrial ripples.

Mast Camera (Mastcam) images collected by Curiosity indicate that large martian ripples have morphologies unlike aeolian impact ripples. Terrestrial impact ripples have straight crestlines created by lateral grain splash [*Rubin*, 2012], and relatively subdued profiles [*Werner et al.*, 1986]. In contrast, the large ripples of the Bagnold Dune Field have sinuous crest lines and asymmetric topographic profiles with distinct upwind (stoss) and downwind (lee) slope angles. Furthermore, the stoss slopes of the large ripples are mantled by small-scale ripples with a wavelength range of ~ 5-12 cm, which, based on their straight crestline, we interpret as impact ripples similar to those of Earth (Figure 6.1C-D). This interpretation is consistent with recent numerical modeling which predicts that martian impact ripples should have decimeter-scale wavelengths [*Yizhaq et al.*, 2014]. By contrast, the crests of the large ripples are sharp and give way downslope to angle-of-repose slip faces (slopes dipping ~30 degrees downwind; see Section 5.1.3) marked by the presence of grainflows – small avalanche deposits (Figure 6.1D), indicating recent activity. The presence of grainfall (i.e., sand that settles out on the lee slope) and deflected impact ripples on the lee slope indicates aerodynamic influence of the large ripples contemporaneous with small-ripple migration (Figure 6.1D).

We compiled a comprehensive multiscale dataset of aeolian bedform wavelengths on Mars by combining remote measurements from eleven martian sites (see Section 5.1.2; Tables 6.1 and 6.2), with rover measurements from stereo imagery in Gale crater (see Section 5.1.3). Our statistical analysis confirms that Mars has an additional bedform-wavelength mode, and that meter-scale ripples are absent in terrestrial aeolian landscapes (Figure 6.2; Table 6.3).

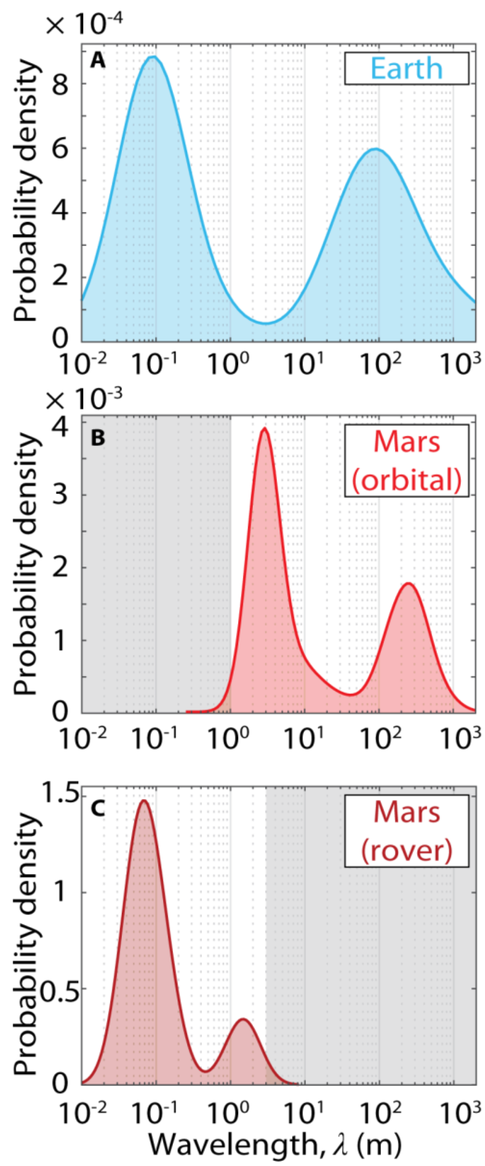

Figure 6.2: Distinct modes of aeolian bedforms on Earth and Mars. Bedform wavelength distribution on (A) Earth (n = 1473), (B) Mars from orbit (n = 2430; shaded area below limit of detection), and (C) the Curiosity rover (n = 44; shaded area constrained by perspective from the ground).

3. Interpretations

Large martian ripples are not simply small dunes because they maintain a stable size, whereas meter-wavelength dunes, which are rare on Earth, grow as they translate downwind [*Kok et al.*, 2012] (see Section 5.1.5). Large martian ripples mantled with impact ripples also cannot be explained as large versions of terrestrial impact ripples forming by large saltation [*Yizhaq et al.*, 2014; *Durán et al.*, 2014]; no existing model can reproduce the coexistence and coevolution of two scales of impact ripples [e.g., *Andreotti et al.*, 2006] (Section 5). Moreover, the large ripple morphology differs significantly from impact ripples. An alternative interpretation of the large ripples is that they are coarse-grained ripples [e.g., *de Silva et al.*, 2013]. However, images from the Mars Hand Lens Imager (MAHLI) show well-sorted large ripples up the dune's stoss slopes (Figure 6.1E), with very fine to medium sand and no significant grain-size differences between the small and large ripples (Figure 6.1E and F). Thus, neither the impact nor coarse-grained hypotheses readily explain the coexistence of two distinct equilibrium scales of active ripples composed of similar sediment size.

Their stable size, sinuous crests, and asymmetric profiles with avalanche faces make the large martian ripples morphologically similar to terrestrial subaqueous current ripples, also called fluid-drag ripples [*Southard and Boguchwal*, 1990a]. If the large martian ripples form aerodynamically (i.e., wind-drag ripples; e.g., *Wilson et al.*, 1972; *Bagnold*, 1941), then theory developed for current ripples should predict their scale once adjusted for martian conditions. Decades of flume experiments [e.g., *Grazer*, 1982; *Yalin*, 1985] have led to scaling relations for current ripples [e.g., *Yalin*, 1985; *Lamb et al.*, 2012]. Following the theoretical framework of *Yalin* [1985], we cast ripple size data in terms of the dimensionless current ripple wavelength, $\lambda^* = \frac{u_*}{\nu}\lambda$ (where λ is ripple wavelength,

ν is kinematic fluid viscosity, u_* is bed shear velocity, and ν / u_* is proportional to the viscous sublayer thickness; e.g., *Yalin*, 1985) is a function of the parameter $\mathrm{Re}_p \sqrt{\tau_*}$ (where Re_p is particle Reynolds number and τ_* is Shields stress (see Section 5.2). These dimensionless variables provide a complete description of ripple-size scaling that accounts for fluid and grain properties, and gravity. A large database of current ripple wavelengths [*Yalin*, 1985], updated here to include results from high viscosity fluids [*Grazer*, 1982], illustrates that

$$\lambda^* = 2453\left(\mathrm{Re}_p \sqrt{\tau_*}\right)^{1/3} \tag{6.1}$$

(Figure 6.3). To compare the predictions of fluid-drag ripple-wavelengths to the large martian ripples, we calculated $\mathrm{Re}_p \sqrt{\tau_*}$ and λ^* for all compiled martian bedforms. Results show that wind-drag ripples on Mars are predicted to be much larger than the decimeter-scale impact ripples due to the high kinematic viscosity in Mars' low-density atmosphere; furthermore, the wavelength of the large martian ripples is consistent with fluid-drag theory (Figure 6.3) across a range of elevations with different atmospheric density (see Section 5.4).

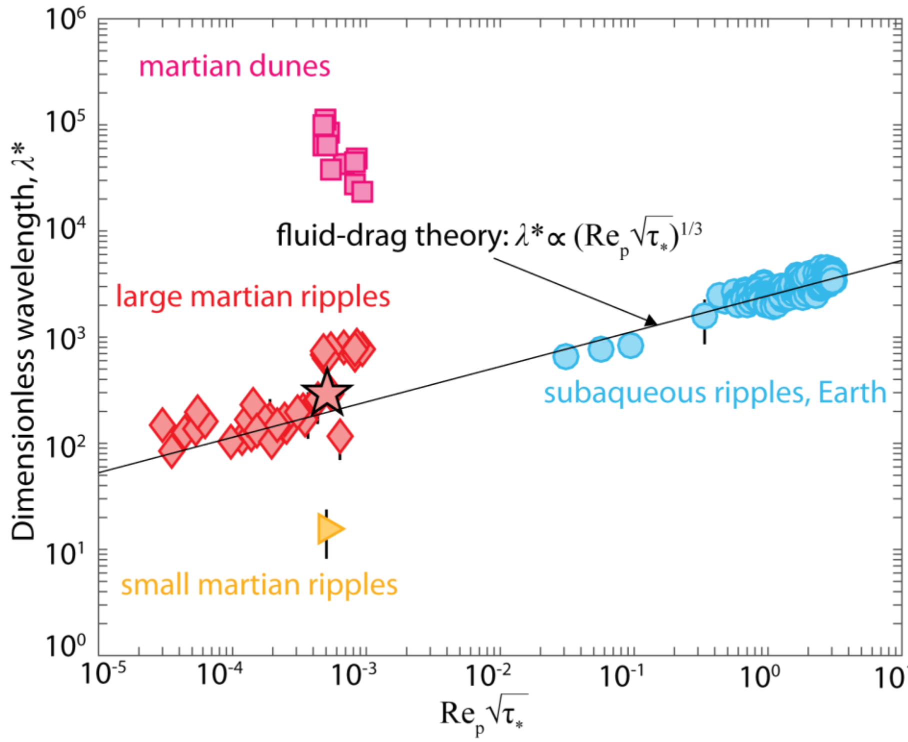

Figure 6.3: Scaling of fluid-drag ripples. Dimensionless bedform wavelength as a function of particle Reynolds number, Re_p, and Shields stress, $\tau *$, quantities that control fluid-drag ripple size [*Yalin*, 1985] (current ripples in blue circles, theory in black line). In contrast to martian dunes (pink squares) and small martian ripples (orange triangles), large martian ripples (red diamonds, n = 7280, measured over 36 locations globally including our measurements and those of *Lorenz et al.*, 2014; red star indicate rover measurements at Gale crater) match fluid-drag ripple theory. Symbols are means and error bars represent standard deviations at a given measurement site; error bars are smaller than marker size where not shown.

4. Discussion and Conclusion

Because wind-drag ripples are predicted to be smaller in thicker atmospheres, identification of these bedforms in ancient sedimentary rocks [e.g., *Grotzinger et al.*, 2005] offers the potential to reconstruct atmospheric loss and the global drying of Mars [e.g., *Hu et al.*, 2015]. Migration of bedforms produces cross-stratification in sedimentary rocks, which can be used to determine their original three-dimensional geometry. Based on morphology and scale, and using a kinematic model [*Rubin and Carter*, 2005] (Figure 6.4), we expect sinuous wind-drag ripples formed under present-day martian atmospheric conditions [*Withers and Smith*, 2006] to form decimeter-thick trough-cross-sets, grouped into larger sets formed by overall migration of the dune. Large-ripple stratification should be distinct from that of compound wind dunes or coarse-grained ripples because compound dunes do not maintain a persistently stable size in the down-dip direction (see Section 5.1.5) and typically form thicker cross-sets, and coarse-grained ripples leave recognizable coarse grained lags. Stratification from the large ripples might also resemble that of subaqueous ripples and dunes. However, identification of distinctive wind-ripple strata (inversely-graded, millimeter-thick continuous layers; e.g., *Hunter*, 1977) coexisting with both decimeter-scale cross-sets and meter-scale dune troughs would enable the definitive interpretation of an aeolian origin, whereas other contextual support, such as fluvial bar sets, desiccation cracks, and soft-sediment deformation, would characterize wet environments [e.g., *Grotzinger et al.*, 2005].

Candidate wind-drag ripples were observed by the Opportunity rover at Cape St. Mary, Victoria crater, in the Burns formation (Figure 6.4) [*Hayes et al.*, 2011], and were recognized as abnormally sinuous and large aeolian ripples at the time. There, repeated 10-20 cm thick trough cross-sets are bounded by meter-scale dune troughs. The morphology, scale, contextual relationship to distinctly larger bounding surfaces, and apparent high deposition rate [*Hayes et al.*, 2011] all support the hypothesis that this stratification was formed by wind-drag ripples. The wind-drag ripple hypothesis therefore indicates a substantially thinned martian atmosphere during deposition of the Late Noachian-Early Hesperian Burns formation (see Section 5.4) [*Arvidson et al.*, 2006]. This interpretation supports models for atmospheric loss based on carbon isotope calculations [e.g., *Hu et al.*, 2015]. The implied paleo-hydrology does not conflict with recent observations from Gale crater [*Mahaffy et al.*, 2015] since the absolute ages of both sequences are highly uncertain, and is also consistent with centimeter-scale trough cross-strata in sulfate-rich sands in the lower Burns formation [*Grotzinger et al.*, 2005]. The latter indicate shallow subaqueous flows discharged from melt or groundwater as brines of high ionic strength due to highly soluble sand grains [*Tosca et al.*, 2005; *Tosca et al.*, 2011; *Lamb et al.*, 2012], rather than sourced from meteoric precipitation under a denser atmosphere. Thus, whereas aqueous activity can be local and sourced from the subsurface [*Ojha et al.*, 2015], widespread shifts in wind-drag ripple size can indicate global changes in atmospheric density, and should prove an important geological indicator of the drying of Mars (see also Section 5.4).

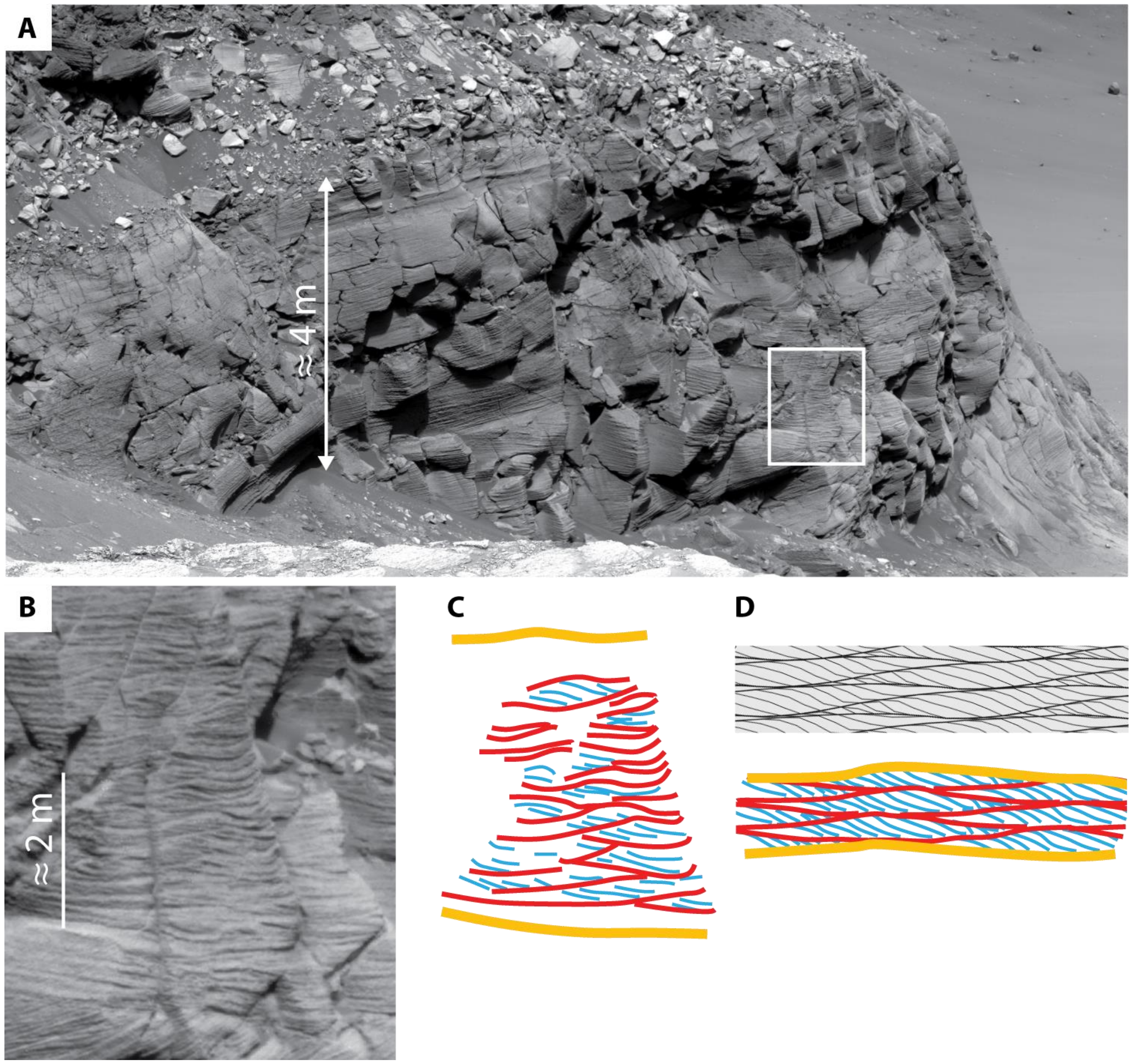

Figure 6.4: Candidate wind-drag ripple stratification on Mars. (A) Mars Exploration Rover Panoramic Camera [*Arvidson et al.*, 2006] image (P2441, sol 1212) of Cape St Mary outcrop, Victoria crater, Mars. White box shows location of (B) decimeter-scale trough cross-strata, and (C) interpretation of stratal features from (B). (D) Uninterpreted (top) and interpreted (bottom) stratification produced by geometric modeling of compound bedforms [*Rubin and Carter*, 2005]. Yellow lines represent surfaces scoured by dune troughs, red lines represent erosional surfaces produced by migration of wind-drag ripples, and blue lines indicate wind-drag ripple cross-stratification.

5. Materials and Methods

5.1. Bedform Compilation

Wavelength data was compiled for Earth and Mars (from orbit and from the ground), and plotted as a Probability Density Function (PDF) to highlight the distribution of bedform wavelengths across all scales. The PDFs were calculated using the kernel density method [*Silverman*, 1981], allowing for the identification of discrete modes. Because the terrestrial dataset was compiled from several studies and our own field and aerial measurements (Section 5.1.1), the relative heights of the ripple and dune modes do not perfectly reflect the area-weighted relative frequency of ripples and dunes. Nevertheless, the natural scale of terrestrial bedforms is well known and is such that there are orders of magnitude more ripples than dunes per unit surface area. While we did not count the entire population of dunes, transverse aeolian ridges (TARs, after the alternative spelling “Transverse Aeolian Ridges”), and ripples across the martian dune fields from orbit, a counting technique was designed to give a fair representation of the density of bedforms per unit surface area (Section 5.1.2), such that the relative heights of peaks in the martian orbital PDF (Figure 6.2B) give a fair representation of the relative frequencies of the different bedforms. All bedforms were measured from the rover dataset, such that Figure 6.2C displays relative peak heights that accurately represent the relative density of small and large ripples per unit land area.

5.1.1. Earth

Wavelength data for terrestrial impact ripples and sand dunes was compiled from the published literature [*Wilson*, 1972; *Lancaster*, 1988; *Anderson*, 1990; *Ewing et al.*, 2006; *Ewing and Kocurek*, 2010], and aerial and field measurements from (i) White Sands National Monument, New Mexico, United States, (ii) Algodones Dunes, California, United States, and (iii) the Oceano Dunes, California, United States. Our dataset is available in an ancillary comma separated value (".csv") file (Table 6.6). Dune wavelength data was collected using aerial photographs and satellite images in geographic information system (GIS) software. Measurements were made using the methods of *Ewing et al.* [2006]. Crestline wavelength measurements were manually digitized by creating line features perpendicular between crestlines. Ripple crestline measurements were made in the field using a tape measure stretched perpendicularly across ripple crestlines.

5.1.2. Mars: Orbital Measurements

The active migration of large ripples and dunes has been observed and quantified in many locations on Mars [*Silvestro et al.*, 2010; *Bridges et al.*, 2011; *Chojnacki et al.*, 2011; *Bridges et al.*, 2012; *Silvestro et al.*, 2013; *Ayoub et al.*, 2014; *Chojnacki et al.*, 2015]. Eleven dune fields (Figure 6.5) were selected for analysis based on location at a range of latitudes and elevations on Mars (Table 6.1). These dune fields host a wide variety of bedform scales that include the range of orbitally recognized bedforms on Mars – large ripples, TARs, and dunes. These classifications were discerned visibly from High Resolution Imaging Science

Experiment (HiRISE) [*McEwen et al.*, 2007] imagery (25-50 cm/pixel) based upon prior descriptions of ripples, TARs, and dunes [e.g., *Bridges et al.*, 2012].

Within each dune field a Region of Interest (ROI) that contained at least one dune with superimposed ripples and adjacent Transverse Aeolian Ridges (TARs) was selected. Ripple, TAR, and dune wavelengths were analyzed from HiRISE imagery using ArcGIS software. HiRISE images have a spatial resolution of > 0.25 m, which allows bedforms ~1 m in size to be resolved. In order to obtain a reasonable statistical representation of ripple and TAR wavelengths, 100 points were randomly distributed within the ROI using the ArcGIS Create Random Points tool (Methods found at http://resources.arcgis.com/en/help/main/10.2/index.html#//00170000002r000000). Where the point fell on a ripple or TAR, which was determined visually, two wavelength measurements were made between the bedform on which the point fell and the adjacent bedform crestlines. If a point did not fall on a bedform, no measurement was made. Dune wavelength measurements were made by measuring from crest to crest for a range of dune sizes within the dune field. For each measurement made, a visual interpretation of the type of bedform was noted either as a ripple, TAR, or dune (Table 6.2). Ripples measured within the Bagnold Dune Field were only digitized from High Dune and Namib Dune (e.g., Figure 6.6 and 6.7), both of which were visited by the Curiosity rover. The ROI for the Bagnold Dune Field is small because it only includes these two dunes.

The rationale for selecting random points was to reduce bias in the wavelength measurements that might artificially influence the wavelength distribution of ripples and dunes. Because most ripple wavelength variability occurs by position on the dune [*Ewing et al.*, 2010; *Bridges et al.*, 2012] rather than across the dune field, a relatively small ROI was generated to ensure that a high density of wavelength measurements was distributed across a small number of dunes. Visual inspection of the random point locations confirmed that the points were distributed among the different slopes of the dune and inter-dune areas, and captured a representative sample of ripple and TAR wavelengths. Any systematic differences in ripple or TAR size is averaged out by this technique. Because only a few dunes are contained within a small ROI, the wavelengths of a range of dunes within the dune field containing the ROI, but outside of the ROI, were measured. Our measured distributions of ripple, TAR, and dune wavelengths falls within the typical range reported by previous studies, which used similar manual digitization methods and automated methods [*Ewing et al.*, 2010; *Silvestro et al.*, 2010; 2013]. Bedforms, as measured from orbital data, which cannot distinguish sub-meter bedforms, show two main modes corresponding to meter-wavelength large ripples and hundreds-of-meter wavelength dunes (Figure 6.2B).

The dataset from *Lorenz et al.* [2014] is added to our compilation. The elevation values reported in *Lorenz et al.* [2014] were measured with respect to the Mars Reconnaissance Orbiter reference ellipsoid. These values were corrected to represent elevation with respect to the geoid for consistency with our measurements from MOLA.

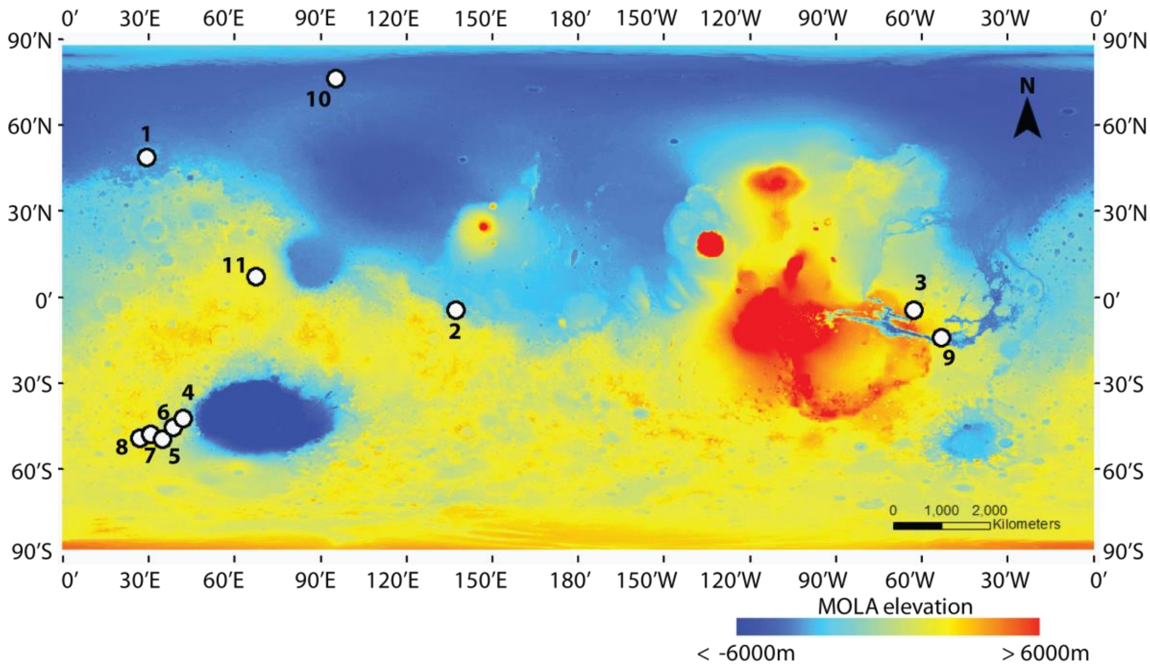

Figure 6.5: **Orbital survey of bedform wavelength.** Locations of bedform wavelength measurements overlain on Mars Orbiter Laser Altimeter (MOLA) color-coded topography. Location numbers correspond to those listed in Tables 6.1 and 6.2.

5.1.3. Mars: Rover Measurements

The Mars Science Laboratory Curiosity rover visited the Bagnold Dune Field (Figure 6.6) and imaged ripples along its traverse. Digital elevation models and orthorectified images were built from Mastcam stereo images (mcam05372, sol 1184). Topographic profiles (Figure 6.9C-D) were measured across the scenes in directions perpendicular to the bedform crest lines, detrended with an order two polynomial, and averaged using a sliding window over 25 points (i.e., a 2.5-cm moving-average, Figure 6.9E). Detrended, smoothed profiles were then compared to the original Mastcam frames to ensure that the measured wavelengths corresponded to actual bedforms. Results are shown in Figure 6.2C. In order to be able to resolve the small ripples, the distance between the rover and the target had to be such that the maximum frame of a Mastcam image was about ~1.5 m wide, a perspective that limited the observation of large ripples and dunes from the ground. Despite these limitations, we were able to measure the wavelengths of both small and large ripples from the ground. The wavelength of all bedforms were measured within each Mastcam frame. The mode corresponding to the large ripples (Figure 6.2C) strongly overlaps with the mode of large ripples as measured from orbit (Figure 6.2B).

Grain sizes were estimated by measuring the intermediate axis of grains from MAHLI images of undisturbed and disturbed surfaces (i.e., grains sitting at and below the surface, respectively), based on the MAHLI pixel size corresponding to the stand-off distance of each given image. Measured grain sizes correspond to very fine (62-125 μm) to medium sand (250-500 μm). The highest resolution MAHLI image (1241MH0005720010403583C00, sol 1241) could not resolve grains below ~30 μm.

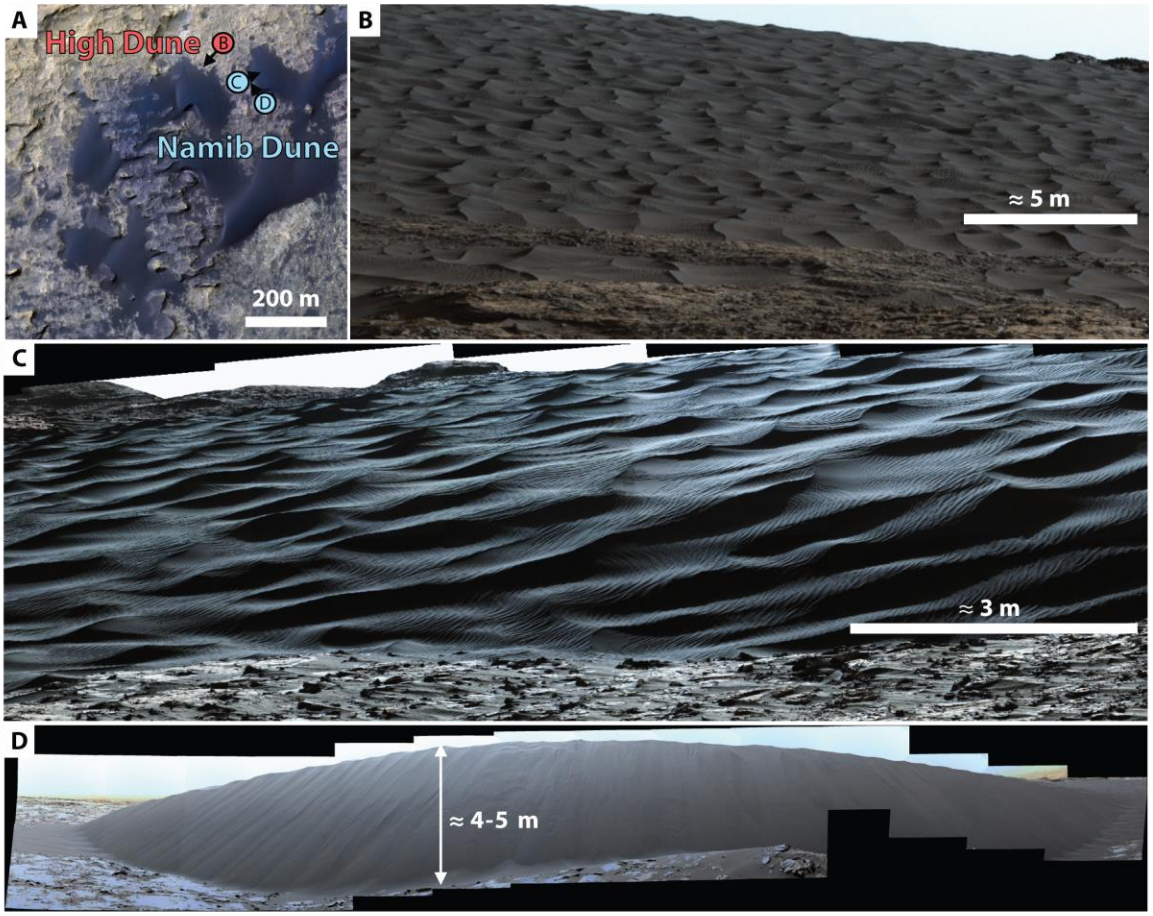

Figure 6.6: Bedforms of the Bagnold Dune Field, Gale crater, Mars, near Curiosity's traverse. (A) HiRISE context map of the Bagnold Dunes (ESP_035917_1755). Dot-and-arrows show rover location and viewing direction of (B) stoss face of High Dune (mcam05301, sol 1169), (C) stoss face of Namib Dune (mcam05392, sol 1190), and (D) secondary lee face of Namib Dune (mcam05496, sol 1200).

5.1.4. Statistical Significance

In order to test that the terrestrial and martian bedform-wavelength distributions are statistically distinct (Figure 6.2A vs. 6.2B and 6.2A vs. 6.2C), we conducted a series of 1000 two-sample Kolmogorov-Smirnov statistical tests for each pair of distributions. Each distribution was first subsampled to a sample size of $n = 40$ using a Metropolis-Hastings algorithm. The null hypothesis "the two samples were drawn from the same distributions" was rejected at the 95% confidence level in > 99% of cases for Earth vs. Mars orbital and Mars rover datasets, respectively.

To further characterize the statistical similarity of individual modes, we (i) subsampled the probability distributions ($n = 40$) using a Metropolis-Hastings algorithm, (ii) calculated kernel density of the subsampled distributions [*Silverman*, 1981], and (iii) identified their modes through a local-maxima-detection routine. This procedure was completed 10 times for each dataset to build a distribution of each individual mode – small terrestrial ripples, terrestrial dunes, large martian ripples from orbit, martian dunes from orbit, small martian ripples from the ground, and large martian ripples from the ground. We then conducted a two-sample Kolmogorov-Smirnov test for each individual pair (*p*-values reported in Table 6.3). Importantly, the two highest *p*-values occur in comparisons of terrestrial impact ripples to small martian ripples, and of terrestrial dunes to martian dunes.

5.1.5. Additional Evidence in Favor of the Wind-Drag Hypothesis

Alternative hypotheses for the formation of the large martian ripples are that they are instead (i) TARs, (ii) compound dunes, (iii) coarse-grained ripples, or (iv) impact ripples.

The occurrence of a small fraction of bedforms tens of meters in wavelength (Figure 6.2B) is the signature of TARs [*Balme et al.*, 2008; *Ewing et al.*, 2010; *Bridges et al.*, 2012]. TARs may form as a result of coarse-grain armoring, giant saltation trajectories, or deposition of dust transported in suspension [*Almeida et al.*, 2008; *Balme et al.*, 2008; *Zimbelman*, 2010; *Geissler*, 2014], and are distinct from the large ripples in activity and morphology: (i) activity of TARs has not been detected [*Bridges et al.*, 2013; *Chojnacki et al.*, 2015], (ii) their wavelengths are generally larger and more widely distributed (e.g., Table 6.2), (iii) they have symmetric topographic profiles [*Zimbelman*, 2010], and (iv) they tend to have a much higher albedo than the dark, active, mafic sands. Thus, the large martian ripples are distinct from TARs.

As seen in Figure 6.7, the bedforms on the stoss of the large dunes do not grow in size as they migrate up the stoss slope, unlike small compound dunes on Earth (Figure 6.8). It was shown that, in places, the wavelength of the large martian ripples may weakly increase or decrease upslope due to local variations in grain size or wind speed [*Vaz et al.*, 2014], although no consistent increase in height and wavelength upslope is observed, contrary to terrestrial compound dunes [*Ewing and Kocurel*, 2010]. Thus, the large martian ripples are distinct from compound dunes.

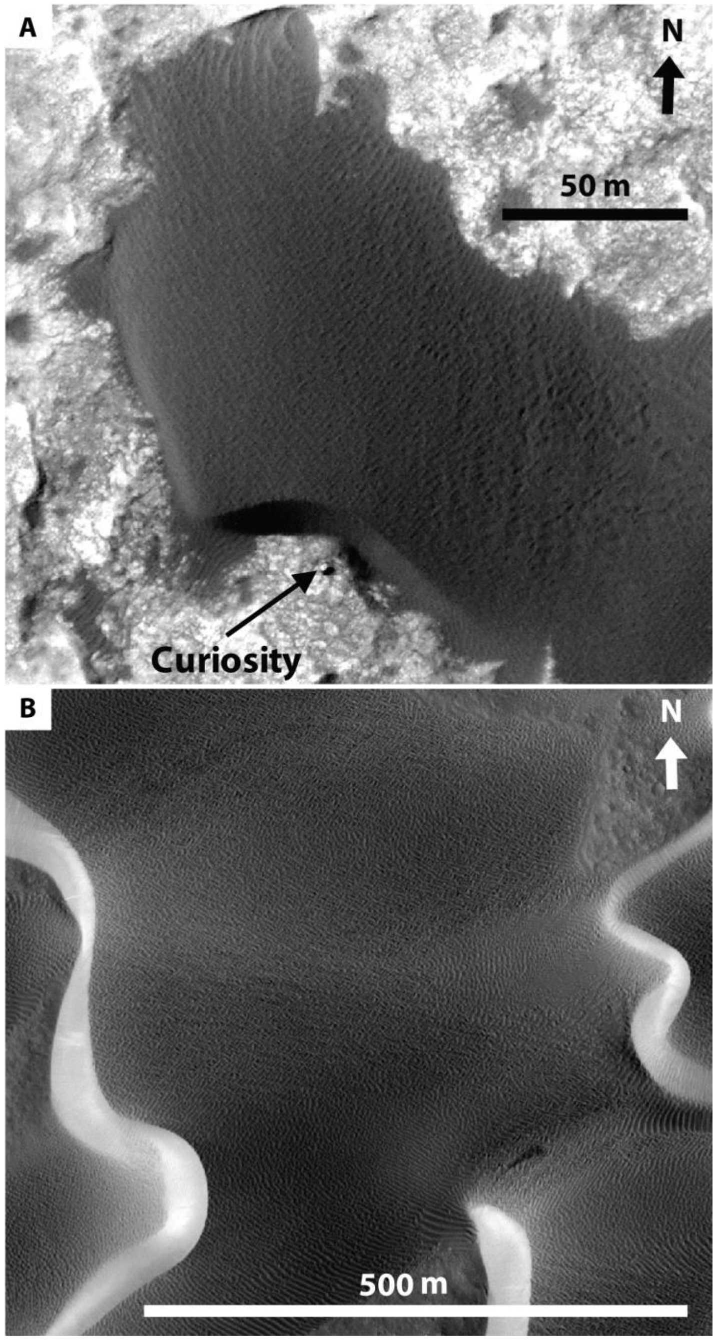

Figure 6.7: Curiosity at Namib Dune, Gale crater, Mars. (A) HiRISE image (ESP_044172_1755, 29 Dec. 2015/sol 1207) of Namib Dune, Gale crater. Figure 6.6D is a panoramic view from the rover location shown in (A). (B) HiRISE image (ESP_038214_1875) of larger dunes at Nili Patera showing that the large ripples do not grow in size up the stoss of their host dune, contrary to compound dunes on Earth (e.g., Figure 6.8). Dune in (B) is about the same size as the dune shown in Figure 6.8.

It is important to evaluate whether the large ripples are composed of coarse grains, which are expected to produce meter-wavelength ripples, known as megaripples or granule ripples, without the need for the wind-drag mechanism. Coarse-grained ripples on Earth typically form in grains larger than about a millimeter up to several centimeters [e.g., Sharp, 1963; Jerolmack *et al.*, 2006; *de Silva et al.*, 2013; *Bridges et al.*, 2015]. Such coarse-grained ripples were observed on Mars by the Spirit rover at “El Dorado” in Gusev crater [*Sullivan et al.*, 2008], and by the Curiosity rover at the base of the stoss slope of “High Dune” in Gale crater, as expected at the upwind margin of a dune field [*Sweet et al.*, 1988]. The vast majority of large martian ripples, however, appear distinct from megaripples in that surface armoring from large grains does not appear to play a role in their formation. In contrast, the armored megaripples at the base of High Dune are expected because the observed ripples sit at the upwind, trailing margin of the dune field [*Bagnold*, 1941] and at the change in slope from the inter-dune area to the stoss slope. The upwind margin concentrates coarse grains, and the abrupt increase in slope onto the stoss side limits the upslope transport of the coarsest grains, which results in a lag deposit. However, the armored ripples give way to well-sorted ripples of very fine to medium sand up the stoss slope toward the dune crest with the morphologic features we described for large ripples (e.g., Figure 6.1D and E). Another observation that suggests that coarse grains are not responsible for the formation of the large ripples is that these bedforms cover the majority of imaged aeolian dunes on Mars, which would require a mechanism that promotes the creation of lag regardless of initial grain-size distributions. In other words, the well-sorted sand that is expected to comprise the dunes, especially on dune lee faces and in the middle of a dune field far from the source area, would have a lag surface or coarse crest. Rather, as lag deposits, coarse-grained ripples should only occupy a fraction of a dune field, consistent with observations of large martian ripples juxtaposed to what are likely true coarse-grained ripples in several locations on Mars [*Ewing et al.*, 2010]. Thus, large martian ripples are distinct from coarse-grained ripples.

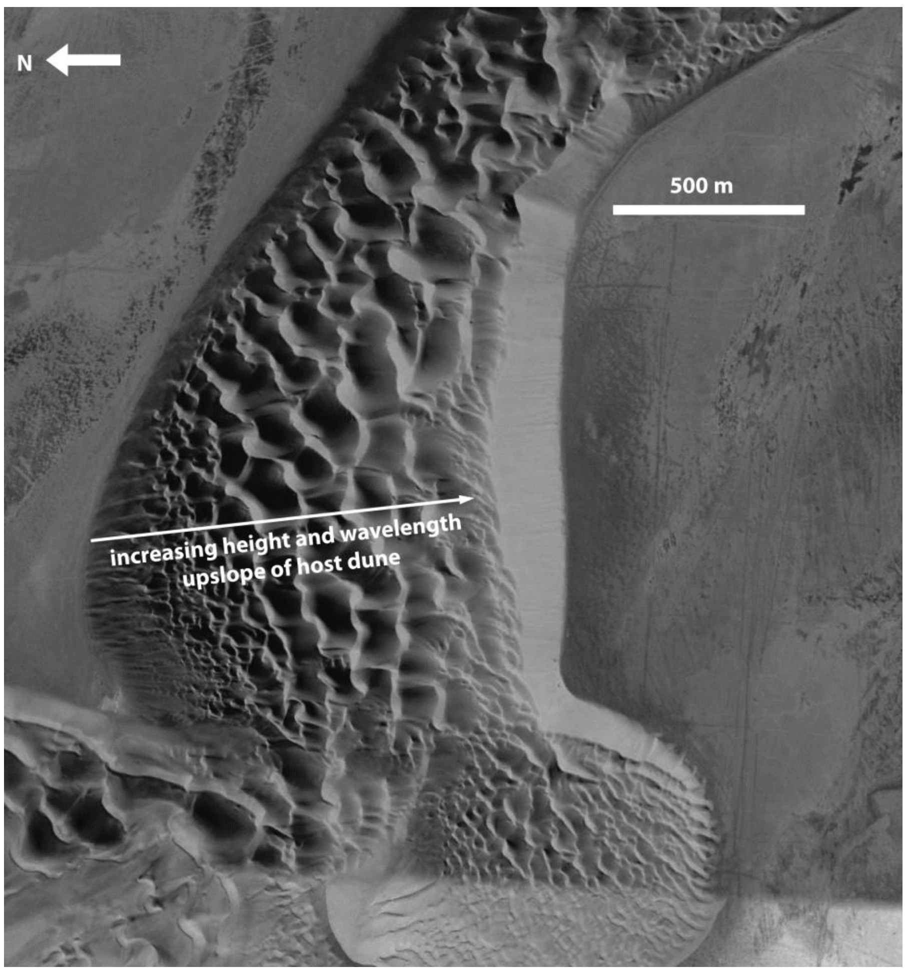

Figure 6.8: Compound dunes on Earth. Compound dunes growing upslope of their host dune, Rub'al Khali, Saudi Arabia. Illumination is from the SE (source: Google Earth; 22.298299 N, 54.172680 E).

The last alternative hypothesis is that the large martian ripples are impact ripples. In order to be a viable hypothesis, an impact mechanism has to (i) be able to generate meter-scale ripples, (ii) allow for two stable and active scales of impact-ripples, and (iii) reproduce the observed morphologies. While some numerical models are able to produce meter-scale impact ripples, they require wind shear velocities at or above the fluid threshold for saltation [e.g., *Durán et al.*, 2014]. Other modeling studies that are able to reproduce transport hysteresis, i.e., to recreate the lowered impact threshold relative to the fluid threshold, predict the formation of decimeter-scale impact ripples for shear velocities above the impact threshold but below the fluid threshold [e.g., *Yizhaq et al.*, 2014], more consistent with our observations of decimeter-scale ripples. However, none of the published models are able to reproduce two superimposed scales of active impact ripples that are stable under the same wind conditions. An experimental study [*Andreotti et al.*, 2006] showed that equilibrated impact ripples subjected to a change in wind conditions either adjust their wavelength if the wind perturbation is large, or adjust their height. Thus, two different wavelengths could possibly be observed together, but one of the two bedform populations would have to be relict. In our case, the relict bedform would necessarily be the large ripples, otherwise, their migration would quickly rework and erase the decimeter-scale ripples. However, observations that large ripples migrate seasonally [*Ayoub et al.*, 2014], that grainflows onlap onto small ripples, and that the small ripples do not rework the crest of large ripples (e.g., Figure 6.1C), each illustrate that both scales of ripples are actively forming and migrating at the same time, under similar wind conditions. Finally, the observed morphologies are inconsistent with an impact mechanism. Terrestrial impact ripples have straight crests due to lateral grain splash. Although large ripples migrating down the sloped flanks of martian dunes appear to have relatively straighter crests (Figure 6.7), their relative two-dimensionality arises from gravity-driven, along-crest transport [*Rubin*, 2012], and large ripples migrating up the stoss slopes of their host dunes are clearly sinuous (see also *Silvestro et al.*, 2016, and *Vaz et al.*, 2016, for a discussion of longitudinal large ripples). Furthermore, the impact mechanism does not promote the formation of angle-of-repose slip faces that extend from ripple brink to base as observed in some large martian ripples. Rather, impact ripples typically show short near-angle of repose slopes at the brink, which quickly give way downslope to lower angled slopes [*Sharp*, 1963; *Werner et al.*, 1986].

5.2. Parameter Calculation for the Earth and Mars Aeolian Ripples Data

In order to estimate the particle Reynolds number, $\mathrm{Re}_p = \frac{u_* D}{\nu}$ (in which u_* is the shear velocity, D is the grain size, and ν is the kinematic viscosity of the fluid), and Shields stress, $\tau_* = \frac{u_*^2}{\sqrt{RgD}}$ (in which $R = \frac{\rho_s - \rho_f}{\rho_f}$ is the submerged reduced density of the sediment, ρ_s and ρ_f are the sediment grain and fluid densities, and g is the acceleration of gravity), for the formation of bedforms on Earth and Mars, typical bed shear velocities, atmospheric densities and viscosities, and grain densities and sizes need to be constrained.

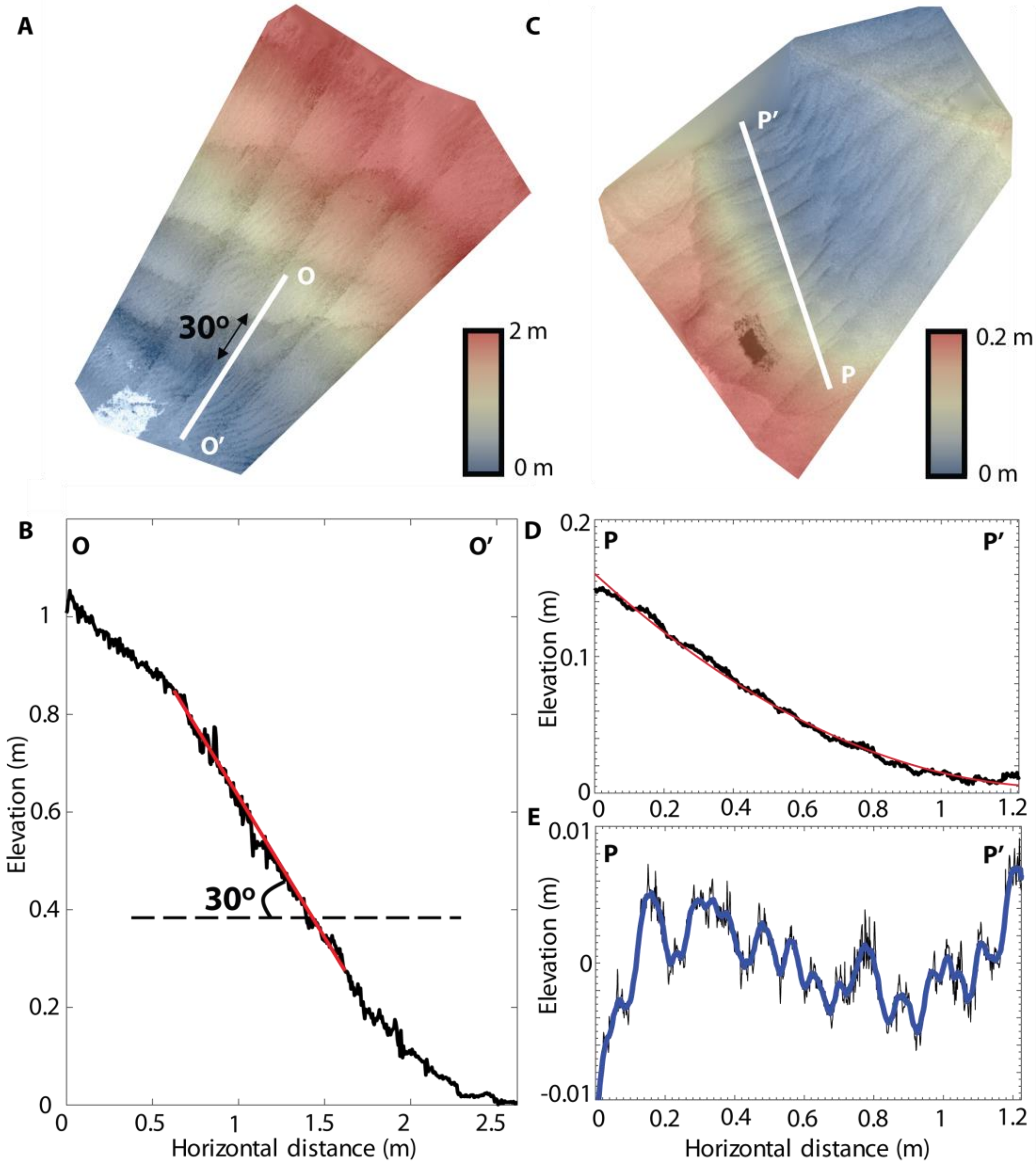

Figure 6.9: Rover measurements. (A) Digital elevation model (DEM) built from the Mastcam stereo pair mcam05418 (sol 1194) with elevation color-coded. White line indicates location of the profiles shown in (B). (B) Topographic profile across a large ripple. Red line represents a linear fit to the angle-of-repose slip face of the large ripple. (C) DEM built from the Mastcam stereo pair mcam05372 (sol 1184) with elevation color-coded. White line indicates location of the profiles shown in (D). (D) Example topographic profile across small ripples. Red line represents a second order polynomial fit used to calculate (E) a corresponding detrended profile. The blue line represents a detrended profile that was smoothed using a 25-point (i.e., 2.5 cm window) moving-average to facilitate bedform identification.

5.2.1. Earth

In order to compare fluid-drag theory to observed terrestrial ripples, we use the dataset of *Wilson* [1972] for grain size and ripple wavelength. We estimated shear velocity through the impact threshold shear velocity, u_{*it}^{Earth}, from grain size, D, based on a fit to field data from [*Bagnold*, 1937; *Chepil*, 1945; *Iversen and Rassmussen*, 1999; *Li and McKenna Neuman*, 2012] compiled in *Kok et al.* [2012],

$$\begin{aligned} u_{*it}^{\text{Earth}} = \exp\Big[& 4.081\times10^{-2}\log(D)^4 + 1.237\log(D)^3 \\ & +13.98\log(D)^2 + 70.35\log(D) + 132.6\Big] \qquad (\text{R}^2 = 0.9976) \end{aligned}. \tag{6.2}$$

We assumed a constant atmospheric density of $\rho_f \approx 1.27$ kg/m^3, a kinematic viscosity of $\nu \approx 1.4\times10^{-5}$ m^2/s, an acceleration of gravity of $g \approx 9.81$ m/s^2, and a quartz density for the grains of $\rho_s \approx 2650$ kg/m^3.

Figure 6.11 illustrates that the range of wavelengths covered by terrestrial aeolian ripples overlaps with the fluid-drag ripple predictions, such that wind-driven fluid-drag ripples (or “wind-drag ripples”) may in fact occur on Earth (e.g. as suggested by *Bagnold*, 1941, and *Wilson*, 1972), but are rarely recognized, possibly because their sizes should be similar to impact ripples. This overlap in scales between impact and fluid-drag aeolian ripples is not expected on Mars, however.

5.2.2. Mars

Most sand transport on Mars likely occurs close to the threshold bed shear velocity required to sustain saltation [*Kok*, 2010b], a value referred to as the impact threshold velocity, u_{*it}. On Earth, the impact threshold is typically 80% of the fluid threshold value, while on Mars, the impact threshold is thought to be up to an order of magnitude lower than the fluid threshold [e.g., *Kok et al.*, 2012]. In order to compare the measured wavelength of martian aeolian bedforms to predictions from fluid-drag theory (Figure 6.3), we set the wind shear velocity to be equal to the impact threshold (i.e., $u_* = u_{*it}$), which is a function of atmospheric pressure, temperature, and grain size.

We calculated impact threshold bed shear velocity, u_{*it}^{Mars}, from grain diameter, D, surface pressure, p, and temperature, T, from the best fit relationship derived by *Kok* [2010b],

$$u_{*it}^{\mathrm{Mars}} = 5.5\times10^{-3}\left(\frac{700\mathrm{Pa}}{p}\right)^{1/6}\left(\frac{220\mathrm{K}}{T}\right)^{2/5} \exp\left[\left(\frac{49\mu\mathrm{m}}{D}\right)^{3} + \left(0.29\mu\mathrm{m}^{-1/2}\right)\sqrt{D} - \left(3.84\times10^{-3}\mu\mathrm{m}^{-1}\right)D\right]. \qquad \mathbf{(6.3)}$$

We consequently needed to estimate D, p, and T. The Opportunity rover measured sizes of mafic sand particle grains of ~ 50-150 μm at Eagle crater [*Soderblom et al.*, 2004], while Spirit measured coarser grain sizes, up to ~ 200-300 μm at El Dorado [*Sullivan et al.*, 2005]. Grain sizes measured by Curiosity at the Namib Dune are typically ~ 200-300 μm (Figure 6.1F). We thus assumed a grain size value of 200 μm. Note that the robustness of the match between the data and the scaling predictions are nearly independent of grain size. We estimated pressure from the elevation, z, of ripple wavelength measurements assuming a constant atmospheric scale height

$$p(z) = \left(610\mathrm{Pa}\right)\exp\left[\frac{-z}{11.2\mathrm{km}}\right], \tag{6.4}$$

consistent with the atmospheric entry profiles of the Mars Exploration Rover missions [*Withers and Smith*, 2006]. We further assume an isothermal atmosphere of $T = 227$ K, a thermal profile suggested by the atmospheric entry profiles of *Withers and Smith* [2006] within the range of elevations covered by the ripple wavelengths measurements. The results are not particularly sensitive to the lapse rate we use to calculate $T(z)$; the R^2 value of the fit for $\lambda^* \propto \left(\mathrm{Re}_p \sqrt{\tau_*}\right)^{1/3}$ when the martian large ripple data are included ranges from 0.9295 to 0.9312 with lapse rates of 0 (isothermal atmosphere; *Withers and Smith*, 2006) to -3.7 K/km, a value consistent with the Viking Lander 1 measurements [*Seiff and Kirk*, 1977].

We estimated atmospheric density at the elevation of the ripples through the ideal gas law

$$\rho_f(z) = \frac{M_{\mathrm{CO_2}}}{r}\frac{p(z)}{T(z)}, \tag{6.5}$$

where $M_{\mathrm{CO_2}}$ is the molar mass of carbon dioxide, and r is the ideal gas constant. We estimated the kinematic viscosity of the atmosphere at elevation z through

$$\nu(z) = \frac{\mu}{\rho_f(z)}, \tag{6.6}$$

where the dynamic viscosity of the atmosphere is assumed to be constant and equal to $\mu \approx 10.8\times10^{-6}$ Pa.s. Finally, reduced gravity was calculated by setting $g \approx 3.78$ m/s^2 and assuming a basaltic density for the grains ($\rho_s \approx 2900$ kg/m^3).

5.3. Current Ripples: Scaling from Flume Experiments

A morphologic characteristic of subaqueous ripples is their often asymmetrical topographic profile (e.g., Figure 6.10). They typically have gentle slopes upstream of a sharp ripple crest, and a near-angle-of-repose slip face downstream. They are often sinuous, and their crest-to-crest wavelength varies with flow and grain properties.

We build on the data compilation of *Yalin* [1985], who compiled flume experiment data from *Barton and Lin* [1955], *Vanoni and Brooks* [1957], *Vanoni and Hwang* [1967], and *Alexander* [1980], which comprise experiments with sand and glass beads of sizes ranging from 105 to 260 μm, where the fluid was either water or glycerine and water solutions. The analysis in *Yalin* [1985] collapsed the ripple wavelength data into a parameter space $X_Y = 3.38\,\mathrm{Re}_p^{1/2}\,\tau_*^{1/4}$ in abscissa and $Y_Y = \dfrac{\lambda}{3.38D}\dfrac{\mathrm{Re}_p^{1/2}}{\tau_*^{1/4}}$ in ordinate, where $\mathrm{Re}_p = \dfrac{u_* D}{\nu}$ is the particle Reynolds number, and $\tau_* = \dfrac{u_*^2}{RgD}$ is the Shields stress (Section 5.2). Nondimensionalization allows for the same information to be recast in multiple non-unique ways, depending on the preferred dimensionless variables. Here we chose to recast the variables of X_Y and Y_Y of *Yalin* [1985] into a more intuitive coordinate system following more recent work on bedform stability [*Southard and Boguchwal*, 1990a; *van den Berg and van Gelder*, 1993; *Lamb et al.*, 2012a]. Thus, we operated the following mapping on the data compilation:

$$\begin{cases} x = \dfrac{X_Y^2}{11.42} = \mathrm{Re}_p \sqrt{\tau_*} \\ y = \lambda^* = X_Y Y_Y = \dfrac{\lambda}{D} \mathrm{Re}_p = \dfrac{\lambda u_*}{\nu} \end{cases}, \tag{6.7}$$

where $(\mathrm{Re}_p \sqrt{\tau_*}, \lambda^*)$ reflects our new coordinate system. The ordinate λ^* is analogous to a nondimensional wavelength, where the normalization factor is proportional to the thickness of the viscous sublayer, consistent with previous theory [*Yalin*, 1977; *Raudkivi*, 1997; *Garia*, 2008]. Based on limited data at low values of $\mathrm{Re}_p \sqrt{\tau_*}$, *Yalin* [1985] hypothesized that λ^* was a constant at low $\mathrm{Re}_p \sqrt{\tau_*}$, i.e., that ripple wavelength was proportional to the thickness of the viscous sublayer. We expanded the parameter space by adding the data of *Grazer* [1982], which was previously analyzed as analogs to ripples formed by viscous brines on Mars [*Lamb et al.*, 2012a]. The data from *Grazer* [1982] was extracted from their Tables 5-10 (pp. 124-129). The experiments used silt sizes of about 21 to 115 μm and water-sucrose solutions with kinematic viscosities ranging from

6×10^{-7} to 1.05×10^{-5} m^2/s to explore very small particle Reynolds numbers and thick viscous sublayers.

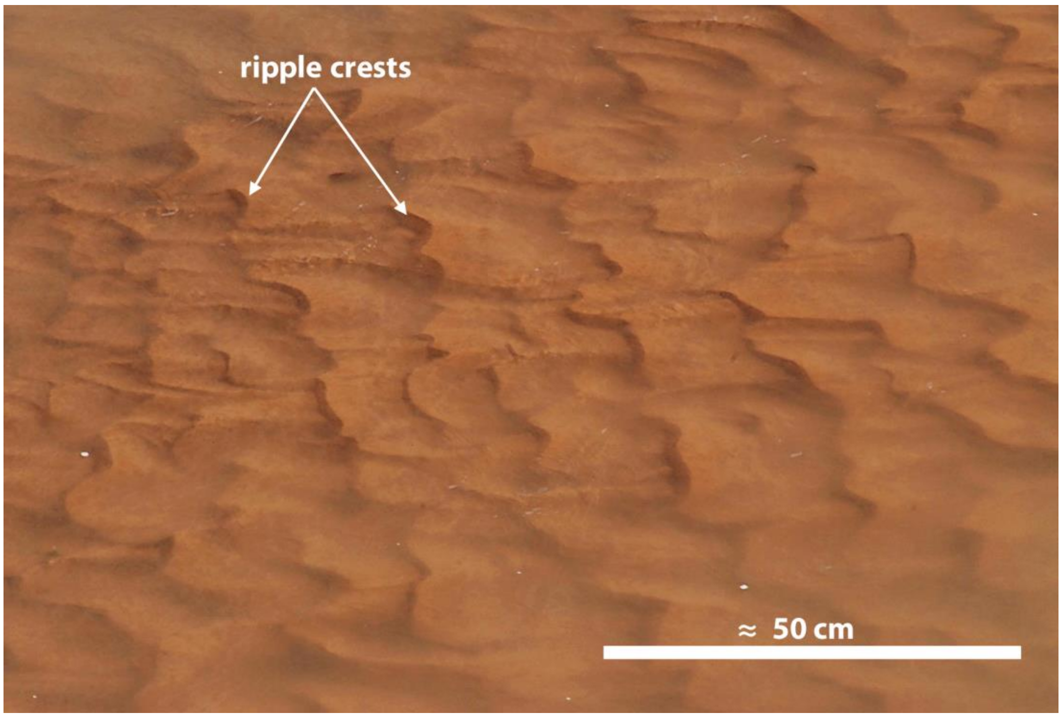

Figure 6.10: Current ripples on Earth. Subaqueous ripples in fine-to-medium sand, in a modern stream near the Canyon de Chelly, Arizona, United States (approximately 36.13 N, -109.46 E). Flow is from the top right corner.

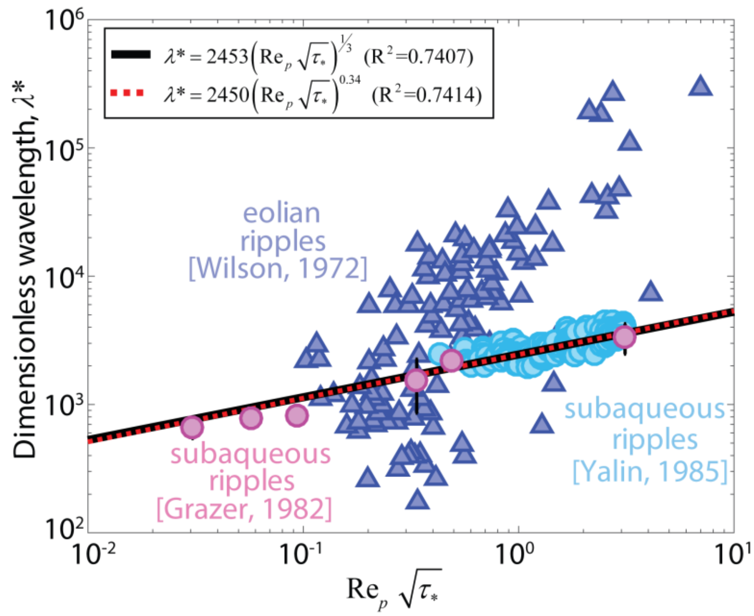

Figure 6.11: Fluid-drag theory. Flume data and aeolian impact ripples compilation recast in terms of dimensionless wavelength $\lambda^* = \dfrac{\lambda u_*}{\nu}$ and $\mathrm{Re}_p\sqrt{\tau_*}$ [*Wilson*, 1972; *Grazer*, 1982; *Yalin*, 1985]. The red dashed line is the best fit power law to all current-ripple data of *Grazer* [1982] and *Yalin* [1985]. The black line is the best fit power law to all current ripple data of *Grazer* [1982] and *Yalin* [1985] using the rationale exponent of 1/3.

Figure 6.11 shows the data of *Grazer* [1982] and *Yalin* [1985] plotted in the new coordinate system, and indicates that dimensionless wavelength, from both datasets, increases with $\mathrm{Re}_p\sqrt{\tau_*}$, inconsistent with the constant dimensionless wavelength hypothesized by *Yalin* [1985]. Because the former study did not distinguish between ripples and dunes, we filtered the sandy bedforms by overlaying the data on the bed stability diagram of *Lamb et al.* [2012a], which itself is a compilation from *Southard and Boguchwal* [1990a] and *van den Berg and van Gelder* [1993]. The bedform stability diagram is a well-accepted phase space that incorporates thousands of observations, and allows one to distinguish ripples from dunes and lower and upper plane bed regimes. The stability diagram itself can be cast in terms of Re_p and τ_*, which allows the ripples in our data compilation to be segregated from other bed states. The best fit power law relationship to the flume data of *Grazer* [1982] and *Yalin* [1985] for current ripples is

$$\lambda^* = 2450\left(\mathrm{Re}_p \sqrt{\tau_*}\right)^{0.34} \quad (\mathrm{R}^2 = 0.7414). \tag{6.8}$$

The best fit exponent of 0.34 is very close to the rational number 1/3. When the exponent is forced to be equal to 1/3, the best fit relationship to the flume data becomes

$$\lambda^* = 2453\left(\mathrm{Re}_p \sqrt{\tau_*}\right)^{1/3} \quad (\mathrm{R}^2 = 0.7407). \tag{6.9}$$

The relationship in Equation (6.9) implies that

$$\lambda = 2453 \frac{\nu^{2/3} D^{1/6}}{(Rg)^{1/6} u_*^{1/3}}. \tag{6.10}$$

Equation (6.10) is in agreement with the predictions of *Middleton and Southard* [1984], *Boguchwal and* Southard [1990], Southard *and* Boguchwal [1990b], and Lamb *et al.* [2012a], and shows that the wavelength of ripples should scale with kinematic viscosity to the power 2/3. Moreover, most flume experiments suggest that there is a weak correlation between ripple spacing and grain size [e.g., *Raudkivi*, 1997; *Baas*, 1999]. Equation (6.10) also predicts that ripple wavelength decreases with reduced gravity and transport stage—relationships that are in agreement with flume data [*Southard and Boguchwal*, 1990b].

5.4. Paleoatmospheric Reconstruction from Martian Outcrops

5.4.1. Technique

The geometry of cross-stratification in sedimentary rocks is a function of the morphology of bedforms, their migration direction, and the rate of net sediment accumulation. In order to anticipate the stratigraphic signature of wind-drag ripples, we employed an algorithm that uses dozens of two-dimensional sine functions to simulate morphology of bedform assemblages, and then moves that evolving morphology through hundreds of steps through time [*Rubin and Carter*, 2005]. To model the martian large ripples, we began with the input values used for Figure 65 of *Rubin and Carter* [2005], changed the superimposed bedforms from dunes to large ripples by reducing their height and wavelength, increased the migration speed of the superimposed large ripples relative to the main dunes as is physically reasonable for smaller bedforms, adjusted the migration direction of the large ripples from directly downslope to obliquely downslope, selected an outcrop orientation through the stratification that most closely reproduced the observed outcrop, and decreased the density of lines in the image to keep them from bleeding together. Results from this modeling exercise suggest that wind-drag ripple cross-stratification would occur in trough cross-sets with preserved foresets bounded by erosional surfaces associated to the wind-drag ripples, themselves bounded by dune-trough scour surfaces.

Theoretical and empirical studies show that subaqueous ripples and dunes, even in the case of zero net deposition, produce cross-sets with thicknesses up to half of the original bedform height, and lengths about half of the original bedform wavelength [*Allen*, 1973; *Paola and Borgman*, 1991; *Leclair*, 2002]. Consequently, a 30 cm high wind-drag ripple could produce a ~15 cm thick cross-set if typical subaqueous preservation ratios hold. Transverse aeolian dunes typically preserve less than 10% of the total bedform height [*Rubin and Hunter*, 1982], although this ratio may be much higher for superimposed dunes, up to 100%. In the following, we illustrate how the ripple wavelength scaling relationship can be used to reconstruct the paleo-atmospheric density from measurements of cross-set thicknesses within the Stimson formation at the Apikuni Mountain section at Marias Pass (Figure 6.12), Gale crater (Figure 6.13).

In order to reconstruct atmospheric density from the thickness of cross-sets, one needs to (i) estimate bedform height from the set thicknesses by assuming a preservation ratio, (ii) estimate bedform wavelength from bedform height, and (iii) solve for atmospheric density based on bedform wavelength using a best fit to our scaling relationship.

In order to place an upper bound on paleo-atmospheric density, we assume a preservation ratio of 100%. Thus, 10-20 cm-thick cross-sets such as those observed at Apikuni Mountain by Curiosity must have been created by the migration of wind-drag ripples with heights of at least ~10-20 cm. Subaqueous and aeolian ripples and dunes have height-to-wavelength ratios ranging from ~0.01 to ~0.1 [e.g., *Guy et al.*, 1966; *Ellwood et al.*, 1975; *Raudkivi*, 1997]. To estimate a conservative upper bound on paleo-atmospheric density, we assume a height-to-wavelength ratio of 0.1, i.e.,

$$\frac{\eta}{\lambda} \approx 0.1, \tag{6.11}$$

where η is the ripple height. Thus, the observed cross-sets must to have been created by wind-drag ripples of wavelengths greater than 1 m. Finally, to take into account the scatter associated with measured wavelengths of wind-drag ripple on Mars, we fit the experimental flume data combined with the martian wind-drag ripple measurements. We find the best fit to be

$$\lambda = 2777 \frac{\nu^{2/3} D^{1/6}}{(Rg)^{1/6} u_*^{1/3}} \tag{6.12}$$

with a coefficient of determination R^2=0.89, a relationship that is virtually undistinguishable from the best fit relationship resulting from the terrestrial data alone (Equation (6.9)). The 2777 factor has a 95% confidence interval of 2615 to 2948.

Figure 6.14 shows how the predicted wavelength λ of wind-drag ripples from Equation (6.12) varies with atmospheric density, and that measured wavelengths of modern large ripples roughly follow the predictions. Figure 6.14 was generated assuming a grain size of 200 μm, grain density of 2900 kg/m^3, atmospheric dynamic viscosity of 10.8×10^{-6} Pa.s, gravitational acceleration of 3.78 m/s^2. Bed shear velocity was assumed to be equal to the impact threshold and calculated as a function of atmospheric density following the semi-analytical formulation of *Kok* [2010b] (all parameter values are summarized in an ancillary ".csv" file, Tables 6.4-6.5). Different atmospheric densities are found under modern conditions due to the wide range in elevation over which bedform-wavelength measurements were made. The ripple measurements of *Lorenz et al.* [2014] were made in the light-toned dusty Tharsis region, while our dataset was acquired over dark mafic sand dune fields. Both datasets show a consistent decrease of ripple wavelength as a function of atmospheric density, but are offset from one another. The offset between the two datasets might arise from (i) model assumptions that are inexact, e.g., wind shear velocities may not be at the threshold value for transport; (ii) differences in particle size and density, e.g., coarse low-density dust aggregates which may be representative of the bed on the Tharsis Montes [*Lorenz et al.*, 2014] would form smaller ripples than in mafic sand; or (iii) an easier detection of smaller ripples in light-toned material due to a higher contrast between the shadows cast by ripple crests and the bed, such that measurements in dark mafic sands are skewed to slightly larger wavelengths. Most large ripples observed in situ by the Curiosity rover at Gale crater have wavelengths closer to ~ 1.5 meter (Figures 6.3 and 6.14). Bed shear velocities are likely to be increasingly larger than the impact threshold as atmospheric density increases, an effect that is not taken into account in this formulation. Conversely, while the wavelength of large ripples is expected to increase with elevation, we expect ripples to cease forming at the elevation at which atmospheric density becomes too low to generate winds that surpass the impact threshold. However, large ripples are observed up to the top of Olympus Mons, suggesting that such a threshold in atmospheric density is not reached at the surface of Mars.

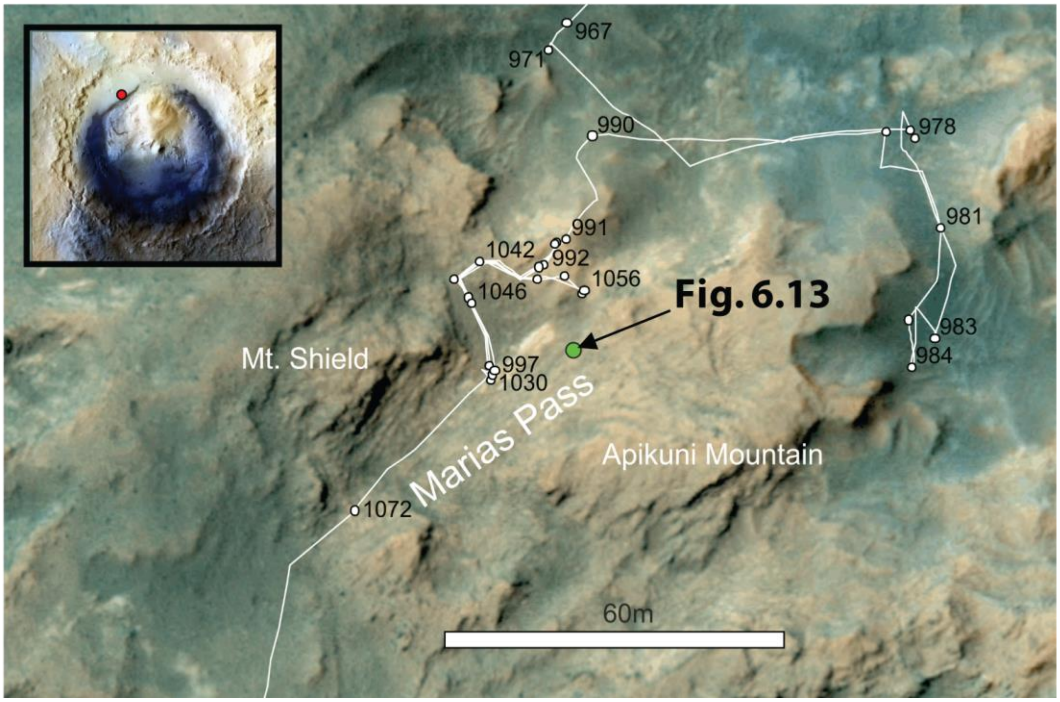

Figure 6.12: Location of the Apikuni Mountain outcrop, Gale crater, Mars. Context map (HiRISE color mosaic, location shown in inset; image credit: JPL-Caltech/University of Arizona) with Curiosity rover traverse overlain (white line) near the Apikuni Mountain section at Marias Pass, Gale Crater, Mars. White circles represent rover locations by sol (adjacent numbers). The green dot indicates location of Figure 6.13. Gale crater (inset) is about 150-155 km in diameter.

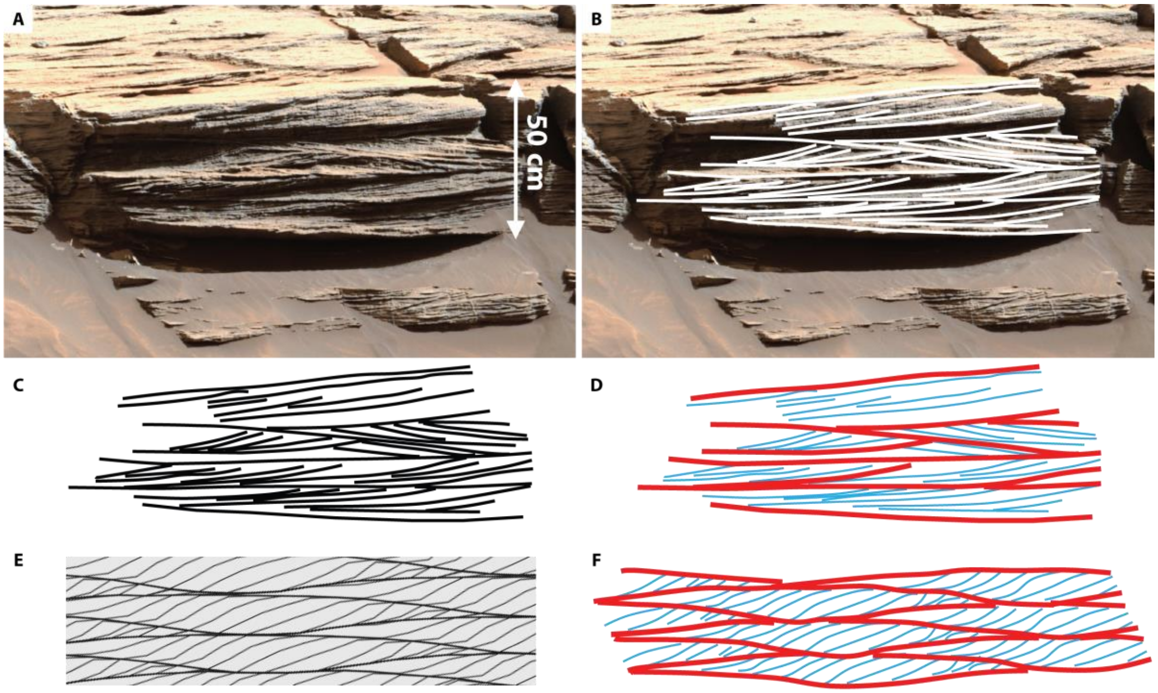

Figure 6.13: Trough cross-stratification in the Apikuni Mountain section of the Stimson formation, Gale crater, Mars. (A) Mastcam image (mcam04395, sol 993) of decimeter-scale trough cross-stratification in the Apikuni Mountain section of the Stimson formation, near Marias Pass, Gale Crater. (B) Interpretation of cross-set geometry overlain on Mastcam image from (A). (C) Uninterpreted stratal features from (B) alone, and (D) interpretation of stratal features from (A). (E) Sketch of expected preserved stratification produced by wind-drag ripples generated using the algorithm of *Rubin and Carter* [2005], and (F) corresponding interpreted stratigraphy. Thick red lines represent erosional surfaces produced by the migration of scours in front of wind-drag ripple lee faces. Thin blue lines indicate wind-drag ripple foreset cross-stratification.

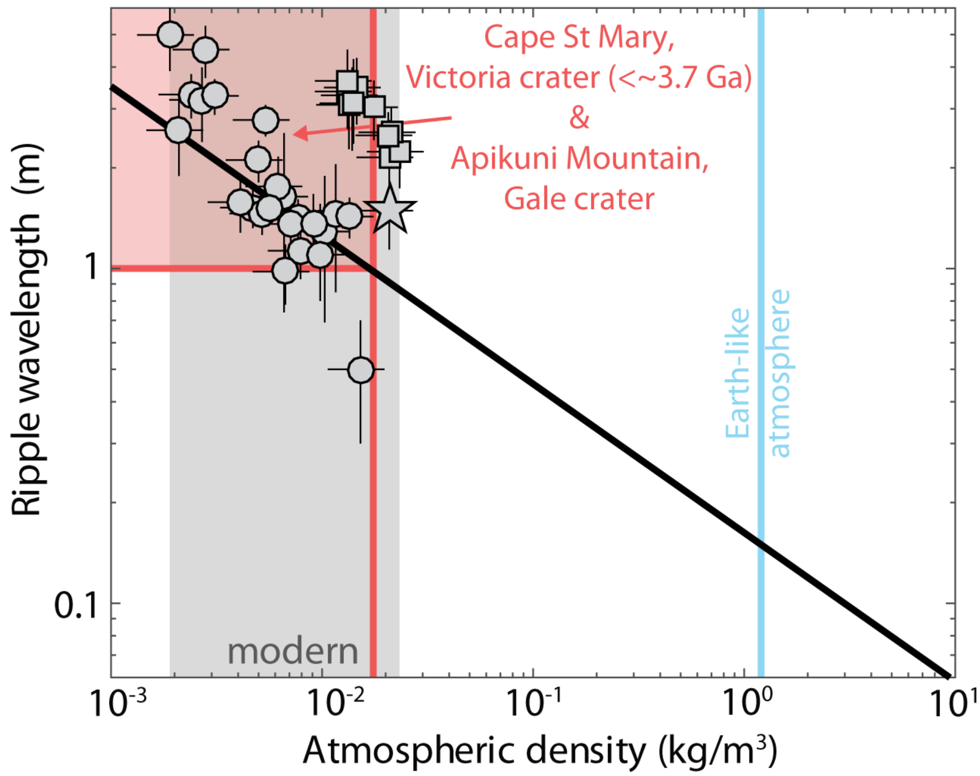

Figure 6.14: Wavelength of wind-drag ripples on Mars as a function of atmospheric density. Predicted wavelength of wind-drag ripples as a function of atmospheric density (black line). Gray circles [*Lorenz et al.*, 2014], squares (this study, orbital) and the star (this study, in situ at Gale crater) represent measured modern large ripples on Mars. Vertical error bars show ± 1σ on the wavelength measurements at each given site; horizontal error bars correspond to typical diurnal and seasonal variations in surface atmospheric density of ± 30% the mean value (consistent with measurements at Gale crater, e.g., http://www.jpl.nasa.gov/news/news.php?release=2016-128). The gray box outlines the range in modern atmospheric densities at the surface of Mars, which vary as a function of elevation. The red horizontal line corresponds to the minimum possible ripple wavelength of 1 m inferred from cross-strata at Cape St. Mary in Victoria crater, and Apikuni Mountain in Gale crater; the vertical red line is the corresponding upper bound on paleo-atmospheric density for 1 m wavelength wind-drag ripples.

5.4.2. Cape St. Mary, Victoria Crater

The Opportunity rover observed centimeter-scale trough cross-stratification in sandstones of the Burns formation at Eagle and Erebus craters (Figure 6.4)

[*Grotzinger et al.*, 2005; 2006; *Metz et al.*, 2009], which were interpreted as the signature of subaqueous ripples in a wet inter-dune environment. The fluvial hypothesis was favored to an aeolian origin on the basis of (i) the three-dimensional geometry of the cross-sets, (ii) their scale, and (iii) their paleo-environmental context. These cross-strata are found in sulfate-rich sands of high solubility [*Grotzinger et al.*, 2005], suggesting that shallow subaqueous flows discharged from melt or groundwater as brines of high ionic strength [*Tosca et al.*, 2005; 2011; *Lamb et al.*, 2012a], rather than sourced from meteoric precipitation under a denser atmosphere. We note that in the absence of additional context (grain size and sedimentary structures like soft-sediment deformation and/or desiccation cracks), the interpretation of the small-scale trough cross-sets is non-unique because they could represent the signature of wind-drag ripples formed in a denser atmosphere. However, independent evidence suggesting wet depositional conditions supports the original interpretation [*Grotzinger et al.*, 2006; *Metz et al.*, 2009]. In contrast, later along its traverse, the Opportunity rover found ~10-20 cm-thick cross-sets superimposed on high angle foresets on the south face of the Cape St Mary outcrop at Victoria crater [*Hayes et al.*, 2011] (Figure 6.4). This cross-stratification was interpreted as the signature of out-of-phase sinuous aeolian bedforms, stratigraphically above the Endurance and Erebus craters sections; in this location, no evidence of originally wet conditions was observed. The 10-20 cm-thick trough cross-sets of Cape St Mary have the scale and geometry we infer to be representative of wind-drag ripple cross-sets formed under conditions similar to present-day Mars. Martian impact ripples are too small to produce the observed set thicknesses. The observed geometry arises from the migration of smaller bedforms across the lee slope of a larger, host bedform. Coarse-grained ripples migrate slower than adjacent dunes, and their migration would likely not form repeated sets suggesting high deposition rates like those observed in Figure 6.4B. Grains have not been directly observed at Victoria crater, but were constrained to be of medium-sand size or finer in other sections of the Burns formation [*Grotzinger et al.*, 2005]. Thus, the decimeter-scale trough cross-strata of Cape St. Mary are reasonably interpreted as wind-drag ripple stratification.

The lower bound on the wavelengths of wind-drag ripple we inferred from the thickness of cross-sets at Cape St. Mary in Victoria crater is highlighted with a red dashed line in Figure 6.14. Based on our observations, the scaling relationship indicates that the martian atmosphere had a density of < ~0.02 kg/m^3, and thus overlaps with the range in modern atmospheric densities at the surface of Mars (~ 0.002-0.023 kg/m^3; gray box). For comparison, under an atmosphere of Earth-like density, wind-drag ripples would have predicted wavelengths of about 12 cm and heights of about 1.2 cm, and thus would form cross-sets < 1.2 cm thick assuming the same preservation and height-to-wavelength ratios.

5.4.3. Other Candidate Wind-Drag Ripple Cross-Stratification

Other potential occurrences of wind-drag ripple cross-stratification in the martian geological record were observed by the Mars Exploration Rover Spirit, but were not recognized as such at the time. Decimeter-thick cross-sets were observed as Spirit explored the Home Plate layered plateau in Gusev crater [e.g., *Lewis et al.*, 2008]. Two interpretations were proposed for the upper Home Plate stratigraphy. A lower unit was thought to be a fallout sedimentary deposit from an explosive volcanic eruption based on its poorly sorted grains, poorly stratified bedding, and the presence of an out-sized clast interpreted as a ballistic volcanic bomb. However, two competing hypotheses were proposed for the upper unit which contains large-scale trough cross-sets of locally well-rounded and well-sorted sand; these were suggested to either result from sand waves associated with the base surge or, alternatively, to be unconformably overlying aeolian deposits [*Squyres et al.*, 2007]. The base-surge interpretation was favored on the basis of a single bedform with a preserved stoss face [*Lewis et al.*, 2008]. Indeed, the preservation of complete bedforms is rare in the terrestrial aeolian rock record [e.g., *Rubin and Hunter*, 1982] owing to generally low aggradation rates of aeolian dune deposits. Nevertheless, wind-drag ripples are several orders of magnitude smaller than their host dunes, and by analogy to terrestrial superimposed dunes may aggrade at rates that are high enough to produce steep angles of climb. Textural similarity between the high degree of roundness and sorting of the sandstone grains, and those grains of the modern aeolian deposits ("El Dorado") adjacent to the Home Plate outcrop (Figure 6 of *Lewis et al.*, 2008) further supports the aeolian interpretation for the upper unit of the Home Plate stratigraphy.

Candidate wind-drag ripple cross-stratification was also observed by Curiosity at Marias Pass in the Stimson formation (Figure 6.12 and 6.13). There, the observed 10-20 cm set-thicknesses are consistent with a substantially thinned martian atmosphere by the time of Stimson deposition (Figure 6.14). The wind-drag ripple interpretation of trough cross-sets at Cape St. Mary is supported by (i) the paleo-environmental context of the outcrop, (ii) the geometry and scale of the cross-sets, and (iii) the coexistence of two distinct scales of cross-sets. In contrast, the candidate cross-strata observed at Home Plate, Gusev crater, and in the Stimson formation at Apikuni Mountain, Gale crater, do not display two distinct scales of cross-sets.

Finally, wind-drag ripples might exist on other planetary bodies in the Solar system, and could be recognized through their distinct morphologies and relatively large sizes on low-atmospheric-density bodies.

Area #	Image Name	Latitude (degrees)	Longitude (degrees East)	Elevation (m)	Pixel Scale (cm)	Location
1	ESP_027864_2295	48.905	29.27	-5684.52	30.8	Acidalia Mensa
2	ESP_018854_1755	-4.586	137.392	-4424.172	27.1	Gale crater
3	ESP_034909_1755	-4.5	297.183	-2560.32	26.7	Juventae Chasma
4	ESP_025042_1375	-42.362	42.037	-457.2	25.2	SE of Yaonis Regio
5	ESP_011421_1300	-49.484	34.847	-108.204	25.6	Hellespontus
6	ESP_041987_1340	-45.422	38.83	121.92	25.2	Proctor crater
7	ESP_011909_1320	-47.786	30.689	533.4	50.7	SE of Proctor crater
8	ESP_024502_1305	-49.041	27.224	672.084	50.6	SW of Proctor crater
9	PSP_001970_1655	-14.235	306.735	-4700	26.6	Coprates Chasma
10	ESP_018011_2565	76.182	95.406	-4300	31.7	North Polar erg
11	ESP_039955_1875	7.167	67.751	682.1424	27.9	S of Nili Patera

Table 6.1: Orbital survey of Martian bedforms: Measurement locations. Location and resolution of analyzed Mars bedforms from HiRISE observations.

Area #	Surface area (km^2)	Dunes Wavelength λ (m)	*N*	TARs Wavelength λ (m)	*N*	Ripples Wavelength λ (m)	*N*	Total number of bedforms
1	1.003	131±57	118	5.2±1.8	30	2.2±0.5	116	162
2	0.041	151±67	44	7.0±2.2	33	2.1±0.6	212	168
3	2.210	235±99	60	16.1±7.8	96	3.0±0.6	62	212
4	1.210	199±75	55	8.8±5.6	12	3.5±0.8	130	153
5	1.214	441±264	49	17.8±14.1	80	3.3±0.9	66	159
6	1.229	334±173	31	7.6±3.1	36	3.1±0.9	136	180
7	1.994	573±263	83	10.3±4.0	40	3.1±0.8	138	195
8	1.118	515±189	14	8.3±4.4	40	3.6±0.9	98	141
9	1.504	264±83	31	-	-	2.6±0.5	96	96
10	0.911	248±124	113	-	-	2.5±0.4	104	104
11	1.041	324±111	165	-	-	3.4±0.8	142	181

Table 6.2: Orbital survey of Martian bedforms: Results. Average measured bedform wavelengths (±1σ). *N* refers to the number of bedforms belonging to each category.

		Mars, orbit		Mars, rover	
		large ripples	**dunes**	**small ripples**	**large ripples**
Earth	**ripples**	3.3×10^{-5}	6.1×10^{-5}	3.1×10^{-2}	1.2×10^{-4}
	dunes	3.3×10^{-5}	2.6×10^{-3}	1.89×10^{-5}	1.2×10^{-4}

Table 6.3: Statistical analysis of bedform-wavelength distributions. *P*-values of the two-sample Kolmogorov-Smirnov test applied to individual subsampled modes from the three datasets.

Table 6.4: Compilation of martian large ripples and calculated parameters (in ancillary file “Lapotre_Chapter6_Tables_4_5”).

Table 6.5: Compilation of martian large ripples from *Lorenz et al.* [2014] and calculated parameters (in ancillary file “Lapotre_Chapter6_Tables_4_5”).

Table 6.6: Full compilation of terrestrial and martian bedform wavelengths (in ancillary file “Lapotre_Chapter6_Table_6”).

Acknowledgments: We thank the MSL engineering and science teams, the Mastcam team, and Malin Space Science Systems, who made the rover observations possible, as well as Bethany Ehlmann and Ken Edgett for insightful comments. Data presented in this paper are archived in the Planetary Data System (pds.nasa.gov), and our compilation is available in a supplementary file. Part of this research was carried out at JPL-Caltech, under a contract with NASA. Work in the UK was funded by the UK Space Agency.

Chapter 7

A PROBABILISTIC APPROACH TO REMOTE COMPOSITIONAL ANALYSIS OF PLANETARY SURFACES

Mathieu G. A. Lapôtre, Bethany L. Ehlmann, and Sarah E. Minson

This chapter was published as:
Lapôtre, M. G. A., et al. (2017), A Probabilistic Approach to Remote Compositional Analysis of Planetary Surfaces, *Journal of Geophysical Research: Planets*, in press.

Notations are summarized in Appendix C.

Abstract. Reflected light from planetary surfaces provides information, including mineral/ice compositions and grain sizes, by study of albedo and absorption features as a function of wavelength. However, deconvolving the compositional signal in spectra is complicated by the non-uniqueness of the inverse problem. Tradeoffs between mineral abundances and grain sizes in setting reflectance, instrument noise, and systematic errors in the forward model are potential sources of uncertainty, which are often unquantified. Here, we adopt a Bayesian implementation of the Hapke model to determine sets of acceptable-fit mineral assemblages, as opposed to single best-fit solutions. We quantify errors and uncertainties in mineral abundances and grain sizes that arise from instrument noise, compositional endmembers, optical constants, and systematic forward model errors for two suites of ternary mixtures (olivine-enstatite-anorthite and olivine-nontronite-basaltic glass) in a series of six experiments in the visible-shortwave infrared (VSWIR) wavelength range. We show that grain sizes are generally poorly constrained from VSWIR spectroscopy. Abundance and grain size tradeoffs lead to typical abundance errors of ≤1 wt% (occasionally up to ~ 5 wt%), while ~3% noise in the data increases errors by up to ~2 wt%. Systematic errors further increase inaccuracies by a factor of 4. Finally, phases with low spectral contrast or inaccurate optical constants can further increase errors. Overall, typical errors in abundance are <10%, but sometimes significantly increase for specific mixtures, prone to abundance/grain-size tradeoffs that lead to high unmixing uncertainties. These results highlight the need for probabilistic approaches to remote determination of planetary surface composition.

1. Introduction

In the past few decades, multispectral and hyperspectral datasets covering the ultraviolet-to-thermal-infrared wavelength ranges have revolutionized our understanding of the surface composition of many planetary bodies. Reflectance spectra allow the detection of key mineral and ice phases, and, when combined with quantitative semi-empirical theories [e.g., *Hapke*, 1981; *Hapke and Wells*, 1981; *Hapke*, 1984; 1986; *Shkuratov et al.*, 1999; *Hapke*, 2002; 2008], enable the estimation of the composition and grain sizes of particulate surfaces ("spectral unmixing"). These models have been tested and used to invert for mineral abundances for laboratory particulate mixtures [e.g., *Clark and Roush*, 1984;

Mustard and Pieters, 1987; 1989; *Hiroi and Pieters*, 1994; *Lucey*, 1998; *Poulet and Erard*, 2004; *Robertson et al.*, 2016] and for planetary surfaces from telescopic and orbiter-based spectroscopic data [e.g., *McCord et al.*, 1998; *Cruikshank et al.*, 2003; *Poulet et al.*, 2008; *Tirsch et al.*, 2011; *Poulet et al.*, 2014; *Edwards and Ehlmann*, 2015; *Goudge et al.*, 2015; *Liu et al.*, 2016; *De Sanctis et al.*, 2016].

In the vast majority of published mineral abundance retrievals, modeled mineral compositions have been found by searching for a best fit to a given spectrum by way of an optimization routine (e.g., using least squares with a grid search, a downhill simplex, etc.), and thus only provide single sets of mineral abundances, and sometimes grain sizes, that fit the data. However, the combined effects of mineral abundances, grain sizes, noise, and the non-linearity of radiative transfer models lead to an ill-posed inverse problem; in particular, several equally good solutions may fit the data. For example, Figure 7.1 shows the laboratory spectrum of a 16 wt% olivine - 16 wt% pyroxene - 68 wt% plagioclase particulate intimate mixture (red) and two modeled spectra (green and blue), which both fit the data equally well (same RMS error) and yet correspond to significantly different modal mineralogies. In this particular case, non-uniqueness arises from tradeoffs between mineral abundances and grain sizes (e.g., see olivine abundances and grain sizes in models 1 and 2; see also Figure 7.2B). Thus, a significant knowledge gap in VSWIR spectroscopy is that of the quantitative errors and uncertainties associated with the inverse determination of mineral abundances and grain sizes. Constraining these would represent a major improvement to commonly used inversion techniques by shedding light onto the reliability of inferred compositions of planetary surfaces, i.e., by providing best-fit estimates with rigorously understood uncertainties.

In this paper, we use a Bayesian approach, namely a Markov-Chain Monte Carlo (MCMC) implementation [*Minson et al.*, 2013] of the Hapke scattering model [*Hapke*, 1981], to illustrate and quantitatively constrain the errors and uncertainties associated with spectral unmixing. We first summarize the inversion workflow, then describe the adopted forward model and Bayesian probabilistic approach. Finally, we illustrate the technique with six computational experiments that were designed to separately quantify the effects of inherently non-unique fits, noise, and specific spectral properties of the endmembers on errors and uncertainties using both simulated and laboratory ternary mixtures (olivine-enstatite-anorthite and olivine-nontronite-basaltic glass). A seventh experiment, where we compare Mars orbiter-based data with ground truth, is the subject of a companion paper [*Lapôtre et al.*, 2017b].

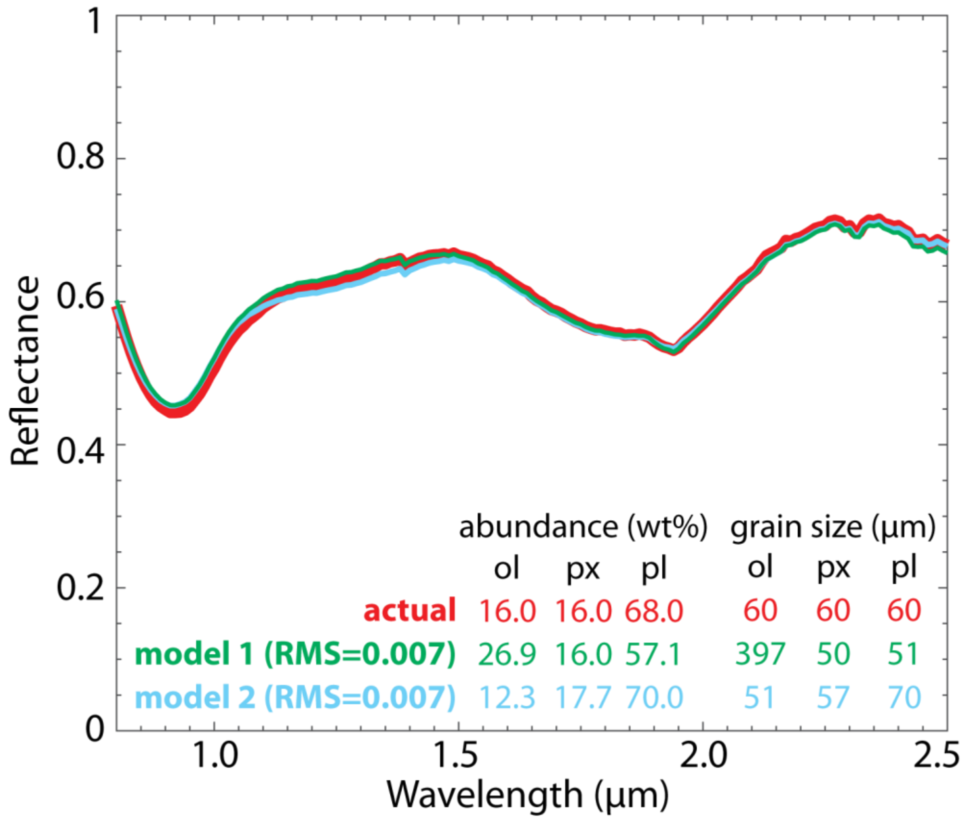

Figure 7.1: Non-uniqueness of spectral unmixing. (A) Example of two different synthetic mixtures fitting a laboratory spectrum equally well, as evaluated by computation of root mean squared error in fit The red spectrum is radiance coefficient as measured in the laboratory from a particulate mixture (~45-75 μm) of 16 wt% olivine ("ol") - 16 wt% pyroxene ("px") - and 68 wt% plagioclase ("pl") from *Mustard and Pieters* [1989] (see Table 7.1 for reference to spectral library). The green and blue spectra are modeled from the optical constants of olivine, pyroxene, and plagioclase using the Hapke forward model. Both models correspond to very different modal compositions and yet, have the same RMS error of 0.007.

2. Methods

In this section, we summarize the recommended workflow for probabilistic spectral unmixing, from the identification of mineral endmembers and calculation of their optical constants, to the forward model we use, and to the MCMC procedure. While we illustrate our approach with the Hapke radiative transfer model [*Hapke*, 1981], this general workflow can be employed regardless of the choice of the forward model details.

2.1. Workflow Overview

As light from an emitting source, e.g., the Sun, is reflected by a geologic surface, its spectrum becomes the carrier of useful compositional information. In particular, the ratio of received-to-incident light spectral flux is a complex convolution of how light interacted with any atmosphere as it travelled to and away from the geologic surface, of how it interacted with individual mineral/mineraloid/ice/organic crystals or grains on the surface, and of illumination geometry. For planetary remote sensing data, the instrument response also modulates the spectral information content of collected light. In this study, we only consider laboratory spectra from light that has not significantly interacted with the atmosphere and with highly stable instruments. Spectral interpretation is thus simplified to (i) knowing the illumination geometry, (ii) having a forward model to predict how mixtures of different mineral grains interact with light, and (iii) inverting for compositional information from the data using the forward model.

The reflectance of a mixture of mineral/mineraloid/icy/organic components is a function of the reflectances of those individual components. Thus, in order to perform spectral unmixing, one first needs to identify what components (all grouped under “mineral endmembers” herein) are present in the target. This identification is complex, and yet critical to the unmixing procedure, as it governs the inputs to the overall algorithm. Identifying what mineral endmembers are appropriate to model spectral data may require an iterative procedure (Section 2.2.1).

Nash and Conel [1974] showed that the VSWIR reflectance of an intimate mixture of grains is not a linear combination of the reflectances of its constitutive mineral endmembers due to multiple scattering of photons. *Hapke* [1981] developed a radiative transfer model that relates the reflectance of a mixture to a linear combination of the single scattering albedos of its constituent endmembers. Because the single scattering albedo of a single mineral is a function of its optical constants (real and imaginary indices of refraction, *n* and *k*, respectively) and grain size, spectral unmixing requires the measurement or computation of the optical constants of all mineral endmembers as a function of wavelength. In the absence of available transmission spectra, optical constants need be determined from laboratory spectra using a radiative transfer model (Section 2.2.3). The Hapke formulation has the advantage that single scattering albedos do mix linearly with mixing coefficients relating grain size and density (Section 2.3). Thus, with the mineral endmembers' optical constants on hand to calculate single scattering albedos, one can invert for the composition and grain sizes of a particulate mixture by minimizing the mismatch between computed mixture spectra and the data.

The goodness of a given forward model may be evaluated by calculating the root mean square (RMS) error between the data and the forward model and minimizing it, e.g., through a brute-force grid search over all parameters or, e.g., a downhill simplex [e.g., *Poulet and Erard*, 2004; *Ehlmann*, 2010]. However, due to the non-uniqueness of the solution (due to, e.g., abundance and grain size tradeoffs and/or noise) and systematic error from the forward model (which affect both optical constants inverted from reflectance spectra and modeled particulate mixtures), we adopt the approach of finding a range of solutions that reasonably match the data (e.g., Figure 7.2A-B). To do so, we use a MCMC approach (Section 2.4) which allows sampling the parameter space at a density that is proportional to the likelihood of a given model, which itself is a function of the goodness of the fit (RMS error) between a given forward model and the data.

The outputs of the MCMC algorithm are the probability densities of mineral abundances (e.g., Figure 7.2C) and grain sizes (e.g., Figure 7.2D). Several useful descriptors may be evaluated from the probability density functions (PDFs), such as (i) the Maximum A Posteriori probability model (or MAP), which corresponds to the most sampled area of the parameter space, i.e., the most probable mineral assemblage, and (ii) the 95% confidence interval of a given parameter, which is a measure of uncertainty (e.g., Figure 7.2C-D). Note that the 95% confidence interval would correspond to $\pm$ 2σ (standard deviation) if the PDFs were Gaussian. The difference between the truth and the MAP is a measure of error, while the width of the 95% confidence interval is a measure of uncertainty (Figure 7.2). Figure 7.2A shows the same laboratory spectrum as in Figure 7.1 (red), along with its corresponding MAP spectrum (blue) and example models that one could deem acceptable (gray), especially if the data were noisy. The PDFs of mineral assemblages are built from the mineral abundances (e.g., Figure 7.2C) and grain sizes (Figure 7.2D) corresponding to those spectra that are deemed acceptable. The MCMC-determined probability density allows the likelihood of any given mineral assemblage to be assessed quantitatively.

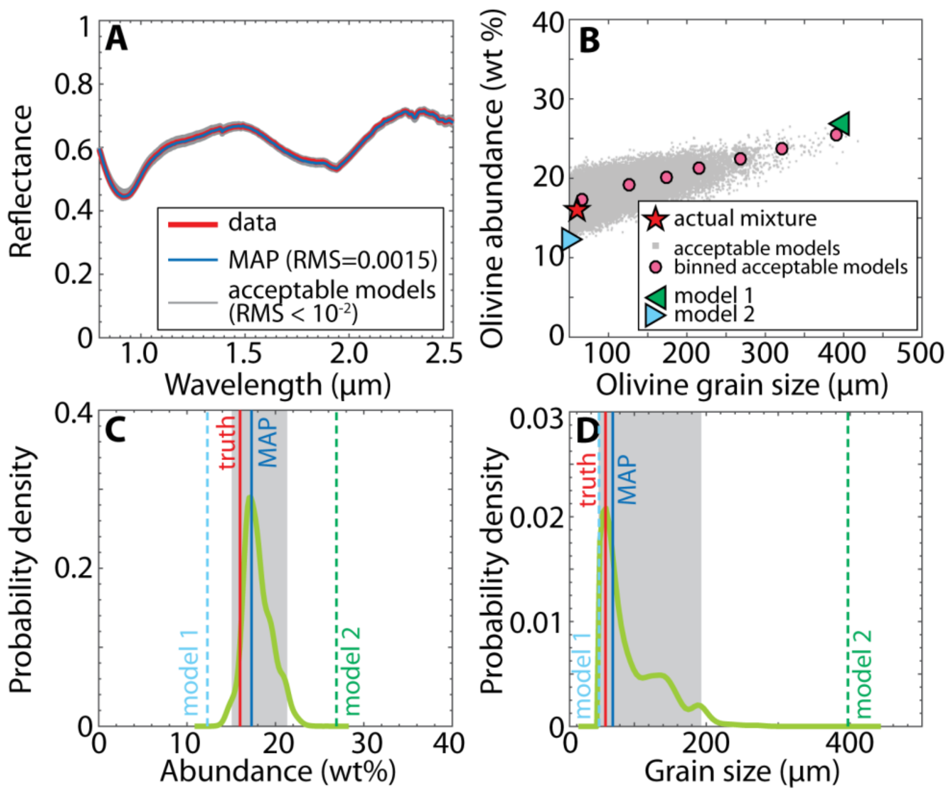

Figure 7.2: Tradeoffs between abundances and grain sizes. (A) Example of the Maximum A Posteriori probability model (MAP; blue) for the same mixture as in Figure 7.1, and set of "acceptable" models (RMS error < 10^{-2}; gray). (B) Correlation between the abundances and grain sizes of olivine that yield acceptable fits to the data (raw model data in gray dots, data binned by mean value over 50-μm size intervals in pink circles; RMS error between 0.0015 and 0.0099). Abundances and sizes corresponding to the actual mixture and models 1 and 2 from Figure 7.1 are denoted by a red star, and green and blue triangles, respectively. Probability density of olivine (C) abundance and (D) grain size as determined from all acceptable models. True and MAP abundances and sizes are indicated by red and blue vertical solid lines, respectively. Vertical dashed lines correspond to the two models shown in Figure 7.1 (model 1 in light blue, model 2 in dark green). Shaded areas correspond to the 95% confidence intervals in olivine abundance and sizes. Note that while the MAP does not coincide with the truth, true abundance and grain size are both accepted with a high probability, emphasizing the usefulness of this probabilistic approach.

2.2. Mineral Endmember Identification and Optical Constants

2.2.1. Endmember Identification

Different approaches in selecting mineral endmembers have been used for different wavelength ranges, from a simple visual inspection of spectra for VSWIR data [e.g., *Poulet et al.*, 2014] to a search over a large spectral library for thermal-infrared spectra [*Feely and Christensen*, 1999]. Statistical methods can also be used to find in-scene endmembers from hyperspectral data cubes [e.g., *Tompkins et al.*, 1997; *Thomas and Bandfield*, 2013]. An additional complication comes from the presence of phases that do not have distinctive absorption features that impart characteristic spectral signatures, e.g., iron-free plagioclases in the VSWIR or halides in the MIR. While increasing the number of mineral endmembers used to perform an inversion typically improves the goodness of the fit, it is unclear whether such an improvement has any physical meaning, i.e., whether constituents modeled at small abundances are actually present.

As an overall approach for VSWIR spectral unmixing, we suggest that mineral endmembers should be selected parsimoniously on the basis of (1) required mineral phases, uniquely identifiable from distinct absorptions in the data (e.g., broad absorptions near 1 μm and 2 μm signal the presence of pyroxenes or basaltic glasses; characteristic sharp absorptions of –OH and H_2O at ~1.4, ~1.9, and ~2.3 μm require the presence of Fe/Mg phyllosilicates), (2) geologic context (e.g., mafic rocks are likely to contain both VSWIR spectrally undistinctive plagioclase as well as pyroxenes), and (3) requirements for overall albedo (e.g., opaque phases, such as kerogens or iron oxides, selected based on context, may be required to match a spectrum’s low albedo). If necessary, more mineral endmembers may be added iteratively.

Mafic mixtures are the focus of this study, as mafic protoliths are common on many planetary surfaces. Common minerals (and absorptions) that may be present in mafic mineral assemblages include olivine (broad 1-μm feature, with a shape that changes depending on Fe content; e.g., *Sunshine and Pieters*, 1998), pyroxenes (broad 1-μm and 2-μm absorptions with positions that shift depending on Fe and Ca content (e.g., *Klima et al.*, 2011, and references therein), plagioclases (which have a 1.3-μm feature for Fe-bearing phases but are otherwise featureless in the VSWIR; e.g., *Cheek and Pieters*, 2014), and iron oxides (which have electronic absorptions at <1 μm but are often featureless in the SWIR; e.g., *Burns*, 1993, and *Morris et al.*, 1993). Clino- and ortho-pyroxenes may both be present depending on the source composition, temperature, and degree of partial melting. Thus, for mafic compositions in the VSWIR wavelength range, we implement the overall endmember selection approach above as follows:

(i) Examine the spectral properties near 1 μm to determine if the shape and breadth of the observed 1-μm feature require olivine to be present.

(ii) If olivine appears to be present, pick a single pyroxene that best matches the ~ 2-μm absorption, if present.

(iii) Add any other phases required by observed absorption features present (e.g., nontronite, saponite, chlorite, or other mafic alteration products).

(iv) Assume the presence of plagioclase and an Fe oxide (inspect the visible spectral range to determine which Fe oxide); those two phases generally tradeoff with each other and with phases with absorptions in setting the overall SWIR albedo.

(v) Iterate and visually inspect fit width near 1-μm to identify the olivine composition (Fo number).

(vi) Inspect the residuals for remaining pyroxene signatures, and add a second pyroxene if it is required to match the width of the ~ 2-μm absorption.

(vii) Other phases may be added from inspection of the remaining residuals or context (e.g., amorphous glass, other Fe oxides, additional hydrated phases, etc.).

Once mineral endmembers are identified using iterative modeling and the qualitative steps described above, their respective densities and optical constants are used as inputs to our quantitative algorithm.

The reflectance or emission of an endmember constituent is a function of its density, grain size, and optical constants. In the MIR for coarse grained samples, the values of the optical constants are such that photons are mostly singly scattered and reflectance or emission spectra acquired in the laboratory can be directly used in modeling (see *Clark*, 1999 for review). For fine-grained constituents in the MIR (<~60 μm; e.g., *Ramsey and Christensen*, 1998) or all grain sizes in the VSWIR, multiple scattering causes grain size to exert a key control on spectral properties. In this case, endmember optical constants must be employed rather than reflectance or emission spectra.

2.2.2. Conversion of Reflectance to Single Scattering Albedo

Optical constants can be derived directly from laboratory measurement of crystalline minerals in transmission [e.g., *Zeidler et al.*, 2011] or estimated from laboratory reflectance spectra of a particulate sample via conversion of its reflectance to its single scattering albedo [*Roush et al.*, 1990; *Lucey*, 1998; *Roush*, 2003; *Trang et al.*, 2013]. Single-scattering albedo is a dimensionless measure of the proportion of light scattered by a grain in a single interaction, expressed as a function of wavelength. For a geometric optics regime (when particles are larger than a few wavelengths of light), *Hapke* [1981] proposed that single scattering albedo, w, and reflectance (precisely, the radiance coefficient), r, are related through

$$r(\mu,\mu_0,\mathrm{g}) = \frac{w}{4(\mu+\mu_0)}\left[(1+B(g))P(g)+H(w,\mu)H(w,\mu_0)-1\right], \qquad (7.1a)$$

where μ_0 is the cosine of the incidence angle, μ the cosine of the emergence angle, *g* the phase angle, *B* the backscattering function, and *P* the phase function of the material. The *H* function is the Chandrasekhar integral function associated with the observation geometry. For the laboratory spectra considered here, we assume $B=0$ (no backscattering at the moderate phase angles measured) and $P=1$ (isotropic scatterers), i.e.,

$$r(\mu,\mu_0) \approx \frac{w}{4(\mu+\mu_0)} H(\mu)H(\mu_0)\ . \qquad (7.1b)$$

Mustard and Pieters [1989] showed that, when grain sizes are known and a more realistic formulation of the photometric phase function is used, inverted abundances can typically be improved by a few weight-percent.

Following *Hapke* [2002], we approximate the Chandrasekhar function by

$$H(\mathrm{x}) \approx \frac{1}{1 - wx\left[r_0 + \frac{(1-2r_0x)}{2}\ln\left(\frac{1+x}{x}\right)\right]}, \tag{7.2}$$

where $r_0 = \frac{1-\gamma}{1+\gamma}$ is the bihemispherical reflectance for isotropic scatterers, $\gamma = \sqrt{1-w}$, and x is used as a generic input variable.

Inverting for w in Equation (5.1b) yields the approximate expression we use for the single scattering albedo,

$$w \approx \frac{4(\mu + \mu_0)r}{H(\mu)H(\mu_0)}, \tag{7.3}$$

where H is calculated from Equation (7.2).

Because Equation (5.1) applies to both the reflectance of a particulate mixture and its individual constituents, one can use the measured reflectance of a pure particulate sample to invert for the single scattering albedo of its constitutive grains. In order to disentangle the effects of composition and grain size on single scattering albedo of mineral endmembers, we now need to express w as a function of the component's optical constants, n and k, and grain diameter, D.

2.2.3. Conversion of Single Scattering Albedo to Imaginary Index of Refraction

Following *Hapke* [1981], the single scattering albedo of a particulate sample can be expressed as

$$w = S_e + (1 - \mathrm{S_e}) \frac{(1 - \mathrm{S_i})}{1 - S_i \Theta} \Theta , \tag{7.4}$$

where

$$S_e = \frac{(n-1)^2 + k^2}{(n+1)^2 + k^2} + 0.05 \tag{7.5}$$

is the surface reflection coefficient for externally incident light,

$$S_i = 1.014 - \frac{4}{n(n+1)^2} \tag{7.6}$$

is the reflection coefficient for internally scattered light [*Lucey*, 1998], and

$$\Theta = \frac{r_i + \exp\left(-\sqrt{\alpha(\alpha + s)\langle D \rangle}\right)}{1 + r_i \exp\left(-\sqrt{\alpha(\alpha + s)\langle D \rangle}\right)} \tag{7.7}$$

is the particle internal transmission coefficient, with r_i, the internal diffusive bihemispherical reflectance inside a particle; α, the internal absorption coefficient; s, the internal scattering coefficient; and $\langle D \rangle$, the mean free path of a photon.

The internal bihemispherical reflectance in a particle can be expressed as

$$r_i = \frac{1 - \sqrt{\dfrac{\alpha}{\alpha + s}}}{1 + \sqrt{\dfrac{\alpha}{\alpha + s}}} , \tag{7.8}$$

where

$$\alpha = \frac{4\pi k}{\lambda} \tag{7.9}$$

is the internal absorption coefficient, with λ, the wavelength of light. We assume $s = 0$, following the reasoning of *Lucey* [1998] for natural particles. Finally, the mean free path $\langle D \rangle$ is estimated from D and n through

$$\langle D \rangle = \frac{2}{3}\left[n^2 - \frac{1}{n}\left(n^2 - 1\right)^{3/2}\right]D\,. \tag{7.10}$$

For typical *n* values (*n* ~ 1.5-2.5), $\langle D \rangle \approx 0.9D$, in keeping with the formulation of *Lucey* (1998).

Combining Equations (7.3)-(7.10) and measurements of pure particulate spectra of known grain sizes, one can solve for the imaginary index of refraction, k, by finding the value of k that minimizes the misfit between the corresponding calculated w (Equations (7.4-7.10)) and the single scattering albedos of the sample (Equation (7.3)) at each wavelength with an assumed *n* and *D*. While there are sophisticated models to calculate both optical constants (n and k) simultaneously (e.g., Kramers-Kronig dispersion theory [*Kronig*, 1926; *Kramers*, 1927]), the real index of refraction, n, does not typically vary by more than ~0.1 within the wavelength range we consider (~0.8-2.5 μm), and we treat it as a constant [e.g., *Roush et al.*, 1990; *Lucey*, 1998; *Roush*, 2003; *Trang et al.*, 2013]. Reductions on uncertainties with variable *n* were explored and found to be unimportant. Ideally, the inversion is performed iteratively for samples of different grain sizes to minimize the uncertainty associated with the effective grain size of a given laboratory sample. Errors of up to 10-15% in endmember reflectance may arise if optical constants are not optimized [e.g., *Lucey*, 1998; *Poulet and Erard*, 2004; *Trang et al.*, 2013].

Now that we can calculate the single scattering albedo of a particulate mixture, w_{mix}, from its reflectance spectrum, and the single scattering albedo of individual endmembers, w_i, from grain size and optical constants, we need to relate w_{mix} to the w_i of its constitutive endmembers.

2.3. Forward Modeling of Mixture Spectra from Mineral Endmembers

While there exist several models to predict the VSWIR spectrum of a particulate mixture from spectra of its individual components [e.g., *Purcell and Pennypacker*, 1973; *Hapke*, 1981; *Shkuratov et al.*, 1999], there is no model that consistently yields better results than the others, and the uncertainties associated with them appear to remain large [e.g., *Poulet et al.*, 2002]. To illustrate the usefulness of our Bayesian approach to VSWIR spectroscopy, we use the widely employed Hapke model [*Hapke*, 1981].

Because the reflectance of a mixture is a non-linear function of the reflectances of its individual mineral components, a first step is to convert reflectance to a quantity that does mix linearly – the single scattering albedo. The single scattering albedo of a mixture of grains, w_{mix}, is a linear combination of the single scattering albedos of its individual endmembers, w_i, such that

$$w_{\mathrm{mix}} = \sum_{i=1}^{N} f_i w_i \,, \tag{7.11}$$

where f_i is the fractional relative cross-section of component *i*, and is given by

$$f_i = \frac{\sigma_i}{\sum_{i=1}^{N} \sigma_i} \,, \tag{7.12a}$$

where

$$\sigma_i = \frac{m_i}{\rho_i D_i} \tag{7.12b}$$

with m_i the mass abundance, ρ_i the density, and D_i the grain size of endmember *i*. Note that Equation (7.12) is mathematically equivalent to the original formulation of Hapke [*Hapke*, 1981], in which f_i is written in terms of bulk density of mineral *i*, i.e., the combined mass of particles of mineral *i* per unit total volume (including void space and other mineral grains). Indeed, in Hapke's formulation, the total-volume terms, which do not vary with index *i*, cancel out; similarly, when using Equation (7.12) and thus mass abundance (i.e., the combined mass of particles of mineral *i* per total unit mass of the particulate mixture), the total-mass term does not vary with index *i*, such that they cancel out when taking the ratio of σ_i to $\sum_{i=1}^{N} \sigma_i$.

The misfit between actual single scattering albedo of a mixture and modeled mixture single scattering albedos is then minimized to invert for mineral abundances (m_i) and grain sizes (D_i). However, as the solution to this inverse problem can be non-unique (e.g., Figure 7.1), we adopt a Bayesian approach to constrain likely mineral assemblages.

2.4. Inverse Model: Bayesian Inversion of Mineral Abundances and Grain Sizes

Traditional optimization methods for solving the unmixing inverse problem identify one possible set of values for grain sizes and mineral abundances. However, we know that there is considerable uncertainty in inverted mineral composition because multiple mineral assemblages are compatible with the observations (e.g., Figures 7.1-7.2). Thus, instead of using an optimization approach, we adopt a Bayesian inversion approach (Section 2.4.1) that allows us to determine the ensemble of all plausible composition models (mineral abundances and grain sizes) that are consistent with both the observations (e.g., Figure 7.2) and our a priori knowledge of likely grain sizes and mineral abundances (Section 2.4.2). Another advantage of Bayesian methods is that we can account for both errors in our measurements (e.g., instrument noise) and errors and uncertainties associated with our physical model for mapping mineral composition into spectral observations (e.g., model inputs, reflectance model physical parameterization, atmospheric correction). In the next subsection, we explore how we build the Bayesian posterior probability density function (PDF), i.e., the PDF that describes the relative probability of different values for mineral abundances and grain sizes given our observations and a priori information.

Unfortunately, except for certain special cases, Bayesian posterior PDFs generally do not have a simple analytical form. Thus, to explore the posterior PDF, we must simulate it by using Markov Chain Monte Carlo (MCMC) to draw a large ensemble of random samples of the posterior PDF. From these samples, we can then estimate any statistics of interest on the mineral assemblage (e.g., mean, median, confidence intervals, etc.). In the following subsections, we describe our sampling methodology.

2.4.1. Principles of Bayesian Inference

Our goal is to infer the PDF that describes the relative plausibility of all potential mineral abundances and grain sizes, given our observations. Mathematically, we write this as $p\left(\mathbf{m},\mathbf{D}\,|\,\mathbf{d}\right)$, i.e., the probability density for different values for our mineral abundances, $\mathbf{m}$, and grain sizes, $\mathbf{D}$, given our observed wavelengths and single scattering albedo data values, $\mathbf{d}$. For our problem, $\mathbf{d}$ is a vector containing the spectral data (of length $2N_d$, containing N_d wavelengths and N_d corresponding single scattering albedo values), and $\mathbf{m}$ and $\mathbf{D}$ are vectors of the values of the mineral abundances and grain sizes that we are trying to assess, each with a length equivalent to the number of components, N.

Bayes' theorem [*Bayes*, 1763] states that the posterior PDF, i.e., the probability of a set of model parameters, $\mathbf{m}$ and $\mathbf{D}$, given the observations, $\mathbf{d}$, is

$$p(\mathbf{m},\mathbf{D}\,|\,\mathbf{d}) \propto p(\mathbf{d}\,|\,\mathbf{m},\mathbf{D})\,p(\mathbf{m},\mathbf{D}), \tag{7.13}$$

where $p\left(\mathbf{m},\mathbf{D}\right) = p(\mathbf{m})\,p(\mathbf{D})$ is the prior PDF that defines the a priori relative probability of different values of the mineral abundances and grain sizes before making any spectral observations. We describe how we represent our a priori knowledge of mineral abundances and grain sizes in Section 2.4.2. The other term in the posterior PDF (Equation (7.13)) is the data likelihood, $p(\mathbf{d}\,|\,\mathbf{m},\mathbf{D})$. Data likelihood is the PDF that describes the probability of having observed the spectral data, $\mathbf{d}$, given a particular set of values for $\mathbf{m}$ and $\mathbf{D}$. If we assume Gaussian errors, then the data likelihood function is a normal distribution.

In detail, let $\boldsymbol{\delta}$ be the measurement predictions corresponding to the data, $\mathbf{d}$, and $G(\mathbf{m},\mathbf{D})$ a function describing the deterministic forward model (i.e., Hapke's model in our case; Section 2.3), such that

$$\boldsymbol{\delta} = G(\mathbf{m},\mathbf{D}) + \mathbf{e} + \boldsymbol{\varepsilon}, \tag{7.14}$$

where $\mathbf{e}$ is the uncertainty due to measurement errors (e.g., associated with the noise in spectral data), and $\boldsymbol{\varepsilon}$ the uncertainty due to model prediction errors (e.g., associated with inaccurate predictions by $G(\mathbf{m},\mathbf{D})$, i.e., the physics in the model). We assume that measurement and prediction errors (each of length $2N_d$), $\mathbf{e}$ and $\boldsymbol{\varepsilon}$, can be modeled by independent Gaussian PDFs, such that the likelihood function $p(\mathbf{d}\,|\,\mathbf{m},\mathbf{D})$ is given by

$$p(\mathbf{d}\,|\,\mathbf{m},\mathbf{D}) = \frac{1}{(2\pi)^{N_d}\left|\mathbf{C}_\chi\right|^{\frac{1}{2}}} \exp\left\{-\frac{1}{2}\left[\mathbf{d}-G(\mathbf{m},\mathbf{D})-\boldsymbol{\eta}\right]^{\mathrm{T}} \mathbf{C}_\chi \left[\mathbf{d}-G(\mathbf{m},\mathbf{D})-\boldsymbol{\eta}\right]\right\}, \tag{7.15}$$

where $\mathbf{C}_\chi$ and $\boldsymbol{\eta}$ are the covariance matrix and mean of the sum $(\mathbf{e}+\boldsymbol{\varepsilon})$, respectively. By definition, $\mathbf{C}_\chi$ is square and of dimensions equal to the length of $\mathbf{d}$ (i.e., $2N_d \times 2N_d$). In our implementation of the algorithm, we assume $\boldsymbol{\eta} = 0$, i.e., we model the uncertainty in our predicted wavelengths and single scattering albedo values with a Gaussian distribution. In other words, we do not expect there to be a consistent bias between our predictions and the observed data values. In this study, we assume that our covariance matrix is isotropic, i.e., that overall error is not a function of wavelength. This assumption can be improved in future implementations with a model for how systematic errors in the Hapke forward model and/or instrument noise vary with wavelength.

2.4.2. A Priori Distributions of Abundances and Grain Sizes

In this section, we describe how we incorporate a priori knowledge on mineral abundances and grain sizes. Specifically, we assume that all values of abundances are equally likely so long as the abundances of all component minerals sum to unity, and we use uniform probability distributions to describe the possible grain sizes with lower and upper bounds based on our knowledge of plausible sizes (e.g., in the case of real planetary surfaces, from thermal inertia, presence of bedforms, etc.).

2.4.2.1. Prior Distribution of Abundances

A requirement for the prior distribution of component abundances is that they must sum up to unity. A Dirichlet distribution is the simplest distribution that satisfies this assumption, and we thus assume that the probability density of abundances (N endmembers) follows a Dirichlet distribution,

$$p(\mathbf{m}) = \mathrm{Dir}(m_1,...,m_N; a_1,...,a_N) = \frac{1}{\mathrm{B}(\mathbf{a})}\prod_{i=1}^{N} m_i^{a_i-1} \tag{7.16}$$

with $0 \le m_i \le 1$ (abundance of mineral i) and $\sum_{i=1}^{N} m_i = 1$, and where a_i are the concentration parameters discussed below, and B is the multinomial beta function

$$\mathrm{B}(\mathbf{a}) = \frac{\prod_{i=1}^{N}\Gamma(a_\mathrm{i})}{\Gamma\left(\sum_{i=1}^{N} a_\mathrm{i}\right)}, \tag{7.17}$$

where $\mathbf{a}$ is the vector $(a_1,...,a_\mathrm{N})$, and Γ the gamma function

$$\Gamma(a_i) = \int_0^\infty x^{a_i-1}e^{-x}\mathrm{dx}\ . \tag{7.18}$$

For $a_i > 0$,

$$\Gamma(a_i) = (a_i - 1)!\ . \tag{7.19}$$

Each concentration parameter, a_i, is a measure of the evenness (uniformity) or sparseness (values concentrated in a single value or narrow range of values) of the individual endmember distribution. When $a_i = 1$ for all N concentration parameters, all sets of probability distributions are equally likely. When $\sum_{i=1}^{N} a_i \to \infty$ instead, only near-uniform individual distributions are likely, i.e., each individual endmember distribution is a 1-dimensional near-uniform distribution. When

$\sum_{i=1}^{N} a_i \to 0$, only distributions with nearly all of the mass being concentrated within one component are likely. We assume $a_i = 1$, such that all sets of probability distributions are equally likely a priori.

2.4.2.2. Prior Distribution of Grain Sizes

In the absence of prior information on grain sizes (or to simulate the lack thereof), we model the a priori grain size probability densities as uniform distributions

$$p(D_i) = U(D_i) = \begin{cases} \dfrac{1}{D_{i,\max} - D_{i,\min}}, \text{ for } D_i \in \left[D_{i,\min}, D_{i,\max} \right] \\ 0, \text{ otherwise} \end{cases}, \tag{7.20}$$

where $D_{i,\min}$ and $D_{i,\max}$ are modeler-defined lower and upper bounds on the grain size range of mineral endmember *i*, respectively. For example, such bounds may be estimated from contextual indicators on planetary surfaces, such as the presence/absence of bedforms or from independent photometric or thermal inertia datasets. We note that the prior distribution on grain size is an "initial guess" of the distribution of grain sizes that may explain the data reasonably well, and thus does not reflect a grain size distribution within a target.

2.4.3. Metropolis Algorithm

Substituting Equations (7.15)-(7.16), and (7.20) into the posterior PDF (Equation (7.13)) forms the product of multivariate normal, Dirichlet, and uniform distributions, which has no simple analytical solution. We thus stochastically simulate the posterior PDF of the observations by using a MCMC algorithm to draw random sample models whose density is proportional to the posterior PDF. The most common MCMC method is the Metropolis algorithm [*Metropolis et al.*, 1953]. The Metropolis algorithm uses a random walk to propose possible samples of some arbitrary target PDF (in this case, our posterior PDF), and then probabilistically chooses to accept or reject each candidate sample based on its probability in the target PDF.

The candidate samples are drawn from some known probability distribution, typically chosen to be a normal distribution. If a candidate sample of random values for our mineral abundances and grain sizes has higher posterior probability than the last sample, it is always accepted. As a result, the sampler obtains samples in the high probability region of the posterior PDF even if the candidate has a low probability in the normal distribution being used to generate candidate samples. If the candidate sample has lower posterior probability than the current sample, the algorithm chooses to accept or reject that sample based on whether its posterior probability is greater than a draw from a standard uniform distribution between 0 and 1. Thus, low probability candidate samples are proportionally accepted less often than high probability candidate samples, creating a population of accepted samples whose density is proportional to the target posterior PDF. However, low probability samples are rarely accepted, assuring that, given enough samples, the random walk eventually leaves a high probability region in which it is currently located, thus ultimately visiting all parts of the potentially multimodal probability distribution describing the relative plausibility of different mineral assemblages.

Mathematically, the Metropolis algorithm works as follows. For notational simplicity, let us describe the unknown values describing the mineral composition with a single variable, $\boldsymbol{\theta} = \left\langle \mathbf{m}^{\mathrm{T}}, \mathbf{D}^{\mathrm{T}} \right\rangle^{\mathrm{T}}$, a vector containing possible values of our mineral abundances, $\mathbf{m}$, and grain sizes, $\mathbf{D}$. The Metropolis algorithm generates sample models $\{\boldsymbol{\theta}_1, \boldsymbol{\theta}_2, ..., \boldsymbol{\theta}_L\}$ (where L is the length of the Markov Chain) of the target PDF via a random walk: given a current sample, $\boldsymbol{\theta}_i$, a new candidate sample, $\mathbf{y}$, is generated and then probabilistically either accepted or rejected as θ_{i+1}. Commonly, $\mathbf{y} = \boldsymbol{\theta}_i + \mathbf{z}$ where $\mathbf{z}$ is drawn from a zero-mean multivariate normal distribution with arbitrary covariance, $\boldsymbol{\Sigma}$. The criterion for accepting or rejecting a sample is

$$\begin{cases} \boldsymbol{\theta}_{i+1} = \mathbf{y} \text{ if } \phi \geq u, \\ \boldsymbol{\theta}_{i+1} = \boldsymbol{\theta}_i \text{ otherwise,} \end{cases} \tag{7.21a}$$

with

$$\phi = \min\left\{1, \frac{p(\mathbf{d} \mid \mathbf{y})\, p(\mathbf{y})}{p(\mathbf{d} \mid \boldsymbol{\theta}_i)\, p(\boldsymbol{\theta}_i)}\right\} = \min\left\{1, \frac{p(\mathbf{d} \mid \mathbf{y})\, p(\mathbf{y})}{p(\mathbf{d} \mid \mathbf{m}_i, \mathbf{D}_i)\, p(\mathbf{m}_i, \mathbf{D}_i)}\right\}, \tag{7.21b}$$

and where u is drawn from the standard uniform distribution, $U(0,1)$, for each candidate sample, and $p(\mathbf{d} \mid \mathbf{y})$ and $p(\mathbf{d} \mid \boldsymbol{\theta}_i)$ are calculated according to Equation (7.15). A non-trivial consequence of this sampling strategy is that the parameter space is sampled with density proportional to the posterior PDF, $p(\mathbf{m}, \mathbf{D} \mid \mathbf{d}) \propto p(\mathbf{d} \mid \mathbf{m}, \mathbf{D})\, p(\mathbf{m}, \mathbf{D})$, even though candidate sample models are proposed from an arbitrary PDF, e.g., $\mathbf{z} \sim N(0, \mathbf{\Sigma})$ [e.g., *Chib and Greenberg*, 1995].

2.4.4. Specifics of our Implementation of the Metropolis Algorithm: Cascading Adaptive Transitional Metropolis in Parallel (CATMIP)

The efficiency of the Metropolis algorithm is limited by several factors. First, if the proposal PDF used to generate candidate samples is very different from the target PDF (which it typically is since we are blindly sampling a target PDF whose shape and features we do not know), very few of our proposed candidate samples are accepted. If the acceptance rate is low, then the random walk explores the posterior PDF very slowly, staying in one location while many candidate samples are proposed and rejected. Second, if the posterior PDF is narrowly peaked, it may take a long time for the random walk to find the high probability region. Third, for multimodal posterior PDFs, it may take a long time for the random walk to move from one high probability region to another. Thus, to increase MCMC sampling efficiency, we use the Cascading Adaptive Transitional Metropolis In Parallel (CATMIP) algorithm [*Minson et al.*, 2013; *Minson et al.*, 2014], an approach that addresses all of these three efficiency issues.

First, CATMIP uses transitional PDFs [*Beck and Au*, 2002; *Ching and Chen*, 2007] – instead of attempting to sample the posterior PDF directly, CATMIP simulates a sequence of transitional PDFs. The first of these transitional PDFs is the prior PDF, which we know and can sample directly using a random number generator. We then use each of these samples as the seed for a Metropolis random walk whose target is a new transitional PDF that is similar to the prior but is slightly closer to the posterior PDF (note that only the last sample from each Markov chain is kept, keeping the total number of samples unchanged). Because this target PDF is, by construction, close to our prior distribution, it takes little sampling effort to redistribute our samples so that their density is proportional to the new target PDF. Once this is accomplished, we then evolve our target PDF slightly closer to the posterior PDF, run the sampling again until we have simulated this new target PDF, and repeat until we finally simulate the posterior PDF itself. By evolving from a set of samples that are distributed according to our relatively flat prior distribution to the potentially highly peaked posterior PDF, we take away from the Metropolis algorithm much of the work of locating the high probability regions of the posterior PDF and distributing our samples with density proportional to the posterior probability.

Mathematically, we write our series of transitional PDFs as,

$$p_j = p_j\left(\mathbf{m},\mathbf{D}\,|\,\mathbf{d},\beta_j\right) \propto p\left(\mathbf{d}\,|\,\mathbf{m},\mathbf{D}\right)^{\beta_j}\ p(\mathbf{m},\mathbf{D})\,, \tag{7.22}$$

where $j = 0,1,...,J$, and $0 = \beta_0 < \beta_1 < ... < \beta_J = 1$ where J is the total number of transitional PDFs (dynamically defined by $\beta_J = 1$). At the initial step, $p_0\left(\mathbf{m},\mathbf{D}\,|\,\mathbf{d},\beta_0 = 0\right) \propto p\left(\mathbf{d}\,|\,\mathbf{m},\mathbf{D}\right)^0 p(\mathbf{m},\mathbf{D}) = p(\mathbf{m},\mathbf{D})$ can be simulated by drawing sample models directly from the prior PDF. For β_1 sufficiently small,

$p_1(\mathbf{m},\mathbf{D}\,|\,\mathbf{d},\beta_1)$ is similar enough to $p_0(\mathbf{m},\mathbf{D}\,|\,\mathbf{d},\beta_0=0)$ that little Monte Carlo simulation is required to update the sample models of p_0 to be distributed according to p_1. Specifically, each sample of p_0 is updated with an independent instance of the Metropolis algorithm. These instances can be run in parallel, greatly decreasing the time required to execute the Monte Carlo sampling. Each succeeding transitional PDF can be similarly efficiently sampled until $p_j(\mathbf{m},\mathbf{D}\,|\,\mathbf{d},\beta_j=1)\propto p(\mathbf{d}\,|\,\mathbf{m},\mathbf{D})^1\,p(\mathbf{m},\mathbf{D})=p(\mathbf{d}\,|\,\mathbf{m},\mathbf{D})\,p(\mathbf{m},\mathbf{D})$ has been sampled, thus simulating the posterior PDF. The values for β_j, which define the series of transitional PDFs, are chosen to optimize the trade-off between improving the ease of sampling each transitional PDF (by evolving β slowly and thus keeping the new transitional PDF close to the previous PDF) with minimizing the number of transitional PDFs that must be sampled before reaching the posterior PDF. To this end, each succeeding value for β_{j+1} is chosen dynamically following *Beck and Zuev* [2013].

CATMIP features other dynamic adaptations to further increase sampling efficiency. First, after each update from β_j to β_{j+1}, we resample our sample models of p_j with probability proportional to $\dfrac{p_{j+1}}{p_j}$ so that sample models are distributed more similarly to p_{j+1} [*Ching and Chen*, 2007]. This allows samples to be instantly relocated from relatively lower probability regions to higher probability regions, combatting all three inefficiencies of the Metropolis algorithm . Second, the efficiency of each instance of the Metropolis algorithm is improved by optimizing the proposal PDF. Specifically, we choose the covariance matrix of the proposal PDF, $\mathbf{\Sigma}$, for p_{j+1} to be the covariance of the sample models of p_j reweighted to account for the updated value of β_{j+1} and scaled according to the acceptance rate from sampling p_j. This way, CATMIP automatically adapts its random walk to the covariances of the target PDF and rescales its step size to take larger steps when the acceptance rate is high and smaller steps when the acceptance rate is low, reducing potential inefficiency of the Metropolis algorithm due to a low acceptance rate. For more details on CATMIP, see *Minson et al.* [2013].

3. Procedure Tests with Ternary-Mixture Experiments

3.1. Experimental Design and Assumptions

We test the accuracy and uncertainties of spectral unmixing, using the workflow and algorithms detailed above in a set of six experiments. In the first four experiments, we consider ternary mixtures of olivine, enstatite, and anorthite with endmembers sieved to 45-75 μm grain sizes (Figure 7.3A; Table G1). The fifth and sixth experiments explore ternary mixtures of olivine, nontronite, and basaltic glass, each sieved to 45-75 μm grain sizes (Figure 7.3B; Table 7.1). The latter mixtures are more challenging due to the presence of basaltic glass, which has a low spectral contrast in the VSWIR wavelength range.

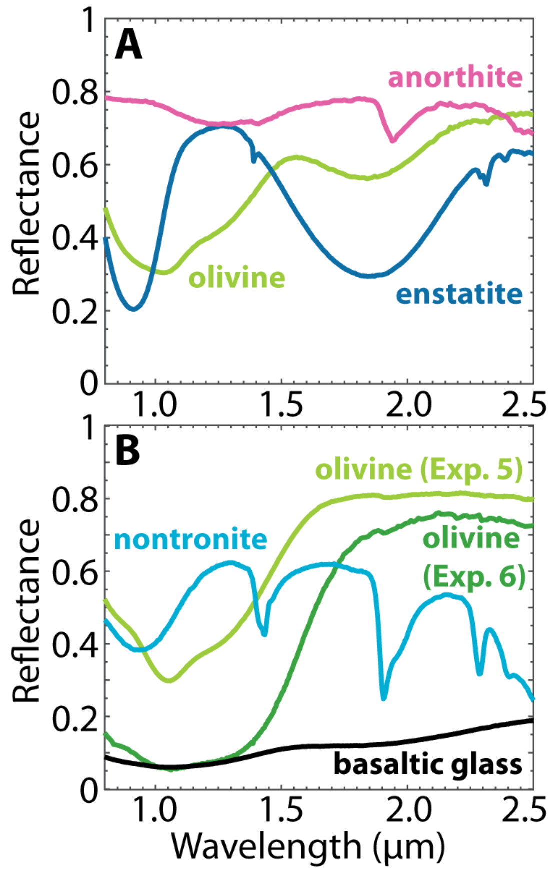

Figure 7.3: Reflectance spectra of mineral endmembers used for (A) the olivine/enstatite/anorthite and (B) olivine/nontronite/basaltic glass mixtures (Table 7.1).

In the first experiment, we explore only computational aspects using synthetic (computed) spectra. We use optical constants inverted from the laboratory reflectance spectra of the mineral endmembers of *Mustard and Pieters* [1987; 1989] and generate a suite of synthetic mixture spectra of known compositions using the forward Hapke model. We then attempt to unmix those same computed spectra back for composition and grain size. This experiment is designed to eliminate effects from any systematic error in the forward model.

That is, we know that the forward model is able to exactly reproduce the mixture spectra because it was directly used to generate them. Thus, Experiment 1 highlights any non-uniqueness in the solution that solely arises from tradeoffs between mineral abundances and grain sizes. Figure 7.4 shows an example computed spectrum for a 33.3 wt% olivine - 33.3 wt% enstatite - 33.3 wt% anorthite mixture (pink spectrum).

In the second experiment, we use the same synthetic spectra of known mineral composition and grain sizes as in the first experiment but added a ~3% Gaussian-distributed white noise to them (e.g., medium blue spectrum in Figure 7.4). This experiment was designed to isolate the added errors and uncertainties associated with instrumental noise by comparison with Experiment 1. While Compact Reconnaissance Orbiter Spectrometer for Mars (CRISM) noisy data are typically Poisson-distributed [e.g., *Kreisch et al.*, 2017], our intent here is not to reproduce accurate noise models for any single dataset but to illustrate more generally how noise affects unmixing errors and uncertainties.

In the third experiment, we invert for composition and grain sizes of the actual, laboratory-measured mixture spectra of *Mustard and Pieters* [1987; 1989] using optical constants derived from the endmember spectra of their experiments. Results from this experiment contain errors and uncertainties associated with both non-uniqueness of the solution, inversion to optical constants with an assumed grain size, imperfections of the forward model, and experimental effects. Thus, comparing Experiment 3 with Experiment 1 (which only incorporates errors and imperfections from non-uniqueness of the solution) allows to constrain with an upper bound the systematic errors arising from the forward Hapke model (e.g., note the difference between the light blue and pink spectra in Figure 7.4). We note that our analysis is similar to the study of *Mustard and Pieters* [1987; 1989] with two important differences: (1) we use known grain size to derive optical constants from the endmembers rather than using endmember single scattering albedo spectra directly in unmixing and (2) then we invert for grain sizes simultaneously with abundance, as opposed to prescribing them in the forward model. There may be some additional contributions to errors from the experiment setup, e.g., settling or sorting of grains in the sample cup; however, these were mitigated for to the greatest extent possible, as described in *Mustard and Pieters* [1987; 1989].

In a fourth experiment, we invert for composition and grain sizes of the same laboratory-measured mixtures as in the third experiment, to which we added Gaussian-distributed white noise (e.g., dark blue spectrum in Figure 7.4). This experiment was designed to isolate the added errors and uncertainties associated with instrumental noise by comparison with Experiment 3. Thus, comparing our Experiments 1-4 with those of *Mustard and Pieters* [1987] (prescribed grain sizes, $P=1$) and *Mustard and Pieters* [1989] (prescribed grain sizes, $B=0$, the effect of P is investigated) allows evaluation of the relative effects on inversion accuracy of noise, solution non-uniqueness when both grain size and abundance are simultaneously solved for, accuracy of the physical scattering model, and prescribed photometric functions.

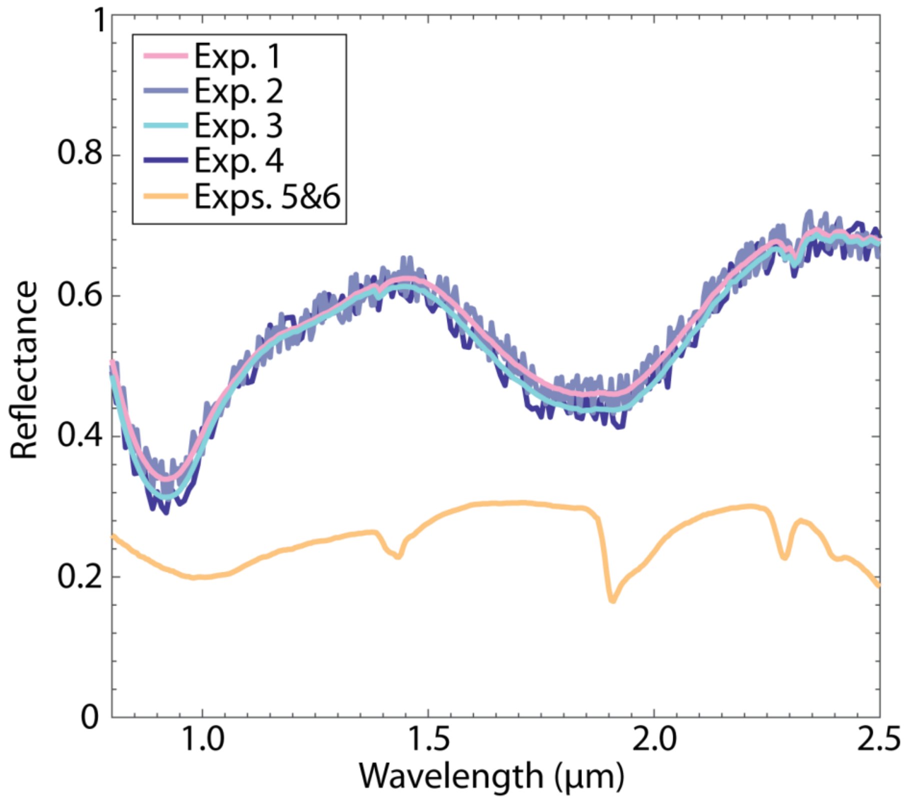

Figure 7.4: Example modelled MAP spectra for the 33.3%/33.3%/33.3% mixtures for all six experiments: computed mafic mixture (Experiment 1; pink), computed noisy mafic mixture (Exp. 2; purple), actual laboratory mafic mixture (Exp. 3; light blue), actual laboratory noisy mafic mixtures (Exp. 4; dark blue), and actual laboratory olivine-nontronite-glass mixture (Exps. 5 and 6; orange). Note that Experiments 1-4 and Experiments 5-6 involve different endmembers, as described in the text.

In the fifth experiment, we invert for composition and grain sizes of ternary laboratory mixtures of olivine, nontronite, and basaltic glass from [*Ehlmann*, 2010] (e.g., orange spectrum in Figure 7.4). This experiment is designed to illustrate the effects of added complexity (vs. Exp. 3), which may arise from hydrated phases with complex particle properties like nontronite [*Pilorget et al.*, 2016] and/or from phases with low spectral contrast like basaltic glass . Note that while in theory plagioclase in the mafic mixtures in experiments 1-4 is a low spectral contrast material, the particular sample used is hydrated, thus imparting spectral features of higher contrast.

Finally, in the sixth experiment, we invert for composition and grain sizes of ternary laboratory mixtures of olivine, nontronite, and basaltic glass (same as Exp. 5) using an input olivine endmember that is different from the actual olivine in the mixture (Figure 7.3B; see also *Trang et al.*, 2013). This experiment is designed to simulate a more “real-life”-like scenario, in which one does not know, a priori, the precise chemical composition of solid solutions in the target, and illustrates errors and uncertainties associated with the choice of mineral endmembers and their optical constants.

Because we use three endmembers to model all mixtures, including pure and binary mixtures, the reported experiments test the ability of our algorithm to identify the absence of a mineral endmember in a geologic target. In order to also test the ability of our algorithm to identify the presence of low spectral contrast mineral endmembers in a geologic target (such as basaltic glass), we performed an experiment similar to Experiment 5, but in which we omitted basaltic glass as an input mineral endmember. At least in the case of this particular set of minerals, modeled spectra did not fit the data, with corresponding RMS errors greater than 2% and as high as 8%, making apparent that at least one additional input mineral endmember was required. Such a procedure highlights the importance of initial iterative selection of endmembers and how an initially high RMS fit can signal missing phases (see section 2.2.1).

A seventh experiment is presented in a separate paper [*Lapôtre et al.*, 2017b]. In the latter, mineral composition and grain sizes of sands at the Bagnold Dunes of Gale crater, Mars, are evaluated from CRISM data and compared with ground-truth measured by the Curiosity rover. This experiment, compared with the first six, incorporates the added complexity of (i) atmospheric corrections, (ii) a large number of mineral endmembers, and (iii) the unknown precise chemical composition of solid solutions.

In all six experiments herein presented, we assume that grains are spherical, isotropic scatterers, and that phase angles are moderate such that backscattering effects can be ignored. Particle shape can also influence reflectance properties (e.g., *McGuire and Hapke*, 1995; *Grundy et al.*, 2000; *Souchon et al.*, 2011; *Pilorget et al.*, 2016) but we do not investigate this effect systematically here. In all experiments, the prior distributions in grain sizes were assumed uniform over a 10-800 μm range, and prior abundances were all assumed to be 33.3 wt%, i.e., to be uniform for each mixture. Finally, the diagonal elements of the covariance $\mathbf{C}_\chi$ were taken equal to $5\text{x}10^{-4}$ in all experiments, a value that was visually assessed to yield a satisfying range in accepted spectra (i.e., allowing for deviations between data and model at approximately the magnitude of instrumental noise; e.g., Figure 7.2A). For each individual mixture (25 mixtures in each of the first four experiments and 30 mixtures in the fifth and sixth experiments), we invert for a Markov-Chain of 25x10^3 accepted models.

In Sections 3.2-3.7, we present and discuss the results of our six experiments. To evaluate model accuracy, we use the mean error, defined as

$$\text{error} = \frac{\sum_{i=1}^{3} \left| m_{i,\text{truth}} - m_{i,\text{MAP}} \right|}{3} \tag{7.23a}$$

and

$$\text{error} = \frac{\sum_{i=1}^{3} \left| D_{i,\text{truth}} - D_{i,\text{MAP}} \right|}{3} \tag{7.23b}$$

as metrics for model error in abundances and grain sizes, respectively. Because all samples were sieved to 45-75 μm, we assume the true grain size, $D_{i,\text{truth}}$, to be equal to 60 μm. In the cases of pure samples or binary mixtures, where not all endmembers are present, the true grain sizes of the absent phase(s) are undefined, and Equation (23b) was modified to only take into consideration those phases that are present in the sample. In addition, we use the width of the 95% confidence interval, defined as the difference between the 2.5th and 97.5th percentiles of each parameter PDFs, as a metric for uncertainty.

Two additional metrics are used to quantify errors and uncertainties integrated over all mixtures for a given set of mineral endmembers – the average mean and absolute maximum errors/uncertainties. The average mean error/uncertainty is the value of the mean error/uncertainty (mean error is as defined in Equation (7.23)) averaged over all mixtures of a given experiment. It is thus a measure of typical errors/uncertainties one might expect from each experiment. The absolute maximum error/uncertainty is the largest discrepancy/uncertainty in either mineral abundance or grain size found across all mixtures of a given experiment for a single phase. It is thus a measure of the "worst case" scenario, i.e., the largest errors/uncertainties one might expect from each experiment.

3.2. Experiment 1: Computed Olivine-Enstatite-Anorthite Mixtures

Figure 7.5 shows errors (A and C) and uncertainties (B and D) associated with mineral abundance and grain size predictions in the first experiment, which used computed spectra of olivine-enstatite-anorthite mixtures. Mean errors and uncertainties in calculated abundances are relatively low for all mixtures (average mean error of ~0.6 wt%, average mean uncertainty of ~7.1 wt%). The absolute maximum error in abundance remains relatively low for this entire experiment (~4.8 wt%; anorthite in a high olivine ternary mixture). Average mean error and uncertainty in grain size over all mixtures are relatively low (26 and 332 μm, respectively), but absolute maximum error (732 μm; anorthite) and uncertainty (774 μm; enstatite) are large. The largest grain size error was found in the ternary mixture with high olivine content. Grain size uncertainties are high for most mixtures. In fact, for the grain size range we permit (10-800 μm), a complete lack of sensitivity to grain size would yield an uncertainty of ~750 μm. Thus, results for the mixtures with the maximum errors and uncertainties suggest that grain size remains basically unconstrained in these cases.

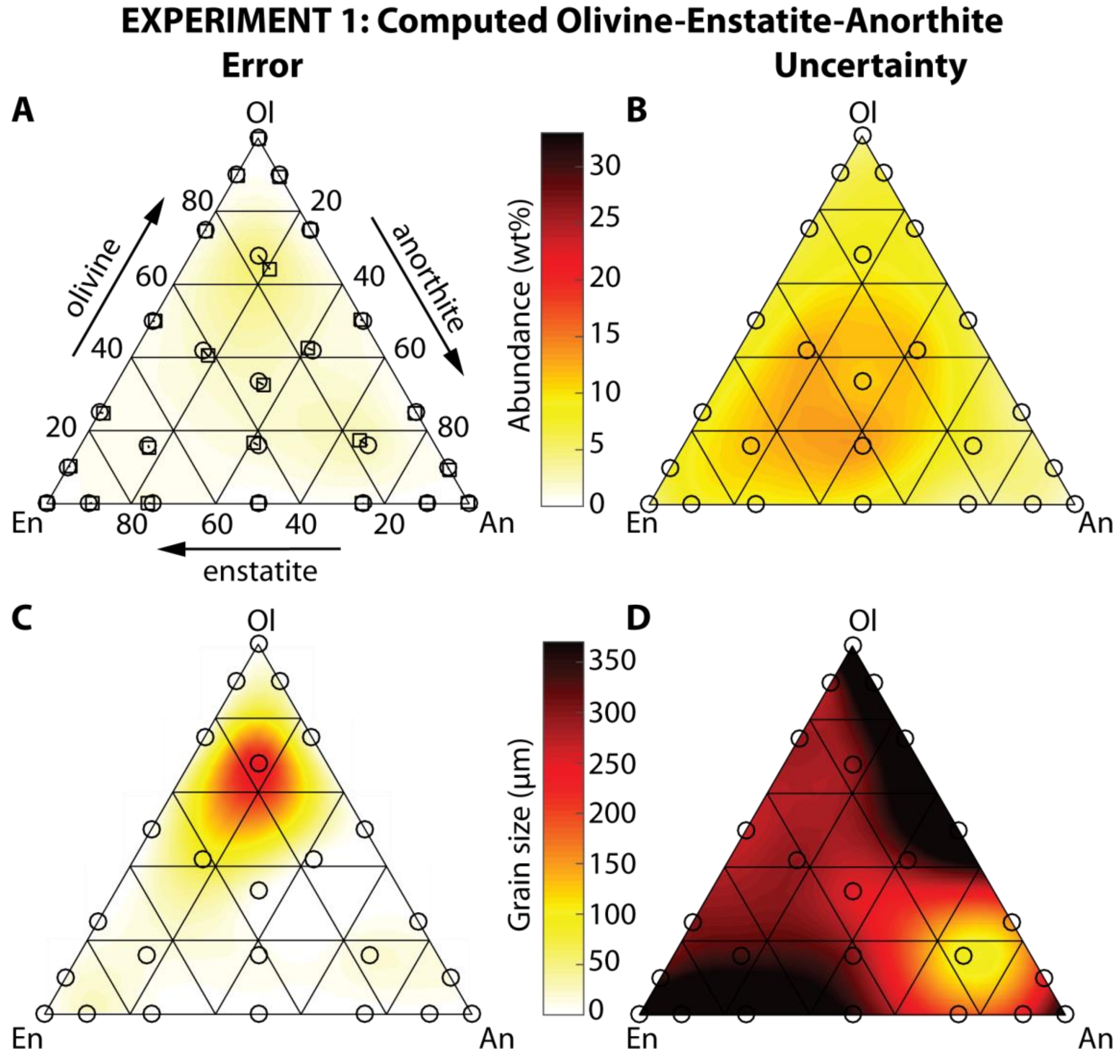

Figure 7.5: Experiment 1 – Ternary plot of mean error in abundance and grain size (A and C, respectively) and mean uncertainty in abundance and grain size (B and D, respectively). In (A), open circles indicate the true compositions corresponding to the input spectra, while open squares indicate their corresponding modeled composition. Solid lines are drawn between true and modeled compositions to avoid confusions when errors are large.

Binary mixtures with low anorthite content produce the largest uncertainties in grain size. Errors in abundances are slightly higher where uncertainties in abundances are higher, which may indicate that tradeoffs between abundances and grain sizes enable different, sometimes less accurate, models to produce satisfying fits to the data. We interpret this result to be caused by abundance-grain size tradeoffs for the two mafic mineral endmembers.

As a sensitivity analysis, we performed the same experiment for synthetic mixtures corresponding to 500 μm grains (compared with 60 μm in Exp. 1). Resulting errors and uncertainties were overall statistically indistinguishable from those of Experiment 1.

3.3. Experiment 2: Noisy Computed Olivine-Enstatite-Anorthite Mixtures

Figure 7.6 shows errors (A and C) and uncertainties (B and D) associated with mineral abundances and grain sizes in the second experiment, which used computed spectra in Experiment 1 with additional, simulated random noise. Average mean error in calculated abundances is slightly higher than in Experiment 1 (~1.3 wt%), but average mean uncertainty is about the same (~7.1 wt%). The absolute maximum error and uncertainty in abundance are ~6.7 wt% (anorthite in a 42 wt% olivine - 16 wt% enstatite - 42 wt% anorthite mixture) and ~15.8 wt% (anorthite in a 75 wt% enstatite - 25 wt% anorthite mixture), respectively. Errors and uncertainties in abundances are roughly homogeneously distributed across the ternary diagram with subtly higher values for ternary mixtures than binary mixtures. Average mean error in grain size is also higher than for Experiment 1 (56 μm), but average mean uncertainty is similar (~338 μm). Patterns in errors and uncertainties for grain size are overall similar to those of Experiment 1. Absolute maximum error (733 μm) and uncertainty (775 μm) in grain size both occur for anorthite, and reflect a lack of sensitivity to anorthite grain size for binary mixtures with low anorthite content.

Compared with Experiment 1, noise in the data appears to have approximately doubled errors but left uncertainties unchanged. The abundance/grain size tradeoff observed in Figure 7.5 for high-olivine ternary mixtures is not readily apparent in Figure 7.6, most likely due to noise increasing the number of acceptable models, effectively smearing the correlation between abundance and grain size.

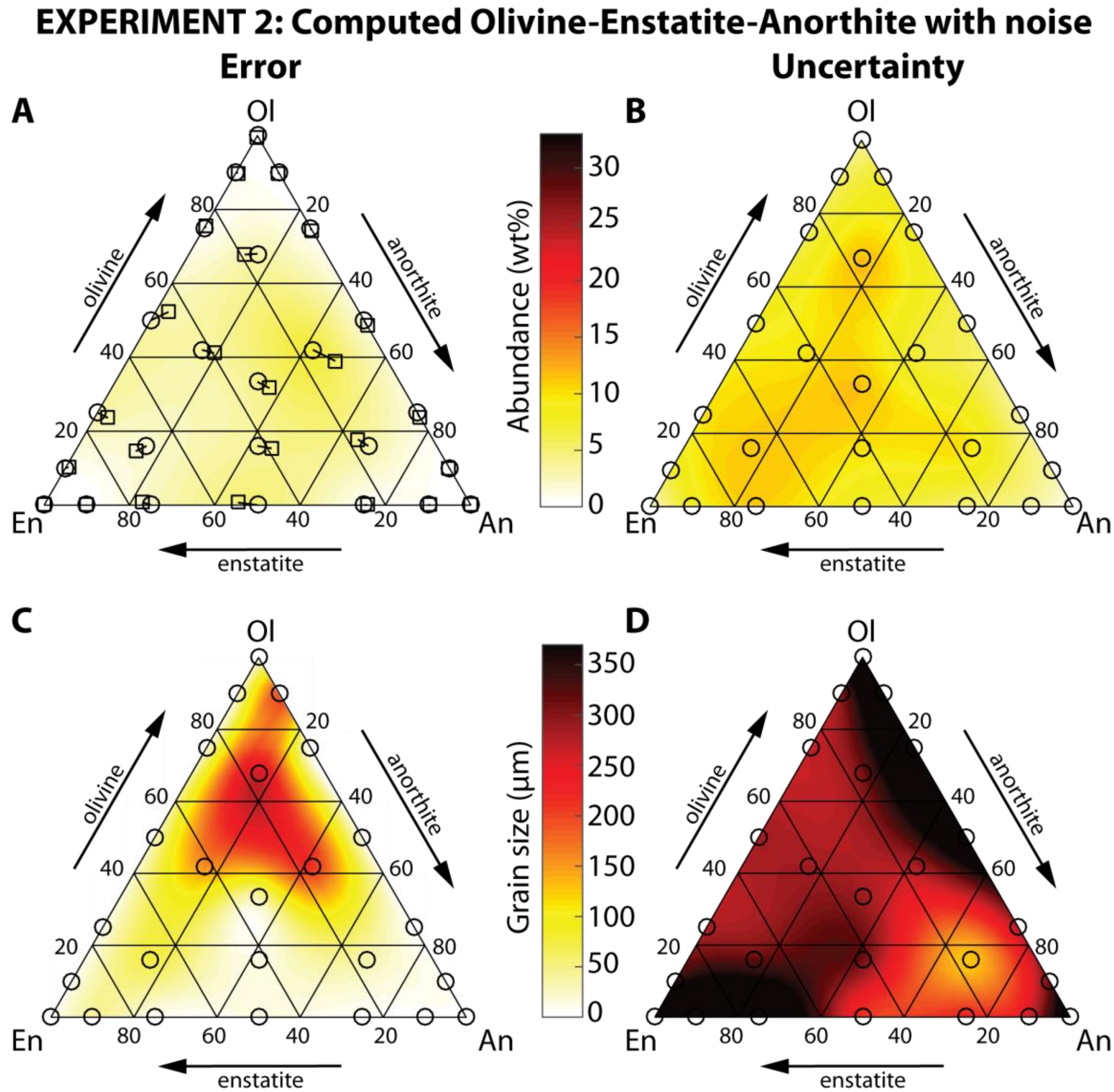

Figure 7.6: Experiment 2 – Ternary plot of mean error in abundance and grain size (A and C, respectively) and mean uncertainty in abundance and grain size (B and D, respectively). In (A), open circles indicate the true compositions of the input spectra herein inverted, while open squares indicate their corresponding modeled composition. Solid lines are drawn between true and modeled compositions to avoid confusions when errors are large.

3.4. Experiment 3: Laboratory-Measured Olivine-Enstatite-Anorthite Mixtures

Figure 7.7 shows errors (A and C) and uncertainties (B and D) associated with mineral abundances and grain sizes in the third experiment, for which we performed unmixing of actual, laboratory-measured mixture spectra. Average mean errors and uncertainties in abundances increase relative to Experiments 1 and 2 (to ~2.5 wt% and ~8.9 wt%, respectively). The absolute maximum error corresponds to a 90% olivine-10% anorthite binary mixture, with a ~13.3 wt% error in olivine (and a >12 wt% error in anorthite). The absolute maximum uncertainty in abundance occurs for a binary mixture (~20.9 wt% for anorthite in a 75 wt% enstatite - 25 wt% anorthite mixture). Average mean error and uncertainty in grain size are of 69 and 374 μm, respectively. Similar to Experiments 1 and 2, mixtures with low anorthite contents yielded less accurate grain sizes, with an absolute maximum error of 680 μm occurring for anorthite in a 90 wt% olivine - 10 wt% anorthite mixture, showing a complete lack of sensitivity to anorthite grain size for those mixtures (absolute maximum uncertainty of 747 μm). Interestingly, grain size uncertainties are lowest for mixtures with olivine and enstatite mixed in roughly equal proportions.

Figure 7.8 shows how error and uncertainty for individual minerals vary with the actual abundance of that same mineral in the mixture for Experiment 3. For these specific endmembers and mixtures, enstatite is generally more accurately (lower error) predicted for low enstatite content, anorthite for high anorthite content, and olivine for intermediate olivine contents (Figure 7.8A-B). For all three phases, abundance is more certainly (lower uncertainty) determined when the mineral is either absent or alone in the sample, i.e., the modeled composition is more likely to be accurate for mixtures dominated by a single phase (Figure 7.8E-F). Grain size errors and uncertainties exhibit a completely different dependence on abundance, and are highest when the abundance of the phase is low (Figure 7.8C-D and G-H). Grain sizes of anorthite are notably the most inaccurately and uncertainly determined, even at intermediate-to-high anorthite contents. Indeed, despite being hydrated, the anorthite sample has a relatively low spectral contrast, such that erroneous grain sizes do not significantly affect the spectral fit.

We find that errors in modeled abundances roughly double when grain sizes are left as free parameters and optical constants are used (Exp. 3 vs. *Mustard and Pieters*, 1987 and 1989, in which grain size was a fixed parameter and unmixing was based solely on endmember single scattering albedo spectra), and that systematic errors in abundances arising from either systematic errors in the forward model or experiment effects (e.g., settling of mineral grains in sample cup) are about four times those associated with solution non-uniqueness alone (Exp. 3 vs. Exp. 1).

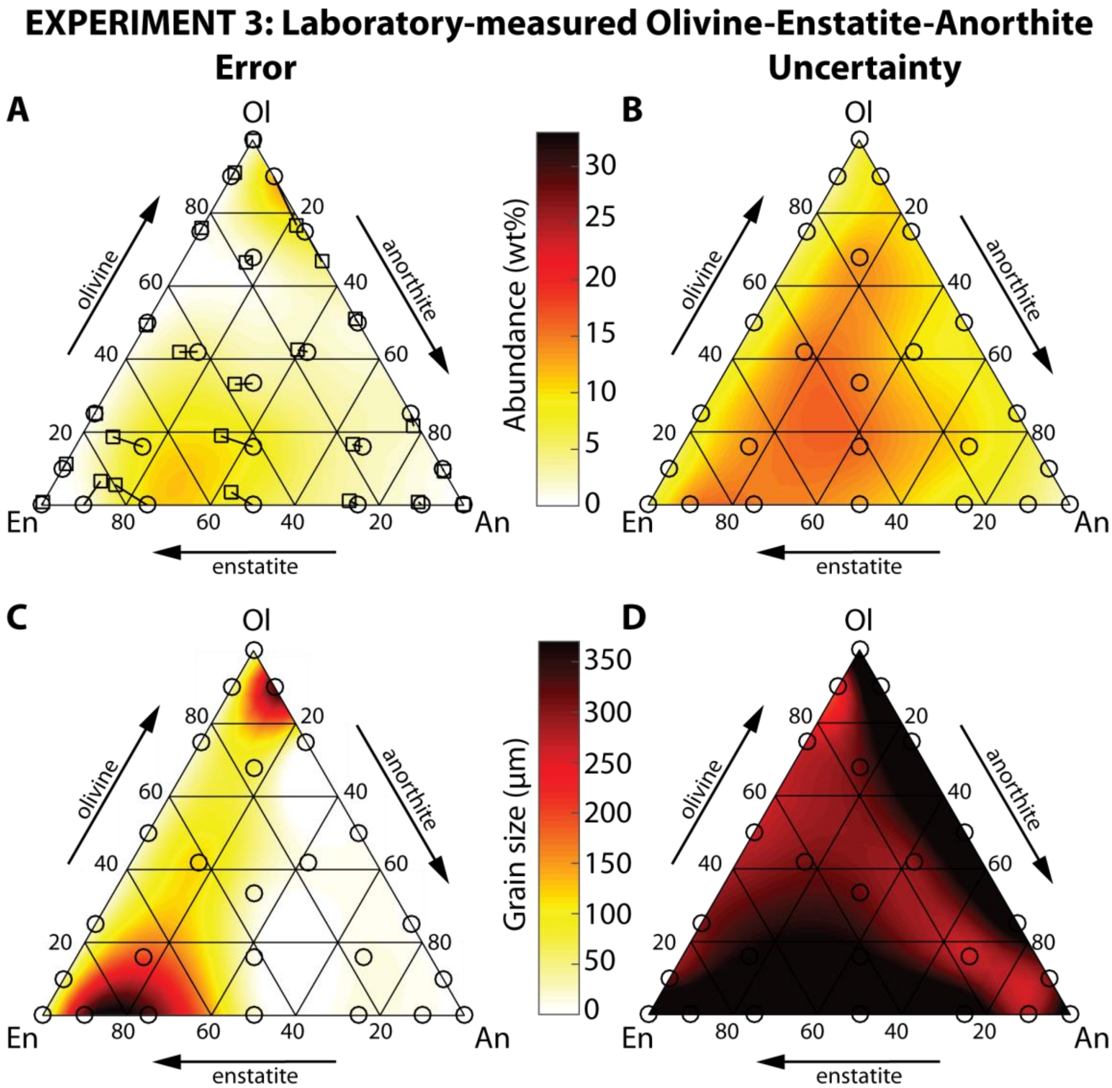

Figure 7.7: Experiment 3 – Ternary plot of mean error in abundance and grain size (A and C, respectively) and mean uncertainty in abundance and grain size (B and D, respectively). In (A), open circles indicate the true compositions of the input spectra herein inverted, while open squares indicate their corresponding modeled composition. Solid lines are drawn between true and modeled compositions to avoid confusions when errors are large.

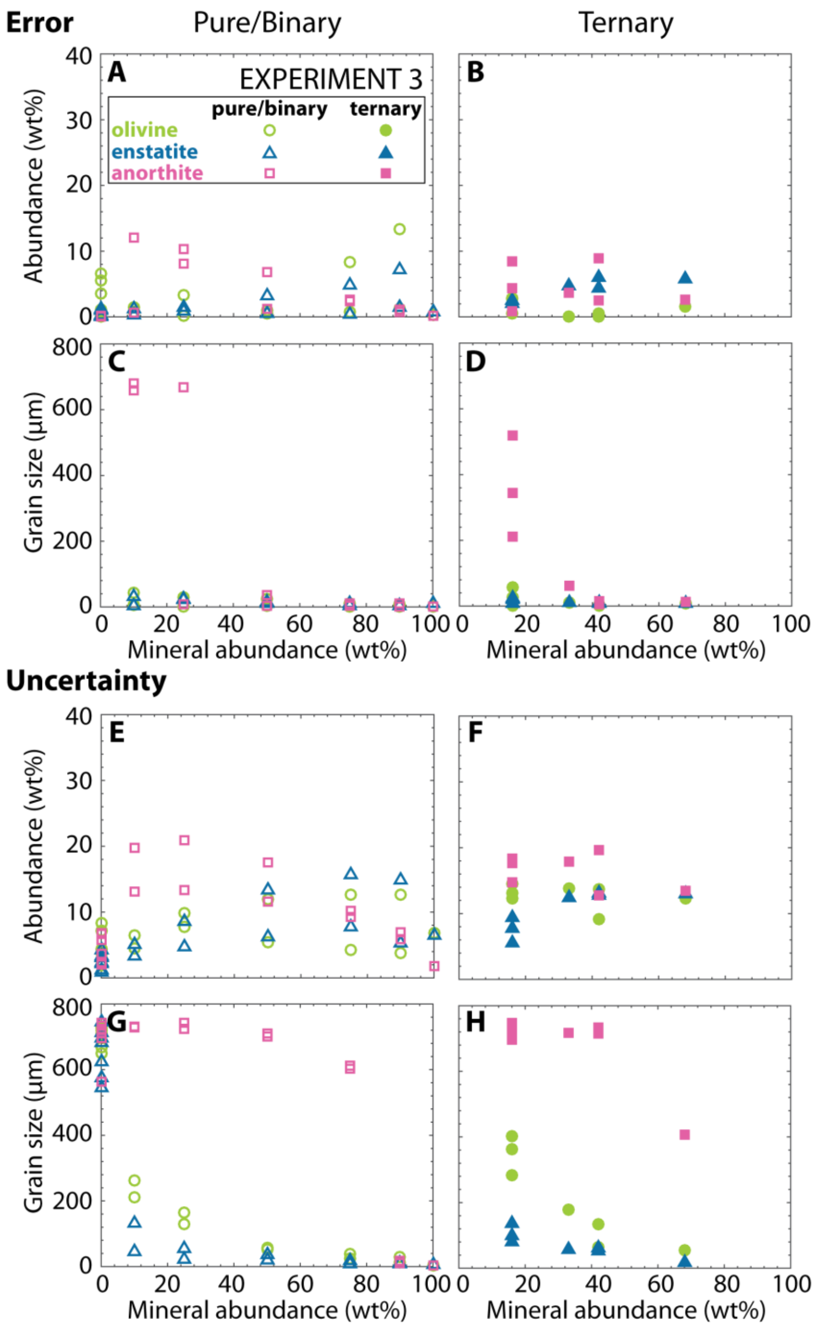

Figure 7.8: Experiment 3 – Variations in error (A-D) **and uncertainty** (E-H) as a function of the actual corresponding mineral abundances for olivine (green circles), enstatite (blue triangles), and anorthite (pink squares) abundances (A-B and E-F) and grain sizes (C-D and G-H), respectively. Pure samples and binary mixtures (A, C, E, G) are denoted by open symbols, while ternary mixtures (B, D, F, H) are denoted by filled symbols.

3.5. Experiment 4: Noisy Laboratory-Measured Olivine-Enstatite-Anorthite Mixtures

Figure 7.9 shows errors (A and C) and uncertainties (B and D) associated with mineral abundances and grain sizes in the fourth experiment, which used laboratory-measured spectra with simulated, random noise. Average mean error in calculated abundances is slightly higher than in Experiment 3 (~2.8 wt%), but average mean uncertainty is similar (~8.8 wt%). The absolute maximum error and uncertainty in abundance are both found to correspond to anorthite, and are ~15.1 wt% (in a 16 wt% olivine - 68 wt% enstatite - 16 wt% anorthite mixture) and ~21.0 wt% (in a 42 wt% olivine - 16 wt% enstatite - 42 wt% anorthite mixture), respectively. Patterns in errors and uncertainties in abundances are very similar to those of Experiment 3. Average mean error in grain size is also higher than for Experiment 3 (97 μm), but average mean uncertainty is similar (~368 μm). Absolute maximum error (722 μm, in a 16 wt% olivine - 68 wt% enstatite - 16 wt% anorthite mixture) and uncertainty (771 μm, in a 90 wt% olivine - 10 wt% anorthite mixture) in grain size both occur for anorthite, and reflect a complete lack of sensitivity to grain size for binary mixtures with anorthite.

Compared with Experiment 3, noise in the data slightly increased errors but left uncertainties unchanged. Finally, the similarities between Experiments 1-4 (e.g., Figures 7.5-7.9) provide confidence that the observed trends are intrinsic to the minerals investigated here and to the Hapke forward model, as opposed to non-reproducible patterns associated with randomness from our Bayesian approach.

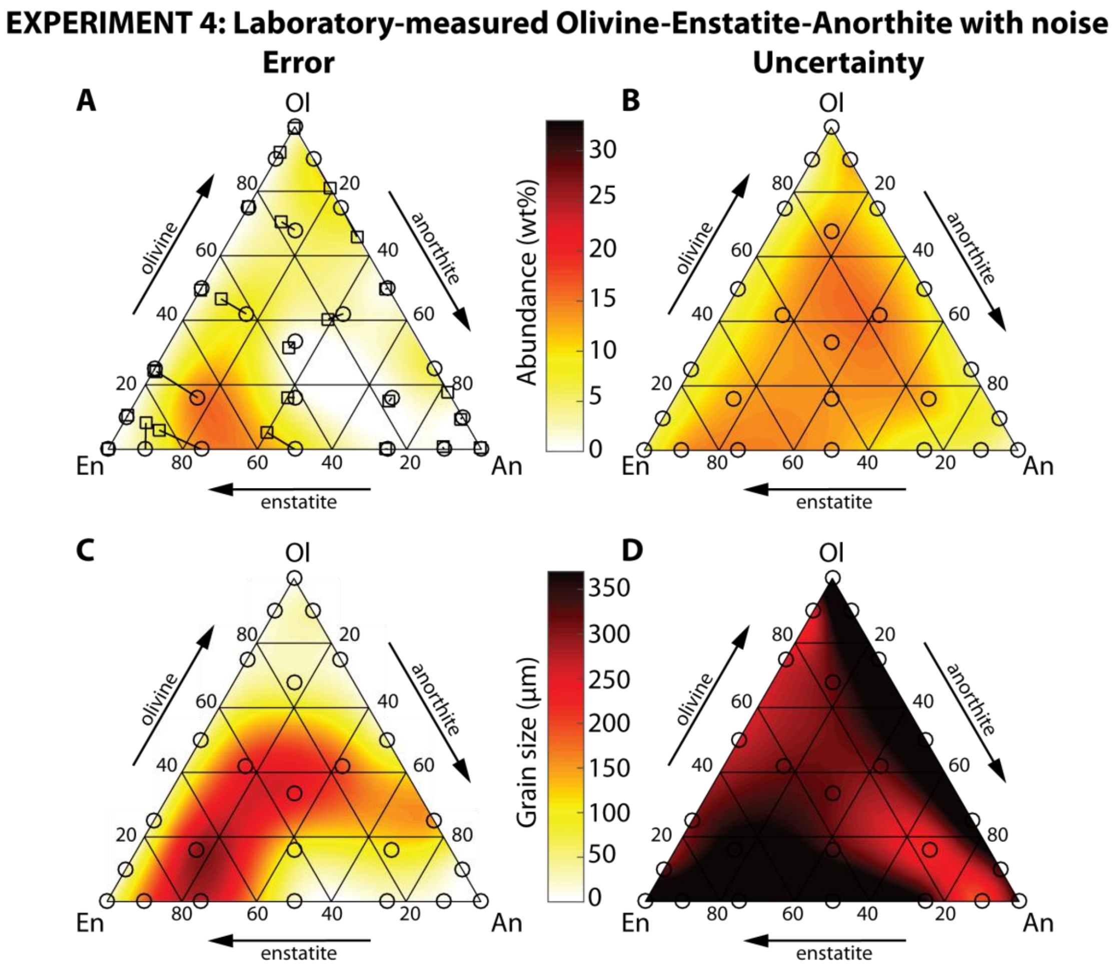

Figure 7.9: Experiment 4 – Ternary plot of mean error in abundance and grain size (A and C, respectively) and mean uncertainty in abundance and grain size (B and D, respectively). In (A), open circles indicate the true compositions of the input spectra herein inverted, while open squares indicate their corresponding modeled composition. Solid lines are drawn between true and modeled compositions to avoid confusions when errors are large.

3.6. Experiment 5: Laboratory-Measured Olivine-Nontronite-Glass Mixtures

Figure 7.10 shows errors (A and C) and uncertainties (B and D) associated with mineral abundances and grain sizes in the fifth experiment, where we performed unmixing of actual, laboratory-measured spectra from a different ternary mixture suite with a low contrast phase (glass). Average mean errors and uncertainties in abundances are yet higher for this set of mineral endmembers than for those of Experiment 4 (~5.6 wt% and ~17.2 wt%, respectively). Absolute maximum error occurs for nontronite (~22.8 wt%, in a 42 wt% olivine - 42 wt% nontronite - 16 wt% glass mixture), and absolute maximum uncertainty occurs for olivine (~48.9 wt% in a 30 wt% olivine - 70 wt% glass mixture). Errors and uncertainties in abundances are generally lower along the olivine – nontronite join and roughly increase as glass content increases. Errors in grain sizes appear to be higher for nontronite-glass binary mixtures of high nontronite content. Average mean error and uncertainty in grain sizes are of 59 μm and 313 μm, respectively. Absolute maximum error in grain size occurs for basaltic glass (700 μm, in a 90 wt% olivine - 10 wt% glass mixture), and absolute maximum uncertainty occurs for olivine (775 μm, for a 100 wt% nontronite sample).

Figure 7.11 shows how error and uncertainty for a given mineral vary with the actual abundance of that same mineral in the mixture. Errors and uncertainties in abundance are sometimes large when a mineral is absent or dominant in the mixture (e.g., no olivine and 95% basaltic glass; Figure 7.11A and E) but are typically highest at intermediate contents (Figure 7.11A-B and E-F). Olivine errors generally decrease at high olivine contents. Interestingly, while uncertainties in olivine and nontronite abundances generally decrease with increasing abundance, the opposite trend is observed for basaltic glass (Figure 7.11E-F). Trends in errors and uncertainties in grain sizes remain similar to those of Experiment 3, with error for a given constituent decreasing with increasing abundance of the phase (Figure 7.11C-D and G-H). The effect is most remarkable for basaltic glass, which has a very large error in grain size at low abundance.

The highest errors in abundance and uncertainties in both abundance and grain size occur for low olivine and nontronite but high glass contents. Basaltic glass, which has a low spectral contrast in this wavelength range, (e.g., Figure 7.3) is thus the likely dominant cause of errors and uncertainties in mineral abundances for this mixture suite, rather than abundance/grain size tradeoffs for a given endmember, which was more important in Experiment 3. Thus, comparing Experiments 3 and 5 highlights the specific challenges of certain mineral assemblages.

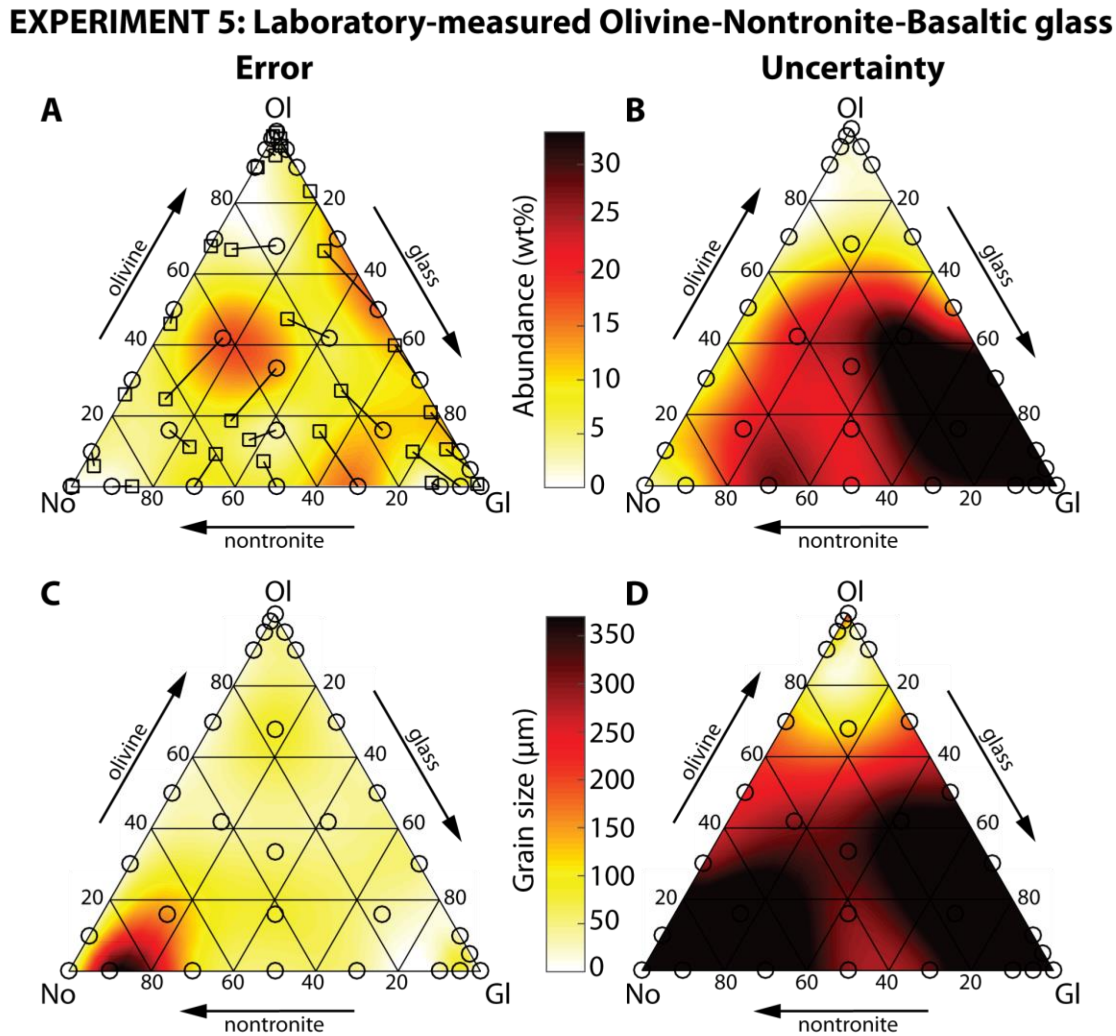

Figure 7.10: Experiment 5 – Ternary plot of mean error in abundance and grain size (A and C, respectively) and mean uncertainty in abundance and grain size (B and D, respectively). In (A), open circles indicate the true compositions of the input spectra herein inverted, while open squares indicate their corresponding modeled composition. Solid lines are drawn between true and modeled compositions to avoid confusions when errors are large.

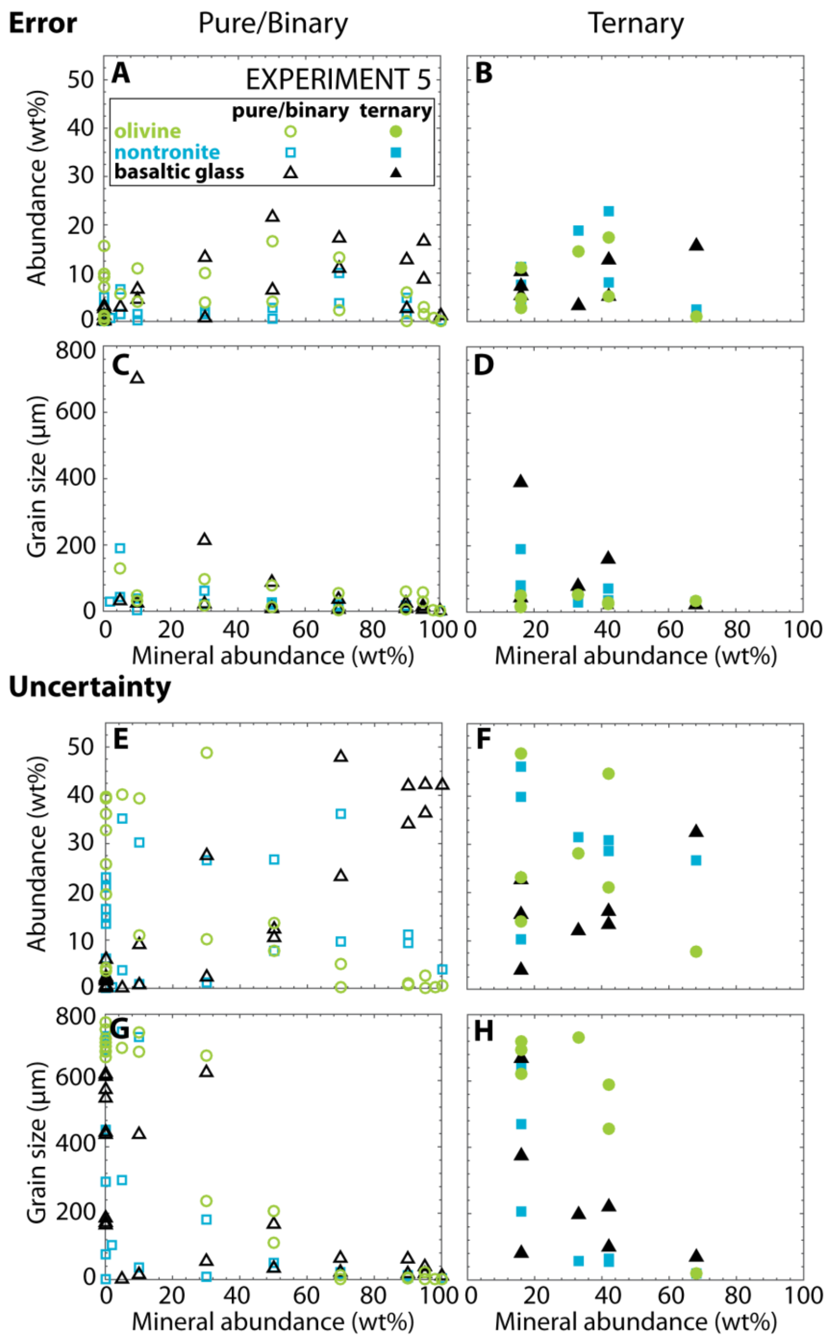

Figure 7.11: Experiment 5 – Variations in error (A-D) **and uncertainty** (E-H) as a function of the actual corresponding mineral abundance for olivine (green circles), nontronite (blue squares), and glass (black triangles) abundances (A-B and E-F) and grain sizes (C-D and G-H), respectively. Pure samples and binary mixtures (A, C, E, G) are denoted by open symbols, while ternary mixtures (B, D, F, H) are denoted by filled symbols.

3.7. Experiment 6: Laboratory-Measured Olivine-Nontronite-Glass Mixtures with a Different Olivine Endmember Optical Constant

In the sixth experiment, we test the effect of discrepancies between the optical constants of mineral endmembers in the target and those used in the inversion. In particular, we investigate the scenario of using an olivine with a different imaginary index of refraction in our forward model (Figure 7.12; Table 7.1). Figure 7.13 shows errors (A and C) and uncertainties (B and D) associated with mineral abundances and grain sizes in the sixth experiment. While the average mean error in abundances is higher than in Experiment 5 (~8.6 wt%), the average mean uncertainty is lower (~15.8 wt%). Absolute maximum error and uncertainty both occur for nontronite (~31.9 wt% and ~41.4 wt%, respectively). Patterns in abundance uncertainties are very similar to those observed in Experiment 5. Similarly, patterns in grain size errors and uncertainties are very similar to those of Experiment 5. Average mean error and uncertainty in grain sizes are of 64 μm and 335 μm, respectively. Absolute maximum error in grain size occurs for basaltic glass (702 μm, in a 90 wt% nontronite - 10 wt% glass mixture), and absolute maximum uncertainty occurs for olivine (766 μm, in a 16 wt% olivine - 16 wt% nontronite - 68 wt% glass mixture).

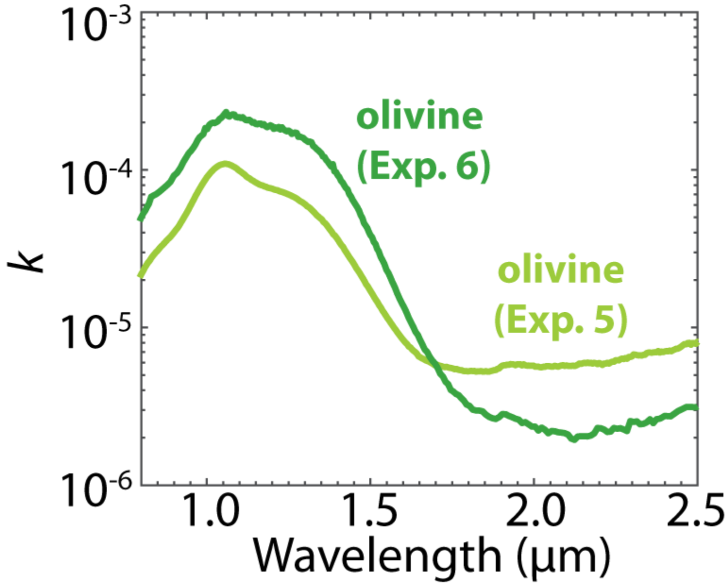

Figure 7.12: Imaginary index of refraction of the olivine endmember we use in Experiment 6 compared with that of the true olivine in the mixture (and used in Exp. 5).

The main difference between Experiments 5 and 6 is that errors in abundance increase, but corresponding uncertainties decrease. We interpret this trend as the result of a generally poorer fit to the data due to the different olivine (higher error) but fewer mineral assemblages yielding acceptable fits (lower uncertainty). Errors in abundance are now clearly highest for mixtures with moderate amounts of olivine.

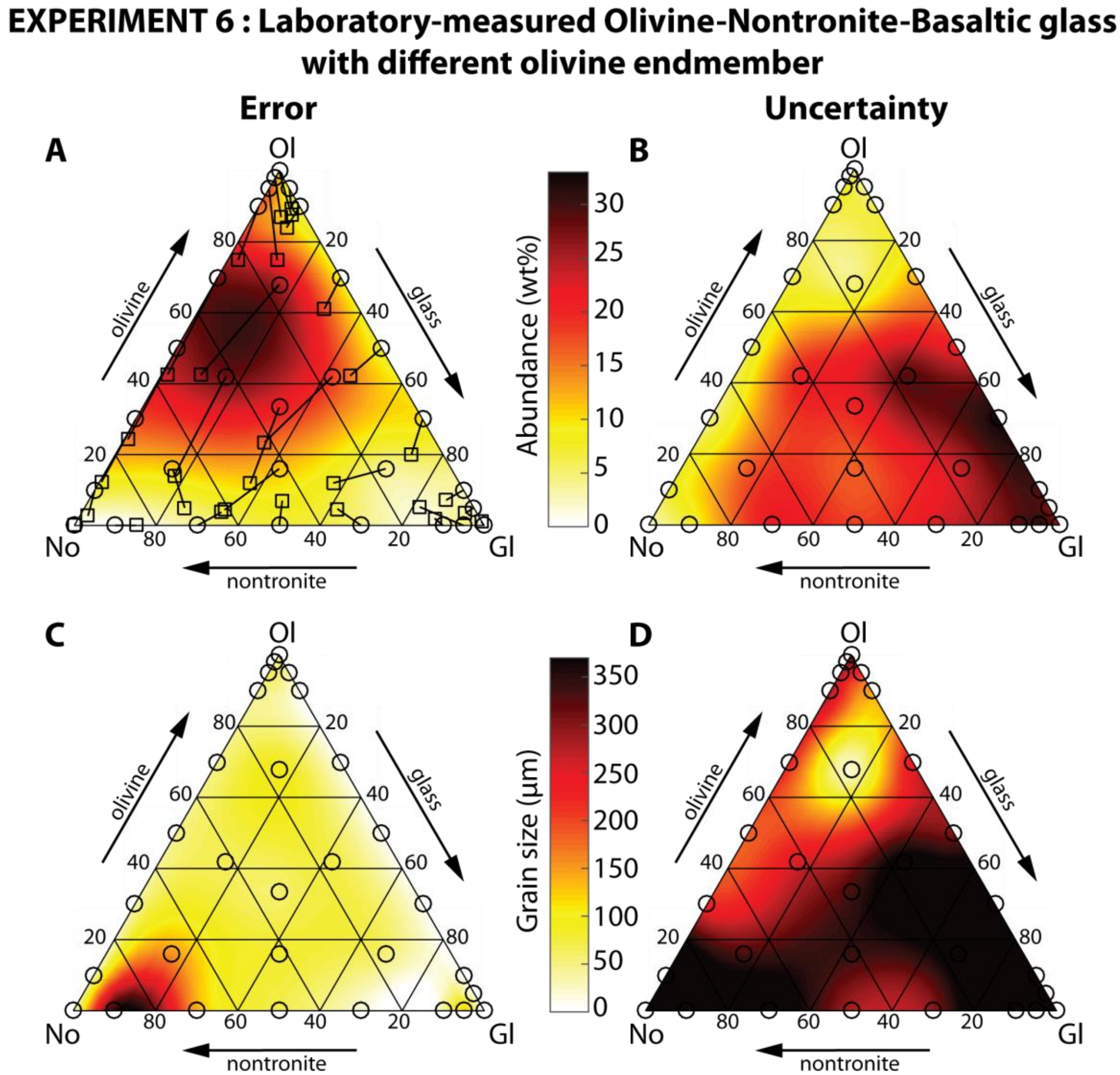

Figure 7.13: Experiment 6 – Ternary plot of mean error in abundance and grain size (A and C, respectively) and mean uncertainty in abundance and grain size (B and D, respectively). In (A), open circles indicate the true compositions of the input spectra herein inverted, while open squares indicate their corresponding modeled composition. Solid lines are drawn between true and modeled compositions to avoid confusions when errors are large.

4. Discussion

Figure 7.14 summarizes the average mean and absolute maximum errors and uncertainties in abundance and grain size for all six experiments. Overall, average errors between MAP modeled compositions and true compositions are low for both mixtures investigated (<10 wt. % abundance; <100 μm in grain size). However, specific mixtures can be more prone to tradeoffs between mineral abundances and grain sizes or have low spectral contrast endmembers, such that relatively large errors may arise (e.g., up to ~32 wt% for one endmember for one mixture in Exp. 6).

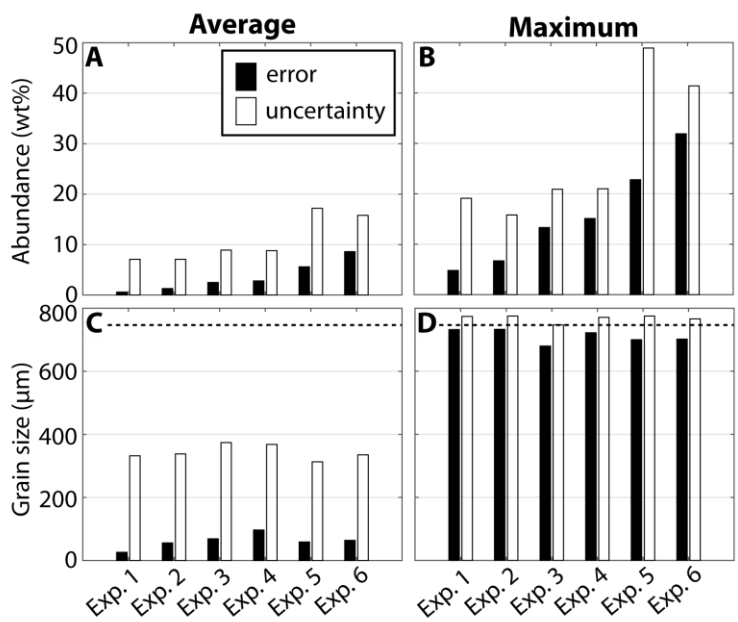

Figure 7.14: Summary of Experiments 1-6. Average mean (A and C) and absolute maximum (B and D) errors (black) and uncertainties (white) of inverted mineral abundances and grain sizes, respectively. Dashed line in (C) and (D) represents the expected uncertainty for uniform grain size distributions over the allowed range, i.e., the uncertainty corresponding to a complete lack of sensitivity of the model on grain size.

Overall, through these six experiments, we showed that:

(i) Spectral unmixing with the Hapke model provides weak constraints on grain size (Exp. 1 and all others). In general, uncertainty on derived grain sizes is large, and there is little sensitivity to grain size for most phases with low abundances.

(ii) The inherent non-uniqueness of the solution alone, due to tradeoffs between abundance and grain size, leads to typical errors < ~5 wt% in abundance for mafic mixtures (Exp. 1).

(iii) A ~3% noise in the data increases errors by up to ~2 wt% (Exps. 1 vs. 2 and Exps. 3 vs. 4).

(iv) The particular tradeoffs leading to errors and uncertainties are intrinsic to the mineral phases in the mixture (Exps. 3 vs. 5). For example, the presence of low-spectral contrast phases such as basaltic glass may further decrease the accuracy of the inversion technique.

(v) Unmixing of laboratory data as opposed to synthesized data increases errors in abundance by a factor of ~4. Thus, if this is due to systematic errors associated with the forward physical model and assumptions therein, were a perfect model to exist, errors in abundance could be reduced by a factor of ~4 (Exps. 1 vs 3). However, uncertainties remain high due to non-uniqueness of the inverse problem. Additional experiments and characterization of samples surfaces might reveal if this were instead an experimental artifact (e.g., settling of certain composition grains away from the optical surface).

(vi) Using slightly inaccurate optical constants may lead to an increase in abundance error (of ~3 wt% in the case of Exp. 6 vs. Exp. 5) but a decrease in abundance uncertainty (of ~1.5 wt%), due to fewer assemblages yielding acceptable fits to the data.

Our results have significant implications for the use of spectral unmixing of VSWIR remote sensing data. First, the Hapke model best-fit can be highly accurate (<1 wt. % error) and, indeed, is accurate (<10 wt. % error) on average. This is true even in the face of significant noise, which slightly increases error but does not appreciably change uncertainty. However, the high magnitude of errors in abundance unmixing results (20-30 wt. %) observed for a small subset of mixtures might lead to incorrect conclusions about composition and thus active geologic processes. Most worrisome is the fact that which mixtures/planetary surfaces will exhibit high errors cannot fully be predicted. One cause for higher errors appears to be low spectral contrast phases, the presence of which is hard to know a priori. A second cause for higher errors may be more tractable: inherent non-uniqueness in fits as the effects of mineral abundance and grain sizes tradeoff within the permitted range of model misfit. Our model results show greater abundance errors than *Mustard and Pieters* [1987] for their mixtures because they constrain grain size while we do not. This emphasizes a key role that independent constraints on grain size – e.g., from thermal inertia [e.g., *Liu et al.*, 2016] or from geologic context [e.g., *Lapôtre et al.*, 2017b] – can have in effectively minimizing the errors in unmixing data. Altogether, our results highlight the importance of calculating uncertainties on unmixing model fits and considering the geological implications of the full range of permitted solutions, rather than interpretations relying on a sole acceptable solution. Our overall recommendation is to report both the MAP and the full 95% confidence interval (or whatever confidence interval is desired) to properly acknowledge the relatively high uncertainties from spectral unmixing [see for an example *Lapôtre et al.*, 2017b].

Additional work might examine the above points (iv)-(vi) through additional laboratory experiments with constituent mixtures relevant to planetary surfaces. In particular for (v), efforts should be made to independently characterize optical surfaces when acquiring spectral data (e.g., by photography or microimaging spectroscopy) to definitively separate systematic errors in the construction of the forward model from experimental effects, thus enabling the formulation of improved radiative transfer models.

5. Conclusion

Reflected light in the VSWIR wavelength range provides key information on surface composition, and mineral/mineraloid/ice/organic abundances and grain sizes can be estimated from spectral unmixing. Nevertheless, our datasets demonstrated that solutions to the quantitative inverse problem are non-unique and highlight the need for more sophisticated unmixing approaches that simultaneously obtain both a best fit and the range of uncertainty, which includes consideration of multiple permitted solutions. Our combined Hapke model with MCMC sampler illustrated the effects of inherent tradeoffs between abundance and grain size, noise in the data, likely systematic model errors, the precise suite of mineral endmembers present, and choice of optical constants. We find that spectral unmixing is only weakly and selectively sensitive to grain size, with virtually no sensitivity to grain size at all for phases with low abundances in the mixtures investigated here. For synthesized spectra of the particular mixture compositions examined, tradeoffs between mineral abundances and grain sizes lead to typical errors in the inverted abundances of ~1 wt% (maximum 5 wt. %), while instrumental noise may increase them by up to ~2 wt%. When actual laboratory data are examined, errors increase by a factor of ~4, likely associated with systematic errors in the forward model, though experimental artifacts cannot be excluded as a contributor to the error. In general, inverted mineral abundances are most accurate and certain when a given mineral is either present at minor abundances or alone in a mixture, while accuracy and certainty in inverted grain sizes increases with the relative abundance of corresponding minerals. For our olivine-nontronite-basaltic glass mixture, we found that typical errors are even higher, generally ~6 wt% but up to ~23 wt% due to the presence of the relatively featureless, low spectral contrast basaltic glass. We also find that using slightly inaccurate optical constants may increase errors but decrease uncertainties in abundances, due to fewer mineral assemblages fitting the data.

Overall, we find that uncertainties associated with spectral unmixing are large. These large uncertainties emphasize the need for (i) more laboratory-based studies encompassing more mineral phases and larger grain-size ranges, and (ii) a probabilistic approach to spectral unmixing that allows characterizing the likelihood of sets of mineral assemblages, and as such characterizes the degree of confidence with which one may interpret spectral data in terms of surface composition.

Suite of mineral endmembers	**Sample type**	***Spectrum ID**
Olivine-enstatite-anorthite (25 spectra)	pure olivine	C1PO17*
	pure enstatite	C2PE12*
	pure anorthite	C1PA12*
	olivine-enstatite binary mixtures	CBXO15-19*
	olivine-anorthite binary mixtures	CBXO20-24*
	enstatite-anorthite binary mixtures	CBXA01-05*
	ternary mixtures	CMXO30-36*
Olivine-nontronite-basaltic glass (30 spectra)	pure olivine (Exp. 5)	C1BE28*
	pure olivine (Exp. 6)	HS285.4B**
	pure nontronite	C1BE100*
	pure glass	C2BE14*
	olivine-nontronite binary mixtures	C1BE30-136*
	olivine-glass binary mixtures	C1BE130-136*
	nontronite-glass binary mixtures	C1BE101-106*
	ternary mixtures	C1BE150-156*

Table 7.1: Reflectance spectra used in this study (*RELAB Brown/NASA-Keck spectral library, ** USGS spectral library; *Clark et al.*, 2007).

Acknowledgments and Data

We thank Ryan Anderson and Tim Titus of the U.S. Geological Survey for reviews of our manuscript, and Yang Liu and William Farrand for their constructive comments. We also thank James Beck for early discussions on MCMC methods. This research utilizes spectra acquired by Carlie Peters, John Mustard, and Bethany Ehlmann with the NASA/Keck RELAB facility at Brown University. All Matlab scripts to run the MCMC procedure are available for download at http://resolver.caltech.edu/CaltechAUTHORS:20170302-115016869. M.G.A.L. was partially funded by a NASA Earth and Space Science Fellowship (12-PLANET12F-0071) and from a MSL Participating Scientist Program grant to B.L.E. We acknowledge the support of a NASA PGG grant to John Mustard for acquisition of mixture data for experiments 5 and 6. Laboratory spectra presented in this paper are available in the RELAB Brown/NASA-Keck spectral library.

C h a p t e r 8

COMPOSITIONAL VARIATIONS IN SANDS OF THE BAGNOLD DUNES, GALE CRATER, MARS, FROM VISIBLE-SHORTWAVE INFRARED SPECTROSCOPY AND COMPARISON WITH GROUND TRUTH FROM THE CURIOSITY ROVER

Mathieu G. A. Lapôtre, Bethany L. Ehlmann, Sarah E. Minson, Raymond E. Arvidson, Francois Ayoub, Abigail A. Fraeman, Ryan C. Ewing, and Nathan T. Bridges

This chapter was published as:
Lapôtre, M. G. A., et al. (2017), Compositional Variations in Sands of the Bagnold Dunes, Gale Crater, Mars, from Visible-Shortwave Infrared Spectroscopy and Comparison with Ground Truth from the Curiosity Rover, *Journal of Geophysical Research: Planets*, in press.

Abstract. During its ascent up Mount Sharp, the Mars Science Laboratory Curiosity rover traversed the Bagnold Dune Field. We model sand modal mineralogy and grain size at four locations near the rover traverse, using orbital shortwave infrared single scattering albedo spectra and a Markov-Chain Monte Carlo implementation of Hapke's radiative transfer theory to fully constrain uncertainties and permitted solutions. These predictions, evaluated against in situ measurements at one site from the Curiosity rover, show that XRD-measured mineralogy of the basaltic sands is within the 95% confidence interval of model predictions. However, predictions are relatively insensitive to grain size and are non-unique, especially when modeling the composition of minerals with solid solutions. We find an overall basaltic mineralogy and show subtle spatial

variations in composition in and around the Bagnold dunes, consistent with a mafic enrichment of sands with cumulative aeolian-transport distance by sorting of olivine, pyroxene, and plagioclase grains. Furthermore, the large variations in Fe and Mg abundances (~20 wt%) at the Bagnold Dunes suggest that compositional variability induced by wind sorting may be enhanced by local mixing with proximal sand sources. Our estimates demonstrate a method for orbital quantification of composition with rigorous uncertainty determination and provide key constraints for interpreting in situ measurements of compositional variability within martian aeolian sandstones.

1. Introduction

Gale Crater was chosen as the landing site for the Mars Science Laboratory (MSL) Curiosity rover because of its well-defined sedimentary rock record, inferred to span a major climate change and drying of the martian surface environment [e.g., *Anderson and Bell III*, 2010; *Milliken et al.*, 2010]. Gale Crater also contains dark mafic sands accumulating on the crater floor as sand sheets and sand dunes (Figure 8.1A) with some fraction of the grains blown out of the crater to the south [*Anderson and Bell III*, 2010; *Day and Kocurek*, 2016; *Day et al.*, 2016]. The Curiosity rover drove through a topographic low within the broad expanse of bedrock that defines the base of Mt. Sharp (officially named Aeolis Mons), which is the principal target of Curiosity's investigation. Mafic sands accumulated near this topographic low form a dune field, informally named the Bagnold Dune Field (Figure 8.1A). The Bagnold Dunes are morphologically diverse: individual barchan dunes at the upwind (or trailing) edge migrate to the southwest, merge into barchanoidal ridges downwind, and ultimately transition into linear dunes paralleling the margins of Mount Sharp (Figure 8.1A). Average wind directions inferred from the orientation of dunes [e.g., *Hobbs et al.*, 2010; *Silvestro et al.*, 2013; *Day and Kocurek*, 2016] and ventifacts [*Bridges et al.*, 2014] are mostly from northeast to southwest near the rover path.

Sand composition in Gale crater was modeled to be olivine-rich [e.g., *Rogers and Bandfield*, 2009] and later estimated to contain olivine of forsterite number (Fo) ~55 [*Lane and Christensen*, 2013], using data from the Thermal Emssion Spectrometer (TES), acquired at a resolution of approximately 3x6 km/pixel. Spectral variability in the visible-to-shortwave infrared (VSWIR) wavelength range was observed at a finer spatial resolution (18 m/pixel) from Compact Reconnaissance Imaging Spectrometer for Mars (CRISM) data acquired in the northeast portion of the dune field, near the Curiosity's landing site [*Seelos et al.*, 2014]. The barchan dunes and the crests of linear dunes have stronger olivine signatures, while the stoss sides of barchanoidal ridges have stronger high-Ca pyroxene signatures (Figure 8.1B-D). These observations likely indicate spatial variability in composition and may result from several mechanisms, including variable dust cover, mixing of different sediment sources, and/or wind sorting of mineral phases by grain size, density, and shape.

Wind sorting has been suggested at various places around Mars. For example, *Chojnacki et al.* [2013] demonstrated variability in the iron oxidation state of materials in sand dunes due to local aeolian fractionation at Capri Chasma and Melas Chasma from High Resolution Imaging Science Experiment (HiRISE) band ratios. Variability in thermal inertia was observed by *Pan and Rogers* [2017] within several dune fields on Mars, indicating spatially inhomogeneous grain size distributions. Global comparisons of sand composition have been made and showed that dark martian sands are primarily mafic with little compositional variation [*Poulet et al.*, 2009; *Tirsch et al.*, 2011]. However, quantitative estimates of variability in modal mineral composition and grain sizes in martian dune fields largely remain to be performed.

The composition of aeolian sedimentary rocks not only reflects that of the sediment source(s) but also subsequent modifications of the primary composition by sorting during transport and post-burrial diagenesis and alteration. Thus, a quantitative understanding of the degree of sand-sorting by martian winds is critical to the interpretation of in situ measurements of the compositional variability of aeolian sedimentary rocks, which have been observed both from orbit [*Milliken et al.*, 2014] and in situ with rovers [*Grotzinger et al.*, 2005; *Siebach et al.*, 2015, 2017;].

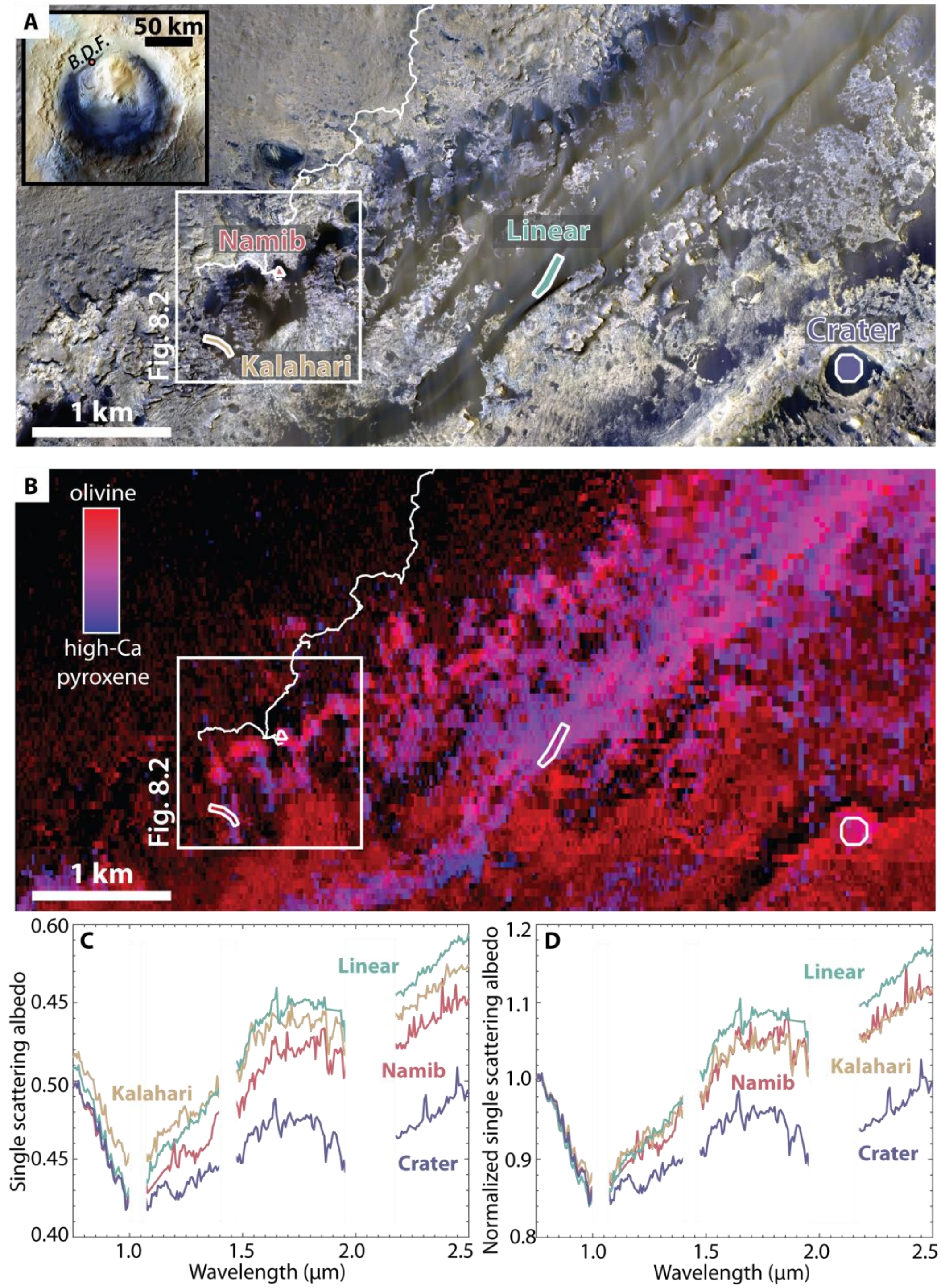

Figure 8.1: The Bagnold Dune Field. (A) HiRISE context map of the Bagnold Dunes of Gale crater, Mars, with ROIs and the traverse of the Curiosity rover up to sol 1371 (thin white line). Inset shows the location of the study area (orange circle) on a CTX/HRSC/Viking composite image of Gale crater, Mars (centered on -4.983ºN 137.765ºE; credit: NASA/JPL-Caltech/ESA/DLR/FU Berlin/MSSS);

the Bagnold Dune Field is labeled “B.D.F.”. The white box outlines the extent of Figure 8.2A-C. (B) Composite CRISM parameter map near the rover traverse within the Bagnold Dune Field with ROIs and the traverse of the Curiosity rover up to sol 1371 (thin white line). Red hues indicate relatively high values of OLINDEX3, i.e., stronger olivine signatures, while blue hues correspond to relatively high values of HCPINDEX2, i.e., stronger high-Ca pyroxene signatures [e.g., *Viviano-Beck et al.*, 2014]. ROIs are outlined. The white box outlines the extent of Figure 8.2A-C. (C) Raw and (D) normalized single scattering albedo spectra of the ROIs herein investigated—Namib Dune, Kalahari Dune, a linear dune, and a crater fill. Spectra in (D) were normalized by their SSA at 0.8 μm to highlight differences in continuum spectral slopes at longer wavelengths.

In this paper, we analyze orbiter-based data to qualitatively map the spectral variability within the Bagnold Dune Field near the rover traverse (Figure 8.1B-D) as well as invert for quantitative sand bulk composition and grain sizes at four unique locations—the Namib and Kalahari Dunes, a linear dune, and a crater fill (Figure 8.1A). We compare our orbital inferences with ground observations from the Curiosity rover at Namib Dune (Figure 8.1A) and infer the magnitude and causes of compositional variations observed from orbit.

2. Methods

2.1 Derived Orbital Data Products

CRISM measures radiance reflected from the martian surface at 544 discrete wavelengths from ~0.4 – 4.0 micrometers [*Murchie et al.*, 2009]. Full resolution targeted (FRT) CRISM scenes have spatial resolutions of ~18 m/pixel, and along-track oversampled (ATO) scenes can be acquired and processed with spatial resolutions of ~12 m/pixel or less [e.g., *Arvidson et al.*, 2015; *Kreisch et* *al.*, 2017]. Surface single scattering albedo (SSA) spectra were retrieved from measured I/F (CRISM image ATO0002EC79) using a lookup table. The latter was derived using a discrete ordinates radiative transfer model (DISORT) of atmospheric contributions from CO_2, CO, H_2O, dust, and ice aerosols [*Stamnes et al.*, 1988], and a martian surface scattering function [*Johnson et al.*, 2006a; *Johnson et al.*, 2006b; *Sullivan et al.*, 2008; *Arvidson et al.*, 2014; *Kreisch et al.*, 2017].

We consider a set of dunes and sand fills near Curiosity's traverse (Figure 8.1A). VSWIR spectra of four regions of interest (ROIs) – two barchan dunes (Namib and Kalahari), a linear dune, and a crater fill (Figure 8.1A) – were selected to be inverted for modal mineralogy. These four sites were chosen because they are most distinct in terms of their overall spectral properties (i) near the rover traverse (Namib and Kalahari) and (ii) within the entire spectral scene (linear dune and crater). We averaged atmospherically-corrected single scattering albedo spectra over four ROIs, comprised of 74, 127, 222, and 284 CRISM ATO pixels on Namib Dune, Kalahari Dune, the linear dune, and the crater fill, respectively (Figure 8.1A). Figures 8.1C and 8.1D show the raw and normalized spectra at the four locations. Masked wavelength regions were removed from our analysis because they contained spurious atmospheric residuals.

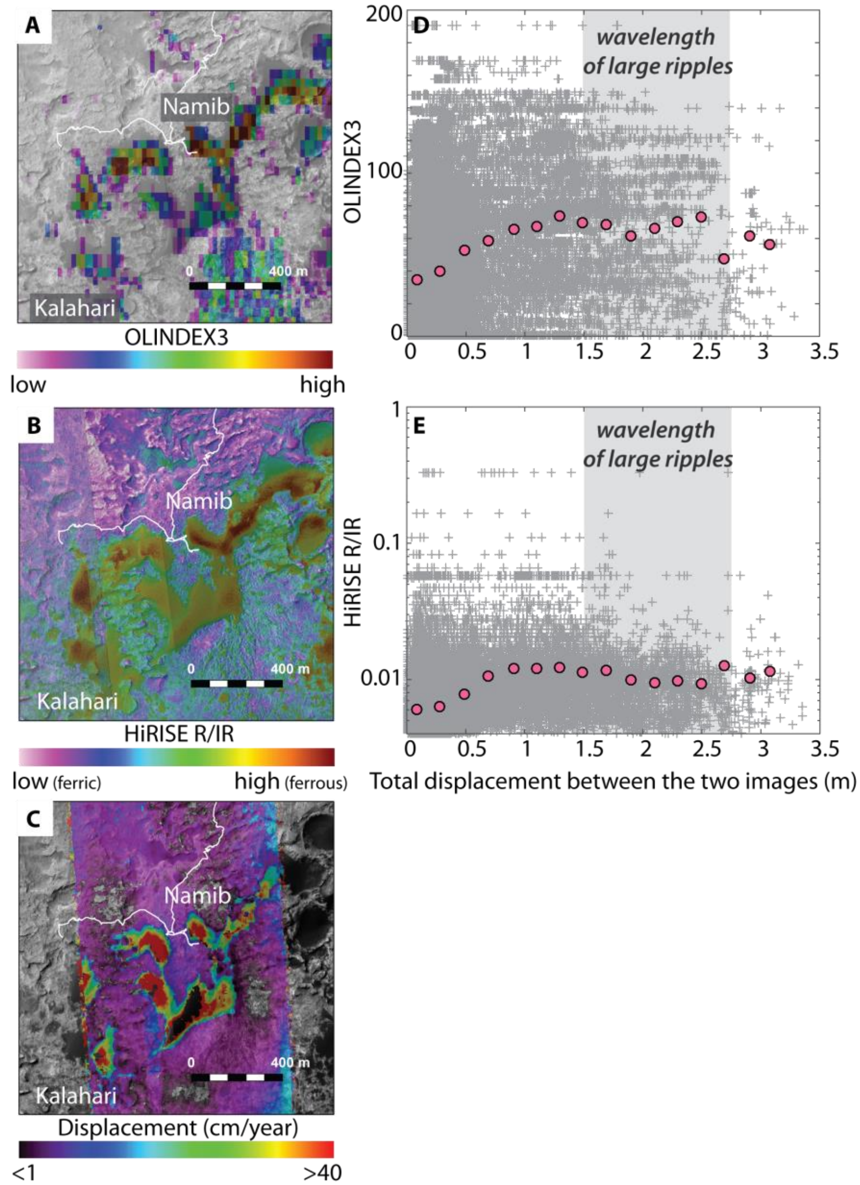

Figure 8.2: Mineralogy, dustiness, and activity of the Bagnold Dunes. Maps of (A) OLINDEX3, (B) HiRISE red/infrared band ratio, and (C) ripple displacements derived from HiRISE image pairs. The white sinuous line shows the traverse of the Curiosity rover up to sol 1371. (D) Scatter plot of OLINDEX3 vs. total ripple displacements, and (E) scatter plot of HiRISE red/infrared band ratio vs. total ripple displacements. Pink circles represent binned data (means). Shaded zones outline the range of large ripple wavelengths at the Bagnold Dunes [*Lapôtre et al.*, 2016b].

Variation in spectral properties can also be tracked over a broad geographic area. Spatial variability in olivine and pyroxene abundance was examined with 18 m/pixel FRT CRISM data and a series of spectral parameters, including OLINDEX3 (Figure 8.2A), which increases with the strength of the 1-μm olivine spectral absorption and is used as a proxy for olivine content and/or grain size [*Viviano-Beck et al.*, 2014]. The ferrous vs. ferric nature of surface materials was mapped at 0.3 m/pixel, using a red/infrared band ratio from HiRISE scenes ESP_021610_1755 and ESP_035772_1755 (Figure 8.2B), [*Delamere et al.*, 2010]. HiRISE red/infrared band ratios are low for ferric (typically dust-covered) and high for ferrous materials (mafic surfaces). Ripple displacements were estimated near the traverse of the Curiosity rover from a time correlation of a HiRISE stereo-pair (ESP_018854_1755, acquired 08/04/2010, and ESP_035772_1755, acquired 03/14/2014), following the technique of *Bridges et al.* [2012], over a total timespan of 1318 Earth days (Figure 8.2C). This technique relies on the movement of ripples exclusively as a proxy for sand flux [e.g., *Ayoub et al.*, 2014].

2.2 Quantitative Mineralogy Using a Bayesian Implementation of the Hapke Radiative Transfer Model

Radiative transfer models [e.g., *Hapke*, 1981] allow inversion of single scattering albedo spectra of planetary surfaces for mineral abundance and grain sizes. Though prior authors have typically presented only a single best-fit solution to estimate mineral abundances, the solution to the inverse problem is highly non-unique due to parameter tradeoffs, e.g., between the abundances of different mineral endmembers and between abundance and grain size of a same mineral endmember. Moreover, noise in the data adds to the uncertainty in selecting a best-fit solution [e.g., *Lapôtre et al.*, 2017a]. In order to allow for a range of modal mineralogies that could reasonably explain the data, given its noise, and to estimate the uncertainty associated with the non-uniqueness of the inversion technique, we adapted a Markov-Chain Monte Carlo (MCMC) algorithm originally implemented to invert for seismic slip along faults [*Minson et al.*, 2013; *Minson et al.*, 2014] to the radiative transfer inverse problem [*Lapôtre et al.*, 2017a]**.** Specifically, the forward model used to estimate the likelihood of a given sample given the data is the geometric optics model for light scattering of *Hapke* [1981]. The MCMC technique allows us to explore the parameter space (mineral abundances and grain sizes) at a sampling density that is proportional to the likelihood of a model given the data, which is a function of the misfit between the modeled spectrum and the data. Consequently, histograms of all accepted model solutions yield the probability densities associated with abundance and grain size of each mineral constituent.

Our general approach in selecting mineral endmembers was to assume no a priori knowledge on their precise chemical compositions, and to determine a parsimonious set of endmembers. Thus, our suite of mineral endmembers was selected on the basis of (i) some of them being optically active and obviously required (e.g., olivine and pyroxenes), and (ii) others being expected in the context of mafic martian sands, and/or consistent with initial tests suggesting their necessity to fit the data properly (e.g., plagioclase, magnetite, hematite, and basaltic glass). In preliminary inversions, we tested the quality of fits to the data using six olivines of variable composition (Fo numbers ranging from 51 to 91), four pyroxenes of variable Ca content (enstatite to diopside), two plagioclases (andesite and labradorite), magnetite, hematite, and a basaltic glass. Hematite did not significantly improve the spectral fits, and was thus removed for the sake of parsimony. Similarly, solid solutions that yielded poor fit residuals were discarded. Our final set of mineral endmembers to model the composition of sands of the Bagnold Dunes include one olivine, two pyroxenes (augite and pigeonite), a plagioclase (labradorite), magnetite, and basaltic glass (Figure 8.3; Table 8.1). Orthopyroxenes and higher Ca pyroxenes produced poorer fits to the 2-μm feature. The higher reflectance plagioclase produced better fits. Multiple olivines were possible, but the Fo51 olivine produced slightly better fits. We show results for both Fo51 olivine (preferred) and Fo80 to illustrate the sometimes subtle effects of mineral solid solution.

The propagation of light in absorbing materials is typically described by a complex-valued index of refraction, with a real part (n), which accounts for reflection and refraction, and an imaginary part (k), which accounts for absorption. Together, n and k are wavelength-dependent properties of a given material and are colloquially referred to as optical constants. Within the wavelength range we consider (0.8-2.5 μm), we assume that the real index of refraction, *n*, of our mineral endmembers is a constant [e.g., as in *Hiroi and Pieters*, 1994], such that the imaginary index of refraction of a given mineral, *k*, can be inverted from its laboratory reflectance spectra acquired at a known grain size. Full methods are described in *Lapôtre et al.* [2017a]. To invert for the optical constants of our mineral endmembers, we used Hapke's theory following methods similar to those of *Lucey* [1998]. We assumed that sand grains are spherical with no internal porosity, scatter isotropically (phase function, P=1) without backscattering (backscattering function, B=0), and used the formulation of *Hapke* [1981] for the particle internal transmission coefficient. Uncertainties associated with the derivation of optical constants from reflectance spectra can be large, often due to uncertainties in grain size and grain size distribution for particulate samples [e.g., *Poulet and Erard*, 2004]. Optical constant error quantification is outside of the scope of the present study because proper assessment of errors requires both reflectance and transmission data of all endmembers, which is not available. Although our model outputs have uncertainties associated with the derivation of optical constants that remain unquantified, we attempted to minimize these by (i) selecting endmember spectra derived from laboratory samples with relatively narrow ranges in grain size (Table 8.1) and/or (ii) comparing our results to other published optical constants [e.g., *Lucey*, 1998; *Denevi et al.*, 2007; *Zeidler et al.*, 2011], such that we can assume that our input optical constants are reasonable estimates. The issue of the effects of uncertain optical constants on mixture modeling is examined further in a companion methods-oriented paper [*Lapôtre et al.*, 2017a].

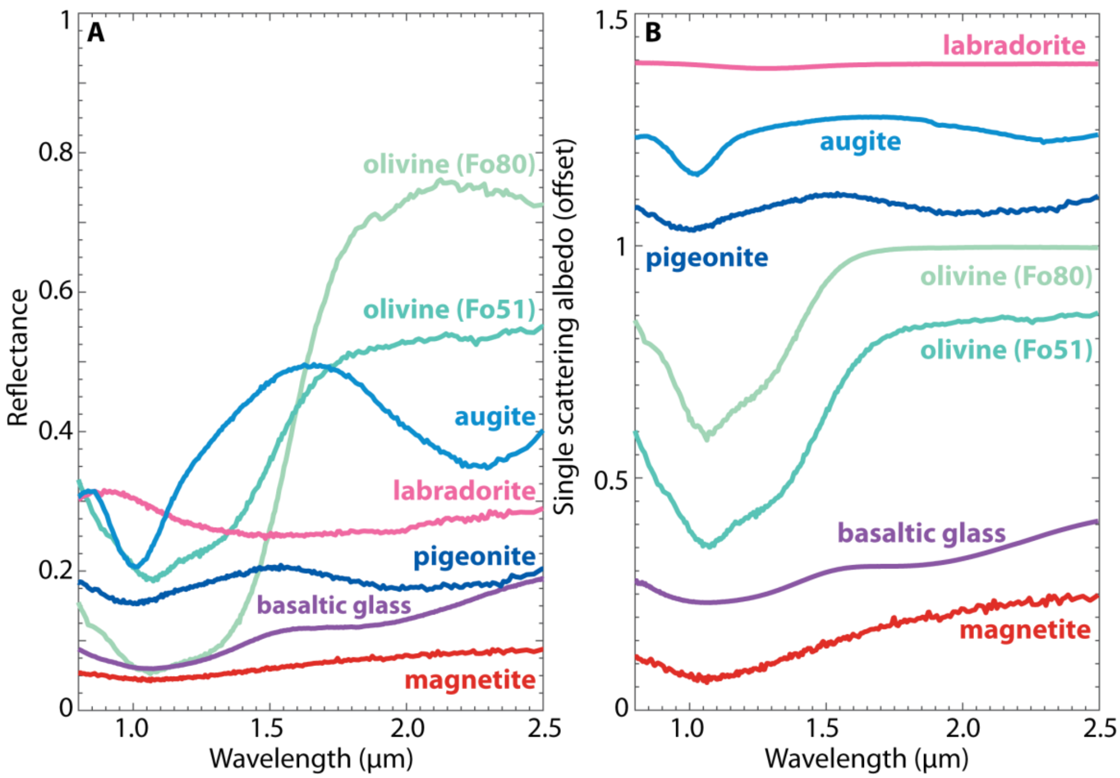

Figure 8.3: Mineral endmembers. (A) Laboratory reflectance spectra of the mineral endmembers used in our inversion of modal mineralogy, and (B) corresponding single scattering albedos calculated for a grain size of 100 μm, and vertically offset for clarity. Sources of the spectra are summarized in Table 8.1.

With the optical constants of endmember mineral phases on hand, the single scattering albedo of a given mineral endmember can be calculated at the desired grain size, and then linear mixtures of those single scattering albedos can be compared with the CRISM-derived single scattering albedo to invert for both mineral abundances and grain sizes [*Mustard and Pieters*, 1987; *Poulet and Erard*, 2004; *Edwards and Ehlmann*, 2015; *Li and Milliken*, 2015; *Robertson et* *al., 2016*]. Specifically, weight abundances and grain sizes of each endmember were sampled independently by our MCMC algorithm and then used together to compute the relative fractional geometric cross-section of each mineral endmember. These were then used with optical constants to compute the modeled spectrum, which was compared with the CRISM single scattering albedo spectrum.

We allowed for a covariance between data and model spectra of $2x10^{-4}$, a value that we found (through trial-and-error) to appropriately account for noise in the single scattering albedo-converted CRISM data (e.g., Figure 8.4). We allowed for grain sizes in the range of 50-800 μm for all mineral phases but magnetite, which we limited to a 10-200 μm range, due to the fact that it rarely occurs as large crystals in igneous systems. The chosen bounds bracket a range of grain sizes (silt to coarse sand) that is consistent with aeolian transport under martian conditions [e.g., Kok, 2010a]. At each location, we inverted for a Markov-Chain of 10^6 models, i.e., 10^6 sets of mineral abundances and grain sizes matching the data within the allowed noise level.

In the following, we use three metrics to describe our results. The "Maximum A Posteriori Probability" model, or "MAP", refers to the most sampled area of the parameter space, i.e., the most probable mineral assemblage. The MAP represents the mode of the 12-dimensional posterior (i.e., output) probability density function (6 abundances and 6 grain sizes) and does not necessarily coincide with the mode for each individual parameter. The "mean" refers to the mean value of the parameter for all accepted models. Finally, the 95% confidence interval is defined as the centered bounds that contain 95% of all samples. Were the individual probability densities to be normally distributed, the 95% confidence interval would correspond to a ± 2σ interval around the mean.

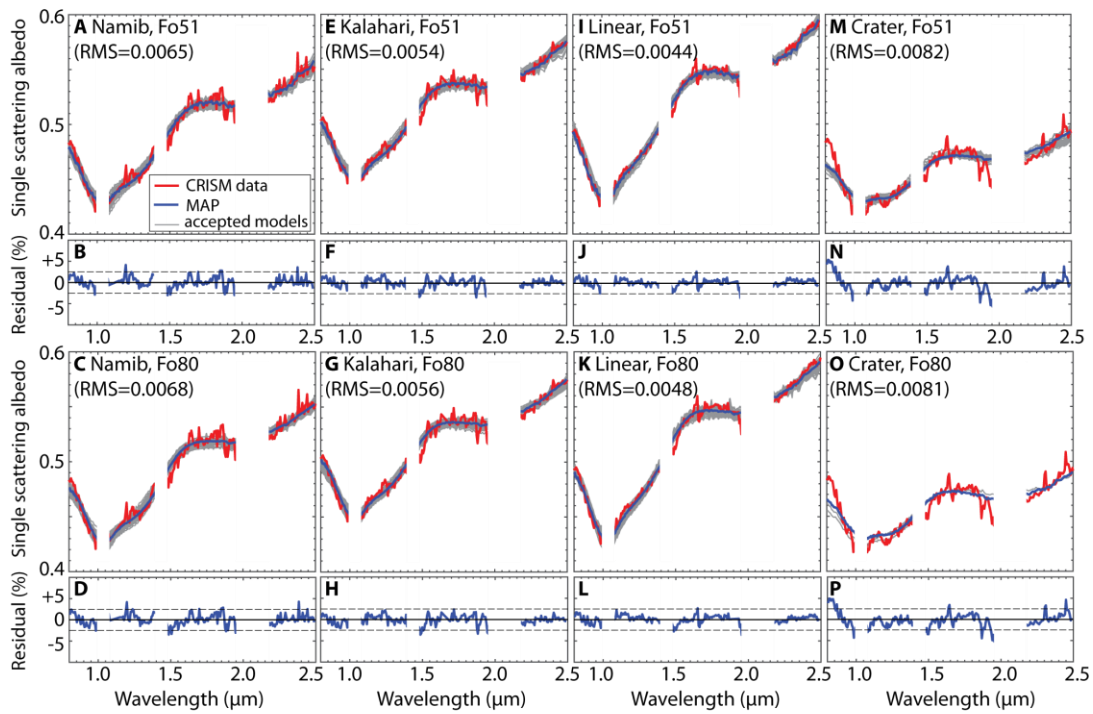

Figure 8.4: Spectral fits. (A,E,I,M) CRISM spectra, Maximum A Posteriori Probability models (MAP), and random subset of 1000 accepted models at Namib Dune (A) Kalahari Dune (E), the linear dune (I), and crater fill (M) using an olivine of Fo51, and (B,F,J,N) corresponding residuals of the MAP. Dashed lines represent a ± 2.5% residual. (C,G,K,O) CRISM spectra, MAPs, and random subset of 1000 accepted models at Namib Dune (C) Kalahari Dune (G), the linear dune (K), and crater fill (O) using an olivine of Fo80, and (D,H,L,P) corresponding residuals of the MAP. Dashed lines represent a ± 2.5% residual.

3. Results

3.1. Properties of Sand Spectra

All spectra have broad ~ 1 μm and ~ 2 μm absorptions, indicative of the presence of olivine and pyroxenes. The main differences between the spectra in Figure 8.1C-D are (i) the strength of the olivine absorption at ~ 1 μm, (ii) the spectral continuum slope at the longer wavelengths, and (iii) the SWIR albedo at wavelengths great than ~ 1 μm. Stronger olivine absorptions, steeper SWIR continuum slopes, and higher SWIR albedos are observed in the barchans and the linear dunes compared with the crater fill. Stronger olivine signatures in select locations might suggest that olivine grains are more abundant and/or coarser in these locations, or that opaque dust does not deposit or is removed in more active areas due to stronger winds, or both.

3.2. Spatial Correlations between Sand Flux, Composition, and Dust

We find that zones of high ripple displacements generally correspond to zones of higher OLINDEX3 and higher red/infrared ratios, e.g., at the Namib and Kalahari dunes (Figure 8.2). This spatial correlation may arise from (i) preferential enrichment of olivine where sand flux is higher and/or from (ii) the olivine signature being preferentially masked by dust in the less active parts of the dune field. Ferrous (Fe^{2+}) minerals tend to have higher red/infrared ratios than ferric (Fe^{3+}) phases like martian dust. The observed correlation between

OLINDEX3 and HiRISE red/infrared ratio suggests dust content is lower where olivine abundance is high (Figure 8.2A-B). There is substantial scatter in the data of either index vs. ripple displacement (Figure 8.2D-E). Nevertheless, we find that total ripple displacement is positively correlated with the binned mean of both the OLINDEX3 (Figure 8.2D) and the HiRISE red/infrared band ratio (Figure 8.2E) for those ripples that migrated less than about a ripple wavelength between the two consecutive HiRISE images.

Untangling the effects of mineral abundances, grain sizes, and dust cover from orbit remains difficult, and ground-truth is required to definitively exclude the possibility that compositional variations merely indicate differences in masking of the primary mineralogy by dust. The Bagnold Dunes were previously determined to be generally dust-free [*Rogers and Bandfield*, 2009] and are relatively active near the rover traverse (e.g., Figure 8.2C) [*Silvestro et al.*, 2013, 2016; *Bridges et al.*, 2017; *Ewing et al.*, in review] with dune displacements of about half those measured in the very active Nili Patera dune field [*Bridges et al.*, 2012], and HiRISE red/infrared band ratios are relatively high over the dunes (Figure 8.2B). In the following section, we quantitatively constrain the modal composition of bulk sands at four locations, assuming that the Bagnold sands are relatively dust-free (an assumption later discussed in Section 4.2).

3.3. Quantifying Modal Mineralogy

Figure 8.4 shows the modeled MAP spectra (blue) at the four selected locations for two different olivine Fo numbers (Fo51 and Fo80), as well as a random subset of 1000 accepted models (gray). The spread in latter spectra illustrate the variability we allowed for through the covariance parameter. Associated residuals are typically less than 2.5%. Root Mean Square (RMS) errors of the MAPs are typically slightly higher for the Fo80 olivine inversions. For both olivine compositions, the crater fill (Figures 8.4M and 8.4O) displays a narrower range in accepted models (i.e., the gray lines are not as spread around the data spectra as for the other locations), which illustrates the fact that very few different models were acceptable according to our likelihood criterion, i.e., that most sampled models were deemed unlikely due to poor fits to the data. We interpret this result, along with the higher residuals, as reflecting a missing endmember in our parsimonious set, which we believe to most likely be fine dust. Indeed, fine ferric veneers over dark mafic materials, such as dust over dark basaltic sands, were shown to display spectral continuum slopes that are more "negative" than that of the underlying dark material alone [*Fischer and Pieters*, 1993], consistent with the observed lower spectral slope over the crater fill (Figure 8.1C).

Inverted mineral abundances are shown in Figures 8.5 and 8.6 for the Fo51 and Fo80 inversions, respectively. These figures are analogous to traditional box plots, but with the shape of each box reflecting the probability density of a given parameter. Within each box, the area that is shaded in a darker hue outlines the 95% confidence interval of the corresponding parameter, while the vertical line and open circle indicate the mean and MAP, respectively. Table 8.2 summarizes the corresponding MAP abundances. Using a 95% confidence interval, inverted ranges in permitted abundances are wide, typically >30 wt%, but their probability densities tend to have distinct modes. With both olivine compositions, probability densities associated with the crater fill are much narrower than for the other locations, reflecting the low number of models deemed acceptable by our MCMC algorithm, and again, likely pointing to a missing component.

Inverted grain sizes are shown in Figures 8.7 and 8.8 using the Fo51 and Fo80 olivine compositions, respectively. It is important to note that inverted grain-size probability densities only reflect the range of sizes that yield satisfying fits to the data, not the true grain-size distributions on the ground. Table 8.3 summarizes the corresponding MAP grain sizes. In contrast to the probability densities of mineral abundances (Figures 8.5 and 8.6), those of grain sizes tend to lack well-defined modes. The overall uniformity of grain size probability densities indicates the relative insensitivity of the inversion to grain size. In particular, mineral phases for which we find the mean model to be similar to the median of the allowed grain size range (dashed line in Figures 8.7 and 8.8 at 425 μm for all phases but magnetite; 105 μm for magnetite) should be considered with caution. Interestingly, the basaltic glass seems to be required to be relatively fine-grained. Grain sizes of other mineral phases are more difficult to constrain from their roughly uniform probability densities, although the grain size probability densities of olivine and pyroxenes appear to be consistently skewed towards relatively coarser and finer sizes, respectively.

Overall, the abundance and grain size distributions are similar between the two tested Fo numbers. Olivine and plagioclase abundances are consistently spatially anti-correlated: olivine abundances decrease from the linear dune to Namib Dune, to Kalahari Dune, and to the crater fill, while plagioclase abundances decrease from the crater fill, to Kalahari Dune, to Namib Dune, and to the linear dune. All four locations appear to have little magnetite (a few percent), and a significant fraction of basaltic glass. However, the spatial trends in pyroxene and basaltic glass abundances differ for the two Fo number cases.

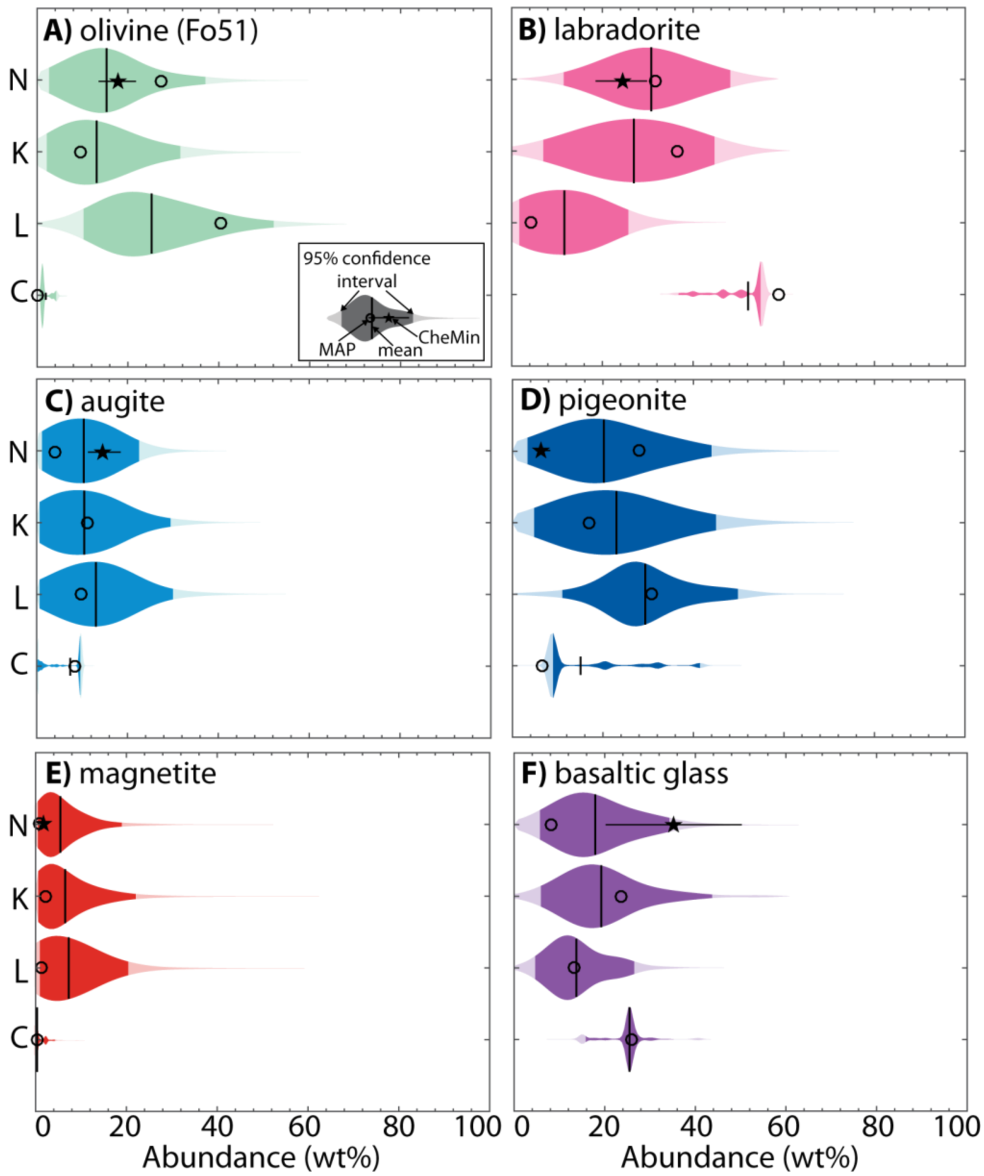

Figure 8.5: Spectral unmixing results: Mineral abundances (Fo51 scenario). Probability densities of mineral abundances resulting from our Bayesian Hapke unmixing modeling using an olivine of Fo51 at the four locations of interest (N = Namib Dune; K = Kalahari Dune; L = linear dune; C = crater fill) for (A) olivine, (B) labradorite, (C) augite, (D) pigeonite, (E) magnetite, and (F) basaltic glass. Solid black lines indicate the mean model, while open circles indicate the MAP. For Namib Dune, abundances inverted by CheMin in the <150 μm fraction (Table 8.4) were renormalized to our endmember phases only, and are indicated by the filled stars. MAP values are summarized in Table 8.2.

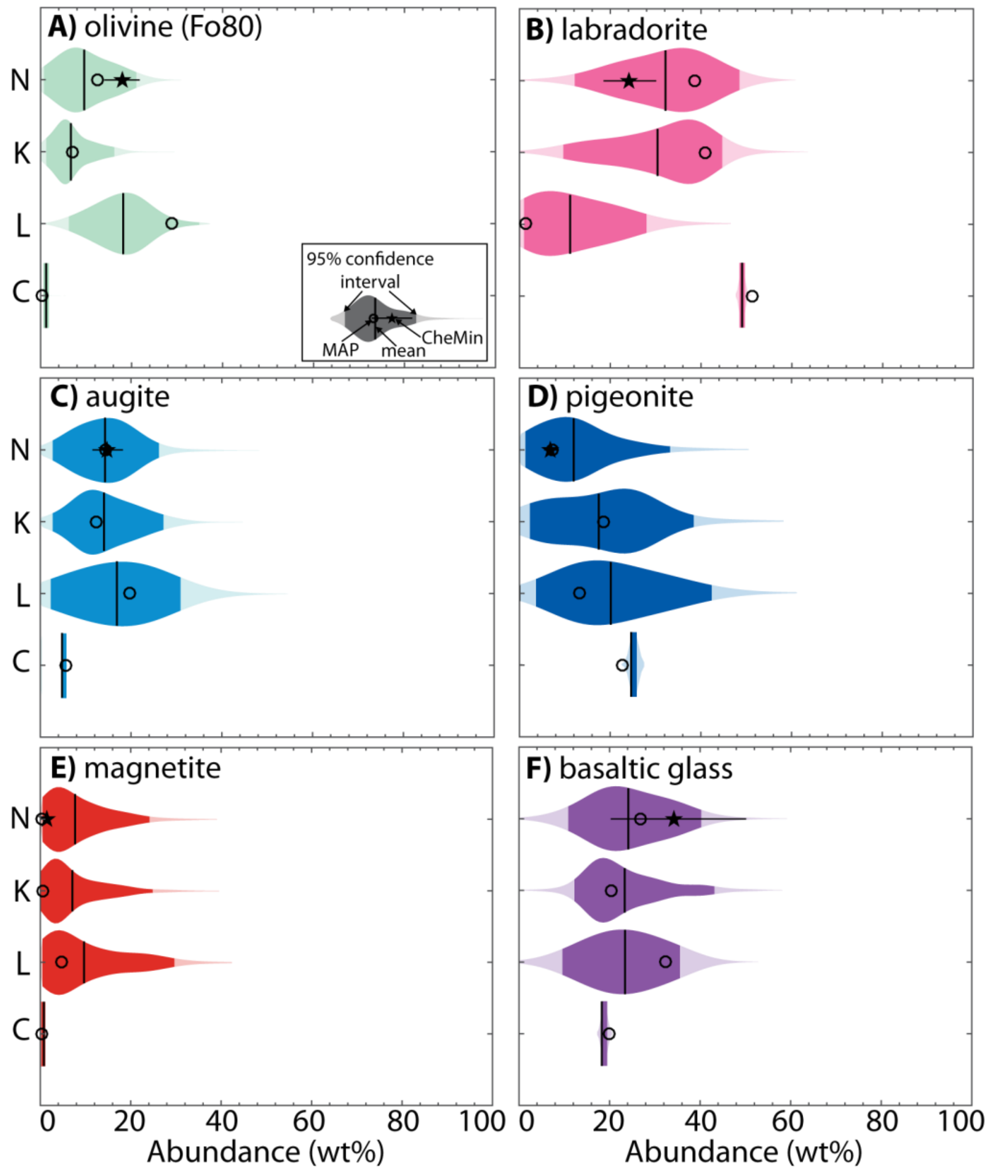

Figure 8.6: Spectral unmixing results: Mineral abundances (Fo80 scenario). Probability densities of mineral abundances resulting from our Bayesian Hapke unmixing modeling using an olivine of Fo80 at the four locations of interest (N = Namib Dune; K = Kalahari Dune; L = linear dune; C = crater fill) for (A) olivine, (B) labradorite, (C) augite, (D) pigeonite, (E) magnetite, and (F) basaltic glass. Solid black lines indicate the mean model, while open circles indicate the MAP. For Namib Dune, abundances inverted by CheMin in the <150 μm fraction are indicated by the filled stars. MAP values are summarized in Table 8.2.

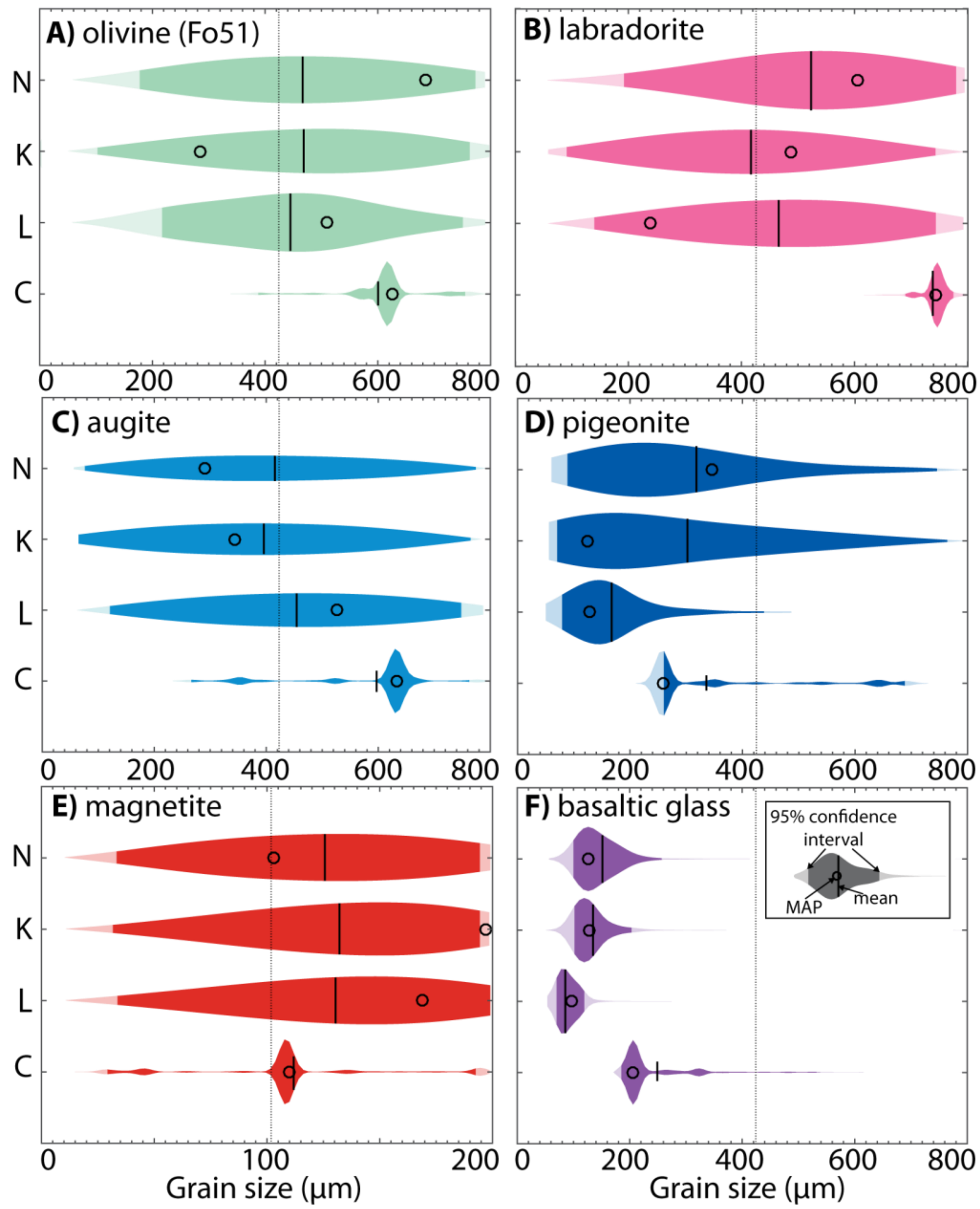

Figure 8.7: Spectral unmixing results: Grain sizes (Fo51 scenario). Probability densities of grain sizes resulting from our Bayesian Hapke unmixing modeling using an olivine of Fo51 at the four locations of interest (N = Namib Dune; K = Kalahari Dune; L = linear dune; C = crater fill) for (A) olivine, (B) labradorite, (C) augite, (D) pigeonite, (E) magnetite, and (F) basaltic glass. Solid black lines indicate the mean model, while open circles indicate the MAP. Vertical dashed lines represent the median of the allowed grain size range, i.e., the mean of a uniform grain size distribution over that range. MAP values are summarized in Table 8.3.

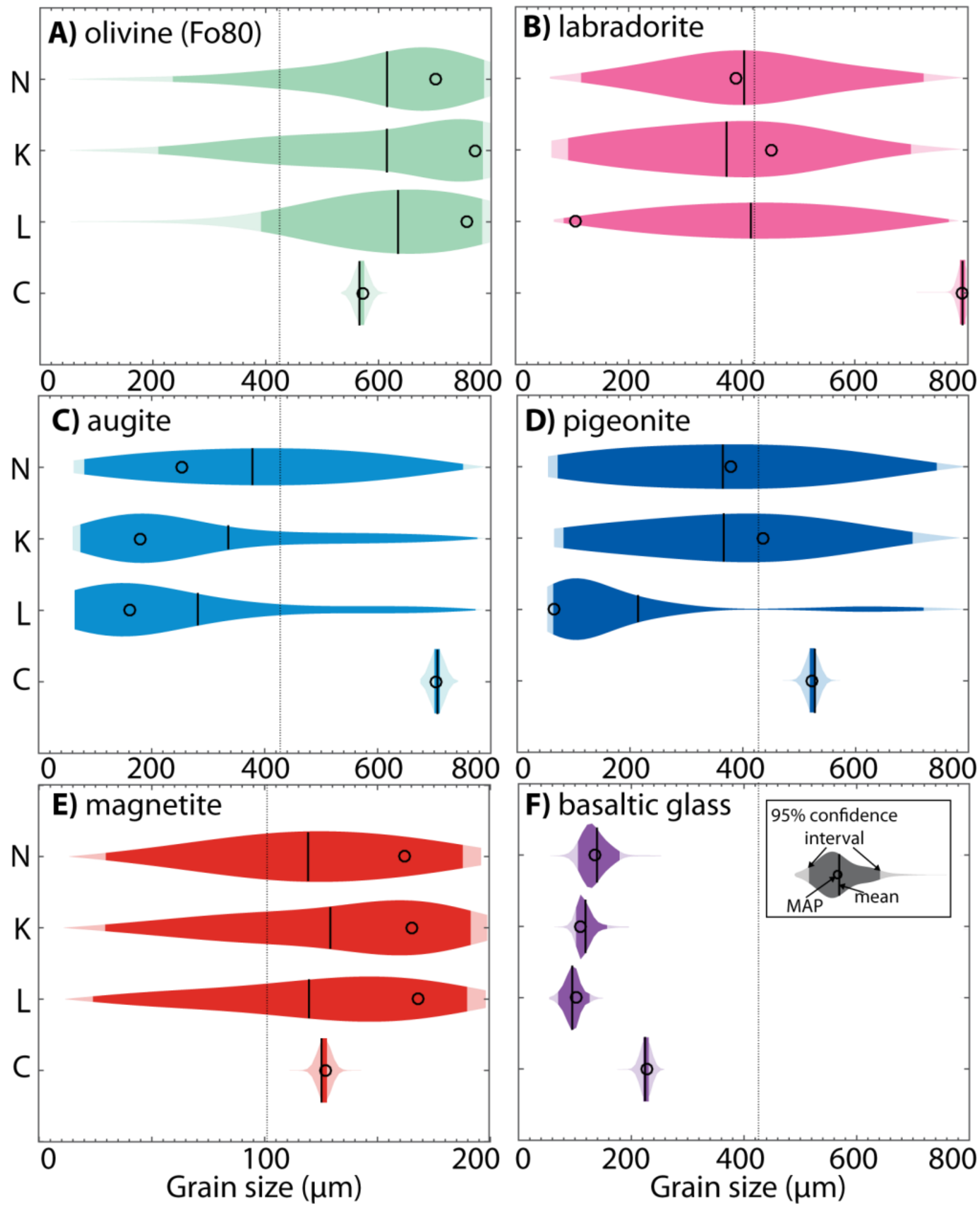

Figure 8.8: Spectral unmixing results: Grain sizes (Fo80 scenario). Probability densities of grain sizes resulting from our Bayesian Hapke unmixing modeling using an olivine of Fo80 at the four locations of interest (N = Namib Dune; K = Kalahari Dune; L = linear dune; C = crater fill) for (A) olivine, (B) labradorite, (C) augite, (D) pigeonite, (E) magnetite, and (F) basaltic glass. Solid black lines indicate the mean model, while open circles indicate the MAP. Vertical dashed lines represent the median of the allowed grain size range, i.e., the mean of a uniform grain size distribution over that range. MAP values are summarized in Table 8.3.

4. Discussion

4.1. Evaluation of the Inversion Technique: Tradeoffs and Solid Solutions

Overall, our inversion technique produces many low RMS fits to spectra at three active sites. As discussed above, the small number of models with low RMS error for the crater-fill site is likely due to non-inclusion of a dust layer on the relatively inactive bedforms. MCMC modeling of SWIR spectra successfully and quantitatively constrains the compositional range of the active sands, though this range is relatively broad, illustrating the inherent non-uniqueness of spectral inversions for basaltic materials. Retrieved plagioclase and magnetite abundances are relatively insensitive to olivine Fo number across sites, and this is likely because their retrieved abundances are governed largely by overall albedo. Additionally, the same trends in relative abundance by site are observed in olivine and plagioclase, regardless of the chosen Fo number. However, modeled abundances of other mafic minerals – augite, pigeonite, and basaltic glass – are affected by the olivine composition used in the model. A key contributor to this tradeoff is the relative similarity of absorption-feature shapes and locations in orthopyroxenes, clinopyroxenes, and basaltic glass. In particular, the position of their absorptions shifts continuously with solid-solution composition. There appear to be abundance-abundance tradeoffs between endmembers and abundance-grain size tradeoffs within a single endmember in setting single scattering albedo values. In particular, we suspect that the challenge of matching the precise shape of the 1-μm absorption (e.g., possibly due to an olivine Mg chemistry that differs slightly between the ground and our laboratory endmembers) is accommodated by tradeoffs between olivine and basaltic glass abundances, which themselves impact the pyroxene abundances and the fit of the 2-μm feature. This caveat reflects the difficulty of inverting for mineral abundances when several solid solutions and/or an amorphous phase with similar spectral properties, in this cases two pyroxenes and mafic glasses, are present.

To summarize, potential sources of uncertainty in MCMC Hapke unmixing results for remote compositional analysis here and for the approach generally include: (i) errors in model inputs, both for laboratory data (e.g., incorrect endmember suite, inaccuracies in optical constants) and in input orbiter-based data (e.g., instrumental noise, incomplete atmospheric correction), (ii) systematic errors in the forward model (e.g., in the physics and assumptions of the Hapke model formulation), and (iii) inherent non-uniqueness of the inverse problem (e.g., tradeoffs between mineral abundances and grain sizes in setting single scattering albedo values). A companion manuscript determines the relative importance of each of these parameters as sources of error and uncertainty [*Lapôtre et al.*, 2017a]. Here, we evaluated the holistic performance of the MCMC Hapke modeling, as could be applied to any planetary surface, using ground truth data acquired by the Curiosity rover of mineralogy and grain size.

4.2. Comparison with In Situ Observations and Measurements from the Mars Science Laboratory Rover at Namib Dune

The Curiosity rover investigated the Namib Dune of the Bagnold Dune Field between sols ~1162 and ~1243 of the MSL mission [*Bridges and Ehlmann*, in revision]. In contrast to previous observations of loose regolith along the rover traverse, the Bagnold sands do not appear to contain intermixed dust, and grains do not form clumps. The absence of dust is also confirmed by in situ compositional datasets [*Ehlmann et al.*, in revision; *Johnson et al.*, 2017; *O'Connell-Cooper et al.*, in revision]. The Mars Hand Lens Imager (MAHLI) documented that sand grains were very fine to medium in size, i.e., with most grains between 40 to 600 µm [*Ehlmann et al.*, in revision; *Edwards et al.*, in revision]. MAHLI data show that many sand grains appear to consist of individual mineral grains, although highly-spherical dark grains could be lithics or beads of basalt or basaltic glass (Figure 8.9). Coarser particles are found on some surfaces near High Dune [*Ehlmann et al.*, in revision]. When sieved and discarded piles were examined, the coarse fractions (>150 um) were found to have spectra, measured in situ, consistent with enrichment in olivine [*Johnson et al.*, 2017]. Additionally, chemical data from the Chemistry & Camera (ChemCam) and Alpha-Particle X-Ray Spectrometer (APXS) datasets indicate that the coarse fraction has elevated MgO, but lower SiO_2, Na_2O, and Al_2O compared with the finer fraction [*Cousin et al.*, in revision; *Ehlmann et al.*, in revision], though some feldspathic quartz grains are also present (see also Figure 8.11A).

Mineral abundances were derived from the sieved fine fraction using the Chemistry & Mineralogy (CheMin) instrument, as summarized in *Achilles et al.* [in revision] (see also Table 8.4). CheMin provides abundances at a high level of confidence for the crystalline phases in the <150-μm size fraction ingested by the instrument; however, abundance estimates of XRD-amorphous phases are much less well constrained, such that uncertainty on absolute abundance of the crystalline phases remain relatively large. In Figures 8.5 and 8.6, the filled star symbols show mineral abundances measured by CheMin at Namib Dune, renormalized to the mineral phases we herein consider, with errors propagated to account for the large uncertainty on the XRD-amorphous component. This amorphous component was estimated by combining CheMin and APXS datasets, and found to represent 35 ± 15 wt% of the fine material at Namib Dunes [*Achilles et al.*, in revision] (Table 8.4).

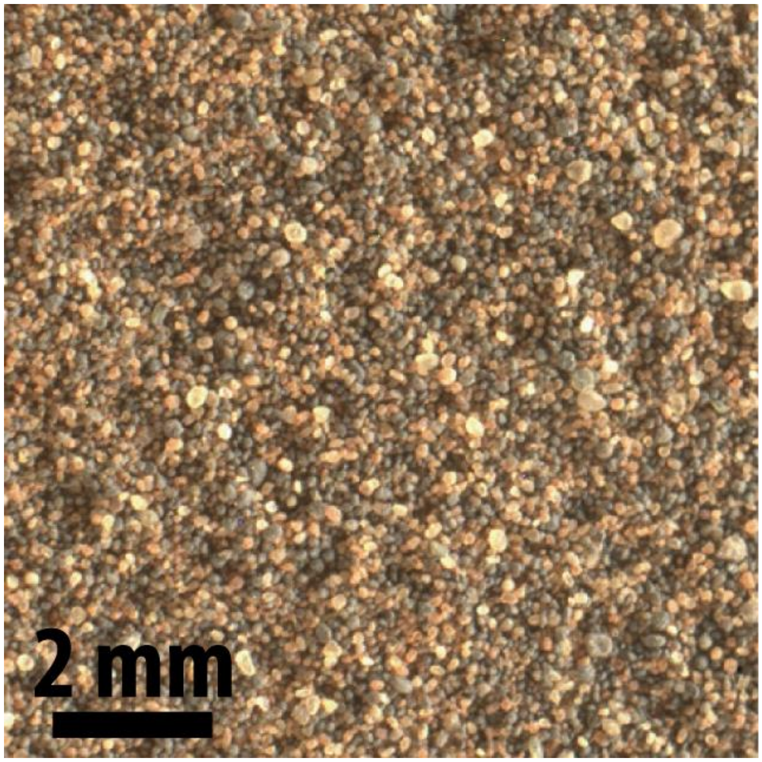

Figure 8.9: Observed sand grains at Namib Dune. MAHLI focus merge product (1242MH0005740000403707R00) of the Otavi target, an undisturbed surface at the Gobabeb sampling site on Namib Dune.

Because in situ modal mineralogy was derived from the fine fraction only, and other ground-based images and compositional datasets show that chemistry varies with grain size and grain size varies between the ripples and interior of the dunes, we do expect some differences between CheMin abundances and our CRISM-based results, which reflect spatially-averaged bulk sand mineralogy at the optical surface. However, we expect these differences to be relatively small, and CheMin abundances offer the opportunity to assess the performance of our inversion technique. CheMin abundances fall within our estimated 95%

confidence intervals for all crystalline phases (Figures 8.5 and 8.6). The proportion of amorphous material measured in situ overlaps with our 95% confidence interval for the abundance of basaltic glass for both Fo numbers (see Namib abundances on Figures 8.5F and 8.6F). Average differences between the MAP and CheMin-derived abundances are 12.8 and 4.9 wt% for Fo51 and Fo80, respectively. Maximum errors are 14.6 wt% for the Fo80 case (labradorite) and 26.9 wt% for the Fo51 case (glass/XRD-amorphous, though this is somewhat uncertain because of the large uncertainties in the calculation of the XRD-amorphous component).

Figure 8.10C also shows a comparison between the CheMin data (filled star) and the MAP (open circle), renormalized to crystalline phases only (i.e., without the basaltic glass). Average differences between the MAP and CheMin-derived abundances are 9.0 and 6.3 wt% for Fo51 and Fo80, respectively. Maximum errors are 19.7 wt% for Fo51 (pigeonite) and 15.9 wt% for Fo80 (labradorite). Inverted abundances using an olivine of Fo51 are very close to those measured by CheMin for olivine, plagioclase, and magnetite. The sum of the pigeonite and augite is also close to ground-truth, although the relative abundances of low and high Ca pyroxenes are not well estimated. When pyroxenes are combined into “total pyroxene”, the mean error of the MAP abundances drops to 1.9 wt%, with a maximum error of 2.8 wt% for olivine. Conversely, the pyroxene abundances and relative proportions appear to be well estimated in our inversion with an olivine of Fo80, but olivine and plagioclase are not as well predicted. For both Fo numbers, the discrepancies between our results and in situ measurements most likely arise from tradeoffs between the abundances and grain sizes of our mineral endmembers, further complicated by mineral endmembers that are not exactly chemically representative of the precise solid solutions on the ground (Table 8.4).

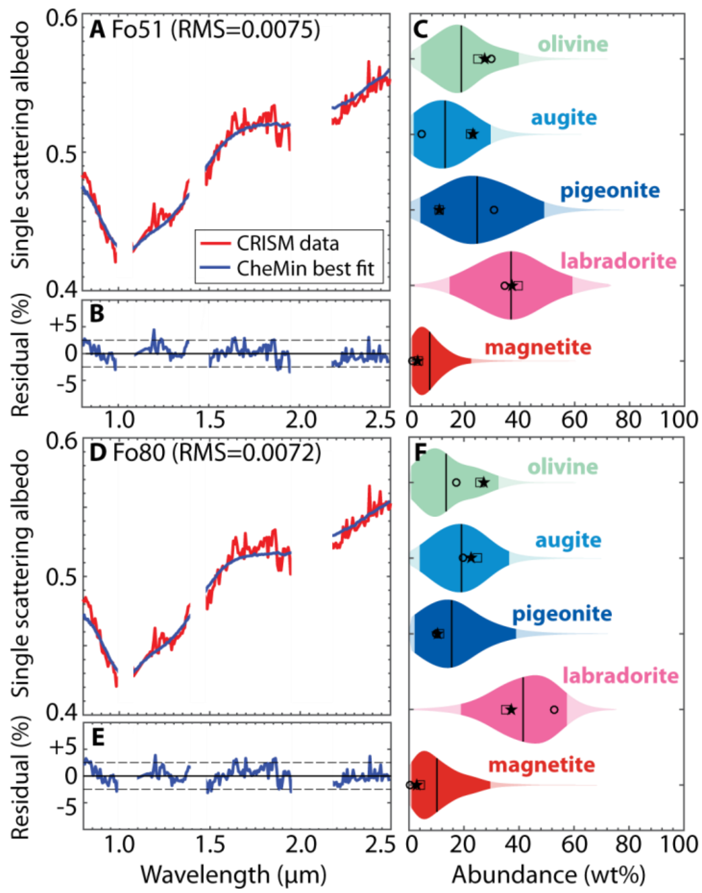

Figure 8.10: Groundtruthing of CRISM-based predictions. (A and D) CheMin best fit model (blue) compared with the Namib Dune single scattering albedo using olivines of Fo51 and Fo80, respectively, and (B and E) corresponding residuals. Dashed lines represent ± 2.5% residual. (C and F) Probability densities of mineral abundances resulting from our Bayesian Hapke unmixing modeling at Namib Dune using olivines of Fo51 and Fo80, respectively, renormalized to crystalline phases only. Solid black lines indicate the mean model, while open circles indicate the MAP, and open squares indicate the inverse model that best approaches CheMin inferences (herein referred to as “CheMin best fit”).

In order to illustrate the usefulness of the Bayesian approach, we identified the accepted model with modeled mineral abundances most closely matching the mineral abundances obtained from CheMin (herein referred to as the CheMin best fit, open squares in Figures 8.10C and 8.10F). Figure 8.10 (A-B and D-E) shows a comparison between the modeled spectrum from the CheMin best fit and the CRISM single scattering albedo data. Interestingly, the RMS errors for the CheMin best fit are 0.0075 and 0.0072 for Fo51 and Fo80, respectively, and are higher than that of the corresponding MAPs (Figures 8.4A and 8.4C; RMS errors of 0.0065 and 0.0068 for Fo51 and Fo81, respectively); this confirms that a simple error minimization algorithm would have missed the true composition under the model and assumptions presented here.

While the RMS errors between CRISM and model spectra are generally lower when using the Fo51 olivine, the aforementioned tradeoffs between solid solutions prevents a confident estimate of olivine chemistry from the VSWIR dataset alone. However, CheMin measurements suggest an olivine of intermediate Mg content, with an estimated Fo of 55 [*Achilles et al.*, in revision]. We hypothesize that the discrepancy in pyroxene chemistry between our Fo51 scenario and ground-truth arises from tradeoffs between the pyroxene phases and the basaltic glass in an attempt to fit the 1-μm absorption whose breadth and position are determined by the Fo number of the olivine. However, the relative proportions of crystalline phases are well-constrained from CRISM when high- and low-Ca pyroxenes are summed and considered as “total pyroxene”. In the following section, we discuss the implications of our inverted mineral compositions for aeolian processes at Gale crater based on our Fo51 scenario.

4.3. Implications for Sorting, Transport Distances, and Sand Sources within the Bagnold Dune Field

The most readily visible compositional variation from VSWIR orbital data within the Bagnold Dunes of Gale crater is that of the mafic phases, in particular the relative enrichment of the barchan dunes in olivine on the upwind, or trailing, edge of the dune field [*Seelos et al.*, 2014] (see also Figure 8.1B). Unmixing results show olivine and plagioclase abundances are anti-correlated at the four locations we investigated (Section 3.2), a trend qualitatively consistent with previous studies of aeolian basaltic sands, which showed that wind sorting tends to segregate felsic and mafic phases on Earth and Mars [*Stockstill-Cahill et al.*, 2008; *Mangold et al.*, 2011]. *Fedo et al.* [2015] suggested that the observed segregation of mafic and felsic minerals in non-chemically weathered basaltic sands of Earth and Mars is primarily controlled by the distribution of phenocrysts in the parent rock, and subsequent sorting of those grains [e.g., *Nesbitt and Young*, 1996; *Fralick*, 2003; *Mangold et al.*, 2011]. The modes and dynamics of sediment transport are dictated by grain densities, sizes, and shapes, which generate feedbacks that govern grain sorting [e.g., *Mason and Folk*, 1958; *Parfenoff et al.*, 1970; *Hunter and Richmond*, 1983; *Anderson and Bunas*, 1993; *Makse*, 2000]. In particular, *Mangold et al.* [2011] showed that windblown basaltic sands in Iceland were enriched in mafic phases as transport distance increases.

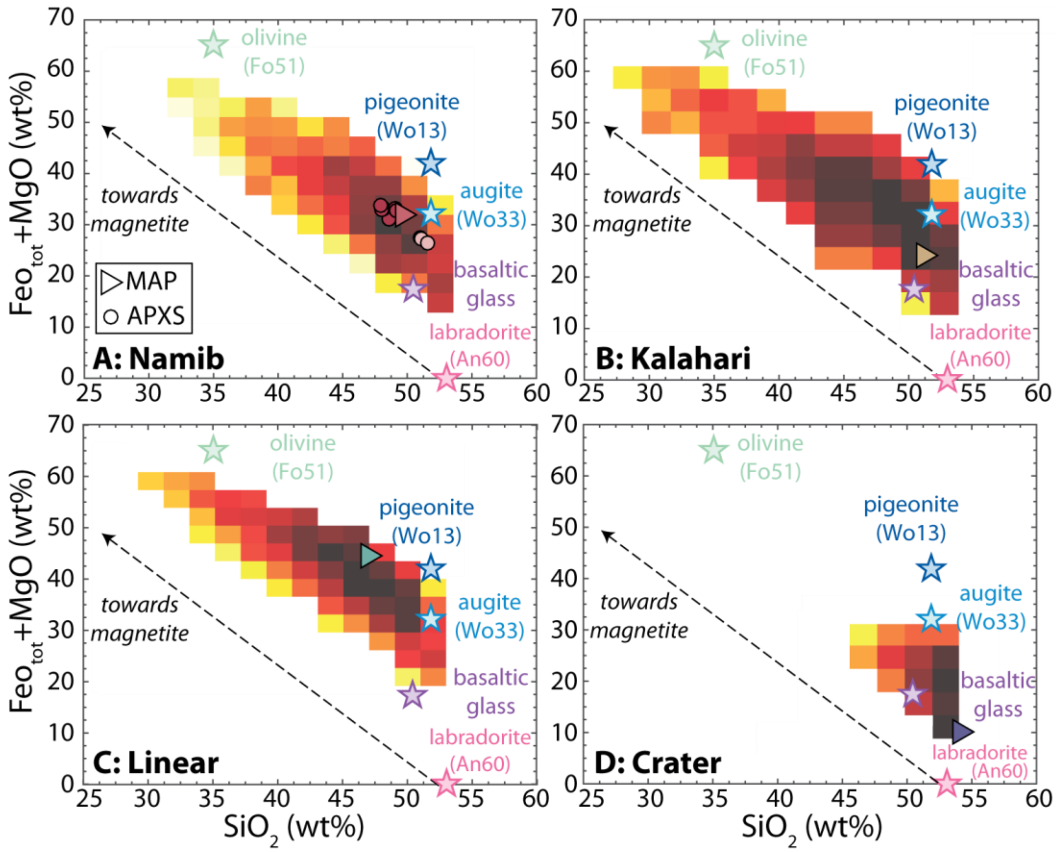

Figure 8.11: Oxides composition. Estimated FeO_{tot}+MgO vs. SiO_2 of all accepted samples (heat map), the MAP (triangle), and mineral endmemebers (stars) at (A) Namib Dune, (B) Kalahari Dune, (C) the linear dune, and (D) the crater fill. Assumptions used to convert mineralogy to oxides abundances are described in Section 4.2. Heat map reflects the density of accepted samples, with darker colors indicating more densely sampled regions. At Namib Dune, the circles indicate APXS measurements, which appear to cluster into two groups—the coarser (more mafic; darker circles) and the finer (more felsic; pale circles) samples. Note that for a direct comparison with our estimates from CRISM, the APXS oxides weight abundances were renormalized to the main seven oxides (SiO_2, Al_2O_3, CaO, FeO, MgO, Na_2O, and K_2O).

To quantitatively compare our results with those of *Mangold et al.* [2011], who only report chemical data, we convert our inverted mineral compositions into oxide abundances. In order to do so, we assume (i) that solid solutions are at thermodynamic equilibrium, (ii) a Fo number of 51 for the olivine, (ii) wollastonite (Wo) numbers of 13 and 33 for the pigeonite and augite, respectively, (iii) an anorthite number (An) of 60 for the plagioclase, and (iv) a composition of the basaltic glass as that of our laboratory basaltic glass (~50.4 wt% SiO_2 and ~17.5 wt% FeO_{tot}+MgO). Use of assumed chemical compositions reflects our approach not to use data only obtainable by Curiosity. We conducted the same analysis using CheMin-derived compositions (Table 8.4), which did not alter the trends.

In (SiO_2, FeO_{tot} + MgO)-space for the four locations (Figure 8.11), estimated compositions for our accepted models (heat map) are spread parallel to the plagioclase-magnetite join, reflecting the primary tradeoff of mixing bright and dark minerals to match the overall albedo of the data. However, the most densely populated region in this oxides space (darker colors in the heat map) plots in a triangle between the plagioclase-olivine join and pyroxenes, and all MAPs plot within this region. At Namib Dune (Figure 8.11A), we compare our estimates to oxide abundances measured by the APXS instrument. APXS data mostly fall into two clusters—coarser samples (darker circles) having elevated Fe and Mg and lower Si than the finer samples (pale circles)—which both fall within the most-densely populated region above the plagioclase-olivine join. Our inverted

MAP at Namib Dune is close to the APXS cluster of coarser samples in this space [*Ehlmann et al.*, in revision; *O'Connell-Cooper et al.*, in revision]. The MAP results for the four locations (Figure 8.12), do not trend along the plagioclase-magnetite join but rather parallel a plagioclase-olivine join in a trend most similar to that of the sand deposits of Stockstill-Cahill et al. [2008] (dark intra-crater sand deposits in Amazonis Planitia, Mars) and Mangold et al. [2011] (non-chemically weathered volcanic sand in Iceland). The latter compositional spread is consistent with sorting and/or mixing of minerals grains.

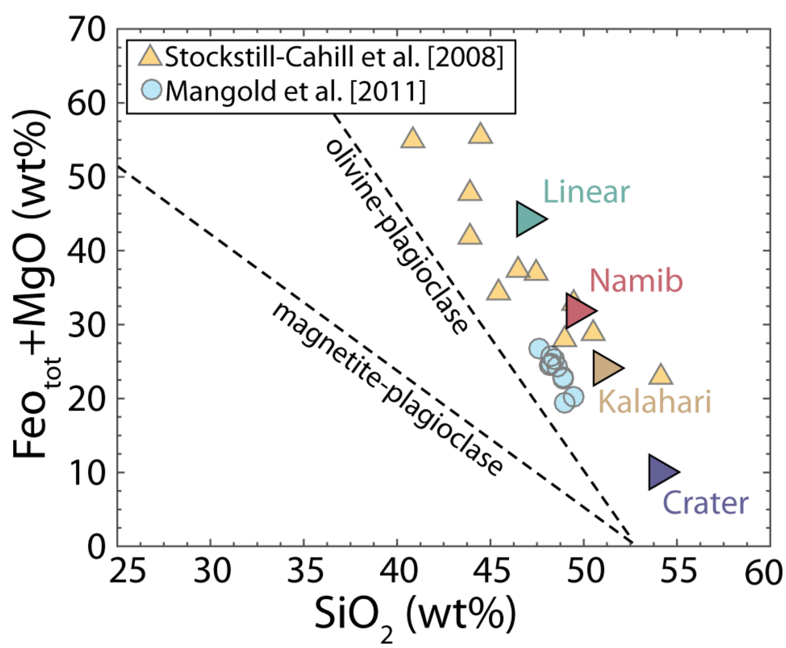

Figure 8.12: Sorting and mixing of basaltic sands by the wind. Comparison between our estimated MAP SiO_2 and FeO_{tot}+MgO compositions at the four sites and observed compositional variations in basaltic sands in Iceland on Earth (blue circles, *Mangold et al.*, 2011) and Amazonis Planitia on Mars (orange triangles, *Stockstill-Cahill et al.*, 2008).

Sorting of mineral grains by the wind likely contributes to compositional and grain size variability observed from orbit (Figure 8.1B) and by the rover (Section 4.2). Indeed, the wind speed required to initiate saltation of sand particles, often parametrized as fluid threshold shear velocity, is a function of grain density, size, and shape [*Bagnold*, 1941; *Shao and Lu*, 2000]. The threshold wind speed to maintain saltation, or impact threshold shear velocity, can be over an order of magnitude lower than the fluid threshold because of the effect of low atmospheric density on saltation trajectories and kinetics [*Kok*, 2010a]. This difference leads to a hysteresis in sand transport, such that winds required to sustain transport are much weaker than those required to initiate it. On Earth, impact and fluid thresholds are more similar [*Kok et al.*, 2012], such that the transport hysteresis is comparatively weak. On Mars, the strong dependence of the impact threshold on grain size suggests that winds below the fluid threshold may be very efficient at size-sorting sand grains.

Dune-forming wind speeds can be estimated from grain densities and sizes under the assumption of spherical grains, though this is an approximation. Based on an air temperature of 225 K and an atmospheric pressure of 6 mbar at Gale crater [e.g., *Haberle et al.*, 2014], we calculate both thresholds for transport under martian conditions from the semi-empirical formulations of *Shao and Lu* [2000] and *Kok* [2010b], which were developed for unimodal grain-size distributions. In reality, bed grain-size distributions have a finite width (very fine to medium sand; *Ehlmann et al.*, in revision), such that the threshold models we employ may be viewed as reasonable approximations. We find that grain size is more important than density in determining thresholds of motion (Figure 8.13).

For the average MAP grain sizes of olivine (~530 μm), bulk pyroxenes (~310 μm), and plagioclase (~520 μm), the required wind speeds to sustain transport of the coarser olivine grains (~0.70 m/s) are about twice those required to sustain transport of the pyroxene grains (~0.34 m/s) and ~25% larger than those required to sustain transport of plagioclase grains (~0.58 m/s). Conversely, the wind speeds required to initiate saltation of all mineral grains are more similar (between ~2.0 and 2.5 m/s). Following the premise that dune-forming winds may be constrained from the size of grains that are barely saltatable [e.g., *Fenton et al.*, 2016], we infer that dune-forming wind shear velocities at the Bagnold Dunes are typically at least 0.4-0.7 m/s with excursions upward of 2.5 m/s. Indeed, if wind speeds were always lower than the fluid threshold, coarse olivine grains could not be transported in saltation at all, while if typical wind speeds were higher than the fluid threshold, coarse olivine grains would be effectively transported across the entire dune field (along with pyroxene grains). While our CRISM-based grain-size estimates tend to be on the higher end of sizes observed on the ground, our wind-shear velocity extrapolations are consistent with Rover Environmental Monitoring Station (REMS) measurements during the martian low-sand flux season (~0.1-0.3 m/s; *Newman et al.*, 2017]), and are consistent with shear velocities inferred from global circulation models and regional studies (0.71-1.22

m/s, assuming an atmospheric density of 0.02 kg/m^3) [*Haberle et al.*, 2003; *Ayoub et al.*, 2014].

In addition to wind-sorting, mixing sediments from two sources would also spread the compositional data parallel to the plagioclase-olivine join. The magnitude of the spread in chemical composition we invert for at our four sites dwarfs that observed by *Mangold et al.* [2011] in Iceland, despite being measured over an order-of-magnitude shorter length scale (few vs. tens of kilometers), but is similar to that estimated by *Stockstill-Cahill et al.* [2008] in Amazonis Planitia over >2000 km**.** It thus seems unlikely that wind-sorting alone could explain such a large compositional spread as what we infer for the Bagnold Dunes, and we hypothesize that the dune field may be replenished in plagioclase from a more proximal sand source. Indeed, the active dunes might be eroding bedrock and incorporating eroded material. MAHLI images of sands near High Dune show sparse but clear evidence for input from local sediment sources (e.g., coarse and irregular bright grains; see *Ehlmann et al.*, in revision). A prediction is that sands further downwind in the dune field, such as the linear dunes, would be more mafic with less felsic input, a hypothesis which could be tested with the acquisition of more in situ data from Curiosity at the linear dunes to the south of Namib Dune. Potential sources include eroded and transported olivine-bearing materials from Gale crater's walls [*Ehlmann and Buz,* 2015] and more local, perhaps more felsic materials, possibly present in the walls too, but certainly present in the coarse-grained conglomerates of Aeolis Palus [*Sautter et al.*, 2015].

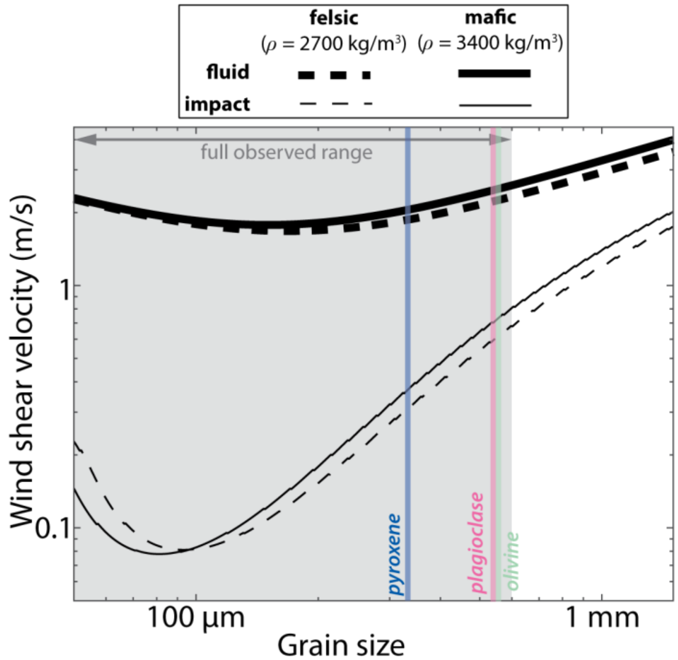

Figure 8.13: Wind shear velocities required to initiate (thick lines) and sustain (thin lines) transport of the inferred grain sizes for olivine (530 µm; green), pyroxene (310 µm; blue), and plagioclase (520 µm; magenta), as estimated from our Fo51 inversion results. Wind shear velocities were estimated using the formulations of *Shao and Lu* [2000] and *Kok* [2010b]. Light gray box outlines the full range of grain sizes observed with MAHLI [*Ehlmann et al.*, in revision].

4.4. Implications for the Interpretation of Martian Aeolian Sandstones

Aeolian sandstones reflect the compositional and size variations of the dune field from which they formed. On Earth, most aeolian sandstones are relatively homogeneous because of the strong sorting effects of wind, and because most large aeolian deposits arise from extensive fluvial and coastal systems, which preferentially sort sand grains prior to the formation of a dune field. Indeed, in well-connected transport pathways, grains of varying mineralogy and sizes are sorted over long transport distances, resulting in homogenous materials in dune fields. Examples include many large aeolian systems, such as the deserts of China, the Middle East, and Africa. In some cases, the compositional and size variations of aeolian dune fields may be high where the source area is nearby and the transport out of the basin is limited [e.g., *Fenton et al.*, 2016], though this type of system only represents a small part of the overall terrestrial aeolian rock record. In addition to sorting, efficient surface weathering can select for the most prevalent and resistant minerals on Earth, such as quartz and potassium feldspar, which make up most of Earth's aeolian sandstones. On Mars however, the formation of aeolian sand and the accumulation and preservation of aeolian sandstones is relatively poorly understood [e.g., *Kocurek and Ewing*, 2012], but our results suggest that primary variations of ~7 wt% in SiO_2 and ~20 wt% in FeO_{tot}+MgO may arise over a length scale of a few kilometers only from sorting of basaltic sand and/or mixing with local sediment sources. If the Bagnold Dunes of Gale crater are representative of the sediments forming aeolian sandstones on Mars, martian aeolian sandstones may be more poorly sorted and compositionally diverse than terrestrial aeolian sandstones. Martian sandstones [e.g., *Grotzinger et al.*, 2005; *Milliken et al.*, 2014; *Banham et al.*, 2016], thus offer the opportunity to characterize ancient aeolian environments and sediment sources if the physical sorting effects on bulk chemistry can be disentangled from chemical changes due to diagenesis and later alteration.

5. Conclusion

Spectral variability, in particular in the signature of mafic minerals, is readily observable from CRISM data over the Bagnold Dune Field at Gale crater. We showed that there is a qualitative correlation between zones of stronger olivine signatures, inferred lower dust cover, and higher sand fluxes. Under the assumption that dust cover is minor within the active dunes, we invert for modal mineralogy and grain sizes of the sands from CRISM shortwave infrared spectra at four locations near the traverse of the Curiosity rover from a Bayesian implementation of the Hapke radiative transfer model. Between sols ~1162 and ~1243, the Curiosity rover investigated the Bagnold Dunes at Gale Crater, offering an unprecedented opportunity to test our orbiter-based predictions against in situ measurements of mineral composition and grain sizes. Our quantitative estimates of bulk mineralogy favorably compare with in situ measurements from the CheMin instrument onboard Curiosity at the Namib Dune sampling site, with an average error of ~9 wt% for crystalline endmembers. Our inversion technique and subsequent comparison with in situ datasets illustrate the difficulty in resolving the precise chemistry of solid solutions on the ground due to spectral tradeoffs between mineral endmembers and grain sizes. However, model results suggest that observed spectral variations within the dune field arise from anti-correlated abundances of olivine and plagioclase grains. Our results are consistent with sorting of the grains during saltation, and in particular with the Earth-based observation that winds tend to segregate mafic and felsic phases. In addition, we hypothesize that multiple sand sources of contrasting compositions may be mixing at the Bagnold Dunes. Altogether, our quantitative constraints provide a guide for the interpretation of both modern and ancient aeolian environments on Mars from measurements of the chemical and mineral compositions of sands.

Mineral endmember		Density (kg/m^3)	Grain size range allowed (μm)	Real index of refraction, *n*	Source	Grain size range of library sample (μm)	Grain size used to calculate *k*, (μm)
olivine	**Fo51**	3320	50-800	1.67	KI3188**	<60	25
	Fo80	3320	50-800	1.67	HS285.4B**	250-1200	300
augite		3400	50-800	1.70	NMNH120049**	<60	35
pigeonite		3380	50-800	1.70	HS199.3B**	75-250	162
labradorite*		2690	50-800	1.56	HS17.3B**	75-250	162
magnetite		5150	10-200	2.42	HS195.3B**	75-250	162
basaltic glass		2780	50-800	1.50	C1BE100***	45-75	60

Table 8.1: Mineral endmembers, assumed densities, allowed grain size ranges, and assumed real index of refraction. The endmember spectra we selected from the USGS Spectral Library [*Clark et al.*, 2007] were acquired with a Beckman spectrometer in directional conical mode, with a measured average phase angle of 30 degrees; we thus assumed an incidence angle of 30° and emission angle of 0° for those spectra. *Contains magnetite as disseminated microscopic impurities. ***Clark et al. [2007]*. ***RELAB Brown/Nasa-Keck spectral library.

(wt%)	Namib		Kalahari		Linear		Crater	
	Fo51	**Fo80**	**Fo51**	**Fo80**	**Fo51**	**Fo80**	**Fo51**	**Fo80**
olivine	27.3	12.6	9.5	7.1	40.5	29.0	0.2	0.4
augite	4.0	14.3	11.2	12.3	9.9	17.7	8.3	5.6
pigeonite	28.1	7.2	16.9	18.7	30.9	13.3	6.5	22.7
labradorite	31.8	38.7	36.6	41.0	4.3	1.1	58.9	51.2
magnetite	0.7	0.3	2.3	0.5	1.3	4.6	0.3	0.3
basaltic glass	8.1	26.9	23.6	20.4	13.2	32.3	25.9	19.2

Table 8.2: MAP abundances (in wt%) at our four regions of interest.

(μm)	Namib		Kalahari		Linear		Crater	
	Fo51	**Fo80**	**Fo51**	**Fo80**	**Fo51**	**Fo80**	**Fo51**	**Fo80**
olivine	685	701	284	772	510	756	625	572
augite	290	253	343	180	526	161	633	704
pigeonite	345	378	125	436	128	66	259	522
labradorite	606	390	487	452	239	106	744	790
magnetite	103	162	197	165	169	168	110	127
basaltic glass	127	135	129	110	96	102	205	228

Table 8.3: **MAP grain sizes** (in μm) at our four regions of interest. Note that for all phases but magnetite, a uniform distribution would have a mean grain size of 425 μm. For magnetite, a uniform distribution would have a mean of 105 μm.

Mineral phases	Abundances (wt%)	Abundances renormalized to crystalline phases only (wt%)
olivine (Fo ~55)	17.5	26.9
high-Ca pyroxene (Wo ~40)	14.9	22.9
low-Ca pyroxene (Wo ~9)	7.1	11.0
plagioclase (An ~63)	24.1	37.0
magnetite	1.4	2.2
XRD-amorphous	35.0	N/A

Table 8.4: Weight abundance of mineral endmembers of interest as measured by the CheMin instrument onboard Curiosity at Namib Dune [*Achilles et al.*, in revision]. Note that throughout this study, we compare our estimated abundance of basaltic glass to that of the XRD-amorphous phase, although the latter may also contain other phases. See [*Achilles et al.*, in revision] for raw data, and associated uncertainties.

Acknowledgments and Data

We are indebted to the MSL Engineering and Science and Operations teams for collecting the in situ data, and Chi Ma of Caltech for compositional measurements of our basaltic-glass sample. We thank Alan Delamere and Rodney Heyd for their guidance on the use of HiRISE band ratios, and Christopher Edwards for providing us with the seamless color HiRISE mosaic shown in Figure 8.1A. Thanks to the CRISM operations team for collecting the dataset and to the CheMin team for rapid sharing of their results from MSL analyses on Mars. We also thank Tim Titus and Jessica Ball of the U.S. Geological Survey for informal reviews of our manuscript, and Ralph Milliken and an anonymous reviewer for thorough reviews that improved our original manuscript. A portion of this research was carried out at the Jet Propulsion Laboratory, California Institute of Technology, under a contract with the National Aeronautics and Space Administration. MGAL was partially funded by a NASA Earth and Space Science Fellowship (12-PLANET12F-0071) and from a MSL participating Scientist Program grant to BLE. AAF also acknowledges funding from a MSL Participating Scientist Program grant. Data presented in this paper is or will be posted on the Planetary Data System (PDS).

Chapter 9

CONCLUDING REMARKS

In this thesis, we aimed at pushing the boundaries of our understanding of sedimentary processes on Earth and Mars, and in particular of how the mechanics of erosion, sediment transport, and deposition are affected by martian environmental conditions. Altogether, this new mechanistic understanding of sedimentary processes enabled us to place quantitative constraints on the hydrology, climate, and habitability of Mars (Figure 9.1).

In Chapter 2, we investigate the mechanics of canyon formation by groundwater-fed springs. Because spring environments are prime astrobiological targets owing to their habitability and preservation potentials, understanding the formation-mechanics of these canyons is critical to assessing their potential as possible future exploration targets. We showed that tradeoffs between rock permeability and the size of eroded material promote canyon formation by groundwater-seepage erosion in sand-sized loose to weakly consolidated sediments; finer-grained sediments have permeabilities that are too low for eroded material to be transported away from a seepage face, while coarser grains are too heavy to be transported by groundwater discharge. Our new theory is supported by physical experiments and natural canyons of known origin on Earth. With this new understanding of groundwater-seepage erosion on hand, we argued that Hesperian amphitheater-headed bedrock canyons near Echus Chasma formed by waterfall-erosion during overland floods (Figure 9.1).

In Chapter 3, we formulated semi-empirical relations to characterize the hydraulics of floods upstream of horseshoe-shaped waterfalls, and in particular, to predict the distribution of flow velocities around the rim of such escarpments. We showed that flow convergence towards canyon heads leads to enhanced flow velocities around the head of horseshoe canyons relative to along the canyon sidewalls, which has significant implication for canyon formation and dynamics.

Combining these scaling relations with waterfall-erosion mechanics, we developed a new paleohydraulic technique to constrain flow discharge, duration, and volume of canyon-carving floods in Chapter 4. We showed that predicted flow discharges are up to over two orders of magnitude lower than one would estimate by making the classic brimful canyon-formation assumption; rather, we find that flow conditions during canyon formation were similar to those of gravel-bedded rivers on Earth, with flows that barely exceeded the thresholds of sediment transport. This finding is fundamental to our understanding of controls on the width of bedrock canyons on Earth, and bears important promise in reevaluating the water budget of Hesperian outflow channels on Mars that we wish to explore in the future. Despite their lower discharge estimates than would be inferred from classic paleohydraulic methods, we find that martian floods were large (10^6-10^7 m^3/s) but short-lived (~ 1 month) (Figure 9.1). In particular, we estimated that a cumulative water volume of $3.5x10^{14}$ m^3 was required to carve seven canyons near Echus Chasma, or about 10% of the volume of the Mediterranean Sea. We estimate that similar water volumes carved a dry cataract near the Ares Vallis outflow channel. A 10^{14} m^3 volume of water delivered to the northern lowlands at once would create a body of water >2 m deep.

In Chapter 5, we compiled an extensive dataset of current ripples formed in flume experiments and natural rivers to develop a universal scaling relation that predicts the equilibrium size of current ripples. In doing so, we identified a new dimensionless quantity, the Yalin number, which plays a major role in controlling the size of ripples and the transition from ripples to dunes. This finding is fundamental to our understanding of bedform stability, suggesting that ripples and dunes are dynamically different, and that the ripple-to-dune transition may be tied to the onset of fully turbulent eddies downstream of the bedform crest. In addition, we predicted the formation of meter-scale ripples in briny flows on Mars and methane flows over icy grains on Titan.

In Chapter 6, we showed that Mars hosts three sizes of wind-blown bedforms, i.e., there is one more mode of aeolian bedform on Mars than in Earth's sandy deserts. Theses extraterrestrial bedforms, the large martian ripples, have morphologies that resemble that of current ripples on Earth's riverbeds. Building on a compilation of martian bedform sizes, we show that the wavelength of large martian ripples decreases with atmospheric density, and that this trend is quantitatively consistent with the scaling relation developed in Chapter 5. Altogether, these results support our interpretation of the large martian ripples as wind-drag ripples that form on Mars due to the lower atmospheric density. A reevaluation of cross-strata in the Burns formation aeolian sandstone at Victoria crater suggests that Mars had a modern-like atmospheric density at the time of deposition, at the turn of the Hesperian period (Figure 9.1). In addition to their significance for the modern and past martian environments, the recognition of wind-drag ripples may change our view of Earth's aeolian bedforms and environments. Do wind-drag ripples exist today on Earth but simply are not recognized as such? Is there a record of Earth's atmospheric pressure in ancient aeolian sandstones? Those are questions we intend to tackle in the future.

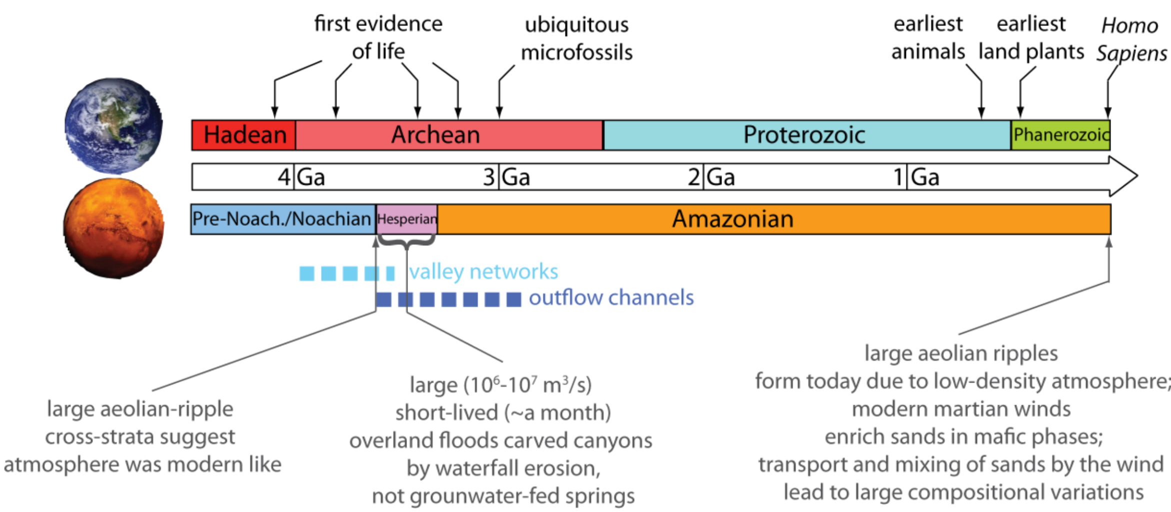

Figure 9.1: Constraints on the hydrology, climate, and habitability of Mars resulting from work presented in this thesis.

In Chapter 7, we developed a new probabilistic framework to invert for mineral composition and grain sizes of particulate planetary regolith from VSWIR data and assess the errors and uncertainties of inversion results. We found that errors are low when mineral endmembers and their chemical composition are well constrained, but uncertainties remain large owing to tradeoffs between mineral abundances and grain sizes. We found that grain sizes are poorly constrained in general. We quantitatively characterized errors and uncertainties associated with imperfections in forward scattering models, instrumental noise, and mineral endmembers and their composition. This new technique has significant promise in determining the composition of planetary surfaces and assessing the degree of confidence of inversion results.

In Chapter 8, we used the new technique developed in Chapter 7 to infer the mineral composition and grain sizes of sands of the Bagnold Dune Field in Gale crater. We found that dust cover, olivine signature, and ripple displacement qualitatively correlate, suggesting that sand mineralogy and flux are interrelated. We conducted the first direct comparison of orbiter and rover-based mineralogy of martian sands by comparing our quantitative estimates of mineral composition at the Namib Dune with compositional data measured by the Curiosity rover at the same location. We found our orbiter-based predictions to be within <13 wt% of ground truth, with the largest discrepancies in the relative contributions of low vs. high Ca pyroxenes. When extended to three other locations across the Bagnold Dune Field, our quantitative estimates of sand mineralogy suggest that the observed spectral variability over the dune field is consistent with an enrichment of mafic mienrals with cumulative transport distance. Cumulatively, we found that both sorting of mineral phases and mixing with locally derived sediment may lead to large, tens of percents ranges in the mafic composition of wind-blown sediment across short, kilometer-scale, distances (Figure 9.1). This result is in strong contrast with terrestrial wind-blown sandstones, which are much more homogenous in mineral composition overall, and places important constraints on future interpretations of the composition of martian aeolian sandstones.

Altogether, the new physics-based theories presented in this thesis collectively place important constraints on the hydrology, climate, and habitability of Mars; we believe that such quantitative constraints, built from a mechanistic dialogue between Earth-based and extraterrestrial observations, will be critical to humankind's success in finding past and extent life on Mars and elsewhere in the solar system.

APPENDIX A.1: NOTATIONS FOR CHAPTER 3

C_f	Dimensionless friction coefficient
Fr	Froude number
Fr_n	Normal Froude number
Fr_0	Froude number at the rim
g	Acceleration of gravity (m/s^2)
h	Flow depth (m)
h_c	Critical flow depth (m)
h_n	Normal flow depth (m)
h_0	Flow depth at the brink (m)
l	Canyon length (m)
$l*$	Downslope backwater parameter
L_b	Backwater length (m)
n	Manning's *n* (s/m$^{1/3}$)
q	Discharge per unit width (m^2/s)
q_n	Upstream discharge per unit width (m^2/s)
q_0	Discharge per unit width at the brink (m^2/s)
$q*$	Normalized cumulative head discharge
Q_h	Total discharge within the canyon head (m^3/s)
Q_n	Normal discharge flowing across a width of a canyon radius (m^3/s)
r	Ratio of flow depth to normal flow depth
S	Bed slope upstream of the waterfall
t	Time (s)
U	Depth-averaged flow velocity (m/s)
U_n	Depth-averaged normal flow velocity (m/s)
U_p	Depth-averaged flow velocity perpendicular to the brink (m/s)
U_x	Depth-averaged downslope component of flow velocity (m/s)
U_y	Depth-averaged cross-slope component of flow velocity (m/s)
U_0	Depth-averaged flow velocity at the brink (m/s)
u_*	Shear velocity (m/s)
w	Canyon width (m)
$w*$	Canyon-to-flood width ratio
$W*$	Lateral backwater Flood-width limitation factor
W	Flood-width (m)
x	Downslope spatial coordinate (m)
y	Cross-slope spatial coordinate (m)
α_{1D}	Acceleration factor at the brink of a 1-D step
α_{2D}	Acceleration factor at the brink of a 2-D canyon
$\alpha*$	Acceleration factor ratio

α^*_h	Acceleration factor ratio at the head center
α^*_w	Acceleration factor ratio at the head-to-wall junction
α^*_t	Acceleration factor ratio at the canyon toe
$\alpha^*_{w,sf}$	Acceleration factor ratio at the head-to-wall junction for a sheet flood
$\alpha^*_{t,sf}$	Acceleration factor ratio at the canyon toe for a sheet flood
ε	Fractional acceleration caused by non-hydrostatic pressure at the rim
θ	Azimuth with respect to the canyon centerline
ρ	Density of water (kg/m^3)
τ_b	Bed shear stress (N/m^2)

APPENDIX A.2: ACCELERATION FACTOR RATIO AND NORMALIZED CUMULATIVE DISCHARGE FIT RELATIONSHIPS

Note that $q*$ in Chapter 3 and $Q*$ in Chapter 4 both refer to normalized cumulative discharge as defined in this appendix.

The acceleration factor ratio at the head α_h^* decreases with Froude number Fr_n for subcritical floods, and is roughly equal to unity for supercritical floods.

$$\alpha_h^* = \begin{cases} 1+0.05(1-\mathrm{Fr}_n)^{1.65} & \text{for } \mathrm{Fr}_n < 1 \\ 1 & \text{for } \mathrm{Fr}_n \geq 1 \end{cases}. \tag{A1}$$

In the case of a sheet flood ($w* << 1$ and $W* > 1$), the acceleration factor ratio at the wall α_w^* decreases with Froude number Fr_n, and the decrease is steeper for Fr_n between 1 and 3.

$$\alpha_{w,sf}^* = 1.47\exp\left[-\left(\frac{\mathrm{Fr}_n+1.18}{1.58}\right)^2\right] - 0.53\exp\left[-\left(\frac{\mathrm{Fr}_n+0.03}{0.53}\right)^2\right] + 85550\exp\left[-\left(\frac{\mathrm{Fr}_n+51}{14.7}\right)^2\right]. \tag{A2}$$

For a sheet flood, the acceleration factor ratio at the toe α_t^* increases with Froude number Fr_n and decreases with the downslope backwater parameter $l*$.

$$\alpha_{t,sf}^* = \begin{cases} (2.08\mathrm{Fr}_n^{0.11} - 1.76)(3.68 l*^{-0.31}) & \text{for } \mathrm{Fr}_n < 1 \\ (2.08\mathrm{Fr}_n^{0.11} - 1.76)(2.02 - 0.29 l*^{0.35}) & \text{for } \mathrm{Fr}_n \geq 1 \end{cases}. \tag{A3}$$

For subcritical non-sheet floods, the acceleration factor at the wall α_w^* decreases with the canyon-width to flood-width ratio w^* and increases with the flood-width limitation factor W^* (as long as $W^*<1$). For supercritical non-sheet floods, the acceleration factor ratio at the wall α_w^* slightly increases with canyon-width to flood-width ratio w^*.

$$\alpha_w^* = \begin{cases} \alpha_{w,sf}^*(1-w^*)^{0.22} G_1 & \text{for } \mathrm{Fr}_n < 1 \\ \alpha_{w,sf}^*(5.80 w^{*0.06} - 4.07) & \text{for } \mathrm{Fr}_n \geq 1 \end{cases}, \qquad \text{(A4)}$$

in which

$$G_1 = \begin{cases} [1.06 - 0.38(1-W^*)^{1.41}] & \text{for } W^* < 1 \\ [1.07 - 7.72\,\mathrm{x}10^{-3} W^*] & \text{for } W^* \geq 1 \end{cases}. \qquad \text{(A5)}$$

The acceleration factor ratio at the toe α_t^* for subcritical non-sheet floods increases with w^* and decreases with W^*. For supercritical non-sheet floods, the acceleration factor ratio at the toe α_t^* increases with both w^* and W^*.

$$\alpha_t^* = \begin{cases} \alpha_{t,sf}^*(0.87 - 21.75 w^{*4.65})\left[1.18\exp(0.01W^*) - 1.39\exp(-0.38W^*)\right] & \text{for } \mathrm{Fr}_n < 1 \\ \alpha_{t,sf}^*(1 + 0.68 w^{*5.09})\left[1.07 - 1.21\exp(-0.49W^*)\right] & \text{for } \mathrm{Fr}_n \geq 1 \end{cases}. \qquad \text{(A6)}$$

Normalized cumulative head discharge q^* decreases with Froude number Fr_n, increases and then decreases with flood-width limitation factor W^*, and either decreases or is constant with canyon-width to flood-width ratio w^* depending on whether the flood is sub- or supercritical.

$$q^* = \begin{cases} \left[1+0.79\exp\left(-2.16\,\mathrm{Fr}_n\right)\right]\left(1.14-0.33w^{*0.37}\right)G_2 & \text{for } \mathrm{Fr}_n < 1 \\ \left[1+0.79\exp\left(-2.16\,\mathrm{Fr}_n\right)\right] & \text{for } \mathrm{Fr}_n \geq 1 \end{cases}, \quad \text{(A7)}$$

in which

$$G_2 = \begin{cases} 1.03-0.16\left(1-W^*\right)^{2.85} & \text{for } W^* < 1 \\ 1.08-0.04W^{*0.31} & \text{for } W^* \geq 1 \end{cases}. \quad \text{(A8)}$$

Note that these fit relationships are valid for the tested range and combinations of dimensionless parameters listed in Table 3.1 but should be used with caution when applied near the edges of the parameter ranges modeled in this study for non-sheet floods. They were tested against test simulations that encompassed different parameter combinations (Figure 3.13, Table 3.1), and are yet to be validated outside of the modeled ranges. Nevertheless, most of the acceleration factor ratios have predictable asymptotical behaviors (Section 5).

APPENDIX B.1: NOTATIONS FOR CHAPTER 4

Symbol	Variable (Unit)
A_c	canyon cross-sectional area (m^2)
A^*	shear stress enhancement factor at the waterfall brink
$A_c{}^*$	normalized critical shear stress for rock toppling
$A_h{}^*$	shear stress enhancement factor at the canyon head
$A_t{}^*$	shear stress enhancement factor at the canyon toe
$A_w{}^*$	shear stress enhancement factor at the canyon wall
C_d	drag coefficient over rock protrusions
C_{f}	dimensionless bed friction coefficient
C_{fb}	dimensionless bed friction coefficient within the canyon
C_{f0}	dimensionless bed friction coefficient at the waterfall brink
d	grain diameter (m)
D	fracture spacing/block size (m)
Fr_n	upstream Froude number
FS	toppling factor of safety
g	acceleration of gravity (m/s^2)
h	flow depth (m)
h_{bf}	flow depth in brimful conditions (m)
h_i	flow depth at initiation of sediment motion (m)
h_n	normal flow depth upstream of the waterfall (m)
h_{nb}	normal flow depth within the canyon (m)
h_0	flow depth at the waterfall brink (m)
H_c	cliff/rock column height (m)
H_p	plunge-pool depth (m)
i	flood intermittency factor
k	bed roughness (m)
l	canyon length (m)
l^*	downslope backwater factor
n	Manning's *n*
q_h	discharge per unit width within the canyon head (m^2/s)
q_n	upstream discharge per unit width (m^2/s)
q_i	discharge per unit width at initiation of sediment motion (m^2/s)

q_n	upstream discharge per unit width (m^2/s)
q_s	sediment capacity per unit width (m^2/s)
$Q_{h,2D}$	discharge within the canyon head as inverted from the 2-D model (m^3/s)
$Q*$	normalized cumulative head discharge
R	reduced density of sediment
S	upstream bed slope
S_b	bed slope within the canyon
T_b	torque per unit width exerted by buoyancy on a rock column (N)
T_d	torque per unit width exerted by flow drag on a rock column (N)
T_f	flood duration (s)
T_g	torque per unit width exerted by gravity on a rock column (N)
T_s	torque per unit width exerted by flow shear on a rock column (N)
U_n	upstream flow velocity (m/s)
U_p	flow velocity at the waterfall brink in the direction perpendicular to the rim (m/s)
U_0	flow velocity at the waterfall brink (m/s)
w	canyon width (m)
$w*$	canyon-to-flood width ratio
W	flood width (m)
$W*$	flood width limitation factor
α	acceleration factor at the brink of a waterfall
$\alpha*$	acceleration factor ratio
α_{1D}	acceleration factor at the brink of a 1-D step
α_{2D}	acceleration factor at the brink of a 2-D canyon
γ	canyon cross-sectional geometry shape factor
δ	volumetric water-to-rock ratio
η	column protrusion height (m)
ρ	density of water (kg/m^3)
ρ_r	density of rock (kg/m^3)
τ_c	critical shear stress for rock toppling (N/m^2)
τ_0	shear stress exerted by flow at the waterfall brink (N/m^2)
$\tau_{0,1D}$	shear stress exerted by flow at the brink of a 1-D step (N/m^2)
$\tau_{0,2D}$	shear stress exerted by flow at the brink of a 2-D canyon (N/m^2)
τ_*	Shields stress for initiation of sediment motion
τ_{*c}	critical Shields stress for initiation of sediment motion

APPENDIX B.2: SHEAR STRESS ENHANCEMENT FACTOR FIT RELATIONSHIPS

Fit relationships for the shear stress enhancement factors were obtained from the numerical simulations of *Lapôtre and Lamb* [2015] through multiple power law regressions, following the technique described in the latter study. All trends are qualitatively similar to those observed for the acceleration factor ratios, $\alpha *$, and are discussed at length in *Lapôtre and Lamb* [2015].

Shear stress enhancement factor at the head, $A_h *$:

$$A_h^* = 0.37\exp\left[-\left(\frac{\mathrm{Fr_n} - 0.17}{0.38}\right)^2\right] + 1.04\exp\left[-\left(\frac{\mathrm{Fr_n} - 2.89}{78.6}\right)^2\right]. \tag{B1}$$

Shear stress enhancement factor at the wall, $A_w *$:

$$A_w^* = 0.79\exp\left[-\left(\frac{\mathrm{Fr}_n - 6.68\mathrm{x}10^{-2}}{1.13}\right)^2\right] G_3, \tag{B2}$$

where

$$G_3 = \begin{cases} \left(1 - w^*\right)^{0.38} G_4 & \text{for } \mathrm{Fr}_n < 1 \\ 1 & \text{for } \mathrm{Fr}_n \geq 1 \end{cases}, \tag{B3}$$

and

$$G_4 = \begin{cases} \left[0.76 - 0.32\left(1 - W^*\right)^{1.44}\right] & \text{for } W^* < 1 \\ \left[1.03 - 0.27 W^{*-2.62}\right] & \text{for } W^* \geq 1 \end{cases}. \tag{B4}$$

Shear stress enhancement factor at the toe, $A_t *$:

$$A_t^* = \left(0.47\mathrm{Fr}_n^{0.47} - 0.26\right) G_5, \tag{B5}$$

where

$$G_5 = \begin{cases} \left(0.79 - 8.24 w^{*3.39}\right)\left(0.47 W^{*0.58} - 0.26\right)\left(8.38 l^{*-0.49}\right) & \text{for } \mathrm{Fr}_n < 1 \\ \left(1 + 0.96 w^{*3.46}\right)\left(1.13 W^{*0.37} - 0.87\right)\left(2.84 - 0.51 l^{*0.31}\right) & \text{for } \mathrm{Fr}_n \geq 1 \end{cases}. \tag{B6}$$

APPENDIX C: NOTATIONS FOR CHAPTER 7

$\mathbf{a}$	Concentration parameters for the Dirichlet distribution
B	Backscattering function
B	Multinomial beta function
$\mathbf{C}_\chi$	Covariance matrix
$\mathbf{d}$	Spectral data
$\mathbf{D}$	Grain sizes (μm)
$\langle D \rangle$	Mean free path (m)
Dir	Dirichlet distribution
$\mathbf{e}$	Measurement error
f	Mineral relative cross-section
g	Phase angle
G	Deterministic forward model
H	Chandrasekhar integral function
J	Number of transitional PDFs in CATMIP [e.g., *Minson et al.*,, 2013]
k	Imaginary refractive index
L	Length of the Markov chain
$\mathbf{m}$	Mineral abundances (wt%)
n	Real refractive index
N	Number of mineral endmembers
N_d	Number of wavelengths/single scattering albedo pairs in the data
p	Probability
P	Phase function
r	Reflectance
r_0	Bihemispherical reflectamce for isotropic scatterers
r_i	Internal bihemispherical reflectance in a particle
s	Volume scattering coefficient inside a particle
S_e	Surface reflection coefficient for externally incident light
S_i	Reflection coefficient for internally scattered light
u	Random draw from the standard uniform distribution, $U(0,1)$
U	Uniform distribution
w	Single scattering albedo
x	Generic variable
y	Candidate sample for the Markov chain
z	Random draw from a zero-mean multivariate normal distribution
α	Internal absorption coefficient

β	Tempering parameter for CATMIP [e.g., *Minson et al.*,, 2013]
γ	$\sqrt{(1-w)}$
Γ	Gamma function
$\boldsymbol{\delta}$	Measurement predictions
$\boldsymbol{\varepsilon}$	Model prediction errors
η	Mean of $(\mathbf{e}+\boldsymbol{\varepsilon})$
$\boldsymbol{\theta}$	Set of model parameters
Θ	Particle internal transmission coefficient
λ	Wavelength of light (μm)
μ	Cosine of the light emergence angle
μ_0	Cosine of the light incidence angle
ρ	Mineral density (kg/m^3)
σ	Mineral cross-section (m^2)
Σ	Covariance of proposal PDF in CATMIP [e.g., *Minson et al.*,, 2013]
ϕ	$\min\left\{1, \frac{p(\mathbf{y}\,\|\,\mathbf{d})}{p(\boldsymbol{\theta}_i\,\|\,\mathbf{d})}\right\}$

BIBLIOGRAPHY

Abrams, D. M., A. E. Lobkovsky, A. P. Petroff, K. M. Straub, B. McElroy, D. C. Mohrig, A. Kudrolli, and D. H. Rothman (2009), Growth laws for channel networks incised by groundwater flow, *Nature Geoscience, 2*(3), 193-196, DOI:10.1038/ngeo432.

Achilles, C. N., R. T. Downs, D. W. Ming, E. B. Rampe, R. V. Morris, A. H. Treiman, S. M. Morrison, D. F. Blake, D. T. Vaniman, R. C. Ewing, S. J. Chipera, A. S. Yen, T. F. Bristow, B. L. Ehlmann, R. Gellert, R. M. Hazen, K. V. Fendrich, P. I. Craig, J. P. Grotzinger, D. J. Des Marais, J. D. Farmer, P. C. Sarrazin, and J. M. Morookian (in revision), Mineralogy of an Active Eolian Sediment from the Namib Dune, Gale Crater, Mars, *Journal of Geophysical Research: Planets*.

Alexander, L. J. D. (1981), *On the geometry of ripples generated by unidirectional open channel flows*, National Library of Canada.

Alho, P., A. J. Russell, J. L. Carrivick, and J. Kayhko (2005), Reconstruction of the largest Holocene jökulhlaup within Jökulsá á Fjöllum, NE Iceland, *Quaternary Science Reviews*, *24*(22), 2319-2334, DOI: 10.1016/j.quascirev.2004.11.021.

Allen, J. (1973), Features of cross-stratified units due to random and other changes in bed forms, *Sedimentology*, *20*(2), 189-202.

Allen, J. R. L. (1982), Sedimentary structures, their character and physical basis: New York, Elsevier, 593 p.

Almeida, M. P., E. J. Parteli, J. S. Andrade, and H. J. Herrmann (2008), Giant saltation on Mars, *Proceedings of the National Academy of Sciences*, *105*(17), 6222-6226, DOI: 10.1073/pnas.0800202105.

Alonso, C. V., S. J. Bennett, and O. R. Stein (2002), Predicting head cut erosion and migration in concentrated flows typical of upland areas, *Water Resources Research*, *38*(12), 39-31, DOI: 10.1029/2001WR001173.

Amidon, W. H., and A. C. Clark (2014), Interaction of outburst floods with basaltic aquifers on the Snake River Plain: Implications for Martian canyons, *Geological Society of America Bulletin*, B31141. 31141, DOI: 10.1130/B31141.1.

Anderson, R., and J. F. Bell III (2010), Geologic Mapping and Characterization of Gale Crater and Implications for Its Potential as a Mars Science Laboratory Site, Mars, 5, 76-128, DOI: 10.1555/mars.2010.0004.

Anderson, R. S. (1990), Eolian ripples as examples of self-organization in geomorphological systems, *Earth-Science Reviews*, *29*(1), 77-96.

Anderson, R. S., and K. L. Bunas (1993), Grain size segregation and stratigraphy in aeolian ripples modelled with a cellular automaton, *Nature*, 365(6448), 740-743.

Andreotti, B., P. Claudin, and O. Pouliquen (2006), Aeolian sand ripples: experimental study of fully developed states, *Physical Review Letters*, *96*(2), 028001, DOI: 10.1103/PhysRevLett.96.028001.

Andrews-Hanna, J. C., and R. J. Phillips (2007), Hydrological modeling of outflow channels and chaos regions on Mars, *Journal of Geophysical Research:Planets*, *112*(E8), DOI: 10.1029/2006JE002881.

Annandale, G. (1995), Erodibility, *Journal of Hydraulic Research*, *33*(4), 471-494.

Armaly, B. F., F. Durst, J. Pereira, and B. Schonung (1983), Experimental and theoretical investigation of backward-facing step flow, *Journal of Fluid Mechanics*, 127, 473–496, DOI:10.1017/S0022112083002839.

Arvidson, R. E., S. W. Squyres, R. C. Anderson, J. F. Bell III, D. Blaney, J. Brueckner, N. A. Cabrol, W. M. Calvin, M. H. Carr, P. R. Christensen, B. C. Clark, L. Crumpler, D. J. Des Marais, P. A. de Souza Jr., C. d'Uston, T. Economou, J. Farmer, W. H. Farrand, W. Folkner, M. Golombek, S. Gorevan, J. A. Grant, R. Greeley, J. P. Grotzinger, E. Guinness, B. C. Hahn, L. Haskin, K. E. Herkenhoff, J. A. Hurrowitz, S. Hviid, J. R. Johnson, G. Klingelhofer, A. H. Knoll, G. Landis, C. Leff, M. Lemmon, R. Li, M. B. Madsen, M. C. Malin, S. M. McLennan, H. Y. McSween, D. W. Ming, J. Moersch, R. V. Morris, T. Parker, J. W. Rice Jr., L. Richter, R. Rieder, D. S. Rodionov, C. Schroder, M. Sims, M. Smith, P. Smith, L. A. Soderblom, R. Sullivan, S. D. Thompson, N. J. Tosca, A. Wang, H. Wankem J. Ward, T. Wdowiak, M. Wolff, and A. Yen (2006), Overview of the spirit Mars exploration rover mission to Gusev Crater: Landing site to Backstay Rock in the Columbia Hills, *Journal of Geophysical Research: Planets*, *111*(E2), DOI: 10.1029/2005JE002499.

Arvidson, R. E., S. W. Squyres, J. F. Bell III, J. Catalano, B. Clark, L. Crumpler, P. de Souza, A. Fairen, W. Farrand, and V. Fox (2014), Ancient aqueous environments at Endeavour crater, Mars, *Science*, 343(6169), 1248097, DOI: 10.1126/science.1248097.

Arvidson, R., J. F. Bell III, J. Catalano, B. Clark, V. Fox, R. Gellert, J. P. Grotzinger, E. Guinness, K. E. Herkenhoff, A. Knoll, M. G. A. Lapôtre, S. M. McLennan, D. Ming, R. Morris, S. L. Murchie, K. Powell, M. Smith, S. W. Squyres, M. Wolff, and J. Wray (2015), Mars Reconnaissance Orbiter and Opportunity observations of the Burns formation: Crater hopping at Meridiani Planum, *Journal of Geophysical Research: Planets*, 120(3), 429-451, DOI: 10.1002/2014JE004686.

Ashley, G. M. (1990), Classification of large-scale subaqueous bedforms: A new look at an old problem, *Journal of Sedimentary Research*, 60, 160–172, DOI:10.2110/jsr.60.160.

Ayoub, F., J.-P. Avouac, C. Newman, M. Richardson, A. Lucas, S. Leprince, and N. T. Bridges (2014), Threshold for sand mobility on Mars calibrated from seasonal variations of sand flux, *Nature Communications*, *5*, DOI: 10.2038/ncomms6096.

Baas, J. H. (1994), A flume study on the development and equilibrium morphology of current ripples in very fine sand, *Sedimentology*, 41, 185–209, DOI:10.1111/j.1365-3091.1994.tb01400.x.

Baas (1999), An empirical model for the development and equilibrium morphology of current ripples in fine sand, *Sedimentology*, 46, 123–138, DOI:10.1046/j.1365-3091.1999.00206.x.

Bagnold, R. (1937), The transport of sand by wind, *Geographical Journal*, *89*(5), 409-438.

Bagnold, R., *The physics of blown sand and desert dunes*. (Methuen and Co., London, 1941), vol. 10, pp. 265.

Baker, V. R., and D. J. Milton (1974), Erosion by catastrophic floods on Mars and Earth, *Icarus*, *23*(1), 27-41.

Baker, V. R. (1982), *The channels of Mars*, 204 pp., University of Texas Press, Austin.

Baker, V. R., R. Strom, V. Gulick, J. Kargel, G. Komatsu, and V. Kale (1991), Ancient oceans, ice sheets and the hydrological cycle on Mars, *Nature*, *352*, 589-594, DOI: 10.1038/352589a0.

Baker, V. R. (2009), High-energy megafloods: planetary settings and sedimentary dynamics, in *Flood and megaflood processes and deposits: recent and ancient examples*, edited by I. A.S., pp. 3-15.

Baker, V. R. (1973), Paleohydrology and sedimentology of Lake Missoula flooding in eastern Washington, *Geological Society of America Special Papers*, *144*, 1-73.

Balme, M., D. C. Berman, M. C. Bourke, and J. R. Zimbelman (2008), Transverse aeolian ridges (TARs) on Mars, *Geomorphology*, *101*(4), 703-720, DOI: 10.1016/j.geomorph.2008.03.011.

Banham, S. S., S. Gupta, D. M. Rubin, J. A. Watkins, D. Y Sumner, J. P. Grotzinger, K. W. Lewis, K. S. Edgett, L. A. Edgar, and K. M. Stack (2016), Reconstruction of an ancient eolian dune field at Gale crater, mars: Sedimentary analysis of the Stimson formation. In Proceedings of the 47th Lunar and Planetary Science Conference, Abstract 2346.

Barnes, M. P., and T. E. Baldock (2006), Bed shear stress measurements in dam break and swash flows, paper presented at International Conference on Civil and Environmental Engineering (ICCEE-2006).

Barree, R., and M. Conway (2004), Beyond beta factors: a complete model for Darcy, Forchheimer, and trans-Forchheimer flow in porous media, paper presented at SPE annual technical conference and exhibition, Society of Petroleum Engineers.

Bartholdy, J., V. B. Ernstsen, B. W. Flemming, C. Winter, A. Bartholoma, and A. Kroon (2015), On the formation of current ripples, *Scientific Reports*, 5, 1–9, DOI:10.1038/srep11390.

Barton, J. R., and P.-N. Lin (1955), *A Study of the Sediment Transport in Alluvial Channels*, Civil Engineering Department, Colorado A and M College.

Bayes, M. (1763), An Essay towards solving a Problem in the Doctrine of Chances, *Philosophical Transactions of the Royal Society*, *53*, 370-418.

Baynes, E. R., M. Attal, A. J. Dugmore, L. A. Kirstein, and K. A. Whaler (2015a), Catastrophic impact of extreme flood events on the morphology and evolution of the lower Jökulsá á Fjöllum (northeast Iceland) during the Holocene, *Geomorphology*, DOI: 10.1016/j.geomorph.2015.05.009.

Baynes, E. R., M. Attal, S. Niedermann, L. A. Kirstein, A. J. Dugmore, and M. Naylor (2015), Erosion during extreme flood events dominates Holocene canyon evolution in northeast Iceland, *Proceedings of the National Academy of Sciences*, *112*(8), 2355-2360, DOI: 10.1073/pnas.1415443112.

Bear, J. (1972), *Dynamics of fluids in porous media*, 764 pp., Elsevier, New York.

Beck, J. L., and S. K. Au (2002), Bayesian updating of structural models and reliability using Markov chain Monte Carlo simulation, *Journal of Engineering Mechanics*, *128*(4), 380-391, DOI: 10.1061/(ASCE)0733-9399.

Beck, J. L., and K. M. Zuev (2013), Asymptotically independent Markov sampling: a new MCMC scheme for Bayesian inference, *International Journal of Uncertainty Quantification*, *3*(5), 445-474.

Bell III, J. F., S. W. Squyres, K. E. Herkenhoff, J. N. Maki, H. M. Arneson, D. Brown, S. A. Collins, A. Dingizian, S. T. Elliot, E. C. Jagerott, A. G. Hayes, M. J. Johnson, J. R. Johnson, J. Joseph, K. Kinch, M. T. Lemmon, R. V. Morris, L. Scherr, M. Schwochert, M. K. Shepard, G. H. Smith, J. N. Sohl-Dickstein, R. J. Sullivan, W. T. Sullivan, and M. Wadsworth (2003), Mars exploration rover Athena panoramic camera (Pancam) investigation, *Journal of Geophysical Research: Planets,* 108(E12), DOI: 10.1029/2003JE0002070.

Benito, G., and J. E. O'Connor (2003), Number and size of last-glacial Missoula floods in the Columbia River valley between the Pasco Basin, Washington, and Portland, Oregon, *Geological Society of America Bulletin*, *115*(5), 624-638, DOI: 10.1130/0016.

Bennett, S., and J. Best (1996), Mean flow and turbulence structure over fixed ripples and the ripple-dune transition, in Ashworth, P.J., et al., eds., Coherent Flow Structures in Open Channels: Hoboken, New Jersey, John Wiley, p. 67–125.

Bennett, S. J. (1999), Effect of slope on the growth and migration of headcuts in rills, *Geomorphology*, *30*(3), 273-290.

Bennett, S. J., and J. Casali (2001), Effect of initial step height on headcut development in upland concentrated flows, *Water Resources Research*, *37*(5), 1475-1484.

Betat, A., C. A. Kruelle, V. Frette, and I. Rehberg (2002), Long-time behavior of sand ripples induced by water shear flow, *The European Physical Journal E*, 8(1), 465–476, DOI: 10.1140/epje/i2001-10110-y.

Bibring, J.-P., Y. Langevin, A. Gendrin, B. Gondet, F. Poulet, M. Berthe, A. Soufflot, R. Arvidson, N. Mangold, and J. Mustard (2005), Mars surface diversity as revealed by the OMEGA/Mars Express observations, *Science*, *307*(5715), 1576-1581.

Bibring, J.-P., Y. Langevin, J. F. Mustard, F. Poulet, R. Arvidson, A. Gendrin, B. Gondet, N. Mangold, P. Pinet, and F. Forget (2006), Global mineralogical and aqueous Mars history derived from OMEGA/Mars Express data, *Science*, *312*(5772), 400-404.

Bishop, C. T. (1977), On the time-growth of dunes [M.S. Thesis], Queen's University, Kingston, Ontario, Canada.

Bjornsson, H. (2003), Subglacial lakes and jökulhlaups in Iceland, *Global and Planetary Change*, *35*(3), 255-271, DOI: 10.1016/S0921-8181(02)00130-3.

Blake, D. F., R. V. Morris, G. Kocurek, S. M. Morrison, R. T. Downs, D. Bish, D. W. Ming, K. S. Edgett, D. Rubin, W. Goetz, M. B. Madsen, R. Sullivan, R. Gellert, I. Campbell, A. H. Treiman, S. M. McLennan, A. S. Yen, J. P. Grotzinger, D. T. Vaniman, S. J. Chipera, C. N. Achilles, E. B. Rampe, D. Sumner, P.-Y. Meslin, S. Maurice, O. Forni, O. Gasnault, M. Fisk, M. Schmidt, P. Mahaffy, L. A. Leshin, D. Glavin, A. Steele, C. Freissinet, R. Navarro-Gonzalez, R. A. Yingst, L. C. Kah, N. T. Bridges, K. W. Lewis, T. F. Bristow, J. D. Farmer, J. A. Crisp, E. M. Stolper, D. J. Des Marais, P. Sarrazin, and the MSL Science Team (2013), Curiosity at Gale crater, Mars: Characterization and analysis of the Rocknest sand shadow, *Science*, *341*(6153), DOI: 10.1126/science.1239505.

Boguchwal, L. A., and J. B. Southard (1990), Bed configurations in steady unidirectional water flows. Part 1. Scale model study using fine sands, *Journal of Sedimentary Research*, 60, 649–657.

Bollaert, E. (2004), A comprehensive model to evaluate scour formation in plunge pools, *International Journal on Hydropower & Dams*, *11*(1), 94-101.

Bresse, J. A. C. (1860), *Cours de mecanique appliquee: professe a l'Ecole Imperiale des Ponts et Chaussees. Hydraulique*, Gauthier-Villars.

Bretz, J. H., H. U. Smith, and G. E. Neff (1956), Channeled Scabland of Washington: New data and interpretations, *Geological Society of America Bulletin*, *67*(8), 957-1049.

Bretz, J. H. (1969), The Lake Missoula floods and the channeled scabland, *The Journal of Geology*, *77*(5), 505-543.

Bridges, N. T., P. E. Geissler, A. S. McEwen, B. J. Thomson, F. C. Chuang, K. E. Herkenhoff, L. P. Leszthelyi, and S. Martínez-Alonso (2007), Windy Mars: A dynamic planet as seen by the HiRISE camera, *Geophysical Research Letters*, *34*(23), DOI: 10.1029/2007GL031445.

Bridges, N. T., F. Ayoub, J. Avouac, S. Leprince, A. Lucas, and S. Mattson (2012a), Earth-like sand fluxes on Mars, *Nature*, *485*(7398), 339-342, DOI: 10.1038/nature11022.

Bridges, N. T., M. C. Bourke, P. E. Geissler, M. E. Banks, C. Colon, S. Diniega, M. P. Golombek, C. J. Hansen, S. Mattson, A. S. McEwen, M. T. Mellon, N. Stantzos, and B. J. Thomson (2012b), Planet-wide sand motion on Mars, *Geology*, *40*(1), 31-34, DOI:10.1130/G32373.1.

Bridges, N. T., P. Geissler, S. Silvestro, and M. Banks (2013), Bedform migration on Mars: Current results and future plans, *Aeolian Research*, *9*, 133-151, DOI: 10.1016/j.aeolia.2013.02.004.

Bridges, N. T., F. Calef, B. Hallet, K. Herkenhoff, N. Lanza, S. Le Mouelic, C. Newman, D. Blaney, M. Pablo, and G. Kocurek (2014), The rock abrasion record at Gale crater: Mars Science Laboratory results from Bradbury landing to Rocknest, *Journal of Geophysical Research: Planets*, 119(6), 1374-1389, DOI: 10.1002/2013JE004579.

Bridges, N. T., M. Spagnuolo, S. de Silva, J. Zimbelman, and E. Neely (2015), Formation of gravel-mantled megaripples on Earth and Mars: Insights from the Argentinean Puna and wind tunnel experiments, *Aeolian Research*, *17*, 49-60, DOI: 10.1016/j.aeolia.2015.01.007.

Bridges, N. T., R. Sullivan, C. E. Newman, S. Navarro, J. van Beek, R. C. Ewing, F. Ayoub, S. Silvestro, O. Gasnault, S. Le Mouelic, M. G. A. Lapôtre, W. Rapin (2017), Martian aeolian activity at the Bagnold Dunes, Gale crater: The view from the surface and orbit, *Journal of Geophysical Research: Planets*.

Bridges, N. T., and B. L. Ehlmann, (in revision), The Bagnold Dune Campaign: Overview and introduction to special issue, *Journal of Geophysical Research: Planets*, in press.

Brownlie, W. R. (1983), Flow Depth in Sand-Bed Channels, *Journal of Hydraulic Engineering*, *109*(7), 959-990.

Burns, R. G. (1993), Rates and mechanisms of chemical weathering of ferromagnesian silicate minerals on Mars, *Geochimica et Cosmochimica Acta*, *57*(19), 4555-4574.

Burr, D. M., J. A. Grier, A. S. McEwen, and L. P. Keszthelyi (2002), Repeated aqueous flooding from the Cerberus Fossae: Evidence for very recently extant, deep groundwater on Mars, *Icarus*, *159*(1), 53-73, DOI: 10.1006/icar.2002.6921.

Burr, D. M. (2010), Palaeoflood-generating mechanisms on Earth, Mars, and Titan, *Global and Planetary Change*, *70*(1-4), 5-13, DOI: 10.1016/j.gloplacha.2009.11.003.

Burr, D. M., J. T. Perron, M. P. Lamb, R. P. Irwin, G. C. Collins, A. D. Howard, L. S. Sklar, J. M. Moore, M. Adamkovics, and V. R. Baker (2013), Fluvial features on Titan: Insights from morphology and modeling, *Geological Society of America Bulletin*, v. 125, 299-321, DOI:10.1130/B30612.1.

Butcher, J. C. (2008), *Numerical methods for ordinary differential equations*, John Wiley & Sons.

Cao, S., and D. W. Knight (1997), Entropy-based design approach of threshold alluvial channels, *Journal of Hydraulic Research*, *35*(4), 505-524.

Carr, M. H. (1979), Formation of Martian flood features by release of water from confined aquifers, *Journal of Geophysical Research*, *84*(NB6), 2995-3007, DOI: 10.1029/JB084iB06p02995.

Carr, M. H. (1986), Mars: A water-rich planet?, *Icarus*, *68*(2), 187-216.

Carr, M. H. (1996), *Water on Mars*, 229 pp., Oxford University Press, New York.

Carr, M. H., and J. W. Head (2010), Geologic history of Mars, *Earth and Planetary Science Letters*, *294*(3-4), 185-203, DOI: 10.1016/j.epsl.2009.06.042.

Carrivick, J. L., F. S. Tweed, P. Carling, P. Alho, P. M. Marren, K. Staines, A. J. Russell, E. L. Rushmer, and R. Duller (2013), Discussion of "Field evidence and hydraulic modeling of a large Holocene jökulhlaup at Jökulsá á Fjöllum channel, Iceland" by Douglas Howard, Sheryl Luzzadder-Beach and Timothy Beach, 2012, *Geomorphology*, *201*, 512-519.

Carter, C. L., and R. S. Anderson (2006), Fluvial erosion of physically modeled abrasion-dominated slot canyons, *Geomorphology*, *81*(1), 89-113, DOI: 10.1016/j.geomorph.2006.04.006.

Chanson, H. (1994), Hydraulics of nappe flow regime above stepped chutes and spillways, *Australian Civil/Structural Engineering Transactions*, (1), 69-76.

Chanson, H. (1995), *Hydraulic design of stepped cascades, channels, weirs and spillways*, Pergamon, Oxford, UK.

Chanson, H. (2002), *Hydraulics of stepped chutes and spillways*, CRC Press.

Chapman, M. G., and K. L. Tanaka (2002), Related magma-ice interactions: Possible origins of chasmata, chaos, and surface materials in Xanthe, Margaritifer, and Meridiani Terrae, Mars, *Icarus*, *155*(2), 324-339, DOI: 10.1006/icar.2001.6735.

Chatanantavet, P., and G. Parker (2009), Physically based modeling of bedrock incision by abrasion, plucking, and macroabrasion, *Journal of Geophysical Research: Earth Surface*, *114*(F4) , DOI: 10.1029/2008JF001044.

Charru, F., B. Andreotti, and P. Claudin (2013), Sand ripples and dunes, *Annual Review of Fluid Mechanics*, 45, 469-493, DOI: 10.1146/annurev-fluid-011212-140806.

Cheek, L. C. and C. M. Pieters (2014), Reflectance spectroscopy of plagioclase-dominated mineral mixtures: Implications for characterizing lunar anorthosites remotely, *American Mineralogist*, *99*(10), 1871-1892, DOI: 10.2138/am-2014-4785.

Chepil, W. (1945), Dynamics of wind erosion 2: Initiation of soil movement, *Soil Science*, *60*(5), 397.

Chib, S., and E. Greenberg (1995), Understanding the metropolis-hastings algorithm, *The American Statistician*, *49*(4), 327-335.

Ching, J., and Y.-C. Chen (2007), Transitional Markov chain Monte Carlo method for Bayesian model updating, model class selection, and model averaging, *Journal of Engineering Mechanics*, *133*(7), 816-832, DOI: 10.1061/(ASCE)0733-9399.

Chojnacki, M., D. M. Burr, J. E. Moersch, and T. I. Michaels (2011), Orbital observations of contemporary dune activity in Endeavor crater, Meridiani Planum, Mars, *Journal of Geophysical Research: Planets*, *116*(E7), DOI: 10.1029/2010JE003675.

Chojnacki, M., D. M. Burr, and J. Moersch (2013), Local sourcing and aeolian fractionation as factors for compositional heterogeneity of martian aeolian bedform sand, paper presented at Lunar and Planetary Science Conference, The Woodlands, TX.

Chojnacki, M., J. R. Johnson, J. E. Moersch, L. K. Fenton, T. I. Michaels, and J. F. Bell III (2015), Persistent aeolian activity at Endeavour crater, Meridiani Planum, Mars; new observations from orbit and the surface, *Icarus*, *251*, 275-290, DOI: 10.1016/j.icarus.2014.04.044.

Chow, V. (1959), *Open channel hydraulics*, McGraw-Hill Book Company, Inc., New York, NY.

Christensen, P. R., J. L. Bandfield, M. D. Smith, V. E. Hamilton, and R. N. Clark (2000), Identification of a basaltic component on the Martian surface from Thermal Emission Spectrometer data, *Journal of Geophysical Research: Planets*, *105*(E4), 9609-9621, DOI: 10.1029/1999JE001127.

Clark, R. N. and T. L. Roush (1984), Reflectance spectroscopy: Quantitative analysis techniques for remote sensing applications, *Journal of Geophysical Research: Solid Earth*, *89*(B7), 6329-6340.

Clark, R. N. (1999). "Spectroscopy of rocks and minerals, and principles of spectroscopy" in *Manual of remote sensing*, Volume *3*, Ed. A.N. Renz, John Wiley and Sons, New York, NY, pp. 3-58.

Clark, R. N., G. A. Swayze, R. Wise, K. E. Livo, T. M. Hoefen, R. F. Kokaly, and S. J. Sutley (2007), USGS digital spectral library splib06a, edited, US Geological Survey Reston, Va.

Coleman, S. E., B. W. Melville, and L. Gore (2003), Fluvial entrainment of protruding fractured rock, *Journal of Hydraulic Engineering*, *129*(11), 872-884, DOI: 10.1061/(ASCE)0733-9429(2003)129.

Costa, J. E. (1983), Paleohydraulic reconstruction of flash-flood peaks from boulder deposits in the Colorado Front Range, *Geological Society of America Bulletin*, *94*(8), 986-1004.

Costa, J. E. (1987), Hydraulics and basin morphometry of the largest flash floods in the conterminous United States, *Journal of Hydrology*, *93*(3), 313-338.

Cousin, A., E. Dehouck, P.-Y. Meslin, O. Forni, A. J. Williams, N. Stein, O. Gasnault, N. T. Bridges, B. L. Ehlmann, S. Shcroeder, V. Payré, W. Rapin, P. Pinet, V. Sautter, S. Maurice, R. C. Wiens (in revision), Geochemistry of the Bagnold Dune Field as observed by ChemCam, and comparison with other aeolian deposits at Gale crater, *Journal of Geophysical Research: Planets*.

Craddock, R. A., and A. D. Howard (2002), The case for rainfall on a warm, wet early Mars, *Journal of Geophysical Research: Planets*, *107*(E11), DOI: 10.1029/2001JE001505.

Craddock, R. A., A. D. Howard, R. P. Irwin, S. Tooth, R. M. Williams, and P.-S. Chu (2012), Drainage network development in the Keanakako'i tephra, Kilauea Volcano, Hawai'i: Implications for fluvial erosion and valley network formation on early Mars, *Journal of Geophysical Research: Planets*, *117*(E8), DOI: 10.1029/2012JE004074.

Crosby, B. T., and K. X. Whipple (2006), Knickpoint initiation and distribution within fluvial networks: 236 waterfalls in the Waipaoa River, North Island, New Zealand, *Geomorphology*, *82*(1), 16-38, DOI: 10.1016/j.geomorph.2005.08.023.

Cruikshank, D. P., T. L. Roush, and F. Poulet (2003), Quantitative modeling of the spectral reflectance of Kuiper belt objects and Centaurs, *Comptes Rendus Physique*, *4*(7), 783-789, DOI: 10.1016/j.crhy.2003.10.007.

Day, M., and G. Kocurek (2016), Observations of an aeolian landscape: From surface to orbit in Gale Crater, *Icarus*, 280, 37-71, DOI: 10.1016/j.icarus.2015.09.042.

Day, M., W. Anderson, G. Kocurek, and D. Mohrig (2016), Carving intracrater layered deposits with wind on Mars, Geophysical Research Letters, 43(6), 2473-2479, DOI: 10.1002/2016GL068011.

Denevi, B. W., P. G. Lucey, E. J. Hochberg, and D. Steutel (2007), Near-infrared optical constants of pyroxene as a function of iron and calcium content. Journal of Geophysical Research: Planets, 112(E5), DOI: 10.1029/2006JE002802.

Delamere, W. A., L. L. Tornabene, A. S. McEwen, K. Becker, J. W. Bergstrom, N. T. Bridges, E. M. Eliason, D. Gallagher, K. E. Herkenhoff, and L. Keszthelyi (2010), Color imaging of Mars by the high resolution imaging science experiment (HiRISE), *Icarus*, 205(1), 38-52, DOI: DOI: 10.1016/j.icarus.2009.03.012.

Delleur, J., J. Dooge, and K. Gent (1956), Influence of slope and roughness on the free overfall, *Journal of the Hydraulics Division, American Society of Civil Engineers*, *82*(4), 1-35.

De Sanctis, M. C., A. Raponi, E. Ammannito, M. Ciarniello, M. J. Toplis, H. Y. McSween, J. C. Castillo-Rogez, B. L. Ehlmann, F. G. Carrozzo, S. Marchi, and F. Tosi (2016), Bright carbonate deposits as evidence of aqueous alteration on (1) Ceres, *Nature*, *536*(7614), 54-57, DOI: 10.1038/nature18290.

de Silva, S. L., M. G. Spagnuolo, N. T. Bridges, and J. R. Zimbelman (2013), Gravel-mantled megaripples of the Argentinean Puna: A model for their origin and growth with implications for Mars, *Geological Society of America Bulletin*, *125*(11-12), 1912-1929, DOI: 10.1130/830916.1.

de Vries, M. (1965), Consideration about non-steady bed-load transport in open channels, paper presented at 11th Congress, in *Int. Assoc. of Hydraul. Res., Leningrad, USSR*, edited, Saint Petersburg, Russia.

Di Achille, G., and B. M. Hynek (2010), Ancient ocean on Mars supported by global distribution of deltas and valleys, *Nature Geoscience*, *3*(7), 459-463, DOI: 10.1038/ngeo891.

DiBiase, R. A., K. X. Whipple, M. P. Lamb, and A. M. Heimsath (2015), The role of waterfalls and knickzones in controlling the style and pace of landscape adjustment in the western San Gabriel Mountains, California, *Geological Society of America Bulletin*, *127*(3-4), 539-559, DOI: 10.1130/B31113.1.

Dietrich, W. E., and T. Dunne (1993), The channel head, in *Channel Network Hydrology*, edited by K. Beven and M. J. Kirkby, pp. 175-219, J. Wiley and Sons.

Dubinski, I. M., and E. Wohl (2013), Relationships between block quarrying, bed shear stress, and stream power: A physical model of block quarrying of a jointed bedrock channel, *Geomorphology*, *180*, 66-81.

Dunne, T. (1990), Hydrology, mechanics, and geomorphic implications of erosion by subsurface flow, *Geological Society of America*, Special Paper 252, 1-28.

Durán, O., P. Claudin, and B. Andreotti (2014), Direct numerical simulations of aeolian sand ripples, *Proceedings of the National Academy of Sciences*, *111*(44), 15665-15668, DOI: 10.1073/pnas.1413058111.

Edwards, C. S., and B. L. Ehlmann (2015), Carbon sequestration on Mars, *Geology*, 43(10), 863-866, DOI: 10.1130/G36983.1.

Edwards, C. S., S. Piqueux, V. E. Hamilton, R. L. Fergason, K. E. Herkenhoff, A. R. Vasavada, L. Sacks, K. Lewis, M. D. Smith (in revision), The Thermophysical Properties of the Bagnold Dunes, Mars: Ground Truthing Orbital Data, *Journal of Geophysical Research: Planets*.

Ehlmann B. L. (2010), Early Mars Environments Revealed Through Near-Infrared Spectroscopy of Alteration Minerals [PhD thesis]: Brown University, 325 p.

Ehlmann, B. L., and C. S. Edwards (2014), Mineralogy of the Martian Surface, *Annual Review of Earth and Planetary Sciences*, *42*, 291-315, DOI: 10.1146/annurev-earth-060313-055024.

Ehlmann, B. L., and J. Buz (2015), Mineralogy and fluvial history of the watersheds of Gale, Knobel, and Sharp craters: A regional context for the Mars Science Laboratory Curiosity's exploration, *Geophysical Research Letters*, 42(2), 264-273, DOI: 10.1002/2014GL062553.

Ehlmann, B. L., F. S. Anderson, J. Andrews-Hanna, D. C. Catling, P. R. Christensen, B. A. Cohen, C. D. Dressing, C. S. Edwards, L. T. Elkins-Tanton, K. A. Farley, C. I. Fassett, W. W. Fischer, A. A. Fraeman, M. P. Golombek, V. E. Hamilton, A. G. Hayes, C. D. K. Herd, B. Horgan, R. Hu, B. M. Jakosky, J. R. Johnson, J. F. Kasting, L. Kerber, K. M. Kinch, E. S. Kite, H. A. Knutson, J. I. Lunine, P. R. Mahaffy, N. Mangold, F. M. McCubbin, J. F. Mustard, P. B. Niles, C. Quantin-Nataf, M. S. Rice, K. M. Stack, D. J. Stevenson, S. T. Stewart, M. J. Toplis, T. Usui, B. P. Weiss, S. C. Werner, R. D. Wordsworth, J. J. Wray, R. A. Yingst, Y. L. Yung, and K. J. Zahnle (2016), The sustainability of habitability on terrestrial planets: Insights, questions, and needed measurements from Mars for understanding the evolution of Earth-like worlds, *Journal of Geophysical Research: Planets*, *121*(10), 1927-1961, DOI: 10.1002/2016JE005134.

Ehlmann, B. L., K. S. Edgett, B. Sutter, C. N. Achilles, M. L. Litvak, M. G. A. Lapôtre, A. A. Fraeman, R. E. Arvidson, D. F. Blake, N. T. Bridges, P. G. Conrad, A. Cousin, R. T. Downs, T. Gabriel, R. Gellert, V. E. Hamiltn, C. Hardgrove, J. R. Johnson, S. Kuhn, P. R. Mahaffy, S. Maurice, M. McHenry, P.-Y. Meslin, D. W. Ming, M. E. Minitti, J. M. Morookian, R. V. Morrid, C. D. O'Connell-Cooper, P. C. Pinet, S. K. Rowland, S. Schroder, K. L. Siebach, N. T. Stein, L. M. Thompson, D. T. Vaniman, A. R. Vasavada, D. F. Wellington, R. C. Wiens, A. S. Yen (in revision), Chemistry, Mineralogy, and Grain Properties at Namib and High Dunes, Bagnold Dune Field, Gale crater, Mars: A Synthesis of Curiosity Rover Observations, *Journal of Geophysical Research: Planets*.

Ellwood, J. M., P. D. Evans, and I. G. Wilson (1975), Small scale aeolian bedforms, *Journal of Sedimentary Research*, *45*(2).

Engelund, F., and E. Hansen (1967), A monograph on sediment transport in alluvial streams: Teknisk Forlag Skelbrekgade 4 Copenhagen V, Denmark., p. 63.

Ewing, R. C., G. Kocurek, and L. W. Lake (2006), Pattern analysis of dune-field parameters, *Earth Surface Processes and Landforms*, *31*(9), 1176-1191, DOI: 10.1002/esp.1312.

Ewing, R. C., A.-P. B. Peyret, G. Kocurek, and M. Bourke (2010), Dune field pattern formation and recent transporting winds in the Olympia Undae Dune Field, north polar region of Mars, *Journal of Geophysical Research: Planets*, *115*(E8), DOI: 10.1111/j.1365-3091.2009.01143.x.

Ewing, R. C., M. G. A. Lapôtre, K. Lewis, M. Day, N. Stein, D. M. Rubin, N. T. Bridges, R. Sullivan, W. W. Fischer, M. P. Lamb, S. Gupta (in review), Sedimentary processes of the Bagnold Dunes: Implications for the eolian rock record of Mars. *Journal of Geophysical Research: Planets.*

Farmer, J. D., and D. J. Des Marais (1999), Exploring for a record of ancient Martian life, *Journal of Geophysical Research: Planets*, 104(E11), 26977-26995, DOI: 10.1029/1998JE000540.

Farr, T. G., P. A. Rosen, E. Caro, R. Crippen, R. Duren, S. Hensley, M. Kobrick, M. Paller, E. Rodriguez, and L. Roth (2007), The shuttle radar topography mission, *Reviews of Geophysics*, *45*(2), DOI:10.1029/2005RG000183.

Fassett, C. I., and J. W. Head (2008a), Valley network-fed, open-basin lakes on Mars: Distribution and implications for Noachian surface and subsurface hydrology, *Icarus*, *198*(1), 37-56, DOI: 10.1016/j.icarus.2008.06.016.

Fassett, C. I., and J. W. Head (2008b), The timing of martian valley network activity: Constraints from buffered crater counting, *Icarus*, *195*(1), 61-89, DOI: 10.1016/j.icarus.2007.12.009.

Fedo, C. M., I. O. McGlynn, and H. Y. McSween (2015), Grain size and hydrodynamic sorting controls on the composition of basaltic sediments: Implications for interpreting martian soils, *Earth and Planetary Science Letters*, 423, 67-77, DOI: 10.1016/j.epsl.2015.03.052.

Feely, K. C., and P. R. Christensen (1999), Quantitative compositional analysis using thermal emission spectroscopy: Application to igneous and metamorphic rocks, *Journal of Geophysical Research*, *104*(E10), 24,195-124,210.

Fenton, L. K., J. L. Bishop, S. King, B. Lafuente, B. Horgan, D. Bustos, and P. Sarrazin (2016), Sedimentary differentiation of aeolian grains at the White Sands National Monument, New Mexico, USA, *Aeolian Research*, in press, DOI: 10.1016/j.aeolia.2016.05.001.

Ferguson, R., and M. Church (2004), A simple universal equation for grain settling velocity, *Journal of Sedimentary Research*, *74*(6), 933-937, DOI: 10.1306/051204740933.

Fernandez, R., J. Best, and F. Lopez (2006), Mean flow, turbulence structure, and bed form superimposition across the ripple-dune transition, *Water Resources Research*, 42, W05406, DOI:10.1029/2005WR004330.

Fernandez Luque, R., and R. Van Beek (1976), Erosion and transport of bed-load sediment, *Journal of Hydraulic Research*, *14*(2), 127-144.

Feurich, R., F. Kettner, and N. Olsen (2011), Three-Dimensional Numerical Investigation of Spillway and Reservoir Hydraulics, paper presented at

Proceedings of the 34th World Congress of the International Association for Hydro-Environment Research and Engineering: 33rd Hydrology and Water Resources Symposium and 10th Conference on Hydraulics in Water Engineering, Engineers Australia.
Fischer, E. M. and C. M. Pieters (1993), The continuum slope of Mars: Bidirectional reflectance investigations and applications to Olympus Mons, *Icarus*, 102(2), 185-202.
Flint, J.-J. (1973), Experimental development of headward growth of channel networks, *Geological Society of America Bulletin*, *84*(3), 1087-1094.
Flores-Cervantes, J. H., E. Istanbulluoglu, and R. L. Bras (2006), Development of gullies on the landscape: A model of headcut retreat resulting from plunge pool erosion, *Journal of Geophysical Research: Earth Surface*, *111*(F1), DOI: 10.1029/2004JF000226.
Fralick, P.W. (2003), Geochemistry of clastic sedimentary rocks: Ratio techniques, in Lentz, D.R., ed., Geochemistry of Sediments and Sedimentary Rocks: Toronto, Ontario, Canada, Geological Association of Canada, Geotext 4, p. 85–104.
Gabel, S. L. (1993), Geometry and kinematics of dunes during steady and unsteady flows in the Calamus River, Nebraska, USA, *Sedimentology*, v. 40, 237-269.
Garcia, M., and Y. Nino (1993), Dynamics of sediment bars in straight and meandering channels: experiments on the resonance phenomenon, *Journal of Hydraulic Research*, *31*(6), 739-761.
Garcia, M. (2008), Sediment transport and morphodynamics, in *Sedimentation engineering: processes, measurements, modeling, and practice*, edited by M. Garcia, American Association of Civil Engineers.
Geissler, P. E. (2014), The birth and death of transverse aeolian ridges on Mars, *Journal of Geophysical Research: Planets*, *119*(12), 2583-2599, DOI: 10.1002/2014JE004633.
Gilbert, G. K. (1907), The rate of recession of Niagara Falls, *U.S. Geological Survey Bulletin*, *306*, 1-31.
Golombek, M. P., and R. J. Phillips (2010), Mars tectonics: Chapter 5, in *Planetary Tectonics*, edited by T. R. Watters and R. A. Schultz, pp. 183-232, Cambridge Univ. Press, Cambridge, U. K.
Goudge, T. A., J. F. Mustard, J. W. Head, M. R. Salvatore, and S. M. Wiseman (2015), Integrating CRISM and TES hyperspectral data to characterize a halloysite-bearing deposit in Kashira crater, Mars, *Icarus*, *250*, 165-187, DOI: 10.1016/j.icarus.2014.11.034.
Grant, G. E. (1997), Critical flow constrains flow hydraulics in mobile-bed streams: A new hypothesis, *Water Resources Research*, *33*(2), 349-358.
Grazer, R. A. (1982), Experimental study of current ripples using medium silt [M.S. Thesis]: Massachusetts Institute of Technology, 131 p.
Grotzinger, J., J. F. Bell III, K. Herkenhoff, J. Johnson, A. Knoll, E. McCartney, S. McLennan, J. Metz, J. Moore, and S. W. Squyres (2006), Sedimentary textures formed by aqueous processes, Erebus crater, Meridiani Planum, Mars, *Geology*, *34*(12), 1085-1088, DOI: 10.1130/G22985A.1.

Grotzinger, J. P., R. E. Arvidson, J. F. Bell III, W. Calvin, B. C. Clark, D. A. Fike, M. Golombek, R. Greeley, A. Haldemann, K. E. Herkenhoff, B. L. Lolliff, A. H. Knoll, M. C. Malin, S. M. McLennan, T. Parker, L. Solderblom, J. N. Sohl-Dickstein, S. W. Squyres, N. J. Tosca, W. A. Watters (2005), Stratigraphy and sedimentology of a dry to wet eolian depositional system, Burns formation, Meridiani Planum, Mars, *Earth and Planetary Science Letters*, *240*(1), 11-72, DOI: 10.1016/j.epsl.2005.09.039.

Grotzinger, J. P., J. Crisp, A. R. Vasavada, R. C. Anderson, C. J. Baker, R. Barry, D. F. Blake, M. Conrad, K. S. Edgett, B. Ferdowski, R. Gellert, J. B. Gilbert, M. Golombek, J. Gomez-Elvira, D. M. Hassler, L. Jandura, M. Litvak, P. Mahaffy, J. Maki, M. Meyer, M. C. Malin, I. Mitrofanov, J. J. Simmonds, D. Vaniman, R. V. Welch, R. C. Wiens (2012), Mars Science Laboratory mission and science investigation, *Space Science Reviews*, *170*(1-4), 5-56, DOI: 10.1007/s11214-012-9892-2.

Grotzinger, J. P., A. G. Hayes, M. P. Lamb, and S. M. McLennan (2013), Sedimentary processes on Earth, Mars, Titan, and Venus, *Comparative Climatology of Terrestrial Planets*, 1, 439–472.

Grotzinger, J. P., D. Y.Sumner, L. C. Kah, K. Stack, S. Gupta, L. Edgar, D. Rubin, K. Lewis, J. Schieber, N. Mangold, R. Milliken, P. G. Conrad, D. Des Marais, J. Farmer, K. Siebach, F. Calef III, J. Hurowitz, S. M. McLennan, D. Ming, D. Vaniman, J. Crisp, A. Vasavada, K. S. Edgett, M. C. Malin, D. Blake, R. Gellert, P. Mahaffy, R. C. Wiens, S. Maurice, J. A. Grant, S. Wilson, R. C. Anderson, T. F. Bristow, W. E. Dietrich, G. Dromart, J. Eigenbrode, A. Fraeman, C. Hardrgrove, K. Herkenhoff, L. Jandura, G. Kocurek, S. Lee, L. A. Leshin, R. Leveille, D. Limonadi, J. Maki, S. McCloskey, M. Meyer, M. Minitti, H. Newsom, D. Oehler, A. Okon, M. Palucis, T. Parker, S. Rowland, M. Schmidt, S. W. Squyres, A. Steele, E. Stolper, R. Summons, A. Treiman, R. Williams, A. Yingst, and the MSL Science Team (2014), A habitable fluvio-lacustrine environment at Yellowknife Bay, Gale Crater, Mars, *Science*, 343(6169), DOI: 10.1126/science.1242777.

Grotzinger, J. P., S. Gupta, M. C. Malin, D. M. Rubin, J. Schieber, K. Siebach, D. Y. Sumner, K. M. Stack, A. R. Vasavada, R E Arvidson, F. Calef III, L. Edgar, W. F. Fischer, J. A. Grant, J. Griffes, L. C. Kah, M. P. Lamb, K. W. Lewis, N. Mangold, M. E. Minitti, M. Palucis, M. Rice, R. M. E Williams, R. A. Yingst, D. Blake, D. Blaney, P. Conrad, J. Crisp, W. E. Dietrich, G. Dromart, K. S. Edgett, R. C. Ewing, R. Gellert, J. A. Hurowitz, G. Kocurek, P. Mahaffy, M. J. McBride, S. M. McLennan, M. Mischna, D. Ming, R. Milliken, H. Newsom, D. Oehler, T. J. Parker, D. Vaniman, R. C. Wiens, S. A. Wilson (2015), Deposition, Exhumation, and Paleoclimate of an Ancient Lake Deposit, Gale Crater, Mars, *Science*, 350(6257), DOI: 10.1126/science.aac7575.

Grundy, W. M., S. Douté, and B. Schmitt (2000), A Monte Carlo ray-tracing model for scattering and polarization by large particles with complex shapes, *Journal of Geophysical Research: Planets*, *105*(E12), 29291-29314, DOI: 10.1029/2000JE001276.

Guy, H. P., D. B. Simons, and E. V. Richardson (1966), “Summary of alluvial channel data from flume experiments, 1956-61”, 462-I, *2330-7102* (U.S. Geological Survey), 104 p.

Haberle, R. M., J. R. Murphy, and J. Schaeffer (2003), Orbital change experiments with a Mars general circulation model, *Icarus*, *161*(1), 66-89, DOI: 10.1016/S0019-1035(02)00017-9.

Haberle, R., J. Gomez-Elvira, M. Torre Juarez, A. M. Harri, J. Hollingsworth, H. Kahanpaa, M. Kahre, M. Lemmon, F. Martin-Torres, and M. Mischna (2014), Preliminary interpretation of the REMS pressure data from the first 100 sols of the MSL mission, *Journal of Geophysical Research: Planets*, 119(3), 440-453, DOI: 10.1002/2013JE004488.

Hager, W. H. (1983), Hydraulics of plane free overfall, *Journal of Hydraulic Engineering*, *109*(12), 1683-1697.

Hager, W. H., and D. D. K. Hutter (1984), Approximate treatment of plane channel flow, *Acta Mechanica*, *51*(1-2), 31-48.

Hancock, G. S., R. S. Anderson, and K. X. Whipple (1998), Beyond power: Bedrock river incision process and form, *Rivers over rock: Fluvial processes in bedrock channels*, 35-60.

Hanna, J. C., and R. J. Phillips (2006), Tectonic pressurization of aquifers in the Harrison, K. P., and R. E. Grimm (2005), Groundwater-controlled valley networks and the decline of surface runoff on early Mars, *Journal of Geophysical Research: Planets*, *110*(E12), DOI: 10.1029/2005je002455.

Hapke, B. (1981), Bidirectional reflectance spectroscopy: 1. Theory, *Journal of Geophysical Research: Solid Earth*, *86*(B4), 3039-3054.

Hapke, B., and Wells, E. (1981), Bidirectional reflectance spectroscopy: 2. Experiments and observations, *Journal of Geophysical Research: Solid Earth*, *86*(B4), 3055-3060.

Hapke, B. (1984), Bidirectional reflectance spectroscopy: 3. Correction for macroscopic roughness, *Icarus*, *59*(1), 41-59.

Hapke, B. (1986), Bidirectional reflectance spectroscopy: 4. The extinction coefficient and the opposition effect, *Icarus*, *67*(2), 264-280.

Hapke, B. (2002), Bidirectional reflectance spectroscopy: 5. The coherent backscatter opposition effect and anisotropic scattering, *Icarus*, *157*(2), 523-534, DOI: 10.1006/icar.2002.6853.

Hapke, B. (2008), Bidirectional reflectance spectroscopy: 6. Effects of porosity, *Icarus*, *195*(2), 918-926, DOI: 10.1016/j.icarus.2008.01.003.

Harrison, K. P., and R. E. Grimm (2005), Groundwater-controlled valley networks and the decline of surface runoff on early Mars, *Journal of Geophysical Research: Planets*, *110*(E12), DOI:10.1029/2005JE002455.

Harrison, K. P., and R. E. Grimm (2008), Multiple flooding events in Martian outflow channels, *Journal of Geophysical Research: Planets*, *113*(E2), DOI: 10.1029/2007JE002951.

Haviv, I., Y. Enzel, K. X. Whipple, E. Zilberman, J. Stone, A. Matmon, and L. Fifield (2006), Amplified erosion above waterfalls and oversteepened bedrock reaches, *Journal of Geophysical Research: Earth Surface, 111*(F4), DOI: 10.1029/2006JF000461.

Hayes, A. G., J. P. Grotzinger, L. A. Edgar, S. W. Squyres, W. A. Watters, and J. Sohl-Dickstein (2011), Reconstruction of eolian bed forms and paleocurrents from cross-bedded strata at Victoria Crater, Meridiani Planum, Mars, *Journal of Geophysical Research: Planets*, *116*(E7), DOI: 10.1029/2010JE003688.

Head, J. W., A. L. Nahm, D. R. Marchant, and G. Neukum (2006), Modification of the dichotomy boundary on Mars by Amazonian mid-latitude regional glaciation, *Geophysical Research Letters*, *33*(8), DOI: 10.1029/2005GL024360.

Hiroi, T. and C. M. Pieters (1994), Estimation of grain sizes and mixing ratios of fine powder mixtures of common geologic minerals, *Journal of Geophysical Research: Planets*, 99(E5), 10867-10879.

Hobbs, S. W., D. J. Paull, and M. C. Bourke (2010), Aeolian processes and dune morphology in Gale Crater, *Icarus*, 210(1), 102-115, DOI: 10.1016/j.icarus.2010.06.006.

Howard, A. D., and G. Kerby (1983), Channel changes in badlands, *Geological Society of America Bulletin*, *94*(6), 739-752.

Howard, A. D. (1987), Groundwater sapping on Earth and Mars, in *Sapping Features of the Colorado Plateau*, edited by A. D. Howard, R. C. Kochel and H. R. Holt, NASA Special Publication.

Howard, A. D., and C. F. McLane (1988), Erosion of cohesionless sediment by groundwater seepage, *Water Resources Research*, *24*(10), 1659-1674, DOI: 10.1029/WR024i010p01659.

Howard, A. D. (1994), A detachment-limited model of drainage basin evolution, *Water Resources Research*, *30*(7), 2261-2285.

Hu, R., D. M. Kass, B. L. Ehlmann, and Y. L. Yung (2015), Tracing the fate of carbon and the atmospheric evolution of Mars, *Nature Communications*, *6*, DOI: 10.1038/ncomms10003.

Hunter, R. E. (1977), Basic types of stratification in small eolian dunes, *Sedimentology*, *24*(3), 361-387.

Hunter, R. E. and B. M. Richmond (1983), Storm-controlled oblique dunes of the Oregon coast, *Geological Society of America Bulletin*, 94(12), 1450-1465.

Ikeda, S. (1984), Prediction of alternate bar wavelength and height, *Journal of Hydraulic Engineering*, *110*(4), 371-386.

Irwin, R. P., and A. D. Howard (2002), Drainage basin evolution in Noachian Terra Cimmeria, Mars, *Journal of Geophysical Research: Planets*, *107*(E7), 10-11-10-23, DOI: 10.1029/2001JE001818.

Irwin, R. P., S. Tooth, R. A. Craddock, A. D. Howard, and A. B. de Latour (2014), Origin and development of theater-headed valleys in the Atacama Desert, northern Chile: Morphological analogs to martian valley networks, *Icarus*, *243*, 296-310, DOI:10.1016/j.icarus.2014.08.012.

Iversen, J. D., and K. R. Rasmussen (1999), The effect of wind speed and bed slope on sand transport, *Sedimentology*, *46*(4), 723-731.

Izumi, N., and G. Parker (1995), Inception of channelization and drainage basin formation: upstream-driven theory, *Journal of Fluid Mechanics*, *283*, 341-363.

Izumi, N., and G. Parker (2000), Linear stability analysis of channel inception: downstream-driven theory, *Journal of Fluid Mechanics*, *419*, 239-262.

Jerolmack, D. J., and D. Mohrig (2005), A unified model for subaqueous bed form dynamics, *Water Resources Research*, 41, W12421, DOI:10.1029/2005WR004329.

Jerolmack, D. J., D. Mohrig, J. P. Grotzinger, D. A. Fike, W. A. Watters (2006), Spatial grain size sorting in eolian ripples and estimation of wind conditions on planetary surfaces: Application to Meridiani Planum, Mars, *Journal of Geophysical Research: Planets*, *111*(E12), DOI: 10.1029/2005JE002544.

Johannesson, H. (2014), *Geological Map of Iceland (1:600,000). Bedrock Geology.*, 2nd edition ed., Icelandic Museum of Natural History and Iceland Geodetic Survey.

Johnson, J. R., W. M. Grundy, M. T. Lemmon, J. F. Bell III, M. J. Johnson, R. G. Deen, R. E. Arvidson, W. H. Farrand, E. A. Guinness, and A. G. Hayes (2006a), Spectrophotometric properties of materials observed by Pancam on the Mars Exploration Rovers: 2. Opportunity, *Journal of Geophysical Research: Planets*, 111(E12), DOI: 10.1029/2006JE002762.

Johnson, J. R., W. M. Grundy, M. T. Lemmon, J. F. Bell III, M. J. Johnson, R. G. Deen, R. E. Arvidson, W. H. Farrand, E. A. Guinness, and A. G. Hayes (2006b), Spectrophotometric properties of materials observed by Pancam on the Mars Exploration Rovers: 1. Spirit, *Journal of Geophysical Research: Planets*, 111(E2), DOI: 10.1029/2005JE002494.

Johnson, J. R., C. Achilles, J. F. Bell III, S. Bender, E. Cloutis, B. L. Ehlmann, A. A. Fraeman, O. Gasnault, V. E. Hamilton, S. Le Mouelic, S. Maurice, P. Pinet, L. Thompson, D. Wellington, and R. C. Wiens (2017), Visible/near-infrared spectral diversity from in situ observations of the Bagnold Dune Field sands in Gale Crater, Mars, *Journal of Geophysical Research: Planets*, in press, DOI: 10.1002/2016JE005187.

Kamphuis, J. (1974), Determination of sand roughness for fixed beds, *Journal of Hydraulic Research*, *12*(2), 193-203.

Kauffman, J., K. Othberg, V. Gillerman, and D. Garwood (2005), Geologic map of the Twin Falls 30x60 minute quadrangle, *Idaho: Moscow, Idaho, Idaho Geological Survey*, scale 1:100,000.

Kleinhans, M. (2005), Flow discharge and sediment transport models for estimating a minimum timescale of hydrological activity and channel and delta formation on Mars, *Journal of Geophysical Research: Planets*, *110*(E12), DOI: 10.1029/2005JE002521.

Klima, R. L., C. M. Pieters, J. W. Boardman, R. O. Green, J. W. Head, P. J. Isaacson, J. F. Mustard, J. W. Nettles, N. E., Petro, M. I. Staid, and J. M. Sunshine (2011), New insights into lunar petrology: Distribution and composition of prominent low-Ca pyroxene exposures as observed by the

Moon Mineralogy Mapper (M3), *Journal of Geophysical Research: Planets*, *116*(E6), DOI: 10.1029/2010JE003719.

Kocurek, G., and R. C. Ewing (2012), Source-to-sink: An Earth/Mars comparison of boundary conditions for eolian dune systems, in Sedimentary Geology of Mars, edited by J. P. Grotzinger and R. E. Milliken, SEPM Special Publication, Tulsa, OK, 102, 151–168, DOI: 10.2110/pec.12.102.0151.

Kok, J. F. (2010a), Difference in the wind speeds required for initiation versus continuation of sand transport on Mars: Implications for dunes and dust storms, *Physical Review Letters*, 104(7), 074502, DOI: 10.1103/PhysRevLett.104.074502.

Kok, J. F. (2010b), An improved parameterization of wind-blown sand flux on Mars that includes the effect of hysteresis, *Geophysical Research Letters*, 37(12), DOI: 10.1029/2010GL043646.

Kok, J. F., E. J. Parteli, T. I. Michaels, and D. B. Karam (2012), The physics of wind-blown sand and dust, *Reports on Progress in Physics*, 75(10), 106901, DOI: 10.1088/0034-4885/75/10/106901.

Komar, P. D. (1980), Modes of sediment transport in channelized water flows with ramifications to the erosion of the Martian outflow channels, *Icarus*, *42*(3), 317-329.

Komatsu, G., and V. R. Baker (1997), Paleohydrology and flood geomorphology of Ares Vallis, *Journal of Geophysical Research: Planets*, *102*(E2), 4151-4160, DOI: 10.1029/96je02564.

Kovacs, A., and G. Parker (1994), A new vectorial bedload formulation and its application to the time evolution of straight river channels, *Journal of Fluid Mechanics*, *267*, 153-183.

Kramers, H. A. (1927), La diffusion de la lumiere par les atomes, Atti del Congresso Internazionale dei Fisici, Como, 2, 545-557.

Kreisch, C. D., J. A. O'Sullivan, R. E. Arvidson, D. V. Politte, L. He, N. T. Stein, J. Finkel, E. A. Guinness, M. J. Wolff, and M. G. A. Lapôtre (2017), Regularization of Mars Reconnaissance Orbiter CRISM Along-Track Oversampled Hyperspectral Imaging Observations of Mars, *Icarus*, 182, 136-151, DOI: 10.1016/j.icarus.2016.09.033.

Kronig, R. D. L. (1926), On the theory of dispersion of x-rays, *Journal of the Optical Society of America*, 12(6), 547-557.

Kurganov, A., S. Noelle, and G. Petrova (2001), Semidiscrete central-upwind schemes for hyperbolic conservation laws and Hamilton-Jacobi equations, *SIAM Journal on Scientific Computing*, *23*(3), 707-740.

Laity, J. E., and M. C. Malin (1985), Sapping processes and the development of theater-headed valley networks on the Colorado Plateau, *Geological Society of America Bulletin*, *96*(2), 203-217.

Lamb, M. P., A. D. Howard, J. Johnson, K. X. Whipple, W. E. Dietrich, and J. T. Perron (2006), Can springs cut canyons into rock?, *Journal of Geophysical Research: Planets*, *111*(E7), DOI: 10.1029/2005JE002663.

Lamb, M. P., A. D. Howard, W. E. Dietrich, and J. T. Perron (2007), Formation of amphitheater-headed valleys by waterfall erosion after large-scale slumping on Hawai'i, *Geological Society of America Bulletin*, *119*(7-8), 805-822, DOI:10.1130/B25986.1.

Lamb, M. P., W. E. Dietrich, S. M. Aciego, D. J. DePaolo, and M. Manga (2008), Formation of Box Canyon, Idaho, by megaflood: Implications for seepage erosion on Earth and Mars, *Science*, *320*(5879), 1067-1070, DOI:10.1126/science.1156630.

Lamb, M. P., and W. E. Dietrich (2009), The persistence of waterfalls in fractured rock, *Geological Society of America Bulletin*, *121*(7-8), 1123-1134, DOI:10.1130/B26482.1.

Lamb, M. P., and M. A. Fonstad (2010), Rapid formation of a modern bedrock canyon by a single flood event, *Nature Geoscience*, *3*(7), 477-481, DOI: 10.1038/ngeo894.

Lamb, M.P., J. P. Grotzinger, J. B. Southard, and N. J. Tosca (2012a), Were aqueous ripples on Mars formed by flowing brines, *Sedimentary Geology of Mars*, 102, 139–150.

Lamb, M. P., J. A. Nittrouer, D. Mohrig, and J. Shaw (2012b), Backwater and river plume controls on scour upstream of river mouths: Implications for fluvio-deltaic morphodynamics, *Journal of Geophysical Research: Earth Surface*, *117*(F1), DOI: 10.1029/2011JF002079.

Lamb, M. P., B. H. Mackey, and K. A. Farley (2014), Amphitheater-headed canyons formed by megaflooding at Malad Gorge, Idaho, *Proceedings of the National Academy of Sciences*, *111*(1), 57-62, DOI:10.1073/pnas.1312251111.

Lamb, M. P., N. J. Finnegan, J. S. Scheingross, and L. S. Sklar (2015), New insights into the mechanics of fluvial bedrock erosion through flume experiments and theory, *Geomorphology*, *244*, 33-55, DOI: 10.1016/j.geomorph.2015.03.003.

Lancaster, N. (1988), Controls of eolian dune size and spacing, *Geology*, *16*(11), 972-975.

Lane, M. D., and P. R. Christensen (2013), Determining olivine composition of basaltic dunes in Gale Crater, Mars, from orbit: Awaiting ground truth from Curiosity, *Geophysical Research Letters*, 40(14), 3517-3521.

Lapôtre, M. G. A., and M. P. Lamb (2015), Hydraulics of floods upstream of horseshoe canyons and waterfalls, *Journal of Geophysical Research: Earth Surface*, *120*(7), 1227-1250, DOI:10.1002/2014JF003412.

Lapôtre, M. G. A., M. P. Lamb, and R. M. Williams (2016a), Canyon formation constraints on the discharge of catastrophic outburst floods of Earth and Mars, *Journal of Geophysical Research: Planets*, *121*(7), 1232-1263, DOI:10.1002/2016JE005061.

Lapôtre, M. G. A., R. C. Ewing, M. Lamb, W. W. Fischer, J. P. Grotzinger, D. Rubin, K. Lewis, M. Ballard, M. Day, S. Gupta, S. Banham, N. T. Bridges, D. Des Marais, A. Fraeman, J. Grant, K. Herkenhoff, D. Ming, M. Mischna, M. Rice, D. Sumner, A. Vasavada, and R. Yingst (2016b), Large Wind Ripples on

Mars: A Record of Atmospheric Evolution, *Science*, 353(6294), 55-58, DOI: 10.1126/science.aaf3206.

Lapôtre, M. G. A., B.L. Ehlmann, and S.E. Minson (2017a), A Probabilistic Approach to Remote Compositional Analysis of Planetary Surfaces, *Journal of Geophysical Research: Planets*, in press, DOI: 10.1002/2016JE005248.

Lapôtre, M. G. A., Ehlmann, B. L., Minson, S. E., Arvidson, R. E., Ayoub, F., Fraeman, A. A., Ewing, R. C., and Bridges, N. T. (2017b), Compositional variations in sands of the Bagnold Dunes at Gale crater, Mars, from visible-shortwave infrared spectroscopy and comparison with ground-truth from the Curiosity rover, *Journal of Geophysical Research – Planets*, in press, DOI: 10.1002/2016JE005133.

Larsen, I. J., and M. P. Lamb (2016), Progressive incision of the Channeled Scablands by outburst floods, *Nature*, *538*(7624), 229-232, DOI:10.1038/nature19817.

Lasue, J., N. Mangold, E. Hauber, S. Clifford, W. Feldman, O. Gasnault, C. Grima, S. Maurice, and O. Mousis (2013), Quantitative assessments of the martian hydrosphere, *Space Science Reviews*, *174*(1-4), 155-212, DOI: 10.1007/s11214-012-9946-5.

Leask, H. J., L. Wilson, and K. L. Mitchell (2007), Formation of Mangala Valles outflow channel, Mars: Morphological development and water discharge and duration estimates, *Journal of Geophysical Research: Planets*, *112*(E8), DOI: 10.1029/2006JE002851.

Leclair, S. F. (2002), Preservation of cross-strata due to the migration of subaqueous dunes: an experimental investigation, *Sedimentology*, *49*(6), 1157-1180, DOI: 10.1046/j.1365-3091.2002.00482.x.

Leeder, M. (1983), On the interactions between turbulent flow, sediment transport and bedform mechanics in channelized flows, *Modern and Ancient Fluvial Systems Special Publication*, 6, 5–18.

Lewis, K. W., O. Aharonson, J. P. Grotzinger, S. W. Squyres, J. F. Bell III, L. S. Crumpler, and M. E. Schmidt (2008), Structure and stratigraphy of home plate from the spirit mars exploration rover, *Journal of Geophysical Research: Planets*, *113*(E12), DOI: 10.1029/2007JE003025.

Li, B., and C. McKenna Neuman (2012), Boundary-layer turbulence characteristics during aeolian saltation, *Geophysical Research Letters*, *39*(11), DOI: 10.1029/2012GL052234.

Li, S., and R. E. Milliken (2015), Estimating the modal mineralogy of eucrite and diogenite meteorites using visible–near infrared reflectance spectroscopy, *Meteoritics and Planetary Science*, 50:11, 1821-1850, DOI: 10.1111/maps.12513.

Liu, Y., T. D. Glotch, N. A. Scudder, M. L. Kraner, T. Condus, R. E. Arvidson, E. A. Guinness, M. J. Wolff, and M. D. Smith (2016), End-member identification and spectral mixture analysis of CRISM hyperspectral data: A case study on southwest Melas Chasma, Mars, *Journal of Geophysical Research: Planets*, *121*(10), 2004-2036, DOI: 10.1002/2016JE005028.

Lobkovsky, A. E., B. Jensen, A. Kudrolli, and D. H. Rothman (2004), Threshold phenomena in erosion driven by subsurface flow, *Journal of Geophysical Research: Earth Surface*, *109*(F4), DOI:10.1029/2006JF000517.

Lobkovsky, A. E., B. E. Smith, A. Kudrolli, D. C. Mohrig, and D. H. Rothman (2007), Erosive dynamics of channels incised by subsurface water flow, *Journal of Geophysical Research: Earth Surface*, *112*(F3), DOI:10.1029/2004JF000172.

Lorenz, R. D., N. T. Bridges, A. A. Rosenthal, and E. Donkor (2014), Elevation dependence of bedform wavelength on Tharsis Montes, Mars: Atmospheric density as a controlling parameter, *Icarus*, *230*, 77-80, DOI: 10.1016/j.icarus.2013.10.026.

Lowell, P. (1895), *Mars*, 228 pp., New York, Haugton-Mifflin.

Lucey, P. G. (1998), Model near-infrared optical constants of olivine and pyroxene as a function of iron content, *Journal of Geophysical Research: Planets*, 103(E1), 1703-1713.

Luo, W., R. E. Arvidson, M. Sultan, R. Becker, M. K. Crombie, N. Sturchio, and Z. El Alfy (1997), Ground-water sapping processes, western desert, Egypt, *Geological Society of America Bulletin*, *109*(1), 43-62.

Mackey, B. H., J. S. Scheingross, M. P. Lamb, and K. A. Farley (2014), Knickpoint formation, rapid propagation, and landscape response following coastal cliff retreat at the last interglacial sea-level highstand: Kaua'i, Hawai'i, *Geological Society of America Bulletin*, B30930. 30931.

Mackin, J. H. (1961), A stratigraphic section in the Yakima Basalt and the Ellensburg Formation in south-central Washington, State of Washington Department of Conservation, Division of Mines and Geology, Olympia, WA.

Mahaffy, P. R., C. R. Webster, J. C. Stern, A. E. Brunner, S. K. Atreya, P. G. Conrad, S. Domagal-Goldman, J. L. Eigenbrode, G. J. Flesch, L. E. Christensen, H. B. Franz, C. Freissinet, D. P. Galvin, J. P. Grotzinger, J. H. Jones, L. A. Leshin, C. Malespin, A. C. McAdam, D. W. Ming, R. Navarro-Gonzalez, P. B. Niles, T. Owen, A. A. Pavlov, A. Steele, M. G. Trainer, K. H. Williford, J. J. Wray, and the MSL Science Team (2015), The imprint of atmospheric evolution in the D/H of Hesperian clay minerals on Mars, *Science*, *347*(6220), 412-414, DOI: 10.1126/science.1260291.

Makse, H. A. (2000), Grain segregation mechanism in aeolian sand ripples, *The European Physical Journal E*, 1(2-3), 127-135, DOI: 10.1007/pl00014592.

Malde, H. E. (1960), Evidence in the Snake River plain, Idaho, of a catastrophic flood from Pleistocene Lake Bonneville, *US Geological Survey Professional Paper 400b*, 295-297.

Malde, H. E. (1968), The catastrophic late Pleistocene Bonneville flood in the Snake River plain, Idaho, US Govt. Print. Off.

Malde, H. E. (1991), Quaternary geology and structural history of the Snake River Plain, Idaho and Oregon, *The Geology of North America*, *2*, 251-281.

Malin, M. C., J. F. Bell III, B. A. Cantor, M. A. Caplinger, W. M. Calvin, R. T. Clancy, K. S. Edgett, L. Edwards, R. M. Haberle, and P. B. James (2007), Context camera investigation on board the Mars Reconnaissance Orbiter, *Journal of Geophysical Research: Planets*, *112*(E5), DOI:10.1029/2006JE002808.

Manga, M. (2004), Martian floods at Cerberus Fossae can be produced by groundwater discharge, *Geophysical Research Letters*, *31*(2), DOI: 10.1029/2003gl018958.

Mangold, N., C. Quantin, V. Ansan, C. Delacourt, and P. Allemand (2004), Evidence for precipitation on Mars from dendritic valleys in the Valles Marineris area. *Science*, *305*(5680), 78-81, DOI: 10.1126/science.1097549.

Mangold, N., V. Ansan, P. Masson, C. Quantin, and G. Neukum (2008), Geomorphic study of fluvial landforms on the northern Valles Marineris plateau, Mars, *Journal of Geophysical Research: Planets*, *113*(E8), DOI:10.1029/2007JE002985.

Mangold, N., D. Baratoux, O. Arnalds, J.-M. Bardintzeff, B. Platevoet, M. Gregoire, and P. Pinet (2011), Segregation of olivine grains in volcanic sands in Iceland and implications for Mars, *Earth and Planetary Science Letters*, 310(3), 233-243, DOI: 10.1016/j.epsl.2011.07.025.

Mantz, P. A. (1978), Bedforms produced by fine, cohesionless, granular and flakey sediments under subcritical water flows, *Sedimentology*, 25, 83-103.

Marra, W. A., L. Braat, A. W. Baar, and M. G. Kleinhans (2014a), Valley formation by groundwater seepage, pressurized groundwater outbursts and crater-lake overflow in flume experiments with implications for Mars, *Icarus*, *232*, 97-117, DOI: 10.1016/j.icarus.2013.12.026.

Marra, W. A., E. Hauber, S. J. McLelland, B. J. Murphy, D. R. Parsons, S. J. Conway, M. Roda, R. Govers, and M. G. Kleinhans (2014b), Pressurized groundwater outflow experiments and numerical modeling for outflow channels on Mars, *Journal of Geophysical Research: Planets*, *119*(12), 2668-2693, DOI: 10.1002/2014JE004701.

Mason, C. C., and R. L. Folk (1958), Differentiation of beach, dune, and aeolian flat environments by size analysis, Mustang Island, Texas, *Journal of Sedimentary Research*, 28(2), 211-226.

Mason, P. J., and K. Arumugam (1985), Free jet scour below dams and flip buckets, *Journal of Hydraulic Engineering*, *111*(2), 220-235.

McCord, T. B., G. B. Hansen, F. P. Fanale, R. W. Carlson, D. L. Matson, T. V. Johnson, W. D. Smythe, J. K. Crowley, P. D. Martin, A. Ocampo, and C. A. Hibbitts (1998), Salts on Europa's surface detected by Galileo's near infrared mapping spectrometer, *Science*, *280*(5367), 1242-1245.

McEwen, A. S., E. M. Eliason, J. W. Bergstrom, N. T. Bridges, C. J. Hansen, W. A. Delamere, J. A. Grant, V. C. Gullick, K. E. Herkenhoff, L. Keszthelyi, R. L. Kirk, M. T. Mellon, S. W. Squyres, N. Thomas, C. M. Weitz (2007), Mars reconnaissance orbiter's high resolution imaging science experiment (HiRISE), *Journal of Geophysical Research: Planets*, *112*(E5), DOI: 10.1029/2005JE002605.

McGuire, A. F. and B. Hapke (1995), An experimental study of light scattering by large, irregular particles, *Icarus*, *113*(1), 134-155.

McIntyre, N., N. H. Warner, S. Gupta, J.-R. Kim, and J.-P. Muller (2012), Hydraulic modeling of a distributary channel of Athabasca Valles, Mars, using a high-resolution digital terrain model, *Journal of Geophysical Research: Planets*, *117*(E3), DOI: 10.1029/2011JE003939.

McKay, D. S., E. K. Gibson Jr, K. L. Thomas-Keprta, H. Vali, C. S. Romanek, S. J. Clemett, X. D. F. Chillier, C. R. Maechling, and R. N. Zare (1996). Search for past life on Mars: possible relic biogenic activity in Martian meteorite ALH84001, *Science*, *273*(5277), 924.

Meinzer, O. E. (1927), Large springs in the United States, U.S. Geological Survey Water Supply Paper, 42-51.

Meresse, S., F. Costard, N. Mangold, P. Masson, G. Neukum, and H. C.-I. Team (2008), Formation and evolution of the chaotic terrains by subsidence and magmatism: Hydraotes Chaos, Mars, *Icarus*, *194*(2), 487-500, DOI: 10.1016/j.icarus.2007.10.023.

Metropolis, N., A. W. Rosenbluth, M. N. Rosenbluth, A. H. Teller, and E. Teller (1953), Equation of state calculations by fast computing machines, *The Journal of Chemical Physics*, *21*(6), 1087-1092.

Metz, J. M., J. P. Grotzinger, D. M. Rubin, K. W. Lewis, S. W. Squyres, and J. F. Bell III (2009), Sulfate-rich eolian and wet interdune deposits, Erebus crater, Meridiani Planum, Mars, *Journal of Sedimentary Research*, *79*(5), 247-264, DOI: 10.2110/jsr.2009.033.

Meyer-Peter, E., and R. Muller (1948), Formulas for bed-load transport, paper presented at Proceedings of the 2nd Meeting of the International Association for Hydraulic Structures Research, International Association of Hydraulic Research Delft.

Middleton, G. V., and J. B. Southard (1984), Mechanics of Sediment Movement: Providence, Rhode Island, Society of Economic Paleontologists and Mineralogists, Short Course 3, Second Edition, 401 p., 13-14 March.

Milazzo, M. P., L. P. Keszthelyi, W. L. Jaeger, M. Rosiek, S. Mattson, C. Verba, R. A. Beyer, P. E. Geissler, A. S. McEwen, and R. T. Hi (2009), Discovery of columnar jointing on Mars, *Geology*, *37*(2), 171-174, DOI: 10.1130/g25187a.1.

Miller, M., I. McCave, and P. Komar (1977), Threshold of sediment motion under unidirectional currents, *Sedimentology*, *24*(4), 507-527.

Milliken, R., J. P. Grotzinger, and B. Thomson (2010), Paleoclimate of Mars as captured by the stratigraphic record in Gale Crater, *Geophysical Research Letters*, 37(4), DOI: 10.1029/2009GL041870.

Milliken, R., R. C. Ewing, W. W. Fischer, and J. Hurowitz (2014), Wind-blown sandstones cemented by sulfate and clay minerals in Gale Crater, Mars, *Geophysical Research Letters*, 41(4), 1149-1154, DOI: 10.1002/2013GL059097.

Minson, S., M. Simons, and J. Beck (2013), Bayesian inversion for finite fault earthquake source models-I: theory and algorithm, *Geophysical Journal International*, 194(3), 1701-1726, DOI: 10.1093/gji/ggt180.

Minson, S., M. Simons, J. Beck, F. Ortega, J. Jiang, S. Owen, A. Moore, A. Inbal, and A. Sladen (2014), Bayesian inversion for finite fault earthquake source models-II: the 2011 great Tohoku-oki, Japan earthquake, *Geophysical Journal International*, 198(2), 922-940, DOI: 10.1093/gji/ggu170.

Morris, R. V., D. C. Golden, J. F. Bell III, H. V. Lauer, and J. B. Adams (1993), Pigmenting agents in Martian soils: Inferences from spectral, Mössbauer, and magnetic properties of nanophase and other iron oxides in Hawaiian palagonitic soil PN-9, *Geochimica et Cosmochimica Acta*, *57*(19), 4597-4609.

Mungkasi, S., and S. G. Roberts (2011), A finite volume method for shallow water flows on triangular computational grids, paper presented at 2011 International Conference on Advanced Computer Science and Information System (ICACSIS), IEEE.

Mungkasi, S., and S. G. Roberts (2013), Validation of ANUGA hydraulic model using exact solutions to shallow water wave problems, paper presented at Journal of Physics: Conference Series, IOP Publishing.

Murchie, S. L., F. P. Seelos, C. D. Hash, D. C. Humm, E. Malaret, J. A. McGovern, T. H. Choo, K. D. Seelos, D. L. Buczkowski, and M. F. Morgan (2009), Compact Reconnaissance Imaging Spectrometer for Mars investigation and data set from the Mars Reconnaissance Orbiter's primary science phase, *Journal of Geophysical Research: Planets*, 114(E2), DOI: 10.1029/2009JE003344.

Mustard, J. F., and C. M. Pieters (1987), Quantitative abundance estimates from bidirectional reflectance measurements, *Journal of Geophysical Research: Solid Earth*, 92(B4), E617-E626.

Mustard, J. F., and C. M. Pieters (1989), Photometric phase functions of common geologic minerals and applications to quantitative analysis of mineral mixture reflectance spectra, *Journal of Geophysical Research: Solid Earth*, *94*(B10), 13619-13634.

Nash, D., and J. Conel (1974), Spectral reflectance systematics for mixtures of powdered hypersthene, labradorite, and ilmenite, *Journal of Geophysical Research*, *79*(11), 1615-1621.

Nesbitt, H. W., and G. M. Young (1996), Petrogenesis of sediments in the absence of chemical weathering: effects of abrasion and sorting on bulk composition and mineralogy, *Sedimentology*, 43(2), 341-358.

Newman, C., J. Gomez-Elvira, M. Marin, S. Navarro, J. Torres, M.I. Richardson, J.M. Battalio, S.D. Guzewich, R. Sullivan, M. de la Torre, A.R. Vasavada, and N.T. Bridges (2017), Winds measured by the Rover Environmental Monitoring Station (REMS) during the Mars Science Laboratory (MSL) rover's Bagnold Dybes Campaign and comparison with numerical modeling using MarsWRF, *Icarus*, 291, 203-231, DOI: 10.1016/j.icarus.2016.12.016.

Nielsen, O., S. Roberts, D. Gray, A. McPherson, and A. Hitchman (2005), Hydrodynamic modelling of coastal inundation, paper presented at MODSIM 2005 International Congress on Modelling and Simulation.

Nikuradse, J. (1933), Stromungsgesetz in rauhren rohren, VDI Forschungshefte 361 (English translation: Laws of flow in rough pipes, 1950), Tech. Rep. NACA Technical Memorandum 1292: Washington, D.C., National Advisory Commission for Aeronautics.

Niño, Y., F. Lopez, and M. Garcia (2003), Threshold for particle entrainment into suspension, *Sedimentology*, 50, 247–263, DOI:10.1046/j.1365-3091.2003.00551.x.

O'Connell-Cooper, C. D., J. G. Spray, L. M. Thompson, R. Gellert, J. A. Berger, N. I. Boyd, E. D. Desouza, G. M. Perrett, M. Schmidt, S. J. VanBommel, and the MSL APXS team (in revision), APXS-derived chemistry of the Bagnold Dune sands: Comparison with Gale crater soils and the global martian average, *Journal of Geophysical Research: Planets*.

O'Connor, J. E., and V. R. Baker (1992), Magnitudes and implications of peak discharges from glacial Lake Missoula, *Geological Society of America Bulletin*, *104*(3), 267-279.

O'Connor, J. E. (1993), Hydrology, hydraulics, and geomorphology of the Bonneville flood, *Geological Society of America Special Papers, 274*, 1-84.

Ojha, L., M. B. Wilhelm, S. L. Murchie, A. S. McEwen, J. J. Wray, J. Hanley, M. Masse, and M. Chojnacki (2015), Spectral evidence for hydrated salts in recurring slope lineae on Mars, *Nature Geoscience*, *8*(11), 829-832, DOI: 10.1038/ngeo2546.

Pacifici, A., G. Komatsu, and M. Pondrelli (2009), Geological evolution of Ares Vallis on Mars: Formation by multiple events of catastrophic flooding, glacial and periglacial processes, *Icarus*, *202*(1), 60-77, DOI: 10.1016/j.icarus.2009.02.029.

Pagliara, S., W. H. Hager, and H.-E. Minor (2006), Hydraulics of plane plunge pool scour, *Journal of Hydraulic Engineering*, *132*(5), 450-461, DOI: 10.1061/(ASCE)0733-9429(2006)132.

Pan, C. and A. D. Rogers (2017), Occurrence and scale of compositional heterogeneity in martian dune fields: Toward understanding the effects of aeolian sorting on martian sediment compositions, *Icarus*, 282, 56-69 DOI: 10.1016/j.icarus.2016.09.021.

Paola, C., and L. Borgman (1991), Reconstructing random topography from preserved stratification, *Sedimentology*, *38*(4), 553-565.

Parfenoff, A., C. Pomerol, and J. Tourenq (1970), Les Mineraux en grains: methodes d'etude et determination, 578 pp., Masson et Cie, Paris.

Parker, G. (1978), Self-formed straight rivers with equilibrium banks and mobile bed. Part 2. The gravel river, *Journal of Fluid Mechanics*, *89*(01), 127-146.

Parker, G., C. M. Toro-Escobar, M. Ramey, and S. Beck (2003), Effect of floodwater extraction on mountain stream morphology, *Journal of Hydraulic Engineering*, *129*(11), 885-895, DOI:10.1061/(ASCE)0733-9429(2003)129:11(885).

Parker, G., P. R. Wilcock, C. Paola, W. E. Dietrich, and J. Pitlick (2007), Physical basis for quasi-universal relations describing bankfull hydraulic geometry of single-thread gravel bed rivers, *Journal of Geophysical Research: Earth Surface*, *112*(F4).

Parker, T. J., R. S. Saunders, and D. M. Schneeberger (1989), Transitional morphology in west Deuteronilus Mensae, Mars: Implications for modification of the lowland/upland boundary, *Icarus*, *82*(1), 111-145.

Pasternack, G. B., C. R. Ellis, K. A. Leier, B. L. Valle, and J. D. Marr (2006), Convergent hydraulics at horseshoe steps in bedrock rivers, *Geomorphology*, *82*(1), 126-145.

Pasternack, G. B., C. R. Ellis, and J. D. Marr (2007), Jet and hydraulic jump near-bed stresses below a horseshoe waterfall, *Water resources research*, *43*(7), DOI: 10.1029/2006WR005774.

Pelletier, J. D., and V. R. Baker (2011), The role of weathering in the formation of bedrock valleys on Earth and Mars: A numerical modeling investigation, *Journal of Geophysical Research: Planets*, *116*, DOI: 10.1029/2011je003821.

Perron, J.T., M. P. Lamb, C. D. Koven, I. Y. Fung, E. Yager, and M. Adamkovics (2006), Valley formation and methane precipitation rates on Titan, *Journal of Geophysical Research: Planets*, 111, DOI: 10.1029/2005JE002602.

Petroff, A. P., O. Devauchelle, D. M. Abrams, A. E. Lobkovsky, A. Kudrolli, and D. H. Rothman (2011), Geometry of valley growth, *Journal of Fluid Mechanics*, *673*, 245-254, DOI: 10.1017/s002211201100053x.

Pillans, B. (1985), Drainage initiation by subsurface flow in South Taranaki, New Zealand, *Geology*, *13*(4), 262-265.

Pilorget, C., J. Fernando, B. L. Ehlmann, F. Schmidt, and T. Hiroi (2016), Wavelength dependence of scattering properties in the VIS–NIR and links with grain-scale physical and compositional properties, *Icarus*, 267, 296-314, DOI: 10.1016/j.icarus.2015.12.029.

Poulet, F., J. Cuzzi, D. Cruikshank, T. L. Roush, and C. Dalle Ore (2002), Comparison between the Shkuratov and Hapke scattering theories for solid planetary surfaces: Application to the surface composition of two Centaurs, *Icarus*, *160*(2), 313-324, DOI: 10.1006/icar.2002.6970.

Poulet, F., and S. Erard (2004), Nonlinear spectral mixing: Quantitative analysis of laboratory mineral mixtures, *Journal of Geophysical Research: Planets*, *109*(E2), DOI: 10.1029/2003JE002179.

Poulet, F., N. Mangold, D. Loizeau, J.-B. Bibring, Y. Langevin, J. Michalski, and B. Gondet (2008), Abundance of minerals in the phyllosilicate-rich units on Mars, *Astronomy and Astrophysics*, *487*(2), L41-L44, DOI: 10.1051/0004-6361:200810150.

Poulet, F., N. Mangold, B. Platevoet, J.-M. Bardintzeff, V. Sautter, J. Mustard, J.-P. Bibring, P. Pinet, Y. Langevin, and B. Gondet (2009), Quantitative compositional analysis of martian mafic regions using the MEx/OMEGA reflectance data: 2. Petrological implications, *Icarus*, 201(1), 84-101, DOI: 10.1016/j.icarus.2008.12.042.

Poulet, F., J. Carter, J. Bishop, D. Loizeau, and S. Murchie (2014), Mineral abundances at the final four Curiosity study sites and implications for their formation, *Icarus*, *231*, 65-76, DOI: 10.1016/j.icarus.2013.11.023.

Purcell, E. M. and C. R. Pennypacker (1973), Scattering and absorption of light by nonspherical dielectric grains, *The Astrophysical Journal*, *186*, 705-714.

Rajaratnam, N., and D. Muralidhar (1968), Characteristics of the rectangular free overfall, *Journal of Hydraulic Research*, *6*(3), 233-258.
Ramsey, M. S., and P. R. Christensen (1998), Mineral abundance determination: Quantitative deconvolution of thermal emission spectra, *Journal of Geophysical Research*, 103, no. B1, 577-596.
Rathburn, S. L. (1993), Pleistocene cataclysmic flooding along the Big Lost River, east central Idaho, *Geomorphology*, *8*(4), 305-319.
Raudkivi, A. J. (1997), Ripples on stream bed, *Journal of Hydraulic Engineering*, 123, 58-64.
Rengers, F. K., and G. Tucker (2014), Analysis and modeling of gully headcut dynamics, North American high plains, *Journal of Geophysical Research: Earth Surface*, DOI: 10.1002/2013JF002962.
Richards, K. J. (1980), The formation of ripples and dunes on an erodible bed, *Journal of Fluid Mechanics*, 99, 597–618, DOI:10.1017/S002211208000078X.
Richardson, K., and P. A. Carling (2006), The hydraulics of a straight bedrock channel: Insights from solute dispersion studies, *Geomorphology*, *82*(1), 98-125, DOI: 10.1016/j.geomorph.2005.09.022.
Roberts, S., O. Nielsen, and J. Jakeman (2008), Simulation of tsunami and flash floods, in *Modeling, Simulation and Optimization of Complex Processes*, edited, pp. 489-498, Springer.
Roberts, S., O. Nielsen, D. Gray, and J. Sexton (2009), ANUGA User Manual, *Geoscience Australia*.
Robertson, K. M., R. E. Milliken, and S. Li (2016), Estimating mineral abundances of clay and gypsum mixtures using radiative transfer models applied to visible-near infrared reflectance spectra, *Icarus*, 277, 171-186, DOI: 10.1016/j.icarus.2016.04.034.
Robinson, M. S., and K. L. Tanaka (1990), Magnitude of a Catastrophic Flood Event at Kasei Valles, Mars, *Geology*, *18*(9), 902-905, DOI: 10.1130/0091-7613(1990)018.
Rogers, A. D., and J. L. Bandfield (2009), Mineralogical characterization of Mars Science Laboratory candidate landing sites from THEMIS and TES data, *Icarus*, 203(2), 437-453, DOI: 10.1016/j.icarus.2009.04.020.
Rotto, S., and K. L. Tanaka (1995), *Geologic/geomorphologic map of the Chryse Planitia region of Mars (1:5,000,000)*, US Geological Survey.
Rouse, H. (1936), Discharge characteristics of the free overfall, *Civil Engineering*, *6*, 257-260.
Rouse, H. (1937), Pressure distribution and acceleration at the free overfall, *Civ. Eng*, *7*(7), 518.
Rouse, H. (1950), Engineering hydraulics, edited, John Wiley & Sons, New York.
Roush, T. L., J. Pollack, F. Witteborn, J. Bregman, and J. Simpson (1990), Ice and minerals on Callisto: A reassessment of the reflectance spectra, *Icarus*, *86*(2), 355-382.
Roush, T. L. (2003), Estimated optical constants of the Tagish Lake meteorite, *Meteoritics and Planetary Science*, *38*(3), 419-426, DOI: 10.1111/j.1945-5100.2003.tb00277.x.

Rubin, D. M., and D. S. McCulloch (1980), Single and superimposed bedforms: a synthesis of San Francisco Bay and flume observations, *Sedimentary Geology*, *26*(1-3), 207-231.

Rubin, D. M., and R. E. Hunter (1982), Bedform climbing in theory and nature, *Sedimentology*, *29*(1), 121-138.

Rubin, D. M., and C. L. Carter (2005), Bedforms 4.0: MATLAB code for simulating bedforms and cross-bedding, *U.S. Geological Survey Open-File Report* 2331-1258.

Rubin, D. M. (2012), A unifying model for planform straightness of ripples and dunes in air and water, *Earth-Science Reviews*, *113*(3), 176-185, DOI: 10.1016/j.earscirev.2012.03.010.

Ruff, S. W., and P. R. Christensen (2002), Bright and dark regions on Mars: Particle size and mineralogical characteristics based on Thermal Emission Spectrometer data, *Journal of Geophysical Research: Planets*, *107*(E12), 2-1-2-22, DOI: 10.1029/2001JE001580.

Sautter, V., M. Toplis, R. Wiens, A. Cousin, C. Fabre, O. Gasnault, S. Maurice, O. Forni, J. Lasue, and A. Ollila (2015), In situ evidence for continental crust on early Mars, *Nature Geoscience*, 8(8), 605-609, DOI: 10.1038/ngeo2474.

Sayers, A. T. (1990), *Hydraulic and compressible flow turbomachines*, McGraw-Hill London etc.

Schorghofer, N., B. Jensen, A. Kudrolli, and D. H. Rothman (2004), Spontaneous channelization in permeable ground: Theory, experiment, and observation, *Journal of Fluid Mechanics*, *503*, 357-374, DOI:10.1017/S0022112004007931.

Schumm, S., K. Boyd, C. Wolff, and W. Spitz (1995), A ground-water sapping landscape in the Florida Panhandle, *Geomorphology*, *12*(4), 281-297.

Scott, W. E. (1982), *Surficial geologic map of the eastern Snake River Plain and adjacent areas, 111 to 115 west, Idaho and Wyoming (1:250,000)*, U.S. Geological Survey.

Seelos, K. D., F. P. Seelos, C. E. Viviano-Beck, S. L. Murchie, R. E. Arvidson, B. L. Ehlmann, and A. A. Fraeman (2014), Mineralogy of the MSL Curiosity landing site in Gale crater as observed by MRO/CRISM, *Geophysical Research Letters*, 41(14), 4880-4887, DOI: 10.1002/2014GL060310.

Seidl, M. A., J. K. Weissel, and L. F. Pratson (1996), The kinematics and pattern of escarpment retreat across the rifted continental margin of SE Australia, *Basin Research*, *8*(3), 301-316.

Seiff, A., and D. B. Kirk (1977), Structure of the atmosphere of Mars in summer at mid-latitudes, *Journal of Geophysical Research*, *82*(28), 4364-4378.

Seminara, G., and M. Tubino (1989), Alternate bars and meandering, in *River meandering*, edited by S. I. a. G. Parker, pp. 267-320, American Geophysical Union, Washington D. C.

Shao, Y., and H. Lu (2000), A simple expression for wind erosion threshold friction velocity, *Journal of Geophysical Research: Atmospheres*, 105(D17), 22437-22443, DOI: 10.1029/2000JD900304.

Sharp, R. P. (1963), Wind ripples, *The Journal of Geology*, 617-636.

Sharp, R. P., and M. C. Malin (1975), Channels on Mars, *Geological Society of America Bulletin*, *86*(5), 593-609.

Shean, D., J. Fahle, M. C. Malin, L. Edwards, and L. Posiolova (2011), MRO CTX stereo image processing and preliminary DEM quality assessment, paper presented at Lunar and Planetary Science Conference.

Shepherd, R. G. (1989), Correlations of permeability and grain size, *Ground Water*, *27*(5), 633-638.

Shields, A. (1936), Anwendung der Aehnlichkeitsmechanik und der Turbulenzforschung auf die Geschiebebewegung, 36 pp, Preussischen Versuchsanstalt fur Wasserbau.

Shipton, Z. K., J. P. Evans, K. R. Robeson, C. B. Forster, and S. Snelgrove (2002), Structural heterogeneity and permeability in faulted eolian sandstone: Implications for subsurface modeling of faults, *AAPG Bulletin*, *86*(5), 863-883.

Shkuratov, Y., L. Starukhina, H. Hoffmann, and G. Arnold (1999), A model of spectral albedo of particulate surfaces: Implications for optical properties of the Moon, *Icarus*, *137*(2), 235-246.

Siebach, K., J. P. Grotzinger, S. M. McLennan, M. B. Baker, R. Gellert, J. A. Hurrowitz, and D. L. Blaney (2015), Sorting out APXS compositional variations in Gale crater sedimentary rocks, Mars. In Geological Society of America Annual Meeting, Paper 94-2.

Siebach, K. L., M. B. Baker, J. P. Grotzinger, S. M. McLennan, R. Gellert, L. Thompson, and J. A. Hurowitz (2017), Sorting out Compositional Trends in Sedimentary Rocks of the Bradbury Group (Aeolus Palus), Gale Crater, Mars, *Journal of Geophysical Research: Planets*, 122(2),295-328, DOI: 10.1002/2016JE005195.

Silverman, B. W. (1981), Using kernel density estimates to investigate multimodality, *Journal of the Royal Statistical Society. Series B (Methodological)*, 97-99.

Silvestro, S., L. K. Fenton, D. A. Vaz, N. T. Bridges, and G. Ori (2010), Ripple migration and dune activity on Mars: Evidence for dynamic wind processes, *Geophysical Research Letters*, *37*(20), DOI: 10.1029/2010GL044743.

Silvestro, S., D. A. Vaz, R. C. Ewing, A. P. Rossi, L. K. Fenton, T. I. Michaels, J. Flahaut, and P. E. Geissler (2013), Pervasive aeolian activity along rover Curiosity’s traverse in Gale Crater, Mars, *Geology*, *41*(4), 483-486, DOI: 10.1130/G34162.1.

Silvestro, S., D. A. Vaz, H. Yizhaq, and F. Esposito (2016), Dune-like dynamic of Martian Aeolian large ripples, *Geophysical Research Letters*, 43(16), 8384-8389, DOI: 10.1002/2016GL070014.

Smith, J. D. (1970), Stability of a sand bed subjected to a shear flow of low Froude number, *Journal of Geophysical Research*, 75, 5928–5940, DOI:10.1029/JC075i030p05928.

Smith, D. E., M. T. Zuber, H. V. Frey, J. B. Garvin, J. W. Head, D. O. Muhleman, G. H. Pettengill, R. J. Phillips, S. C. Solomon, and H. J. Zwally (2001), Mars Orbiter Laser Altimeter: Experiment summary after the first year of global mapping of Mars, *Journal of Geophysical Research: Planets*, *106*(E10), 23689-23722, DOI:10.1029/2000JE001364.

Soderblom, L. A., R. C. Anderson, R. E. Arvidson, J. F. Bell III, N. A. Cabrol, W. Calvin, P. R. Christensen, B. C. Clark, T. Economou, and B. L. Ehlmann (2004), Soils of Eagle crater and Meridiani Planum at the Opportunity rover landing site, *Science*, *306*(5702), 1723-1726, DOI: 10.1126/science.1105127.

Souchon, A. L., P. C. Pinet, S. D. Chevrel, Y. H. Daydou, D. Baratoux, K. Kurita, M. K. Shepard, and P. Helfenstein (2011), An experimental study of Hapke's modeling of natural granular surface samples, *Icarus*, *215*(1), 313-331, DOI: 10.1016/j.icarus.2011.06.023.

Southard, J. B., and L. A. Boguchwal (1990a), Bed configurations in steady unidirectional water flows. Part 2. Synthesis of flume data, *Journal of Sedimentary Research*, 60, 658–679, DOI:10.1306/212F9241-2B24-11D7-8648000102C1865D.

Southard, J. B., and L. A. Boguchwal (1990b), Bed configurations in steady unidirectional water flows. Part 3. Effects of temperature and gravity, *Journal of Sedimentary Research*, 60, 680–686, DOI:10.2110/jsr.60.680.

Squyres, S. W., O. Aharonson, B. C. Clark, B. A. Cohen, L. Crumpler, P. De Souza, W. H. Farrand, R. Gellert, J. Grant, and J. P. Grotzinger (2007), Pyroclastic activity at home plate in Gusev Crater, Mars, *Science*, *316*(5825), 738-742, DOI: 10.1126/science.1139045.

Stamnes, K., S.-C. Tsay, W. Wiscombe, and K. Jayaweera (1988), Numerically stable algorithm for discrete-ordinate-method radiative transfer in multiple scattering and emitting layered media, *Applied Optics*, 27(12), 2502-2509.

Stein, R. A. (1965), Laboratory studies of total load and apparent bed load, *Journal of Geophysical Research*, 70, 1831-1842.

Stein, O., and P. Julien (1993), Criterion delineating the mode of headcut migration, *Journal of Hydraulic Engineering*, *119*(1), 37-50.

Stein, O., P. Julien, and C. Alonso (1993), Mechanics of jet scour downstream of a headcut, *Journal of Hydraulic Research*, *31*(6), 723-738.

Stein, O. R., and D. A. LaTray (2002), Experiments and modeling of head cut migration in stratified soils, *Water Resources Research*, *38*(12), 20-21-20-12, DOI: 10.1029/2001WR001166.

Stockstill-Cahill, K. R., F. S. Anderson, and V. E. Hamilton (2008), A study of low-albedo deposits within Amazonis Planitia craters: Evidence for locally derived ultramafic to mafic materials, *Journal of Geophysical Research: Planets*, 113(E7), DOI: 10.1029/2007JE003036.

Sunshine, J. M. and C. M. Pieters (1998), Determining the composition of olivine from reflectance spectroscopy, *Journal of Geophysical Research*, *103*(E6), 13675-13688.

Sullivan, R., D. Banfield, J. F. Bell III, W. Calvin, D. Fike, D., M. Golombek, R. Greeley, J. P. Grotzinger, K. E. Herkenhoff, D. J. Jerolmack, M. C. Malin, D.

Ming, L. A. Soderblom, S. W. Squyres, S. Thompson, W. A. Watters, C. M. Weitz, and A. Yen (2005), Aeolian processes at the Mars exploration rover Meridiani Planum landing site, *Nature*, *436*(7047), 58-61, DOI: 10.1038/nature03641.

Sullivan, R., R. E. Arvidson, J. F. Bell III, R. Gellert, M. Golombek, R. Greeley, K. Herkenhoff, J. Johnson, S. Thompson, and P. Whelley (2008), Wind-driven particle mobility on Mars: Insights from Mars Exploration Rover observations at El Dorado and surroundings at Gusev Crater, *Journal of Geophysical Research: Planets*, *113*(E6), DOI: 10.1029/2008JE003101.

Sweet, M., J. Nielson, K. Havholm, and J. Farrelley (1988), Algodones dune field of southeastern California: case history of a migrating modern dune field, *Sedimentology*, *35*(6), 939-952.

Tanaka, K., J. Skinner Jr, J. Dohm, R. Irwin III, E. Kolb, C. Fortezzo, T. Platz, G. Michael, and T. Hare (2014), *Geologic map of Mars: U.S. Geological Survey Scientific Investigations Map 3292, scale 1:20,000,000*, U.S. Geological Survey.

Thomas, N., H. Sierks, C. Barbieri, P. L. Lamy, R. Rodrigo, H. Rickman, D. Koschny, H. Uwe Keller, J. Agarwal, M.F. A'Hearn, F. Angrilli, A.-T. Auger, M. A. Barucci, J.-L. Bertaux, I. Bertini, S. Besse, D. Bodewits, G. Cremonese, V. Da Deppo, B. Davidsson, M. De Cecco, S. Debei, M. Ramy El-Maarry, F. Ferri, S. Fornasier, M. Fulle, L. Giacomini, O. Groussin, P. J. Gutierrez, C. Guttler, S. F. Hviid, W.-H. Ip, L. Jorda, J. Knollenberg, J.-R.. Kramm, E. Kuhrt, M. Kuppers, F. La Forgia, L. M. Lara, M. Lazzarin, J. J. Lopez Moreno, S. Magrin, S. Marchi, F. Marzari, M. Massironi, H. Michalik, R. Moissl, S. Mottola, G. Naletto, N. Oklay, M. Pajola, A. Pommerol, F. Preusker, L. Sabau, F. Scholten, C. Snodgrass, C. Tubiana, J.-B. Vincent, and K.-P. Wenzel (2015), The morphological diversity of comet 67P/Churyumov-Gerasimenko, *Science*, *347*(6220), DOI: 10.1126/science.aaa0440.

Thomas, N., and J. Bandfield (2013), Identification of Spectral Endmembers in CRISM Data Using Factor Analysis and Target Transformation, paper presented at 44th Lunar and Planetary Science Conference, The Woodlands, Tex.

Tinkler, K. (1997), Critical flow in rockbed streams with estimated values for Manning's n, *Geomorphology*, *20*(1), 147-164.

Tirsch, D., R. Jaumann, A. Pacifici, and F. Poulet (2011), Dark aeolian sediments in martian craters: Composition and sources, *Journal of Geophysical Research: Planets*, 116(E3), DOI: 10.1029/2009JE003562.

Tokyay, N. D., and D. Yildiz (2007), Characteristics of free overfall for supercritical flows, *Canadian Journal of Civil Engineering*, *34*(2), 162-169.

Tomasson, H. (2002), Catastrophic floods in Iceland, in *Extremes of the Extremes: Extraordinary Floods*, edited by A. Snorrason, et al., pp. 121-126.

Tompkins, S., J. F. Mustard, C. M. Pieters, and D. W. Forsyth (1997), Optimization of endmembers for spectral mixture analysis, *Remote Sensing of Environment*, *59*(3), 472-489.

Tosca, N. J., S. M. McLennan, B. C. Clark, J. P. Grotzinger, J. A. Hurowitz, A. H. Knoll, C. Schroder, and S. W. Squyres (2005), Geochemical modeling of evaporation processes on Mars: Insight from the sedimentary record at Meridiani Planum, *Earth and Planetary Science Letters*, *240*(1), 122-148, DOI: 10.1016/j.epsl.2005.09.042.

Tosca, N. J., S. M. McLennan, M. P. Lamb, and J. P. Grotzinger (2011), Physicochemical properties of concentrated Martian surface waters, *Journal of Geophysical Research: Planets*, *116*(E5), DOI: 10.1029/2010JE003700.

Trampush, S., S. Huzurbazar, and B. McElroy (2014), Empirical assessment of theory for bankfull characteristics of alluvial channels, *Water Resources Research*, *50*(12), 9211-9220, DOI: 10.1002/2014WR015597.

Trang, D., P. G. Lucey, J. J. Gillis-Davis, J. T. Cahill, R. L. Klima, and P. J. Isaacson (2013), Near-infrared optical constants of naturally occurring olivine and synthetic pyroxene as a function of mineral composition, *Journal of Geophysical Research: Planets*, *118*(4), 708-732, DOI: 10.1002/jgre.20072.

Tucker, G. E., L. Arnold, R. L. Bras, H. Flores, E. Istanbulluoglu, and P. Solyom (2006), Headwater channel dynamics in semiarid rangelands, Colorado high plains, USA, *Geological Society of America Bulletin*, *118*(7-8), 959-974.

van den Berg, J.-I., and A. van Gelder (1993), A new bedform stability diagram, with emphasis on the transition of ripples to plane bed in flows over fine sand and silt, *Alluvial Sedimentation* (Special Publication 17 of the IAS), 66, 11.

Vanoni, V. A., and N. H. Brooks (1957), *Laboratory studies of the roughness and suspended load of alluvial streams*, California Institute of Technology Sedimentation Laboratory.

Vanoni, V. A., and L.-S. Hwang (1967), Relation between bed forms and friction in streams, *Journal of the Hydraulics Division*, *93*(3), 121-144.

Vaz, D. A., and S. Silvestro (2014), Mapping and characterization of small-scale aeolian structures on Mars: An example from the MSL landing site in Gale Crater, *Icarus*, *230*, 151-161, DOI: 10.1016/j.icarus.2013.08.007.

Vaz, D. A., S. Silvestro, P. T. Sarmento, and M. Cardinale (2016), Migrating meter-scale bedforms on Martian dark dunes: Are terrestrial aeolian ripples good analogues?, *Aeolian Research*, in press, DOI: 10.1016/j.aeolia.2016.08.003.

Venditti, J. G., M. Church, and S. J. Bennett (2005), Morphodynamics of small-scale superimposed sand waves over migrating dune bed forms, *Water Resources Research*, 41, DOI: 10.1029/2004WR003461.

Vigilar, J., G. Gregorio, and P. Diplas (1997), Stable channels with mobile bed: formulation and numerical solution, *Journal of Hydraulic Engineering, 123*(3), 189-199.

Vigilar, J., G. Gregorio, and P. Diplas (1998), Stable channels with mobile bed: model verification and graphical solution, *Journal of Hydraulic Engineering*, *124*(11), 1097-1108.

Villanueva, G., M. Mumma, R. Novak, H. Kaufl, P. Hartogh, T. Encrenaz, A. Tokunaga, A. Khayat, and M. Smith (2015), Strong water isotopic anomalies in the martian atmosphere: Probing current and ancient reservoirs, *Science*, *348*(6231), 218-221, DOI: 10.1126/science.aaa3630.

Viviano-Beck, C. E., F. P. Seelos, S. L. Murchie, E. G. Kahn, K. D. Seelos, H. W. Taylor, K. Taylor, B. L. Ehlmann, S. M. Wisemann, and J. F. Mustard (2014), Revised CRISM spectral parameters and summary products based on the currently detected mineral diversity on Mars, *Journal of Geophysical Research: Planets*, 119(6), 1403-1431, DOI: 10.1002/2014JE004627.

Wang, C. Y., M. Manga, and J. C. Hanna (2006), Can freezing cause floods on Mars?, *Geophysical Research Letters*, *33*(20), DOI: 10.1029/2006gl027471.

Warner, N., S. Gupta, J.-P. Muller, J.-R. Kim, and S.-Y. Lin (2009), A refined chronology of catastrophic outflow events in Ares Vallis, Mars, *Earth and Planetary Science Letters*, *288*(1), 58-69, DOI: 10.1016/j.epsl.2009.09.008.

Warner, N. H., S. Gupta, J.-R. Kim, S.-Y. Lin, and J.-P. Muller (2010), Retreat of a giant cataract in a long-lived (3.7-2.6 Ga) martian outflow channel, *Geology*, *38*(9), 791-794.

Werner, B. T., P. K. Haff, R. P. Livi, and R. S. Anderson (1986), Measurement of eolian sand ripple cross-sectional shapes, *Geology*, *14*(9), 743-745.

Whipple, K. X., G. S. Hancock, and R. S. Anderson (2000), River incision into bedrock: Mechanics and relative efficacy of plucking, abrasion, and cavitation, *Geological Society of America Bulletin*, *112*(3), 490-503.

Williams, G. P. (1967), Flume experiments on the transport of a coarse sand, Volume No. 562-B, U.S. Geological Survey, 37 p.

Williams, R. M., R. J. Phillips, and M. C. Malin (2000), Flow rates and duration within Kasei Valles, Mars: Implications for the formation of a Martian ocean, *Geophysical Research Letters*, *27*(7), 1073-1076.

Williams, R. M., and M. C. Malin (2004), Evidence for late stage fluvial activity in Kasei Valles, Mars, *Journal of Geophysical Research: Planets*, *109*(E6), DOI: 10.1029/2003JE002178.

Wilson, I. G. (1972), Aeolian bedforms—their development and origins, *Sedimentology*, *19*(3-4), 173-210.

Wilson, L., G. J. Ghatan, J. W. Head, and K. L. Mitchell (2004), Mars outflow channels: A reappraisal of the estimation of water flow velocities from water depths, regional slopes, and channel floor properties, *Journal of Geophysical Research: Planets*, *109*(E9), DOI: 10.1029/2004JE002281.

Withers, P., and M. D. Smith (2006), Atmospheric entry profiles from the Mars exploration rovers Spirit and Opportunity, *Icarus*, *185*(1), 133-142, DOI: 10.1016/j.icarus.2006.06.013.

Wohl, E. E. (1992), Bedrock benches and boulder bars: Floods in the Burdekin Gorge of Australia, *Geological Society of America Bulletin*, *104*(6), 770-778.

Wohl, E. E. (2008), The effect of bedrock jointing on the formation of straths in the Cache la Poudre River drainage, Colorado Front Range, *Journal of Geophysical Research: Earth Surface*, *113*(F1), DOI: 10.1029/2007JF000817.

Wordsworth, R. D. (2016), The climate of early Mars, *Annual Review of Earth and Planetary Sciences*, *44*, 381-408, DOI:10.1146/annurev-earth-060115-012355.

Yalin, M. S. (1977), *Mechanics of sediment transport*, Pergamon Press.

Yalin, M. S., and E. Karahan (1979), Inception of sediment transport, *Journal of the Hydraulics Division*, *105*(11), 1433-1443.

Yalin, M. S. (1985), On the determination of ripple geometry, *Journal of Hydraulic Engineering*, 111, 1148–1155, DOI:10.1061/(ASCE)0733-9429(1985)111:8(1148).

Yamaguchi, Y., A. B. Kahle, H. Tsu, T. Kawakami, and M. Pniel (1998), Overview of advanced spaceborne thermal emission and reflection radiometer (ASTER), *IEEE Transactions on geoscience and remote sensing*, *36*(4), 1062-1071.

Yizhaq, H., J. F. Kokand I. Katra (2014), Basaltic sand ripples at Eagle Crater as indirect evidence for the hysteresis effect in martian saltation, *Icarus*, *230*, 143-150, DOI: 10.1016/j.icarus.2013.08.006.

Zegers, T. E., J. H. P. Oosthoek, A. P. Rossi, J. K. Blom, and S. Schumacher (2010), Melt and collapse of buried water ice: An alternative hypothesis for the formation of chaotic terrains on Mars, *Earth and Planetary Science Letters*, *297*(3-4), 496-504, DOI: 10.1016/j.epsl.2010.06.049.

Zeidler, S., T. Posch, H. Mutschke, H. Richter, and O. Wehrhan (2011), Near-infrared absorption properties of oxygen-rich stardust analogs-The influence of coloring metal ions, *Astronomy and Astrophysics*, 526, A68, DOI: 10.1051/0004-6361/201015219.

Zimbelman, J. R. (2010), Transverse aeolian ridges on Mars: first results from HiRISE images, *Geomorphology*, *121*(1), 22-29, DOI: 10.1016/j.geomorph.2009.05.012.

Zoppou, C., and S. Roberts (1999), Catastrophic collapse of water supply reservoirs in urban areas, *Journal of Hydraulic Engineering*, *125*(7), 686-695.

Zuluaga, L. F., H. Fossen, and A. Rotevatn (2014), Progressive evolution of deformation band populations during Laramide fault-propagation folding: Navajo Sandstone, San Rafael monocline, Utah, USA, *Journal of Structural Geology*, *68*, 66-81, DOI:10.1016/j.jsg.2014.09.008.